b
UNIVERSITÄT
BERN

UNIVERSITÀ DEGLI STUDI DI CATANIA
UNIVERSITÀ DEGLI STUDI DI PALERMO
UNIVERSITÄT BERN

DOTTORATO DI RICERCA IN
SCIENZA DEI MATERIALI E NANOTECNOLOGIE
XXXI CICLO

Alice Sciortino

The Fundamental Photophysics of Fluorescent Carbon Nanodots

Tutor:

Dr. F. Messina (UniPA)

Prof. Dr. A. Cannizzo (UniBe)

Coordinatore:

Prof.ssa M. G. Grimaldi (UniCT)

Tesi per il conseguimento del titolo di Dottore di Ricerca

Settembre 2018

Contents

Preface

Carbon Nanodots (CDs) are a new protagonist of carbon-based nanoscience by which the paradigm of carbon as a *black* material unable to emit light has been completely revolutionised. They have been emerging as a new frontier in Nanoscience at the beginning of 2000s [1,2], and their potential is evident from the explosion of the number of studies, now ranging in the thousands per year.

CDs are nanoparticles (usually spherical) composed by carbon, oxygen and hydrogen with a size smaller than $\approx$ 10 nm (Figure 1). Their most important hallmark is their strong luminescence, which is combined with many additional benefits as the low cost and ease of synthesis, the high water solubility, the biocompatibility and non-toxicity, the great sensitivity to the external environment, and a marked electron donating and accepting capabilities. The combination of all of these characteristics guarantees the possibility to use CDs in a very broad range of applications which encompasses many different fields as optoelectronics or sensing.

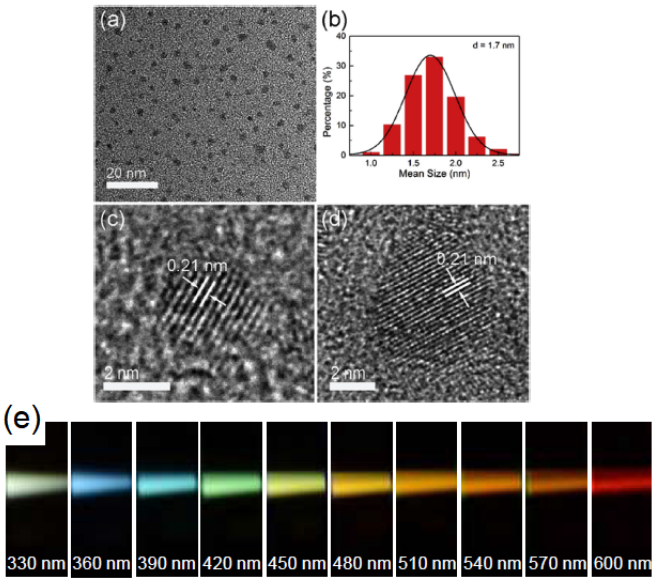

Figure 1: (a) Transmission electron microscopy image of CDs; (b) Size distribution of CDs; (c) and (d) examples of single crystalline CDs from (a) [From [3]]. (e) Example of tunable fluorescence of CDs photographed during the photoexcitation at different wavelengths (indicated in figure) [adapted from [4]]

Actually, the term CDs includes nanomaterials which display a wide range of possible structures and variable optical properties. Indeed, in the literature, it is common to find different *sub-types* of CDs: they can be graphitic [1], amorphous [5], disks of graphene (called graphene quantum dots - GQDs) [6] or with a C_3N_4 core [7,8]; they can be hydrophilic or hydrophobic [9]; they can emit blue [10], green [1], or red light [11]; their emission can be independent of the

excitation wavelength [12], or more commonly tunable (peak of the emission depends on the excitation wavelength) [13]; their fluorescence intensity can be sensitive to one particular ion in solution [14, 15] or they respond to a variety of interactions with other systems, such as carbon nanotubes (CNTs) [5]. Besides, CDs can be synthesized by many different procedures (*top-down* or *bottom-up*) which yield subtypes of CDs capable of emitting fluorescence at different wavelengths.In all the synthesis approaches, their surface is *passivated* (during or after the synthesis) by external agents [16] to get bright emission. The term *passivation* indicates the formation of a layer of functional groups or molecules which bind to the carbonaceous core. Such a layer is usually required for CDs to display a high luminescence, although the passivating groups are not fluorescent by themselves. All of this leads to the existence in the literature of diverse sub-types of CDs with different core and surface structure, and different specific optical characteristics.

Despite of this, there are common characteristics which are recurrent almost in every type of CDs as the small size ($\approx$ 10 nm or less) and the core+corona (the shell around the core) structure which are found to be crucial to obtain CDs with a visible photoluminescence with a high emission efficiency.

Carbon dots research is still in a developing phase despite thousands of studies have already been published on the subject, and several scientific open questions exist about their optical behaviour, the fundamental nature of the electronic states, the key factors determining their bright fluorescence, and the relation between structure and emission. As a consequence, a large effort is in progress to find the most effective ways to tailor them for specific applications.

In this Thesis, we carried out an investigation of the fundamental physics of different families of CDs with the aim to achieve an exhaustive understanding of their entire photocycle from femtosecond to the steady state. To do this, it was necessary to relate the optical properties to the structural ones, and to study the influence of various possible interactions with external agents. Thus, electronic transitions of CDs having different structures or exposed to different environments have been studied by the combined use of several experimental techniques. In particular, as an important novelty in the field, a variety of new methods which involve ultrafast spectroscopic techniques have been used. Ultrafast spectroscopy is a powerful tool to investigate in real time electronic and vibrational processes with picosecond (10^{-12} s) and femtosecond (10^{-15} s) time resolution. With the use of these methods it was possible to map the photocycle of CDs revealing several dynamics which occur on short time scale as solvation, charge transfer, and fluorescence quenching.

The Thesis is organized in 9 chapters. The first three are introductory, while Chapters 4 to 9 are devoted to the presentation of the results.

- Chapter 1 reviews the literature of Carbon Nanodots focusing the attention on the open questions addressed during this Thesis: the emission mechanisms of CDs, the origin of fluorescence tunability and the interactions with the external environment. In addition, a paragraph is entirely devoted to review the existing experiments on CDs with ultrafast spectroscopies, still very few in the literature;

- Chapter 2 gathers the theoretical background useful to describe the basic photophysics of these systems;

- Chapter 3 includes the description of the synthesis procedures of the different CDs studied in this work, of the experimental setups and the underlying theoretical background (in particular for the ultrafast techinques) and of the data analysis procedures we used throughout our research;

- Chapter 4 presents the basic structural and optical characterization of home-synthesized

CDs. This characterization reveals two families of CDs with different properties and, in particular, highlights the discovery of CDs with a new core structure, never reported before in the literature;

- Chapter 5 addresses the emission mechanisms of CDs by comparing different families of CDs synthesized by diverse methods. These studies have been conducted with the use of steady state and nanosecond time resolved spectroscopy trying to separate the role of surface or core in the electronic transitions which produce an emission;
- Chapter 6 presents our experiments aimed at disclosing the entire photocycle of different CDs by the combined use of various femtosecond methods;
- Chapter 7 is focused on the investigation of the interaction between ions in solution with a specific family of CDs. In particular, the interaction between CDs and metal ions is studied down to the femtosecond scale;
- Chapter 8 investigates fluorescence tunability of CDs taking as a model a specific family of CDs. The tunability and inhomogeneity, for the first time in CDs literature, have been studied by femtosecond hole burning experiments.
- Chapter 9 gathers the main conclusions and discusses some proposals for further work.

Most of the results presented in this work have been already published as papers on scientific Journals.

Part I

Introduction

Chapter 1

State of the Art

The aim of this first chapter is to give an introduction on the general properties of Carbon dots and on the open questions which are debated in the literature. The most relevant aspects to this work are discussed, to provide an overview of the established knowledge, but also to underline the lively debate which pervades the entire literature.

In particular, a general phenomenological overview on the most relevant synthesis procedures, on the structural and optical properties, and on the applications is given. In the following paragraphs, the open questions existing in the literature are analysed in more details to present the state of the art.

1.1 Carbon Nanodots: An overview

Synthesis

Many different routes to produce CDs have been reported in the literature. Generally speaking, they can be categorized in two families: *top-down* and *bottom-up* approaches (Figure 1.1).

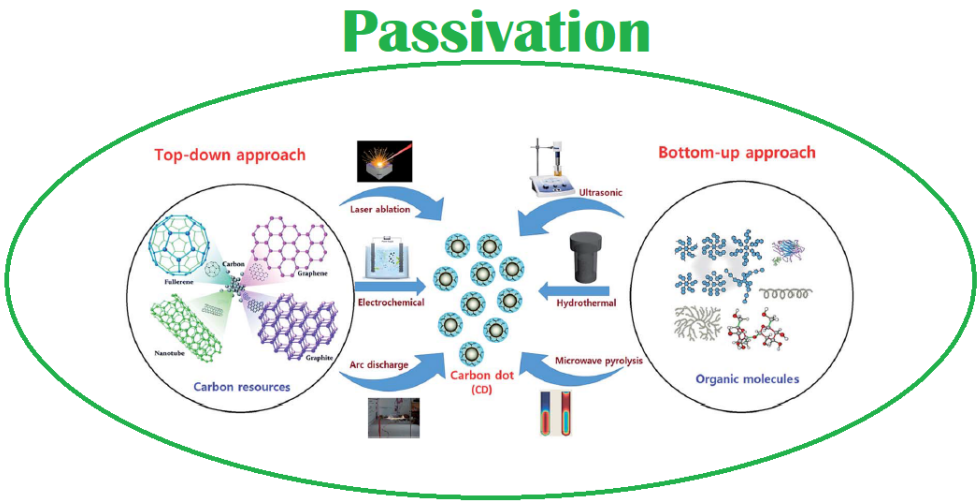

Figure 1.1: Representation of the possible synthesis methods to prepare carbon dots (adapted from [17]).

Top-down methods involve the disruption of bulk carbon precursors as graphite or nanomaterials with higher dimensionality than CDs (considered zero-dimensional) as carbon nanotubes

(1D material). Several methods are used in the literature (Figure 1.1): laser ablation [1], electrochemical synthesis [18], arc discharge [2], or chemical oxidation [19]. In many cases, the products from these types of synthesis are not fluorescent immediately after it. However, many groups reported that they can be transformed into highly fluorescent nanoparticles by passivating their surface, after the synthesis, with various polar moieties producing, in this way, highly fluorescent nanoparticles [1, 19].

On the contrary, bottom-up syntheses consist usually in the carbonization of different molecular precursors as citric acid [20], sucrose [21], etc. which produce "pure" carbon-core CDs, or other molecular precursors as urea [7], and thiourea [22] which dope their structure with nitrogen or sulphur atoms. Bottom-up syntheses are usually achieved in *one pot*: CDs emission is very bright without any passivation procedure. This evidence suggests that the surface structure of the as-synthesized CDs spontaneously achieves the appropriate characteristics needed for an intense fluorescence.

While the structure of CDs obtained by top-down synthesis typically resembles the structure of the precursors (e.g. graphitic CDs from laser ablation or electrochemical oxidation of graphite), bottom-up routes yield a larger variety of CD structures and sometimes lead to the formation of small fluorescent molecules together with the dots, as will be described in more detail in the next paragraph.

Here, representative examples of preparation methods are reported in order to give a comprehensive overview on the several ways to produce CDs.

Laser Ablation Laser ablation was the first method used to produce CDs in a controlled way [1].

It is a top-down method which is frequently used for the production of many different types of nanoparticles. Laser ablation consists in the interaction of laser pulses with the surface of a target (solid precursor) and the consequent ejection of materials in the form of nanoparticles [23].

In the first study focusing on the synthesis of CDs [1], the authors ablated a graphite target under an argon flow in the presence of water vapor, obtaining non-luminescent carbon nanoparticles (and aggregates of them). Only after an acidic treatment of the surface and the following surface passivation by organic molecules, those carbon nanoparticles become bright luminescent and, therefore, can be called *carbon dots*. After the first pioneering laser ablation of CDs, many other studies have been conducted on this synthesis protocol in order to control the characteristics of the synthesized materials. Changing laser ablation parameters, as the pulse duration or laser wavelength, can be used to control CDs characteristics, as observed for other nanomaterials [23]. In the case of CDs, some works focused on the effects of ablation parameters as the wavelength [24] or the duration of the pulses used to ablate [25].

Hu et al. [25] discovered that a one-step synthesis from graphite flakes in polymer solution changing pulse duration (from 0.3 ms to 1.5 ms) of a 1064 nm laser beam is an effective way to control CDs size (from 3 nm to 13 nm). These sub-sets present different morphology and various core structure: the smallest particles are single mono-crystals and the other are composed by multiple crystalline grains, and show a quantum yield which decreases with increasing size. A passivation procedure is not needed after this synthesis procedure, suggesting that surface passivation probably occurs simultaneously to the formation of nanoparticles, caused by the presence of the polymeric solution. Varying pulse duration seems to change the conditions of the nucleation and growth process and, therefore, changes the size distribution.

Also the laser wavelength is a fundamental parameter during the ablation of a target. In ref. [24] the authors demonstrate that ablating graphite with a wavelength in the UV-range (355 nm) produces 5 nm crystalline CDs without the formation of any aggregates, whereas the use of a beam at 532 nm or 1064 nm produces lots of carbon aggregates. Also in this case, no post-synthesis functionalization is needed to obtain highly fluorescent CDs. In fact ,the laser ablation

is performed in acetone solution and probably laser interaction with the solvent could induce the formation of radicals through the dissociation of solvent molecules, and their subsequent attachment to the surface of the nanoparticles, inducing their functionalization with ketone groups. Moreover, the authors studied the influence of the irradiation time and found a peak of emission efficiency after 150 s of ablation which decreases with longer times.

Electrochemical synthesis Electrochemical synthesis is a top-down method which consists in a redox reaction of chemical compounds in an electrochemical cell which occurs under the influence of an electric current applied between two electrodes (solids) separated by the electrolyte (liquid) [26].

The first electrochemical synthesis of CDs was reported by Zhu et al. [10]. They demonstrated this novel method for the production of graphitic CDs with highly blue luminescence where multi-walled carbon nanotubes (MWCNTs) were used as an electrode during the synthesis. The use of precursors with graphitic structure seems to produce prevalently graphitic CDs or GQDs [6,27,28].

Many other works have been published on CDs obtained from electrochemical synthesis. An important step forward in the literature was the discover of the importance of alkaline environment [27]. In fact, Li et al. demonstrated that using graphite rods as both the electrodes in an alkaline environment (NaOH/EtOH) it was possible to produce graphitic CDs with bright emission, while the same experiment in acidic condition did not produce any fluorescent CDs. They suspected that the presence of OH^- groups is the key factor for the formation and for the oxidation of CDs surface which makes them luminescent. Also, Shinde et al. [6] demonstrated the importance of the electrolyte showing that in an aqueous medium they were able to produce graphene nanoribbons from MWCNTs, while in non-aqueous media they obtained luminescent GQDs. Moreover, they were able to control the size of the product from 3 nm to 8 nm, tuning the time of the electrochemical synthesis from 15 h to 7 h. Another way to tune and control the diameter of CDs is to vary the applied potential [28]. It seems that the higher is the applied voltage, the smaller are the synthesized dots.

Thermal and Microwave Decomposition Thermal and microwave decompositions are two similar bottom-up procedures which consist in the carbonization of molecular precursors caused by thermal reactions, generally carried out in liquid phase (hydrothermal or solvothermal synthesis). The first thermal decomposition used for the production of CDs was reported by Bourlinos et al. [9]. They prepared two different amorphous CDs from two different precursors. One sample was hydrophilic and it results from the carbonization of 2-(2-aminoethoxy)-ethanol salt. The other was organophilic and comes from the carbonization of octadecyl ammonium citrate salt.

The first microwave pyrolysis was reported in 2009 by Zhu et al. [16]. They succesfully produced luminescent CDs by the carbonization of aqueous solution with different amounts of poly-(ethylene glycol) (PEG-200) and different saccharides (glucose, fructose etc). These dots are amorphous and display the typical fluorescence tunability, and the authors noticed that CDs are not luminescent if during the synthesis PEG-200 is not present, this probably indicates that the role of PEG-200 is to passivate, during the synthesis, the surface of nanoparticles.

Since these two works, several more studies used these techniques to synthesize CDs because of many advantages with respect to top-down methods. In fact, the synthesis is low cost (some authors used as precursors raw materials as orange juice [29], grass [13], etc), fast (few minutes), and does not need any further passivation, differently from most top-down routes. Furthermore, these syntheses allow to easily introduce external atoms which dope the system changing its structural and optical characteristics. In fact, bottom-up methods have allowed to obtain the CDs with the highest emission efficiencies reported in the literature so far. The common doping agents are Nitrogen [4,7,8,14,20,30–32], Sulphur [15,33,34], Boron [35–38] and Phosphorous [39,40] atoms.

It seems, in fact, that the introduction of these doping agents modifies completely the structure and increases, for instance, the emission quantum efficiency of the produced sample, although the physical mechanisms behind this is still unclear [7, 8]. In particular, addition of Nitrogen atoms seems to dramatically enhance the emission quantum yield. Indeed, N-doping even in low content has been supposed to be responsible of a new electron trapping surface state facilitating a high yield of radiative recombination [41, 42]. However, the influence of nitrogen atoms on the emission remains poorly understood, since there are several possible sites of nitrogen in N-doped CDs. Besides superficial organic moieties such as amide and amine [41, 42] some studies have found that nitrogen influences the electronic properties by taking part to the core structure [43]. Indeed, high levels of N-doping sometimes result in the formation of particular networks such as carbon nitride nanocrystals [7], which are difficult or impossible to obtain by top down methods (more details in following paragraphs).

Purification and Separation Methods One widespread problem of CDs production methods is the heterogeneity of CDs, in the sense that several syntheses reported in the literature yield CDs with a large degree of structural heterogeneity, as for example very broad size distributions, large dot-to-dot variations in surface structure, optical heterogeneity, or the contamination of the sample by small fluorescent molecules produced together with CDs. Therefore, the use of a purification method is often needed to purify the system, and sometimes is also used to select some sub-sets of CDs based on their size or their surface structure. In some cases, separation methods have indeed been used simply to select to select the most fluorescent part of a CD sample, out of a heterogeneous distribution of fluorescent quantum yields [44]. The most common purification methods are dialysis [45, 46] used to purificate a sample from small impurities, centrifugation [47], mostly used to remove any aggregates, size exclusion chromatography [48–50], and high performance liquid chromatography (HPLC) [51,52]. Size exclusion chromatography (SEC) allows to separate the nanoparticles by their size. In ref [48], the authors take advantage of this to obtain two fractions with different morphological and optical properties. In particular, they succeed in having two distinct CD samples which emit respectively in the green (the smaller) or in the blue (the bigger). Arcudi et al. [49] used SEC in order to obtain a quasi-monodispersed samples, and in ref [51] the authors used HPLC to obtain different fractions with different optical features which can be related to the size of the samples. Having a monodispersed sample or a sample with a well-defined optical feature is very helpful in order to simplify the system and to understand, for instance, the emission mechanism and its relation to the specific structure.

The structure

Core and surface structures of CDs are quite variable in the literature. On one hand, core structure can be crystalline or amorphous, and on the other hand, the corona which envelops the core can host different polar, or apolar groups, the structure of which ranges from small functional groups to long atomic chains. This opens a great range of possibilities to design different types of CDs. In the attempt to rationalize this variability, several authors tried to classify existing CDs in various sub-types [53]. However, no universal classification is currently accepted in the literature. For the purpose of this work, it is useful to attempt here a sort of classification of the most relevant types of CDs found in the literature (Figure 1.2).

Spherical graphitic CDs are probably the most common in the literature [1,20,25,49,50,54–57]. As in graphite, the core is composed by layers of sp^2-hybridized carbon stacked on top of each other, where the lateral dimension of the layers is limited by the overall dot diameter which is typically of a few nanometers. The crystalline nature of the core is usually confirmed by the combination of different structural techniques, such as high resolution transmission microscopy

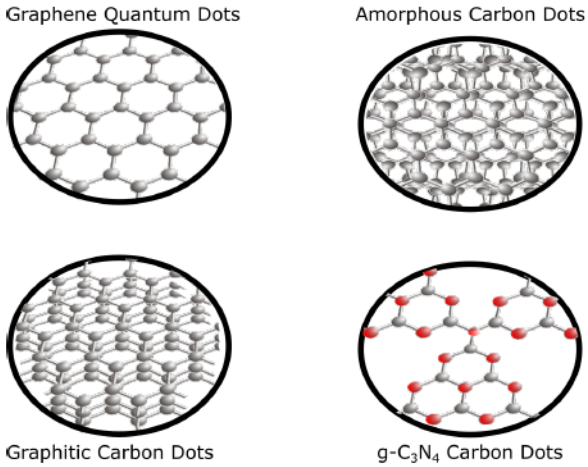

Figure 1.2: Schematic representation of commonly reported core structures of CDs.

(HRTEM), X-ray diffraction (XRD), and Raman spectroscopy, as reported in Figure 1.3 where the graphitic core is visualized by HRTEM measurements, and confirmed by Raman spectrum. More-

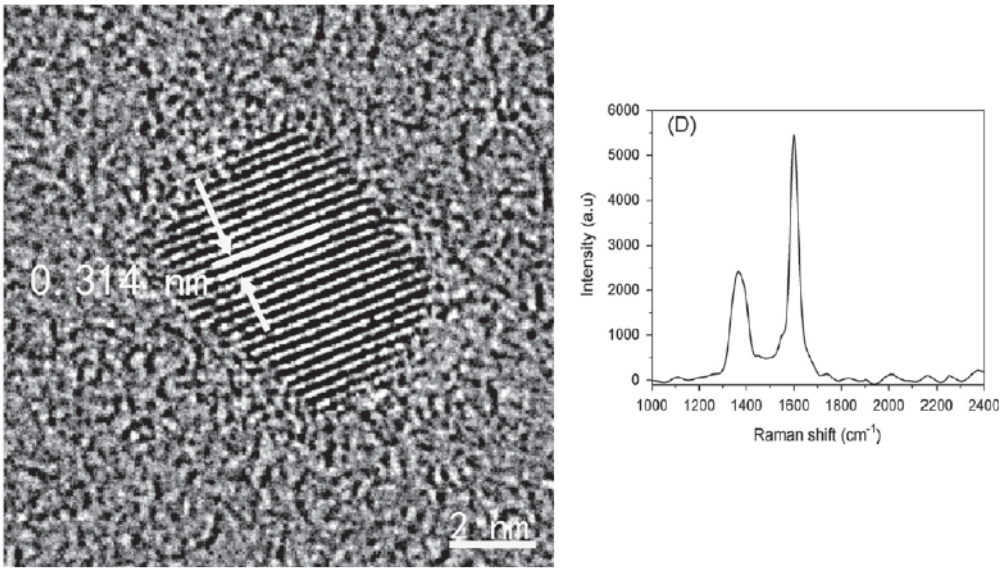

Figure 1.3: HRTEM image (left) of CDs with graphitic core structure; the average lattice spacing of these CDs is 0.314 nm which is compatible with the (002) planes of graphite. Raman spectrum (right) of graphitic CDs; the spectrum shows two peaks at 1369 cm^{-1}, assigned to the D band associated to sp^3 hybridization and at 1590 cm^{-1}, assigned to the G band which is associated to sp^2 hybridization of carbon. [Adapted from [57]]

over, HRTEM combined with atomic force microscopy (AFM) allows to have information not only on the core structure but also on its extension and morphology. This, for instance, guarantees the discrimination between graphitic dots and graphene dots [6, 51, 58]. The latter are not spherical particles but are small disks made by 1-3 layers of graphene stacked on each other, they display similar phenomenological optical characteristics compared to spherical CDs, and again the emission mechanisms controlling them are unclear.

However, CDs with crystalline cores are not limited to a graphitic structure. In fact, other possible structures were reported for CDs synthesized in special conditions, notably CDs with

graphitic carbon nitride cores (g-C_3N_4), as reported by a few works [7, 59]. This structure apparently shows up when the amount of nitrogen as a doping agent is so large that the core structure is forced to diverge from its graphitic nature. Similar to graphite, g-C_3N_4 is a layered material, and each layer consists in the repetition of a structural motif consisting in three hexagonal rings where carbon and nitrogen atoms in sp^2 hybridization are alternated (Figure 1.2).

Besides the crystalline varieties, it is possible to find many examples of amorphous CDs [5, 9, 13, 29, 60–62] which contain a mixture of sp^2 and sp^3 hybridized carbon, without any long periodicity in the core. Except for the core structure, however, they apparently exhibit rather similar characteristics with respect to crystalline dots, such as high fluorescence.

Last but not least, recently a new core structure has been proposed in the case of CDs synthesized by bottom-up procedures. This core structure involves the aggregation of small molecules which are formed usually during the carbonization of citric acid [63, 64], and kept together by comparatively weak interaction ($\pi - \pi$, H-bonds, Van der Waals) into a quasi-spherical shape.

Until now only a core classification was presented. Also the surface of the dots can be very variable and hosts a variety of functional groups which can be identified by several techniques as infrared absorption (IR) technique, thermal gravimetric analysis (TGA). Generally speaking, the surface functional groups establish if the sample is hydrophilic or hydrophobic [9, 65]. However, most synthesis routes yield CDs which are highly water soluble, a characteristic which is very useful for many applications as discussed in the next paragraph, due to the abundance of surface polar groups, such as Hydroxyl, Carboxyl, Carboxylate, Amine, and Amide. Beside "standard" polar groups, some authors passivated the surface with more complex molecules as polyethyleneimine (a long chain which contains primary, secondary and tertiary amine groups), still obtaining highly fluorescent CDs [60, 66–68].

Usually, the presence of a proper surface passivation is compulsory to have bright fluorescence. In fact, deliberate chemical passivation of the surface is often necessary after the synthesis (especially in top-down cases) in order to obtain highly fluorescent CDs [1, 54–56, 69]. Passivation procedures consist in the chemical treatment of the surface of the nanoparticle with different solvents or molecules as acetone or polyethylene glycol (PEG).

Based on the major influence of the surface passivation on the fluorescence, and considering that both amorphous and crystalline dots display a similar optical phenomenology, it may seem that the core has a negligible influence on the emission mechanism and that only the surface plays a key role in the emission. Despite of this, some authors [70, 71] provided evidence that the core can be fundamental in the photocycle of CDs as the surface, as will be explained in more details in the next section.

Optical properties: an outline

Photoluminescence is the most intriguing and the most unclear characteristic of CDs. It is strong [12, 52, 72–74], *tunable* [1, 4, 19, 66, 73], and very sensitive to local environment: solvents [75, 76], ions [15, 18, 59], pH [68], external agents such as carbon nanotubes (CNTs) [5, 56]. Moreover, it usually occurs only when the particles are well dispersed. In fact, aggregation seems to turn off the emission [77, 78].

Usually, electronic absorption covers both UV- and visible range. This allows to photo-excite CDs in a very broad spectral range causing the tunability of the emission: the position of the emission peak changes with the excitation wavelength (Figure 1.4). This provides a multi-color emission from blue to green, and sometimes to the red, although the absorption and the emission efficiency usually decrease at longer wavelengths [79]. This emission is often combined with a high quantum yield which, however, strongly depends on the synthesis conditions. Many works demonstrate that this emission is very sensitive to the external environment and strongly responds to its changes [5, 76, 80–82]. For instance, CDs show a clear dependence of the emission band

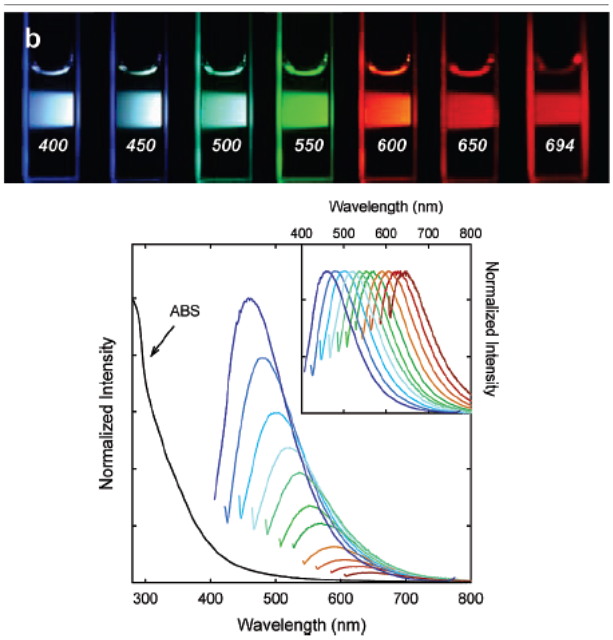

Figure 1.4: Top panel: Solution of CDs excited at the indicated wavelengths and photographed. Bottom panel: Absorption spectrum (black curve) and emission spectra at different excitation wavelengths (Inset: emission normalized spectra). [Adapted from [1]]

(peak and/or shape) on the solvent polarity (solvatochromic behaviour) [76] although it has been generally very difficult to find a rationale for such a behavior. In addition, CDs respond to metal ions in solution. In fact, their fluorescence can be either quenched or enhanced in presence of metal cations (Hg^{2+}, Cu^{2+}, Fe^{3+}, Ag^{+}, ...), the specific response being strongly dependent on the particular structure of CD. Some CDs are also sensitive to other agents in solution as CNTs [5] or various molecules [80–82].

Overall, the optical properties of CDs are competitive to fluorescent semiconductor quantum dots (QDs). Compared to them, luminescent CDs are superior in terms of aqueous solubility, high resistance to photobleaching, low toxicity and good biocompatibility [53]. Besides, they do not usually show blinking effects, they display strong absorption in the blue and UV ranges, and their reported QYs are steadily increasing, due to the progressive improvement of the synthesis procedures.

This unique blend of properties make CD very interesting and promising for many applications which are described in the next paragraph.

Applications

CDs offer the perspective of a C-based equivalent of optically-active quantum dots (QDs) with the additional benefits of C-based materials, as the absence of toxic elements (typically heavy metal atoms) which limit the use of QDs in biological field. Their bright emission combined with the marked electron-donor capability can be exploited, for instance, in optoelectronic devices [67, 83–86]; furthermore, the sensitivity of the emission to metal ions in solution is exploited to create nanosensors capable of recognizing different cations [87–93]. Their non-toxicity is taken as an advantage to perform *in vivo* [94–98] and *in vitro* [32, 81, 89, 99–101] bioimaging experiments and to perform drug delivery experiments [102]. The range of applications in which CDs have shown their potential is extremely wide: for examples, antiviral [103, 104] and antibacteri-

cal [105] capacities of CDs were recently discovered, and they were used as *nanoweapons* against mosquitos [106], and as component of fluorescent inks [20,48]. The majority of CDs-based devices have been developed and tested just in the laboratory environment so far. However, their commercial and industrial exploitation should not be too far. Here, the aim is to give a general survey on several potential applications, in order to illustrate the extensive applicability of CDs.

Nanosensing Applications In the literature, nanosensors based on CDs were developed by two different strategies: i) the nanosensors simply consisted of "pure" CDs as from the synthesis or passivated through specific target groups; and ii) the functional sensing nanomaterial was a composite obtained by coupling CDs with other nano- or micro-materials.

The use of CDs as "raw" sensors is quite common in the literature. Differently prepared CDs can be applied to detect various metal cations as Hg^{2+}, Cu^{2+}, Fe^{3+} [87–91], or small molecules or macromolecules in solution [98, 107–109]. Typically, when CDs are dissolved in a solution with a specific analyte, their luminescence is quenched (decreases), allowing to detect the analyte with high sensitivity and, often, high selectivity, as obtained by a proper engineering of the surface functional groups, interacting only with a given type of metal cation. The detection sensitivity can be very high and the minimum concentration of detectable ions can be as low as femtomolar [110]. However, the causes of quenching are very debated and may involve different fundamental interactions, such as a charge transfer from the dot to the ions, which hinders the radiative recombination [111], or by a Fluorescence Resonance Energy Transfer (FRET) or an energy transfer phenomenon from the dots to the acceptor, quenching the emission of CDs and enhancing the emission of the latter [112, 113]. Because of such a poor understanding, the engineering of these applications still proceeds mostly through trial-and-error routes.

As compared to metal cations or small neutral molecules, it is less common to find in the literature examples where CDs are used to detect anions [114] probably because CDs surface is usually negatively charged [115, 116]. The few existent articles describe the detection of negative ions as PO_4^{3-}, or S^{2-}, or SCN^- through the combination of CDs and a cation [92, 93, 117]. CDs emission, quenched by the cation, is recovered by the presence of anions which inhibits the quenching effect of the cations. This strategy is sometimes used in the second type of nanosensors. In some works, the authors proposed CD-based nanosensors where CDs are coupled to molecules [112, 118] as rhodamine, or to nanomaterials such as gold nanoparticles [117], or metal organic frameworks [113, 119–121]. The sensing occurs both by emission quenching or emission enhancing as a result of the detachment, for instance, of the nanoparticle from the surface of the dot induced by the presence of the analyte.

CDs are used also as, so-called, ratiometric sensors. Taking advantage of the simultaneous presence of two emission bands peaked at different wavelengths (characteristic called dual emission), it is possible to check the variation of their intensity ratio in order to have information on the amount of the detected analyte [122, 123]. Indeed, in the same sample, different interactions with the analyte can affect the chromophores responsible of the two bands. Therefore, the analyte can quench them at different rates, causing a change of their intensity ratio. This allows to use the variation of the intensity ratio between them as a physical quantity to trace the amount and the type of the analyte.

Biological and Nanomedical Applications To be safely applied in bioimaging, biosensing and nanomedicine, biological effects of a nanomaterial should be extensively investigated. Traditional QDs, such as CdTe, have been used in various optical bioimaging experiments. Considering that QDs often contain toxic heavy metals, their application has to be well controlled because of toxicity and environmental problems. Due to the bright photoluminescence and low toxicity, CDs are an attractive candidate for bioimaging applications. Indeed, cytotoxicity studies in vivo (on

zebrafish [97]) and in vitro [95, 96] generally show that CDs are not toxic. For instance, Kang et al. [97] demonstrated that the introduction of CDs into zebrafish embryos and larvae does not influence their development. Furthermore, they established the possible use of CDs as fluorescent bioimaging agents in living systems.

Other studies revealed further benefits of CDs for these applications. For instance, Shereema et al. [99] demonstrated their antiangiogenic effect on vessels by finding a significant reduction in the proliferation of tumoral membranes after a treatment with CDs. This gave the basis for using CDs in the field of cancer therapy.

Additionally to medical applications as anticancer or cancer targeting [96], they can be used as photo-activated [103] or not [104] antiviral agents, and photo-activated antibacterical [105] agents. For instance, they were used to reduce the entry of hepatitis C viruses into monkey kidney cancer cells and human lung cancer cells physically blocking the passage of the virus [104].

Furthermore, the versatility and ease of functionalization of CDs, combined with their bright fluorescence allow to use them as highly multifunctional nanotools. The combined use of these advantages is reported in ref [101] where CDs are decorated with a mitochondria targeting ligand and functionalized with a photoresponsive NO-releasing ligand (Figure 1.5). This system recognizes cancerous cells, wherein it attaches to the mitochondria and, then, upon irradiation it is able to release for a long time nitric oxide which is known to be a good therapeutic agent.

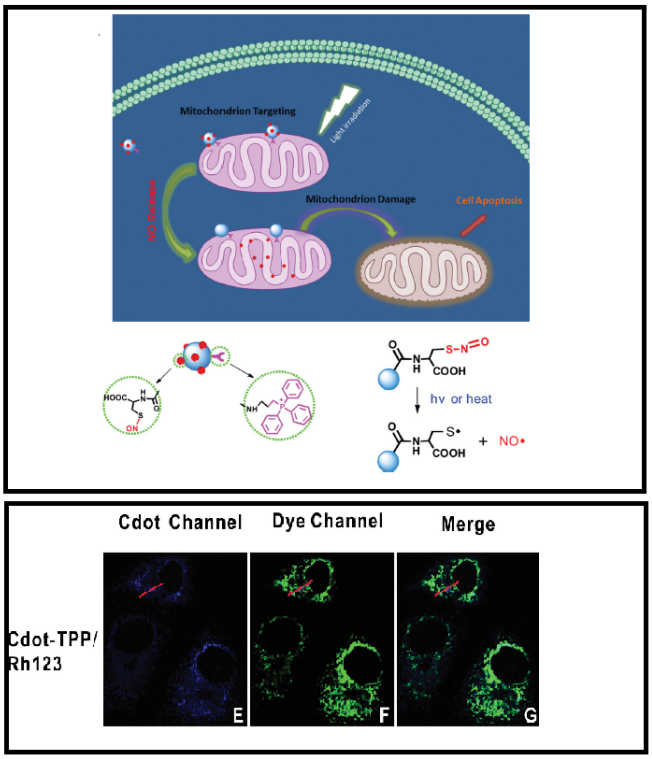

Figure 1.5: Top panel: Schematic illustration of the action of CDs-target complexes on mitocondria, and the structure of the complex with its action of releasing nitric oxide. Bottom panel: Confocal microscopy images of cancer cells in which CDs+Rhodamine123 are injected. Rhd123 is a target for mitocondria and it is evident that the complexes target them. [adapted from [101]]

Optoelectronic Devices Beside sensing and biological applications, CDs are promising components of optoelectronics devices thanks to their strong absorption, high and tunable emission but also to their electron donating and accepting character.

Many authors employed them in the construction of light emitting diodes (LED) where CDs can be used in two different ways: as fluorescent downconverters [85], or as the active layer in an electroluminescent device [67]. The former is founded on the capacity of CDs to be photoexcited by UV and blue light and the following visible emission and exploits the tunability of the emission and the high quantum yield in order to obtain white LED. The latter design takes advantage of the electroluminescence from a CDs layer using CDs as an emitting layer in a multilayered structure after the external injection of charges.

Another important use of CDs is in solar cells [83,84]. In fact, it is well known that CDs display a long tail of strong visible absorption, very convenient to harvest solar light. Combining this with the high capability to accept or donate an electron from the photo-excited state, they become an excellent candidate to be used as sensitizer in a solar cells, the photocathode of which can be built, for instance, by sensitizing TiO_2 with CDs [84]. Furthermore, it seems that using a CDs film as an intermediate layer in a solar cell is very helpful to speed up the electron injection between other materials, as for example from a perovskite layer to titanium dioxide one [83].

Photocatalysis CDs have been proposed as good candidates in photocatalytic applications thanks to their absorption and electron transfer properties and to the ease of coupling to other materials as TiO_2 [124] or Fe_2O_3 [125] or SiO_2 [27]. A photocatalyst is a substance which upon photo-excitation becomes capable to speed up a chemical process.

In general, they are employed in two different ways as pictured in Figure 1.6 [124]. On one hand, taking advantage of their visible absorption they are used to absorb light after which they transfer the photocreated electron to the coupled semiconductor, which usually is only a UV-absorber (Figure 1.6b) In this way, the catalytic action of the composite is extended throughout the visible range. On the other hand, they can be used as acceptor of charge carriers from the photoexcited semiconductor in order to slow down or suppress the recombination of electrons and holes (Figure 1.6a), thus increasing the possibility of chemical reaction and, therefore, enhancing photocatalytic properties.

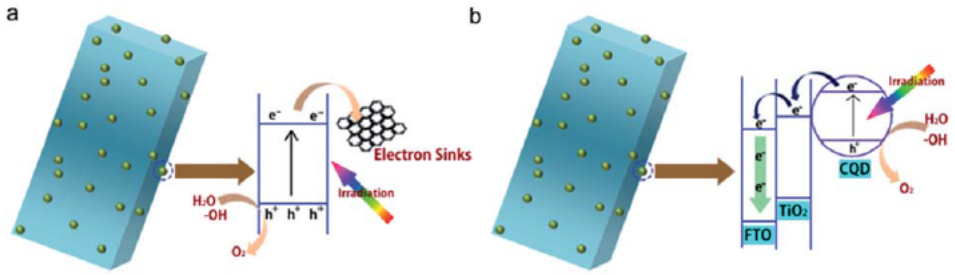

Figure 1.6: Possible uses of CDs (yellow spheres) in a photocatalytic application: a) as electron acceptor (electron sink) from the semiconductor surface (blue block) increasing the photocatalytic activity of the semiconductor, b) as electron donor creating a cascade of electrons from CDs LUMO to semiconductors. [124]

Although most of the photocatalytic applications of CDs are based on CD-semiconductor composites, some works reported photocatalysis of "raw" or simply-functionalized CDs, such as water splitting or CO_2 conversion [126]. Cao et al. functionalized CDs with a shell of gold or platinum and used them to harvest visible photons, followed by charge separation on the particle surface in order to drive the photocatalytic process for the reduction of CO_2, or for the photo-production of H_2 molecules from water splitting. Mehta et al. [127] made the "opposite" nano-devices which are composed by a core of gold functionalized with a surface nanometric layer structurally equivalent

to a CD. The authors took advantage of the surface plasmon resonance of gold nanoparticles to enhance the photoexcitation of the composites, ultimately resulting in the production of hydrogen by splitting water molecules.

1.2 Emission Mechanisms

CDs display a very bright fluorescence which is not common in other carbon-based nanomaterials.

CDs emission bands are always very broad (FWHM $\approx$ 80 nm), they are usually combined with a structureless absorption spectrum which decreases at long wavelengths. Additionally, sharper bands are sometimes superimposed to this structureless absorption curve, and they are usually associated to transitions as $n \rightarrow \pi^*$ localized on surface groups. The variability of CDs synthesis routes and structure complicates the clarification of the emission mechanism. In this respect, an important goal would be disentangling the contribution of quantum effects, of surface states, or of molecular-like states to the emission mechanism, associating them to the core and surface structures of different CDs.

On the one hand, the small size of the system would suggest that the emission should stem from a quantum confinement effect. On the other hand, the role of passivation and the sensitivity to external agents point to a fundamental role of the surface states [1] Furthermore, recent experimental evidences have strongly suggested that the emission of some CD sub-types is actually related to molecular fluorophores, either free or adsorbed on the surface of the dots [47, 128]. In this paragraph, the various proposed models are explained in order to give a complete view on the open debate.

A phenomenon typical of semiconductor QDs as CdSe or PbSe, is the so-called *Quantum confinement effect*: if the size of a crystal is reduced below the exciton Bohr radius of the same bulk material, the optical and electronic properties become size-dependent. The most peculiar consequences of this regime are the increase of the band gap, the progressive transition from a continuous to a sparse density of states, and the significant change of the photoexcited relaxation dynamics [129, 130]. These effects are rather common in semiconductor quantum dots as for CdTe or CdSe.

Moving to carbon materials, a sheet of graphene is a perfect π-conjugated carbon monolayer without electronic bandgap, therefore it is not emissive unless suitable modifications. Researchers tried to increase its energy gap in order to obtain fluorescence. To do this, the common strategies are to cut graphene sheets into small pieces, in order to enter in quantum confinement regime, or to manipulate the structure in order to exploit emission from structural defects, as for functionalized CNTs or nanodiamonds [131, 132]. Despite the possible manipulations of carbon materials, the emission is not typically in the visible spectral range as for CDs, but it is in the near-infrared range [131].

Considering the CDs, according to their small sizes, one can hypothesize that the emission originates from this effect. Indeed, some authors demonstrated that CDs are luminescent only if they are *small enough* (usually $<$ 10 nm), while in other works the authors controlled the size of CDs during the synthesis [133] or after it by fractionation procedures [27], and recorded an emission which displays a regular size-dependence. Typically, these works reported that the smallest CDs display the bluest emission, as expected in a quantum confinement regime. For instance Li et al. [27] reported an optical study of four CD fractions sized from 1 nm to 4 nm which are characterized by an emission which blueshifts with the reduction of the size (Figure 1.7). Despite these evidences, the size of the particle should be smaller than 10 nm (the typical size of the dots) to have an emission in the visible range.

In accordance with quantum confinement, many theoretical simulations on GQDs show that the emission peak depends on the number of *graphene-like* rings or, in other words, on the size of

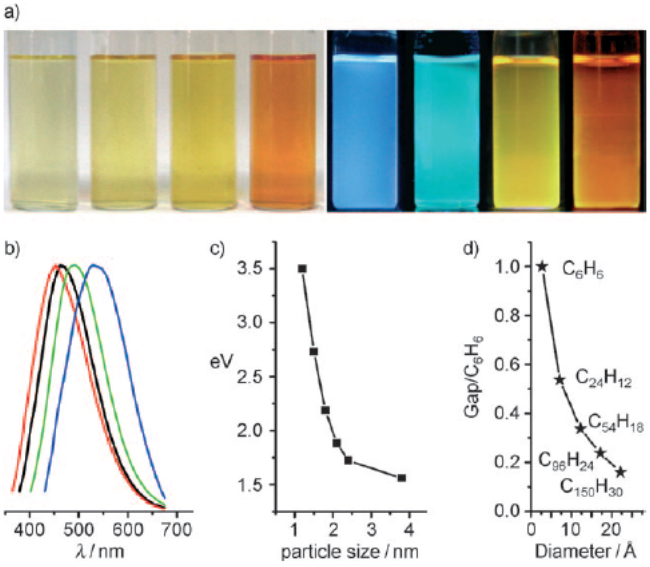

Figure 1.7: (a) Solutions of CDs with different sizes under daylight (left) and UV light (right; 365 nm). (b) Emission spectra of different fractions: the red, black, green, and blue lines are the emission spectra for blue-, green-, yellow-, and red-emitting CDs appearing in panel (a), respectively. (c) CDs size vs the emission peak. (d) HOMO–LUMO gap dependence on the size of the graphite fragments, as obtained by quantum chemical calculations [27].

sp^2 domains [133–136]. This type of emission involves band-to-band transitions and is sometimes called *intrinsic emission*, many authors referring to the states involved in these transitions as intrinsic states. However, CD optical properties cannot be simply explained, in general, by the transitions between intrinsic states only. In fact, the emission of many CDs seems overwhelmingly influenced by *extrinsic* contributions usually related, to the surface as emission from surface defects or from molecular-like states [133]. Indeed, there are many experimental evidences which support the idea of an emission which comes from the surface. An appropriate passivation procedure is crucial to obtain highly fluorescent carbon nanoparticles. More generally, chemical characteristics of the surface, as for example the degree of oxidation, seem to have a dramatic influence on the emission quantum yield [137]. These surface treatments probably change the number of surface emissive traps, their emission efficiency and stability and the alignment of the energy levels with respect to the energy gap, influencing the emission peak and the quantum yield. More over, a second model is sometimes invoked in the literature which assigns the origin of the emission to surface localized defects independent of the crystalline structure of the core [9].

The involvement of intrinsic and extrinsic states in the optical response of CDs are not mutually exclusive. In fact, the interplay between the two is largely debated in the literature. Wang et al. [138] tried to disentangle the role of the core and the surface investigating three samples with a different degree of crystallization of the core and similar emission characteristics. By ultrafast spectroscopy (see section 1.5 and 3.2 for more information on the techniques), they demonstrated that the excited-state behavior is the same in all the samples but the quantum yield depends on the crystallization degree. In particular, according to them, the core is photoexcited and an exciton is created, then it is transferred to the surface and the charges are separated on surface traps. Finally, recombination of the trapped charges produces the emission. In another work on GQDs, Zhu et al. [133] compared the spectroscopic properties of four samples with different sizes finding that the intrinsic state depends on the size but the optical properties are conditioned by the edge

states, which are states at the edges of the GQDs. The emission depends on the alignment between the edge state and the intrinsic state. When a system is photoexcited, the intrinsic states are populated, and if the edge states are intra-gap states, they are populated from the intrinsic states and therefore the emission originates from the radiative recombination from the edge states to the ground state; on the contrary, if the energy separation between the edge states and the ground states is higher than the band gap, they are not involved in the emission, which comes from band-to-band recombination (Figure 1.8). These two schemes rely on the idea that the core is directly

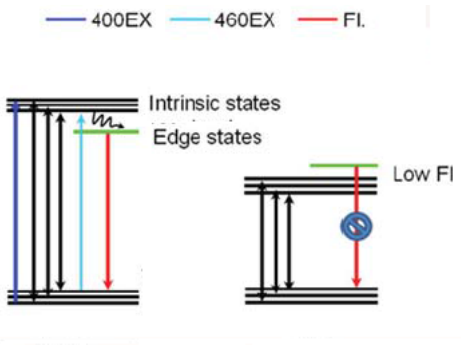

Figure 1.8: The suggested energy levels of different samples, as proposed in [133]. Left illustration: the intrinsic state depends on size, hence the energy level offset. Energy level offset between intrinsic state and edge state, which ultimately decides the optical properties. Adapted from [133].

photoexcited and, afterwards, the exciton is transferred to surface trap states.

Recently, another model gains consensus to explain the origin of CDs emission which is the involvement of emissive transition of fluorescent single molecule attached to CD surfaces, especially in some sub-types of blue-emitting CDs [139, 140], or emissive transition of aggregates of several molecular chromophores in some types of dual-emitting dots (from blue to green) [141]. Many authors noticed that bottom-up syntheses can produce small fluorescent molecular chromophores together with CDs. In particular, this happens when the precursors are citric acid and a N-containing precursor. In particular, during its thermal decomposition the formation of 2-pyridone derivatives can occur [50, 139], more precisely identified by many authors as citrazinic acid [63, 140, 141]. The relative yield of citrazinic acid and carbonaceous nanoparticles is supposed to be dependent on synthesis temperature: increasing it leads to more pronounced carbonization, hence a reduction of the small molecules in favour of the carbogenic cores [128, 142]. There are several evidences supporting this idea as the similarity of the typical blue emission band of CDs peaking at 420-440 nm to the blue emission of citrazinic acid [47, 143], theoretical simulations [64, 140], the lack of tunability of this emission band, in striking contrast with the behaviour of CD fluorescence excited at lower energies, which is strongly tunable [128].

Song et al. [128] produced a sample with a blue optical activity independent of excitation wavelength and another emission band which is tunable. They investigated these two activities and suggested that their origin is different: the tunable emission is associated with electronic transitions which involve the core, while the non-tunable one is related to the presence of small molecules in solution. In particular, these molecules are supposed to exist in two forms: free in solution or attached to dot surfaces. Schneider et al. [47], for instance, found that the blue emission of CDs peaking at 430 nm decays with a bi-exponential kinetics, leading to hypotesize the presence of two forms of the same chromophore: one attached to the dot, and the other free in solution. Wang et al. [140] investigated the effect of UV-photobleaching on CDs. They combined experimental studies on CDs and on citrazinic acid with theoretical simulations and proposed a model in which the chromophore is a molecule of citrazinic acid attached to the surface of the dot.

Last but not least, another recently proposed model for the origin of CDs emission pictures CDs as excitonic H-aggregates composed by molecular chromophores stacked on each other [144]. The result of this stacking is the splitting of the excited energy level of single chromophore into two levels and a consequent large Stokes shift typical of CDs. Moreover, this guarantees the exciton delocalization over the entire particle which behaves as a single emissive dot.

Notwithstanding the several studies on the emission mechanisms of CDs, no unique model exists yet to explain its origin. The debate is still open and, probably, it is complicated by the variability of CDs, which not only affects CDs obtained by different synthesis procedures, but is also testified, even more dramatically, by the heterogeneity exhibited by the majority of CD samples.

1.3 Origin of Emission Tunability

One of the most intriguing characteristic of CDs is the tunability of their emission, as mentioned before: the fluorescence peak of a typical CD shifts continuously when changing the excitation wavelength (Figure 1.4). Its origin is very debated in the literature and still lacks a clear explanation. Many authors attribute this tunability to a certain degree of inhomogeneity which typically affects CD sample, caused by the difficulty of tightly controlling the structural characteristics of the product of most synthesis routes. Accordingly, CDs which display an emission independent of the excitation wavelength are considered quite homogeneous [12, 145].

Indeed, such a tunable, multi-colour emission can be very useful in many applications as mentioned in section 1.1, but notwithstanding its benefits, the inhomogeneity of the sample hides spectroscopic information which should be very useful to understand the photophysics of the system and to rationally tailor CDs to specific applications.

At the spectroscopic level, the large inhomogeneity of most CD samples is pointed out by many experimental evidences as broad unstructured absorption or emission bands, non-exponential kinetic traces in fluorescence decay [146], differences between ensemble and single-molecule experimental results [147]. Its structural origin has been related to several factors as a chemical variability on CDs surface structure or charge from dot to dot [69, 148], broad distribution of the size or shape irregularity [27, 51], and differences on the density of emitting states on each dots [48].

Therefore, the problem is twofold. On one hand, synthesis procedures of CDs are still unable to produce CDs with sufficiently homogeneous structural characteristics, such as narrow, monodisperse size distributions. On the other hand, being the origin of CD fluorescence still very debated, more systematic and focused studies are needed to precisely pinpoint the structural parameters which need to be controlled in order to obtain CDs displaying spectroscopically homogeneous optical features. However, the existing attempts to address these problems have produced very contrasting results, as explained hereafter. Therefore, explaining and controlling CD fluorescence tunability remains one of the most debated problems in the literature.

Unfortunately, it is not easy to unravel the knot of heterogeneity with standard optical measurements at the ensemble level. Therefore, a few works have tried to approach the problem by using two alternative ways: a single-molecule investigation [144, 147–149], and fractionation experiments [52, 69].

Fractionation allows to access the characteristics (optical, structural and morphological) of a sub-type of CDs, selected out of a sample according to one physical property (size, surface charge, etc). This should allow to correlate specific structural parameters to the optical properties, and possibly allow to isolate sub-types of monodisperse CDs. Differently, single-molecule experiments can be seen as a *random fractionation* down to the level of single dots, or aggregates of a few dots. These experiments aim to answer to important questions as if the tunability is still preserved at the single dot level (one dot hosts more than one chromophore) or if every dot acts as a single

non-tunable emitter (one dot hosts only one chromophore), or if the fluorescence decay kinetics observed in the overall CD ensemble is the same with respect to the single nanoparticle.

The very few existing experiments on single CDs revealed much information related to emission and to tunability. Dispersing an extremely diluted solution on a substrate allows to collect the emission from individual dots (or small aggregates composed by few dots). Usually, single dots display narrower emission spectra than the ensemble measurements (Figure 1.9a) pointing out the inhomogeneous width of ensemble emission bands, which are probably due to the superposition of the emission of individual dots, the emission peaks of which strongly fluctuate from dot to dot. Furthermore, Ghosh et al. [147] demonstrate the vanishing of the tunability at single dot level, as in Figure 1.9b which suggests that a single dot acts as a *single quantum emitter* (as a single chromophore), with its particular energy gap, and that spectral heterogeneity appears only at an ensemble level due to the superposition of spectral characteristics of several dots [144, 147]. In the

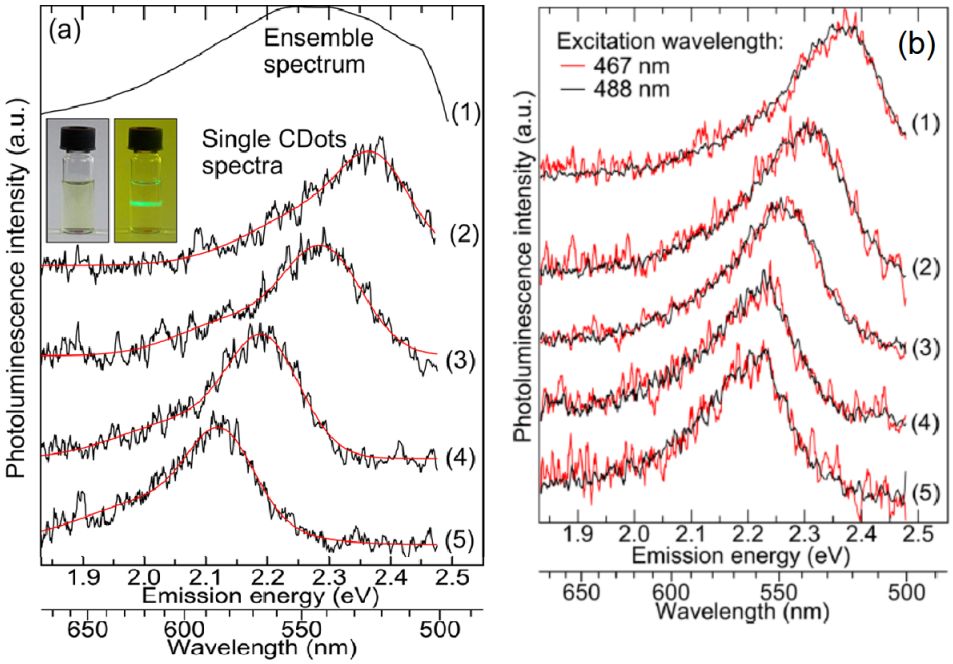

Figure 1.9: (a) Top: ensemble emission spectrum excited at 488 nm; Bottom: emission spectra from individual dots excited 488 nm. (b) Emission spectra from individual dots excited at 467 nm (red curves) and at 488 nm (black curves). [Adapted from [147]]

same work, not only the tunability disappears but also the multi-exponential decay of emission is not observed in single dots, demonstrating that also the multi-exponential decay is a fingerprint of heterogeneity, arising from dot-to-dot differences in excited-state lifetimes [147]. However, these results were disputed by other works. In fact, other papers reported that the tunability is observed even at the single dot level [4], showing that a single dot can emit different colours if excited at variable energy, indicating the presence of independent emission sites within a single-carbon dot, in striking contrasts with the results of ref. [147]. This evident contradiction between the results is probably related to the diverse experimental conditions. In particular because of their very small size, it can be hard to discriminate between truly "single" dots and aggregates of a few dots. Therefore, it is possible that claims of tunability at the single-dot level are actually due to the emission from small aggregates of CDs as sometimes observed in other systems [150] and, therefore, the tunability is just related to the superposition of emission of different dots.

To address the origin of tunability, the second method consists in the selection of a part of the

as-synthesized original sample according to various criteria which span from surface charge [69, 151] to particle size [27, 48, 51, 52]. Regardless, the separation method is helpful to provide a more homogeneous sample which is extracted from the original one. Indeed, these fractions usually display simpler optical characteristics or narrower morphological distribution. Also in this case, the results reported in the literature, and therefore their interpretations, are quite different. By size exclusion chromatography (SEC), Kang et al. [27] separated a CD nanoparticles according to their size. They found that the emission depends on the fraction, although each fraction displays a non-tunable fluorescence. Following this, they claimed that the inhomogeneity and, therefore, the tunability comes from different dots with diverse size. For this reason, they supported the idea of a quantum confinement effect which affects the origin of emission. On the contrary, Wen et al. [48], using the same fractionation method, isolated several fractions with different size, and two of them in particular were considered pure emitters (green and blue, respectively) (Figure 1.10). The smaller fraction emits green fluorescence and the bigger emits blue light, behaviour which is completely in disagreement with a quantum confinement vision. The authors associated the tunability of the main sample to its heterogeneity and, in particular, to a different density and type of functional groups on the surface of each dot which should influence emission colour. Therefore, rather than quantum confinement, the authors propose that differently-sized dots display variable optical properties as a consequence of their different surface-to-volume ratio.

Another commonly used separation procedure is High Performance Liquid Chromatography (HPLC) [51, 52]. The success of the technique is evident from the very different optical properties of the obtained fractions, although it is generally difficult to operate a selection based on a single structural property (size, polarity...). In ref. [52] the subsets show diverse emission bands and the single fractions are non-tunable. According to this, the authors associated the origin of tunability to the inhomogeneity of nanoparticle charge and/or size. Fuyuno et al. [51], using the same technique on a sample of GQDs, accomplished to separate the sample into fractions displaying different optical properties. Despite of this, they did not observe the disappearance of tunability and, therefore, associated the latter to the presence of sp^2 domains with different size and shape on each GQD.

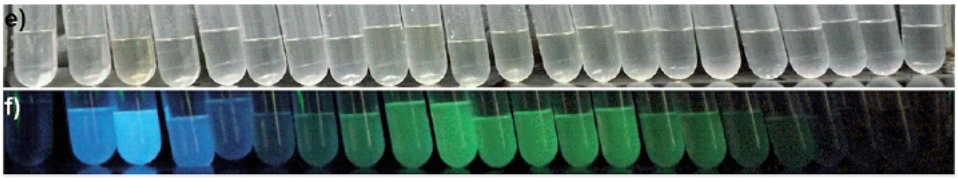

Figure 1.10: Products from a size exclusion chromatography procedure under daylight (top), under UV-light (bottom) [Adapted from [48]]

Gel electrophoresis is another separation method by which it is possible to isolate fractions according to the surface charge. Also with this technique the existing results in the literature are contradictory. In ref. [69], this technique allowed to separate subsets of CDs emitting different colours according to their surface charge, in particular dots with the most negative charge on the surface were found to emit blue light. On the contrary, Ehrat et al. [151] did not succeed in the fractionation of different coloured samples with the same method and they separated a CDs sample into different fractions which display the same emission band.

Despite these contrasting results, most authors still agree to explain tunability as an effect of disorder. It is worth noting that an completely different explanation was proposed in one study based on the result of a solvatochromic investigation [146], where the authors found a very slow solvation mechanism which causes a redshift of the fluorescence spectrum progressing on a time

scale comparable to that of fluorescence decay. This, so-called, red-edge effect (see section 2.2) violates Kasha's rule and therefore explains fluorescence tunability because the relative population of different emissive states becomes dependent on the excitation energy.

1.4 Interactions with external environment

CDs sensitivity to variations of external environment is very well-known. Many articles demonstrate that the fluorescence of CDs is sensitive to external agents in solution as ions or molecules [110, 152], to solvent differences [146], or to changes in pH value [153]. This sensitivity is very useful in several applications as explained in section 1.1 but the fundamental mechanisms behind it are still unclear.

Most CDs are very rich of surface -COOH groups, which are negatively charged in solution. Therefore, the formation of complexes with positively-charged metal ions is favoured, and the observation of such interactions is particularly widespread in the literature. When metal cations, as Hg^{2+}, Cu^{2+}, Fe^{3+}, are dispersed in a CDs solution, they usually produce a quenching of CDs fluorescence. The most accepted explanation invokes an efficient electron transfer from photoexcited CDs to metal ions [110, 154], which prevents the radiative recombination of photo-generated excitons. On one hand, this interaction is not surprising, being very similar to the well-known quenching action of several common cations on the fluorescence of many organic dyes [155]. On the other hand, the tendency of CDs to easily participate to such photo-induced electron transfer reactions supports the hypothesis of CD fluorescence due to surface traps directly exposed to the solvent, because electron transfer generally occurs on very short spatial scales.

In the literature, spectroscopic evidences of these interactions are several and most of them are obtained by steady-state and time resolved spectroscopy (nanosecond to femtosecond) [110, 153, 154]. In some works [110, 153, 154] the emission quenching contributes to support the idea of an electron transfer from CD to the ion due to formation of non-luminescent complexes CD-ion (static quenching, Figure 1.11) [110], and also the reduction of the excited-state lifetime due to collisions between CD and ion (dynamical quenching) supports the correctness of this idea [154]. In general,

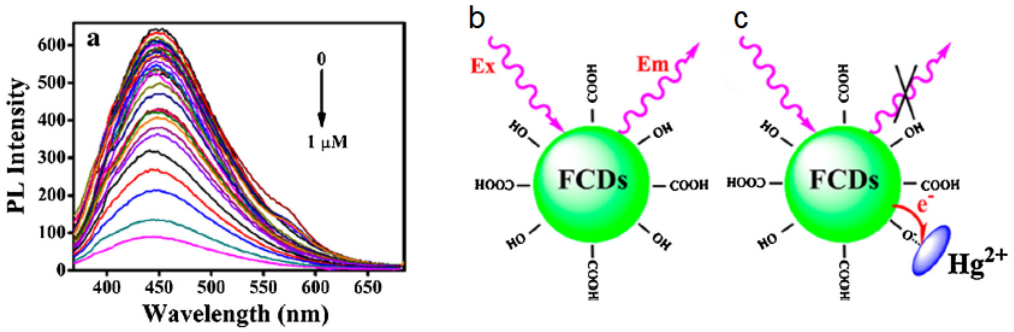

Figure 1.11: Panel (a): Emission spectra of CDs solution with different amount of Hg^{2+} ions. Panel (b) and (c): Schematic illustration of fluorescence and quenching mechanisms, respectevely. [Adapted from [110]]

the fluorescence of CDs usually responds to multiple metal cations, but some works [156, 157] have reported a selective quenching of CDs by specific ions, which is probably due to the specific binding interactions between certain CD surface groups with particular metals. Another recurrent finding in the literature is the selectivity of quenching with a copper ion respect to zinc ion which leads to support the idea of an electron transfer interaction. In fact, copper ions have an open-

shell electronic configuration ($[Ar]^3d^9$) which can host an electron donated from the dot, while, zinc ions have a full-shell and they are not expected to easily accept additional electrons [153].

In general, the ability of CDs to act as efficient photo-activated electron donors is rather well-established and not limited to the interaction with transition metal ions. Besides, depending on surface structure, CDs can also work as photo-excited electron acceptors. For instance, charge transfer dynamics are observed between CDs and molecules [152], or various types of metal complexes [158] or when CDs are adsorbed onto semiconductor surface [27]. This is the phenomenon which allows to use CDs as photosensitizers of semiconductors in photocatalytic devices.

The physical and chemical mechanisms underneath the charge transfer are not clear, as for instance the role of a specific surface structure in mediating the interaction between CD surfaces and the adsorbed, or colliding ion. Even more notably, the dynamics of these processes are quite fast (picosecond or less) and they are invisible with standard spectroscopical methods, therefore ultrafast techniques are necessary to go deeply inside the mechanisms of these interactions.

When CDs are in contact with other electron donors (stronger than CDs) as in ref [152] or [158], they can act as electron acceptor and their fluorescence is quenched because there is a photoinduced electron transfer from the external agent to them. The capability of CDs of behaving more efficiently as electron donors or acceptors is not well understood, but certainly is related to both core and surface structures. As an example, to control this behaviour, which can be useful in photocatalytic or optoelectronic devices, Barman et al. [159] compared the behaviour of CDs subjected to n- or p-type doping. The electron transfer from the dot is favoured in the case of n-type doping (obtained with phosphor), whereas CDs behave as electron acceptors (hole donors) when they are p-doped (by boron doping). Another way to control this aspect is to modify the surface of CDs in order to change their redox potential. Rigodanza and coworkers [160] did this with a reaction between CDs and different quinones, and demonstrated the promising electron transfer properties of CDs in particular surface conditions.

Solvent and pH have a crucial role on the properties of CDs. In particular, solvatochromic changes of the emission have been reported by a few works [75, 146, 161], and the solvent can influence the interaction between photoexcited CDs and various external systems [152, 156]. Moreover, changes in pH value influence emission intensity [154], probably changing the charge state of surface groups [153]. Similar to the electron transfer interactions, also these observations tend to confirm the key role of surface states in the photo-cycle of CDs.

The dependence on pH value is definitely due to the acidic/basic character of the moieties on CD surfaces. Chandra et al. [153] demonstrate that CDs synthesized from different precursors are stable at diverse pH intervals and, consequently, the emission is maximum at different pH. This is caused by presence of various groups on the surface as, for instance, -COOH and -NH_2, which are more stable respectively at pH=9 and pH=3. Another example is reported in ref. [154] where a great amount of H^+ ions in solution can modify the emission. Beside these common surface groups, in fact, also pyridinic nitrogen on the surface of CDs was deemed responsible of emission. Therefore the authors supposed that H^+ ions connect to pyridinic N atoms on the surface of the dot so that these atoms are protonated and when the system is photoexcited there is a proton transfer from pyridinic N to the carbon structure which blocks the emission process.

Solvation usually modifies CDs emission and the interactions between CDs and solvent are both non-specific and site-specific. In other words and depending on cases, CDs can be both sensitive to the polarity of the solvent and also to its capacity to form a hydrogen bond. Solvation studies with the use of steady state and time resolved nanosecond spectroscopy demonstrate these effects through the dependence of the emission band on the polarity of the solvent [63, 152, 162]. However, the existing studies have often reported very complex and irregular solvent response, that have been very difficult to interpret so far [63,76]. As an example, the study in ref. [76] pointed out rather irregular solvent-dependent changes (Figure 1.12) of emission peak and attributed it to

the coexistence of hydrophobic and hydrophilic groups on the surface of CDs.

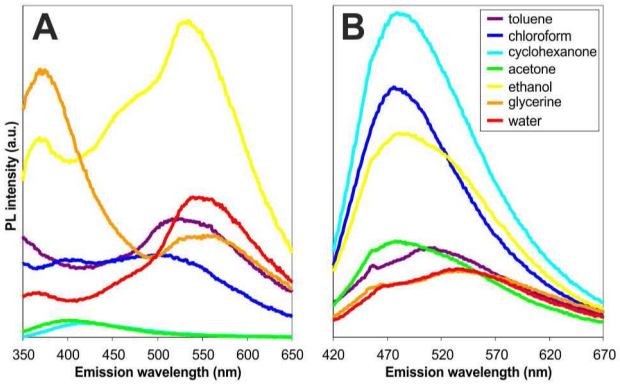

Figure 1.12: Emission spectra of CDs in different solvents excited at 290 nm (a) and 400 nm (b) [From [76]]

1.5 Ultrafast Spectroscopy on Carbon Nanodots

Ultrafast spectroscopy is a powerful tool to investigate in real time electronic and vibrational processes with ps (10^{-12} s) and fs (10^{-15} s) time resolution [163]. In general, these techniques are mandatory to map in full detail the photocycle of a physical system. Indeed, several dynamics can occur on ps or sub-ps time scale as energy relaxation from the initially-excited state to the emissive state, solvation and hydrogen bonding dynamics, charge and energy transfer, and fluorescence quenching. By ultrafast techniques, it is possible to study these mechanisms in real time, which would be hidden in the steady-state spectra.

Ultrafast investigations on CDs recently started to attract interests by a few groups who use transient absorption (TA) spectroscopy [83,161,164], and fluorescence upconversion (FLUC) [165–167] to understand the photocycle of pristine CDs or interacting with other particles or molecules, with the aim of overcoming the severe limitations of previous studies mostly based on steady-state optical methods. TA spectroscopy relies on measuring the variation of the sample absorption spectrum, as a function of time and wavelength, after the system undergoes photoexcitation. FLUC measures the spontaneous emission of the sample, as a function of delay and wavelength, after photoexcitation. Both techniques help to comprehend the dynamics of a photoexcited system and the interactions with the external environment, with femtosecond time resolution.

For instance, these techniques can be used to investigate the photocycle of a sample and sometimes to disentangle the role of core and surface of dots. These experiments make possible to map the relaxation channels which lead to the long-lived emission or to non-radiative recombination which prevents the formation of a long-lived emissive states. In fact, the extensive use of femtosecond spectroscopies to address the photocycle of CDs is one of the main goals of this work, as will be presented in the rest of the Thesis. Hereafter, we briefly discuss some examples of the existing literature on CDs founded on the use of such methods.

Wang et al. [165] provided a model for the emission of GQDs by the combined use of TA and FLUC. These GQDs are characterized by two different emissions characterized by two separate lifetimes. The former is long-lived (few ns) and it is the one responsible for the steady state emission, associated to the presence of functional groups at the edge of GQDs; the lifetime of the latter is very short (less than 2 ps) and related to a band-to-band transition, described by the authors as *dark intrinsic state*. This work points out the utility of ultrafast techniques which are the only way to observe the existence of these short-lived transitions, therefore to disentangle the role of

band-to-band from edge transitions. In this case, the two seem to proceed rather independently from each other, without crosstalk between core and edge states.

Opposite results are presented by Lu et al. [70,71] whose TA experiments suggested an interplay between core and surface. In fact, they disentangled two parallel relaxation channels which contribute to the population, from the photoexcited carbon core, of two different types of surface states: one which recombines in a non-radiative way and another one which is strongly emissive and detectable in steady-state experiments. Thus, differently from the work by Wang et al., these results directly suggest the existence of an interplay between the carbon core and the surface states which contribute to the emission. By FLUC experiments, Wen et al. [166] conducted a study of the dynamics of charge carriers in photo-excited CDs, trying to compare them to the well-known dynamics within photoexcited semiconductor nanoparticles [168]. In their study, they identified time scales related to optical phonon scattering (<5 ps), acoustic phonon scattering (50 ps) and excitons recombination (1.5 ns). Moreover, they identified a fast component of 400 fs which is attributed to surface trapping of electrons from the core into surface states.

Solvation dynamics at the surface of CDs is expected to occur on sub-nanosecond time scales, as usually observed in molecular dyes. Therefore, femtosecond methods are mandatory to study these relaxation effects. However, studies of CD solvation are still very rare. Jing et al. [161], recently observed solvation relaxation for CDs in different solvents, and attributed these dynamics to dipole-dipole interaction between CDs and solvent molecules.

Beside the intrinsic photocycle, ultrafast methods have been used to address the fundamental mechanisms of charge transfer from or to CDs, when they are coupled to other materials as graphene oxide [167] or metal complexes [158]. As mentioned in section 1.4, the emission of CDs is commonly quenched by interaction with a variety of external agents. This effect is tentatively associated with electron transfer form the dot to the coupled system or vice versa. A few works used femtosecond methods to address the problem of electron transfer dynamics from/to CDs to/from various coupled systems. For instance, in ref. [167] the authors studied CDs-graphene oxide (GO) nanocomposites and found a time constant associated to electron transfer from CDs to GO which is 400 fs, or in ref [158] where the interactions between CDs and iridium-ruthenium metal complexes are investigated, from which the authors identified two ultrafast time constants of $\approx$ 1 ps and $\approx$ 20 ps associated to charge transfer from the metal complex to the CDs excited state.

Combining CDs with other materials in solar cells or photocatalytic devices changes the efficiency of the device, increasing or decreasing it. Some authors used femtosecond spectroscopy to investigate the optical response of these devices [164,169,170], or of the component materials used in them. [167,171–173] It is worth reporting here the comparison between two extreme situations. Tetsuka et al. [164] used a sample of nitrogen-functionalized GQDs as a layer within a perovskite solar cell. Using femtosecond TA, they established the speed up in the electron extraction rate from $\approx$ 300 ps to $\approx$ 50 ps caused by the addition of GQDs, as a consequence of which GQDs lead to an increase of the power conversion efficiency. On the other extreme, Margraf et al. [170] demonstrated that the use of CDs as sensitizers in mesoscopic solar cells reduces the performance of the solar cells and attributed this to the not-ideal balance between the charge recombination and the regeneration processes.

Chapter 2

Basic concepts

In this chapter, a few basic theoretical concepts necessary to describe the scientific aspects of the thesis are introduced.

2.1 Optical Spectroscopy

Einstein's coefficients

In this section, the attention is focused on three processes which can involve a two energy level system interacting with radiation: absorption, stimulated emission and spontaneous emission (Figure 2.1). The first process consists in the transition of a system to a higher energy state upon the absorption of a photon resonant with the transition. The second process is the stimulated emission which is considered the inverse transition of the absorption and consists in the emission of a photon under the influence of external irradiation, accompanied by a transition of the system from the upper to the lower energy state. The last process consists in the spontaneous relaxation of a system from an excited state (referred with b) to a lower energy state (referred with a) by the emission of a photon.

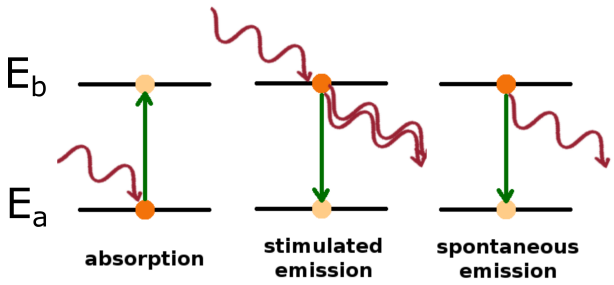

Figure 2.1: Schematic picture of absorption, stimulated emission and spontaneous emission in a two-level system.

These three mechanisms are phenomenologically described by Einstein's coefficients [174], by which the probability per unit time (W) of these events can be written as:

$$W_{b\leftarrow a} = B_{ab}\rho(\upsilon_a) \tag{2.1}$$

$$W_{b\rightarrow a} = B_{ba}\rho(\upsilon_b) \tag{2.2}$$

$$W^{sp}_{b\rightarrow a} = A_{ba} \tag{2.3}$$

where Equations 2.1 to 2.3 describe the transition rate of absorption, stimulated emission and spontaneous emission, respectively, in terms of the respective Einstein's coefficient B_{ab}, B_{ba} and A, and of $\rho(v)$ which is the radiation energy density at the transition frequency.

Expressions of Einstein coefficients in terms of the properties of the two-level systems can be derived by a detailed theoretical treatment of the interaction between light and matter. To simplify the study of this problem, we can consider the light as monochromatic at a frequency v and the system as a two level system which can be outlined by two states Ψ_a and Ψ_b separated by an energy $\Delta E = E_b - E_a = hv_0$.

Generally speaking, it is possible to describe this interaction using the so called *semiclassical approximation* which consists in using a quantum mechanic description for the system, but a classical one for the field [175].

The interaction Hamiltonian between the system and the external field due to an electromagnetic wave can be written as:

$$H(t) = -E\bar{(}t) \cdot \tilde{\mu} \tag{2.4}$$

where $\bar{E}$ is the electrical field of linearly polarized light and $\tilde{\mu}$ is the electric dipole moment, which can be written as:

$$\tilde{\mu} = -e\sum_i \bar{r}_i + e\sum_s Z_s \bar{R}_s = \ = \tilde{\mu_e} + \tilde{\mu_N} \tag{2.5}$$

where e is the electron charge, eZ_s are the charge of the nuclei and r_i and R_s are the electronic and the nuclear coordinates, respectively. From Equations 2.4 and 2.5 and applying the *Fermi's Golden rule* it is possible to write Einstein's Coefficient B_{ab} as [176]:

$$B_{ab} = B_{ba} = \frac{|\mu_{ba}|^2}{6\epsilon_0\hbar^2} \tag{2.6}$$

and, considering the black body radiation, it is possible to obtain the coefficient A as:

$$A_{ba} = \frac{16\pi^2\hbar v_{ba}^3}{c^3} B_{ba} \tag{2.7}$$

where $\hbar$ is Planck's constant, ϵ_0 is the vacuum permittivity and μ_{ba} is the transition dipole moment. If Ψ_a and Ψ_b are the wavefunctions of two states of the system, it is possible to write:

$$\mu_{ba} = \int \Psi_b^* \tilde{\mu} \Psi_a \tag{2.8}$$

Born Oppenheimer approximation

The wavefunction describing the state of a molecule or of a nanocrystal, the typical systems we are interested to in this Thesis, should describe the electronic part as well as the nuclear part. Since this is a multibody problem, solving Schrödinger equation is analytically impossible. For this reason, it is common to adopt the Born-Oppenheimer approximation in order to isolate different features of the problem and to approach them separately. Born-Oppenheimer approximation takes advantage of the adiabatic approximation according to which electrons can adjust themselves quasi-statically to the nuclear motion because they are much lighter and move faster than the nuclei.

The Born-Oppenheimer approximation begins with the factorization of the wavefunction Ψ in an electronic term ($\chi(\bar{r}, \bar{R})$) and in a nuclear term ($\phi_n(\bar{R})$) [177]:

$$\Psi(\bar{r},\bar{R}) = \chi(\bar{r},\bar{R})\phi_n(\bar{R}) \tag{2.9}$$

where $\bar{r}$ are the electronic, $\bar{R}$ are the nuclear coordinates and n indicates the nuclear state. The rationale behind this approximation can be explained as follows.

It is possible to write the Hamiltonian, neglecting relativistic effects, as:

$$\hat{\mathcal{H}} = K_e + V_{ee}(\bar{r}) + V_{eN}(\bar{r},\bar{R}) + K_N + V_{NN}(\bar{R}) \tag{2.10}$$

where K is the kinetic energy related to electrons (e) or nuclei (N) and V_{ee}, V_{NN} and V_{eN} are the Coulombian repulsion between electrons, between nuclei and the Coulombian attraction betwen electrons and nuclei, respectively.

Born-Oppenheimer approximation consists in looking for a solution of Schrödinger equation in the form of Equation 2.9, assuming an adiabatic regime, and solving first Schrödinger equation for the electron motion, initially considering the nuclear position R as mere parameters:

$$\begin{aligned}\hat{\mathcal{H}}_e\chi(\bar{r},\bar{R}) &= (K_e + V_{ee}(\bar{r}) + V_{eN}(\bar{r},\bar{R}))\chi(\bar{r},\bar{R}) = \\ &= \chi(\bar{r},\bar{R})E(\bar{R})\end{aligned} \tag{2.11}$$

In this way, this solution establishes a new potential for the nuclear motion $E(R)$, which can now be solved separately:

$$\hat{\mathcal{H}}\phi_n(\bar{R}) = (E(\bar{R}) + K_N(\bar{R}) + V_{NN}(\bar{R}))\phi_n(\bar{R}) \tag{2.12}$$

Born-Oppenheimer approximation with the adiabatic approximation and with Fermi Golden rule lead to the expression for the transition probability between two states. In fact, considering the different masses between electrons and nuclei and the diverse time scales between an electron transition ($10^{-15}s$ [178]) and the nuclear dynamics ($10^{-12}s$ [178]), it is acceptable to consider that the position and the momentum of nuclei do not change during the electronic transition and, considering also that the probability of transition between two states is proportional to $|\mu_{ab}|^2$ and using Equation 2.5, one can write [176]:

$$\begin{aligned}\mu_{ba} &= \int \Psi_b^*(\bar{\mu_e} + \bar{\mu_N})\Psi_a = \\ &= \int \chi_b^*(\bar{r},\bar{R})\phi_{bn}^*(\bar{R})(\bar{\mu_e} + \bar{\mu_N})\chi_a(\bar{r},\bar{R})\phi_{am}(\bar{R})d\bar{r}d\bar{R} = \\ &= \int \phi_{bn}^*(\bar{R})\chi_b^*(\bar{r},\bar{R})\bar{\mu_e}\chi_a(\bar{r},\bar{R})\phi_{am}(\bar{R})d\bar{r}d\bar{R} + \\ &+ \int \chi_b^*(\bar{r},\bar{R})\phi_{bn}^*(\bar{R})\bar{\mu_N}\phi_{am}(\bar{R})\chi_a(\bar{r},\bar{R})\phi_{am}(\bar{R})d\bar{r}d\bar{R} = \\ &= \mu_{ba}^e \cdot \int \phi_{bn}^*(\bar{R})\phi_{am}(\bar{R})d\bar{R} + \int \phi_{bn}^*(\bar{R})\bar{\mu_N}\phi_{am}(\bar{R})d\bar{R} \underbrace{\left[\int \chi_b^*(\bar{r},\bar{R_0})\chi_a(\bar{r},\bar{R_0})d\bar{r}\right]}_{=0, if\, a\neq b} = \\ &= \mu_{ba}^e \cdot \int \phi_{bn}^*(\bar{R})\phi_{am}(\bar{R})d\bar{R}\end{aligned} \tag{2.13}$$

where Condon approximation has been used. It consists in considering $\chi(\bar{r},\bar{R}) \approx \chi(\bar{r},\bar{R_0})$ where R_0 is the equilibrium position of nuclei. The second term of the sum is equal to zero because the electronic wavefunctions of two different states are orthonormal and the first term is the integral over the electron coordinates which, for the above-mentioned approximations, can be

considered as a constant indicated by μ^e_{ba}. Therefore the transition dipole moment can be written as:

$$|\mu_{ba}|^2 = |\mu^e_{ba}|^2 \left| \int \phi^*_{bn}(\bar{R})\phi_{am}(\bar{R})d\bar{R} \right|^2 \tag{2.14}$$

where the last factor is called the Franck-Condon factor and it is proportional to the overlap between the vibrational wavefunctions [176].

According to Born-Oppenheimer approximation, it is possible to schematize the transition between two states as a vertical transition between the two energy potentials as in Figure 2.2 (Franck-Condon principle). Moreover, Equation 2.14 establishes that the probability of the single vibronic transition depends on the Franck-Condon factor, and also that the shape of the absorption and emission bands depends on it [179].

The nuclear wavefunctions ϕ are often taken to be harmonic oscillator-like. Because the nuclear equilibrium positions are different in ground and excited state, however, ϕ_b and ϕ_a are shifted with respect to each other, and their scalar product can be non-zero even if m$\neq$n. For this reason, the absorption and the luminescence spectra are a collection of multiple lines at different frequencies which correspond to the allowed vibronic transitions (Figure 2.2). The homogeneous broadening of the band (the one related to the Franck Condon factor) is pictured in Figure 2.2 where the peaks of the vibrational states are shown (both in absorption and in emission). In general, the vibrational substructure in the absorption and emission bands is often obscured by inhomogeneous effects such as the solvation and the inhomogeneity of the system (see also section 2.2).

In the same way, the spectral position of the emission band with respect to the absorption band is influenced by vibrational relaxations occuring within the higher electronic state, either associated to internal molecular coordinates or to external factor as the solvent. When the system is photoexcited, it jumps, in a very short time (10^{-15} s), from a vibrational state in the lower energy electronic state to a different vibrational state in the higher energy state. On a time scale which typically consists in a few vibrational periods, the system relaxes to the lowest vibrational energy level of the excited state. Further relaxations (see section 2.2) can occur due to solvent relaxation, typically on a picosecond scale. The following decays usually proceed from the fully relaxed state formed at the end of these processes. Then, in 10^{-9} s (or longer) the system decays in the ground state.

These relaxations explain the difference between the energy positions of the absorption and the emission peak which is called Stokes Shift [178]. Another consequence of the scheme in Figure 2.2 is the so-called Mirror image rule which states that an emission spectrum with all of its vibronic transition should be symmetrical (as a mirror) to the absorption spectrum with respect to the 0-0 transition (zero phonon line).

2.2 Absorption and Emission

Here, we can make a connection between the microscopic quantities discussed in the previous section (Einstein's coefficients) and the macroscopic quantities which can be measured during an experiment of absorption or emission spectroscopy.

The absorption phenomenon occurs when an light beam provides energy to the matter at the expense of its intensity (I). The resulting intensity decrease is proportional to the intensity of the incident light, to the number of the absorber centers (the concentration c_0), the length covered by the beam (dx) and to the attenuation cross section (σ) which depends on the frequency but also on the environment surrounding the absorbers:

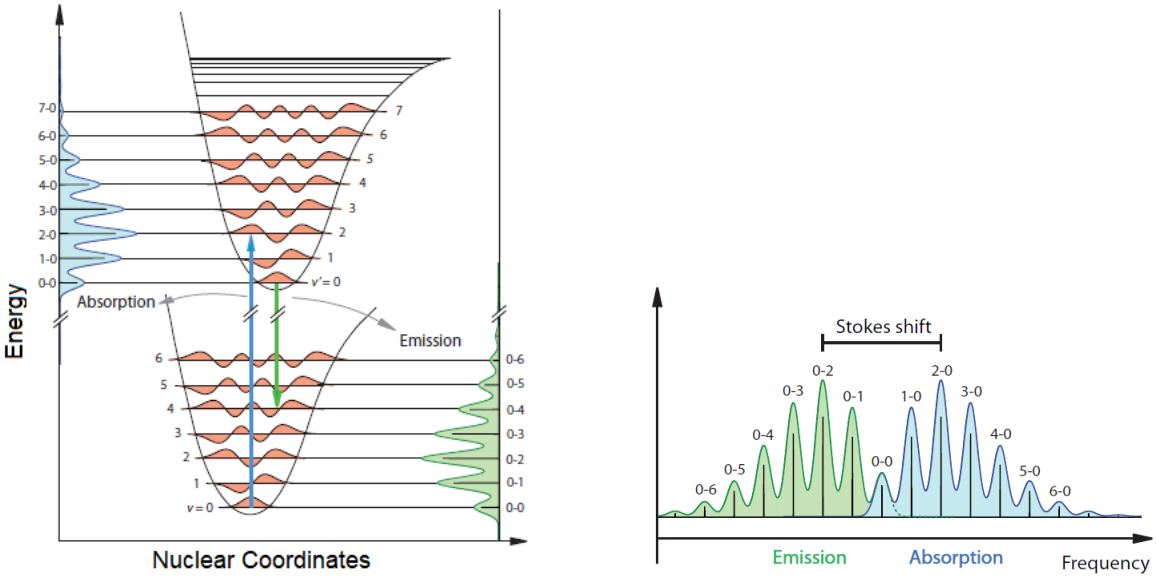

Figure 2.2: Left: Scheme of a vertical electronic transition from a lower energy state to a higher energy state (vertical blue arrow) and the inverse transition (green arrow) with the dependence of the shape of the spectra related to the Franck-Condon factor. Right: Absorption and emission spectra as a function of energy (frequency). The distance between the two maxima represents the Stokes shift, and the sharp peaks depict the transition from or to different vibrational states. It is evident that one spectrum reflects the other.

$$\begin{aligned} dI &= -I\sigma(v)c_0 dx \\ I &= I_0 e^{-\sigma(v)c_0 x} \end{aligned} \tag{2.15}$$

Absorbance, moreover, can be derived from the attenuation of the incident light as in the following equation:

$$\begin{aligned} OD(v) &= log_{10}\frac{I_0(v)}{I(v)} \\ I(v) &= I_0 10^{-OD(v)} \end{aligned} \tag{2.16}$$

Equation 2.16 is the Beer-Lambert's law [180]. In this sense, it is possible to link a macroscopic quantity, the absorbance, to the microscopic one as $OD = \frac{\sigma c_0 x}{2.303}$. It is also possible to write the absorbance as $OD = \epsilon M x$, where ϵ is the, so-called, molar extinction coefficient, proportional to the cross section σ, and M is the molar concentration.

Equation 2.16 can be described in term of Einstein's coefficient. Considering n_{ph} the number of incident photons on N_0 absorbers, the number of absorbed photons is:

$$dn_{ph} = B_{ab}\rho(v)N_0 \quad \text{where} \quad \rho(v_{ab}) = \frac{I(v)}{c} \quad \text{and} \quad N_0 = Vc_0 \tag{2.17}$$

where c is the speed of light, $I(v)$ is the intensity of the beam, and c_0 is the concentration of the absorbers. Therefore, the variation of intensity across the irradiated volume (V) can be written as:

$$dI = B_{ab}\frac{I(v)}{c}N_0\frac{hv}{V} = \frac{B_{ab}hv}{c}c_0 \tag{2.18}$$

where c_0 is the concentration of the sample. The solution of Equation 2.18 is $I = I_0 e^{-\frac{B_{ab}hv}{c}c_0 x}$, and therefore by comparison with Equation 2.15 it is possible to write:

$$\sigma(v) = \frac{B_{ab}hv}{c} \tag{2.19}$$

Beside the attenuation cross section, the absorption strength of a system can also be characterized by another quantity called oscillator strength (f), which estimates the overall, energy-integrated absorption strength of the system, by comparing it to the rate predicted for a classical electric dipole oscillating at the same energy [179]:

$$f = \frac{4.32 \cdot 10^{-9}}{n}\int \epsilon(\nu)d\nu \tag{2.20}$$

$$f = \frac{8\pi^2 m\nu}{3he}|\mu_{ab}|^2 = \frac{mh\nu}{\pi e^2}B_{ab} \tag{2.21}$$

where n is the refractive index, m and e are the electron mass and charge and ν is the frequency of the transition (in cm^{-1}). Thus, Einstein's coefficient B can be experimentally estimated by an absorption measurement if the number of the absorbers is known. An allowed transition is typically characterized by an oscillator strength $f = 0.1 \div 1$, a cross section of $\sigma \approx 10^{-17} \div 10^{-16} cm^2$ and a molar extinction coefficient of $\epsilon \approx 10^4 \div 10^5 M^{-1} cm^{-1}$.

Lifetime and Quantum yield

When N_0 molecules are excited from the ground state to the upper state, the excited molecules undergo radiative and possibly non-radiative decay to the ground state (here, the photo chemical reactions are neglected). The depopulation of the upper state can be described by the following equations:

$$\frac{dN}{dt} = -(k_r + k_{nr})N_0 \Rightarrow N(t) = N_0 \cdot e^{-\frac{t}{\tau}} \tag{2.22}$$

$$where \quad \tau = \frac{1}{k_r + k_{nr}} \tag{2.23}$$

where τ is the total lifetime of the excited state, k_r and k_{nr} are the radiative and non-radiative decay rate, respectively.

It is possible to define another important quantity which is the emission Quantum Yield (QY). It is the ratio between the number of emitted photons and the absorbed photons, and it is also described by the ratio of the radiative decay rate and the total decay rate [178]:

$$QY = \frac{k_r}{k_r + k_{nr}} \tag{2.24}$$

The connection between Einstein's coefficient A and B expressed by Equation 2.6 and 2.7 becomes a connection between two experimental macroscopic quantities: the oscillator strength f and the radiative rate k_R. In fact, the oscillator strength is related to the spontaneous emission coefficient B by Equation 2.21, and A is equal to the radiative rate of the emission which can be obtained by a time resolved fluorescence measurement. The relation between the absorption

strength (expressed by f or ϵ) and the spontaneous decay rate (corresponding to $A = K_R$) can be expressed in a form known as the Strickler-Berg formula, valid for broad molecular bands when the transition is strongly allowed and when no large conformational changes or electronic variations occur [181]:

$$k_r = 2.880 \cdot 10^{-9} n^2 < \nu_f^{-3} >^{-1} \int \frac{\epsilon(\nu)}{\nu} d\nu \tag{2.25}$$

where n is the refractive index, ν_f is the average of the emission frequency in cm^{-1} and $\epsilon(\nu)$ is the extinction molar coefficient.

The last formula connects the lifetime to the area of the absorption band and to the shape of the emission band. This shape is influenced by the Franck Condon factor (Equation 2.14), i.e. by the overlap of the nuclear wavefunctions of two different electronic states, and can be modified by inhomogeneous factors as the presence of solvent fluctuations around the system or inhomogeneity of the system itself.

Until now, a two-level system was described where the transition is very simple, but in general a system can display a complex pattern of energy levels, with multiple possible electronic transitions, and several relaxation phenomena can occur as pictured in Jablonski diagram in Figure 2.3.

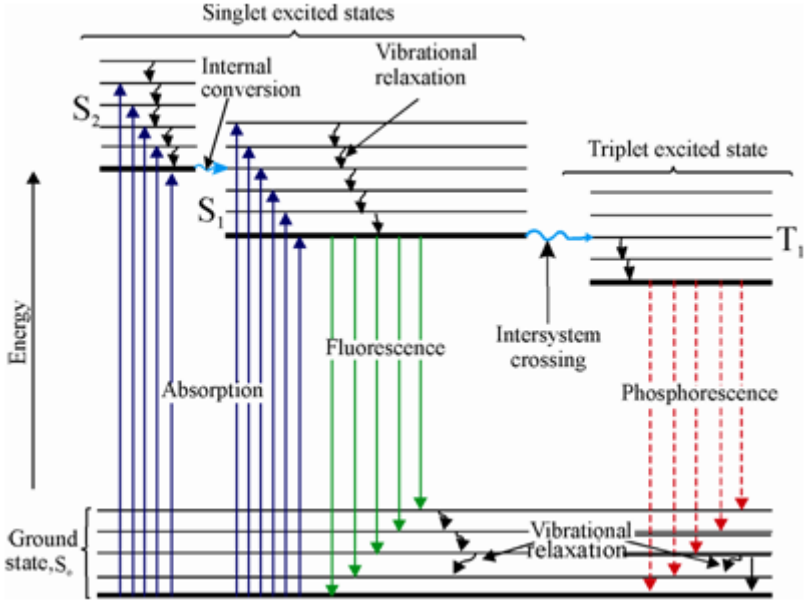

Figure 2.3: Jablonski diagram summarizing the possible processes after photoexcitation (blue arrows). The phenomena are non-radiative (wavy arrows) or radiative (straight arrows).

For example, a system can undergo intersystem crossing which is a non-radiative transition connecting states of different multiplicity, such as singlet to a triplet state. Once the latter is populated, spontaneous emission to the ground state becomes less probable because the singlet-triplet transition is forbidden by the selection rules, and the emitted signal, the so-called phosphorescence, occurs with a very low radiative rate, corresponding to a long time scale, even in the range of milliseconds. Non-radiative decays are basically vibrational relaxations, and they can occur by internal conversion and intersystem crossing. In general, a system which is initially excited to a higher electronic state, will return to the lowest excited state by fast internal conversion and, then, it will produce emission with which it returns to the ground state. This is the so-called Kasha's rule which states that the emission occurs always from the lowest excited state independently

of excitation wavelength. [180] Despite this, violations to this scenario are more and more often reported thanks to the introduction of femtosecond time-resolved spectroscopies [182].

Solvation

As already mentioned, the absorption transition occurs so fast that the system does not have time to react to the external environment. On the contrary, lifetime of photo-excited state is long enough that the system can interact with the external environment. If the surroundings is a polar solvent, one can picture the microscopic interactions with the system as in Figure 2.4. The fluorophore

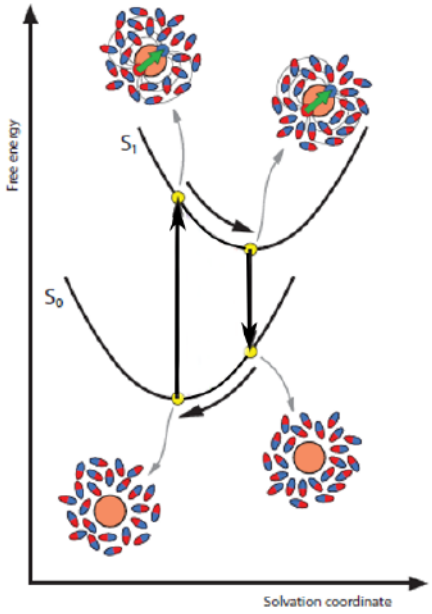

Figure 2.4: Representation of solvatochromic effect on electronic transition. The dipole moment of the ground state is null for simplicity, and the solvent molecules around it have a random orientation. After photoexcitation (1) the dipole moment of the excited state is bigger than zero and it generates an electric field. The solvent molecules are forced to reorganized themselves and in this way, the energy of the excited state decreases (2) producing the Stokes Shift. Afterwards, the chromophore returns to the ground state emitting light (3) and, then, solvent relaxes back to the ground state configuration (4).

is surrounded by the molecules of the solvent which can be schematised as permanent dipoles capable of orienting themselves under the action of an external electrical field or, such as those due to dipolar interactions with the chromophores. After excitation, the chromophore and the solvent dipoles are no longer in equilibrium, because of the photo-induced change of the electronic distribution on the chromophore. The solvent molecules will rotate to align with the local electric field produced by the excited system in order to minimize the electrostatic interaction energy, thus lowering the energy gap between the excited and the ground state. This decrease, due to the

solvent, is called solvatochromic (or dynamical) Stokes shift and it increases the size of total Stokes Shift, adding itself to the vibrational relaxation Stokes shift. A simple theory which can be used to describe solvent effects describes the solvent as a continuum dielectric medium with a certain dielectric constant ϵ and a refractive index n. In this way, and considering chromophores as point dipoles inside a spherical cavity surrounded by the solvent, the solvatochromic shift (Δv_{ss}) can be expressed by the Lippert-Mataga equation [178]:

$$\Delta v_{ss} = \frac{2}{hc}\left(\frac{\epsilon-1}{2\epsilon+1} - \frac{n^2-1}{2n^2+1}\right)\frac{|\bar{\mu_E} - \bar{\mu_G}|^2}{a^3} + cost \tag{2.26}$$

where a is the radius of the cavity (usually chosen in the model to match the size of the chromophore), and μ are permanent dipole moments of the excited (μ_E) and the ground state (μ_G) of the fluorophore. Equation 2.26 gives the absorption-emission Stokes shift (Δv_{ss}), as function of solvent polarity. The effect expressed by Equation 2.26 derives from the combined shifts of the absorption and emission bands: if $\mu_E > \mu_G$, both the absorption and the emission undergo a redshift when increasing the polarity (bathocromic shift), on the contrary, if $\mu_E < \mu_G$ the shift is in the blue (hypsochromic). However, in both cases, the extent of the shifts in absorption and emission are unequal, so that the Stokes shift always increases from the ideal chromophore in gas phase to a solvent with non-negligible polarity, as prescribed by Equation 2.26. Anyway, the Equation 2.26 describes only effects related to the dielectric polarity of the solvents and does not take into consideration other effects as hydrogen bonding interactions and the polarizability of the chromophore. [178]

Solvation usually occurs on multiple time scales in the ps and sub-ps time domain, as reported in Table 2.1 for a few representative solvents, while the fluorescence lifetime is usually several nanoseconds. Thus, the solvation relaxation is usually complete before the fluorescence occurs and with steady state fluorescence experiments the only evidence of solvatochromic effects is solvent-dependence of the peak position of the emission band.

Solvent	τ_1 (ps)	τ_2 (ps)	τ_3(ps)	τ_4 (ps)
H_2O	0.02	0.2	2	-
Ethanol	0.03	0.3	6	40
Dimethylformamide	-	0.2	1.7	29

Table 2.1: Typical values for solvation time scales for few representative solvents [183,184].

In contrast, with the use of ultrafast techniques, it is possible to go deeply inside the solvation process and to study it in "real time". For example, by monitoring the time dependence of the fluorescence on sub-nanosecond time scale, ultrafast experiments allow the direct observation of the so-called inertial solvation ($\tau < 1ps$) and diffusive solvation ($\tau > 1ps$) which show up as the dynamical solvation shift. These experiments can show how the solvation process occurs displaying the dynamical Stokes Shift which is hidden in steady state experiments.

Red-edge effect

In particular situations (e.g. in a viscous solvent at low temperature) the solvation dynamics can become slow enough to occur on a time scale which becomes comparable, or even slower, to that of the excited-state decay. In this situation, a particular effect can occur, known as the red edge effect. For a typical chromophore in an ordinary solvent at room temperature, the solvent

normally fluctuates very fast around the chromophores, and this allows chromophores to explore different configurations causing an inhomogeneous broadening of the emission band (dynamic inhomogeneity), as observed in a steady-state experiment. If the solvation is slow, the situation becomes different. In fact, the fluctuations are slow and the inhomogeneity becomes static on the time scale of the excited-state lifetime. This means that the photoexcitation selects a subset of the system with certain characteristics determined by the solvent. Then, this subset will emit at a particular energy depending on the particular solvent configuration around it. This phenomenon is called red-edge effect [185] which makes the fluorescence peak dependent on the excitation wavelength.

In fact, also other forms of static inhomogeneity which are not related to solvent effects can give rise to a behaviour which is practically equivalent to (and can be named as) a red edge effect which consist in the photoselection of part of a system due to static inhomogeneity of the sample (and not to the solvent). Also in this case, the emission peak is dependent on excitation wavelength but the reason is not a slow solvation, but rather the presence of unequal chromophores with different structures, hence electronic configurations and HOMO-LUMO gaps. Also in this case, the broadening of the band is inhomogeneous and it is related to the superposition of emission bands which peak at various energies [186].

Chapter 3

Experimental setups and procedures

The aim of this chapter is the description of the synthesis procedures, experimental setups and analysis methods used to perform the experiments and to analyse the results.

Specific attention is on the description of setups that I have used firsthand, as opposed to those accessed through collaborations. In particular, a part of the chapter is dedicated to the description of the femtosecond transient absorption setup and to the Fluorescence Upconversion setup which I have built as a part of the Ph.D.

3.1 Synthesis

During this Ph.D., different samples of CDs were studied in order to investigate differences and similarities observed among CDs obtained by diverse synthesis procedures and, therefore, having diverse structures. Some samples were synthesized in house (with a bottom up procedure) and other were got by a collaboration with the University of Cordoba (top down method).

Bottom up synthesis

The synthesis procedure developed in house consists in two steps: the carbonization of the precursors and the separation/purification of the sample. It starts from an aqueous solution (10 mL of milliQ water) of citric acid monohydrate (3 g) and urea (3 g) (Sigma Aldrich). After the solutes are completely dissolved in water, the solution is exposed to microwave irradiation until a complete evaporation of water occurs. The result is a strongly hygroscopic black powder which is dried in vacuum for 90 minutes obtaining a fine black powder made up of aggregates of CDs and, most likely, many other impurities.

Some parameters of the synthesis were changed and, in particular, it is possible to obtain CDs with different structure and different optical properties by changing the ratio between the precursors (citric acid and urea) and, therefore, changing the ratio between nitrogen and carbon (N/C). In particular, during the experiments four different N/C ratios were used to produce CDs: 0.14, 0.34, 0.58 and 0.74. If urea is not added in the synthesis (N/C=0), the product of the procedure is not a powder but rather a gel-like substance. If the amount of urea is increased too much with respect to citric acid (N/C=1, = 1.5, =1.75), the samples are not pure CDs and they contain some other impurities.

The sample can be already studied at this point of the synthesis, but, it probably contains some impurities which can be eliminated by a purification procedure. Thus, some samples undergo a purification/separation procedure which is carried out in collaboration with the group of Prof. G. Giammona (STEBICEF; UNIPA).

In order to begin the separation/purification procedure through a size exclusion chromatography (SEC) the powder is dissolved in water. In order to get a sample with a suitable concentration for efficient column chromatography, the initial solution is concentrated to about 4 $g \cdot L^{-1}$ by using a rotating evaporator at 60 °C, and 50-80 mbar. Then, SEC is carried out using a glass column (100 cm length, 1.5 cm diameter) packed in turn with sephadex G25 (15 g), G15 (15 g) and G10 (30 g), three resins with increasing cut-off values. This specific combination of resins was selected on the basis of previous works in which a clear correlation between the hydrodynamic radius (Hr) and the average molecular weight (Mw) of random polymers was observed [187]. Using that correlation, the limit of exclusion of commercially available resins was converted from Mw to Hr so as to select resins suitable to separate nanoparticles in the 1-6 nm range of diameters. During the SEC procedure, 5 ml of the CDs solutions were added on the stationary phase and, after the complete absorption, ultrapure water was added on the top as eluant (flow = 2.5 ml min^{-1}). On one hand, the SEC eliminates most impurities, such as residuals from the synthesis or small molecules formed as side products of CDs. Besides, SEC separates the nanoparticles into fractions having different characteristics, which will be described in the next chapter.

Top down synthesis

The samples obtained through the collaboration with the group of Prof M. Varcàrcel (Cordoba University) are prepared by two different top down methods.

One of them (hereafter pCQDs) is a graphitic CDs with surface covered by C=O moieties obtained in previous studies [54]. It was synthesised by a top down methodology explained in details in ref [54] and here briefly. 200 mg of MWCNTs in 20 mL of a solution containing 3 : 1 H_2SO_4/HNO_3 were refluxed at 140 °C for 7.5 h. After cooling down to room temperature, 40 mL of acetone were added and a dark brownish solution was left to stand overnight. Such a treatment with acetone allows passivation with C=O moieties of the surface of CDs formed through the chemical oxidation of MWCNTs. The passivated CQDs were then neutralized and centrifuged at 13000 rpm for 10 min to remove large aggregates. Afterward, excess of salts were removed with ethanol by crystallization at low temperatures. The pCQD sample obtained by this procedure, mainly passivated by C=O moieities, was used as the starting point of a series of further passivation reactions aimed at producing other types of CDs with graphitic crystalline cores and different types of surface polar moieties, such as amine groups or thiol groups [55,56].

The second synthesis procedure produces amorphous CDs with the surface full of C=O and -COOH groups [5]. The synthesis consists in the acid hydrolysis of cellulose microcrystals in 12.2 N of H_2SO_4 under reflux conditions for 7 hours. After cooling down, the solution was centrifuged at 13000 rpm for 10 min and neutralized. Excess of salts were removed by crystallization in a mixture of water and ethanol [5].

3.2 Optical Characterization

Steady State Absorption

Absorption measurements were performed at University of Palermo by a double beam spectrophotometer (JASCO V-570) which is equipped with two light sources. The first is a tungsten iodine lamp which operates in the range 340÷2500 nm, and the second is a deuterium discharge tube operating between 190÷340 nm. The light is driven to a monochromator with a 1200 grooves/mm grating. Then, the monochromatic beam is split in two beams. One beam hits the sample, and the other is used as reference. The detection occurs by a photomultiplier tube which measures alter-

natively the two beams. The instrument returns as output the optical density:

$$OD = log_{10}\frac{I_0}{I} \tag{3.1}$$

where I and I_0 are, respectively, the light transmitted by the sample and the reference. The optical density is recorded as a function of excitation wavelength, spanning across the spectral range. It is possible to easily obtain the absorption coefficient using Equation 2.16 and Equation 3.1. Each measurement was carried out at room temperature with a bandwidth of 2 nm.

Steady State Photoluminescence

Stationary photoluminescence (PL) measurements were carried out at University of Palermo by a spectrofluorometer JASCO FP-6500. The excitation source is a 150W Xenon discharge lamp operating in 220÷750 nm range. The excitation light is dispersed by a monochromator with a 1800 grooves/mm grating which gives the possibility to monochromatize the beam with a variable bandwidth (selected by the operator). Then, part of the beam is measured by a photomultiplier to correct the signal for temporal fluctuations, and the rest of the beam is directed through the sample, and the emission is collected in a standard 90° configuration by an additional monochromator (same characteristics of the first monochromator). At this point, the emission is detected by a photomultiplier which gives the output signal $S_R(\lambda_{ex}, \lambda_{em})$ which can be recorded as a function of the emission wavelength (PL spectrum) fixing the excitation wavelength, or as a function of excitation wavelength (PLE spectrum) fixing the emission wavelength. Each measurement was performed at room temperature with a bandwidth of 2 nm. The excitation spectra were recorded in a low absorption condition (< 0.15 OD) in order to avoid any distortion effects.

Analysis procedures In order to analyse the data, both emission and excitation spectra have to be corrected with two procedures. These corrections are needed to take into account the influence of the spectrum of the Xe lamp used for excitation, which is not flat, and of the different instrumental response of the detector system to the various wavelengths.

To correct for the emission spectrum of the lamp, it is necessary to record it. A very concentrated Rhodamine B sample (in ethanol) can be used to this purpose. In fact, this sample shows a Quantum yield of 1 in a large spectral range and this implies that every absorbed photon at every excitation wavelength is converted to an emitted photon at 640 nm (its emission peak). The recorded PLE signal gives the spectrum of the Xenon lamp. Every emission spectrum was corrected by the value of the intensity at its excitation wavelength, in order to make the intensity comparable to each emission spectrum excited at different wavelengths. This correction was also applied to excitation spectra, where the entire spectrum is divided, point-by-point, for the excitation spectrum of the Rhodamine reference.

To obtain the spectral response of the instrument, a synchronous spectrum was recorded ($\lambda_{ex} = \lambda_{em}$) inserting a diffusing object in the sample cavity. This spectrum was corrected for the source spectrum, and the result gives the spectral response of the instrument. Anyway, in the typical emission spectral ranges explored in this Thesis, the spectral response is essentially flat.

Quantum Yield The emission Quantum Yields (QYs) were obtained by comparing the PL intensity of the sample with the PL intensity of a reference aqueous solution of fluorescein at pH=13 ($QY_R = 0.95$). To obtain QY values, we paid attention to perform the measurements of the sample and of the reference during the same day, with the same instrumental parameters and in the same geometrical conditions. The following formula was used to calculate QY [178]:

$$QY = QY_R \cdot \frac{A}{A_R} \frac{1 - 10^{-OD_R}}{1 - 10^{-OD}} \frac{n^2}{n_R^2} \tag{3.2}$$

where A and A_R are the areas under emission curves, OD and OD_R are absorbance values of the sample and the reference at excitation wavelength, n and n_R are the refractive index of the solutions.

Single Molecule Spectroscopy

Single molecule emission measurements were performed in collaboration with University of Amsterdam. The aim of the measurements was to record the emission from single dots in order to measure dot-to-dot fluctuations and the spectral width of the single-dot emission.

The measurements were carried out using an inverted microscope (Zeiss, AxioObserver Z1) coupled to a spectrometer (Princeton Instruments, Acton SP2300) and a CCD (Princeton instruments, Pylon 400B) in a widefield scheme. Continuous wave excitation was provided by the 488 nm ($\sim 90\ W/cm^2$) line of an Ar^+ laser (Spectra-Physics, Stabillite 2017) and the emitted light was collected using a 100x air objective (Zeiss, Epiplan-Neofluar NA 0.75).

Samples with a low average particle density ($< 1/\mu m^2$) were prepared by drop-casting a dilute solution ($\sim 0.5\ \mu g/mL$) of CDs in water on a cleaned cover slip. In this way, it was possible to recognize separate bright spots due to the single dots (or small aggregates of particles). During a time scale of few minutes, the emission from single spots, as observed under the microscope, remained stable under the laser exposure. Each single-dot spectrum required an acquisition time of ∼8 minutes.

Time Resolved Spectroscopy

Time resolved measurements were performed by a setup which can be divided in three different parts: the excitation system, the monochromator and the detector (Figure 3.1). The excitation

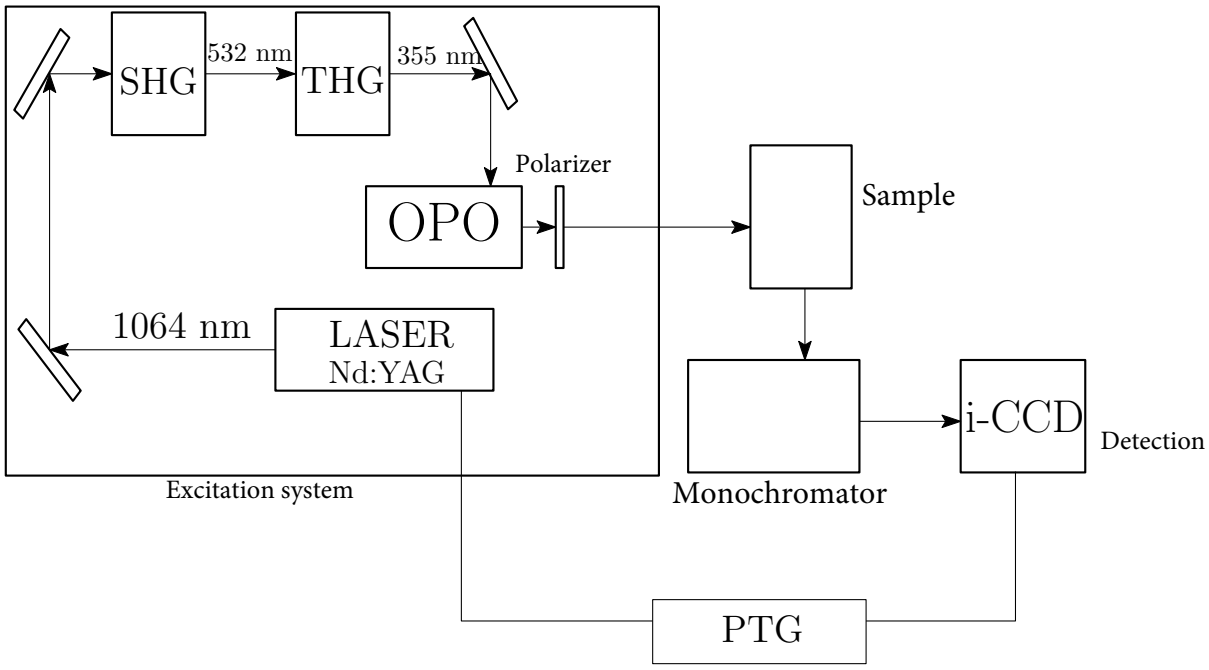

Figure 3.1: Experimental setup used to perform time resolved emission measurements.

system (Vibrant OPOTEK) is a tunable laser which is composed by an optical parametric oscillator (OPO) pumped by a Q-switched Nd:YAG laser. The Q-switched laser (QUANTEL) emits 5 ns pulses at 1064 nm with a maximum repetition rate of 10 Hz. The active laser medium is a Yttrium aluminium garnet doped by Neodymium ions. It is pumped by a Xenon lamp. The Q-switch is triggered by an electro-optic crystal (Pockels cell) placed in the laser cavity. The actions of this pockels cell changes the Q-factor of the cavity: when it is active the Q-factor increases and the laser activity starts with an initially very high population inversion.

The 1064 nm beam is directed into the second harmonic generator (SHG), a crystal where the beam is converted in its second harmonic (from 1064 nm to 532 nm), and then to the third harmonic crystal (THG) to generate the third harmonic of the 1064 nm, that is 355 nm. The 355 nm beam is directed to the OPO which is a based on a non-linear crystal ($\beta - BaB_2O_4$ called $\beta-$BBO) which gives the possibility to generate tunable wavelengths. In particular, from a single beam with frequency ω_p, through this crystal it is possible to obtain two beams (named signal and idler) with different frequency and polarization following the conservation of energy and momentum which in collinear geometry can be written as:

$$\begin{cases} \omega_p = \omega_i + \omega_s \\ \vec{k_p} = \vec{k_i} + \vec{k_s} \rightarrow n_p\omega_p = n_i\omega_i + n_s\omega_s \end{cases} \tag{3.3}$$

where n are the refractive index of the crystal at the considered frequencies and polarizations. The second equation corresponds to the so-called phase matching condition, which can be verified by exploiting the birefringence of the crystal. In fact, the refractive index of at least one of the waves can be continuously changed by rotating the crystal with respect to the incident beam, because it propagates as an extraordinary wave. Therefore, a certain choice of the angle determines the particular signal/idler wavelengths that are generated. After the OPO, the two beams are perpendicularly polarized and inserting a polarizer guarantees the selection of one of them. In this conditions, the signal beam can span from 410 nm to 710 nm, and the idler can span the 710-2400 nm spectral range. It is also possible to introduce in the beam path, three different UV-modules by which the frequency of signal or idler is duplicated in order to reach the range 210-410 nm. The energy of the beam is measured by a pyroelectric detector before the sample cavity.

The excitation beam is directed to the sample through two prisms and the emitted light is collected by a lens and, passing through a slit, is directed to the monochromator and, then, to the detection system. The slit width can be changed manually, determining the spectral resolution in combination with the choice of one of the available gratings. In fact, it is possible to choose three different gratings which differ in the blaze wavelength (λ_B) and in the grooves density:

- λ_B= 300 nm and 150 grooves/mm $\Rightarrow$ spectral resolution of 20 nm/mm
- λ_B= 300 nm and 1200 grooves/mm $\Rightarrow$ spectral resolution of 3 nm/mm
- λ_B= 500 nm and 300 grooves/mm $\Rightarrow$ spectral resolution of 11 nm/mm

The first grating was used and the slit was fixed at 200 μm for every measurement performed during this thesis corresponding to a spectral resolution of 4 nm.

The detection part is entrusted to an Intensified CCD camera (PI-MAX Princeton Instruments) which is synchronized to the excitation laser by programmable timing generator (PTG), triggered by the laser. To collect the emission a lens is used and the light is sent to the monochromator and then to the microchannel plate (MCP) which is an image intensifier composed by a semiconductive glass plate punctured by $10 \div 25$ μm holes (channels). The light dispersed by the monochromator is directed to the photocathode of the MCP which, because of photoelectric effect, emits electrons. The walls of the channels have a high secondary emission coefficient and when hit by electrons,

they generate additional electrons with a gain depending on the voltage at the MCP. The generated electrons are accelerated and hit a phosphor screen causing production of photons. They are transferred to the CCD camera by optical fibers. The photons generate charges on the CCD pixels (1024x256) and these are converted to an analog signal, then digitalized and, finally, transferred to the computer.

The voltage at the photocathode and at the MCP can be modified and this allows to enable and disable the CCD acquisition in a controlled way. In this way, it is possible to acquire the signal in a determined temporal window in order to perform time resolved measurements.

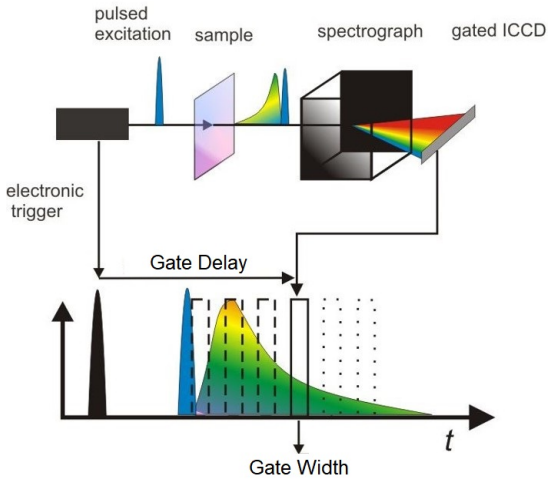

Figure 3.2: Scheme of a time resolved spectroscopic experiment.

The measurement consists of recording the emission spectrum in a fixed temporal window (Gate width), in which the MCP is on, after a specific delay time (Gate delay) from the excitation pulse (Figure 3.2). A complete time-resolved fluorescence measurements consist in a series of measurements with variable Gate delays from the time at which photo-excitation occurs, so as to reconstruct the entire kinetics of the decaying emission band. Gate width and Gate delay are selected by the operator, who can also choose the number of acquisitions through other two parameters in order to increase the signal-to-noise ratio (CCD accumulations and software accumulations).

Transient Absorption spectroscopy

Ultrafast transient absorption (TA) (or Pump/Probe) spectroscopy is a non-linear spectroscopy where one measures the changes in the absorption spectrum of a system following an external excitation. In a standard experiment, the sample is photoexcited by a femtosecond pulse called *pump* and the variations of the absorption spectrum are measured by another ultrafast pulse named *probe*. The probe is usually spectrally broad (400-700 nm) and this allows to record simultaneously changes of the absorption spectrum in a wide spectral range. Moreover, the variations in the entire spectrum are recorded at different time delays between the two pulses, yielding kinetic traces of the time dependent absorption coefficient at every wavelength.

The pump pulse induces the transition of the irradiated sample from its ground state to an upper energy state, and at a certain delay after the excitation, the intensity of the probe is recorded after passing through the excited spot on the sample and compared with the result of an identical measurement without the pump pulse. TA signal is the difference between the absorption with

and without the excitation.

Assuming the number of absorbers in the system as $N_0 = N_g + N_e$, the sum of non-excited (N_g) and the excited absorbers (N_e), the Beer-Lambert law can be used to express the variation of the attenuation cross section($\Delta\sigma$) of a system with a thickness d between the ground state (attenuation cross section σ_g) and the excited state (attenuation cross section σ_e):

$$I_u(\omega) = I_0(\omega)e^{-\sigma_g(\omega)dN_0} \tag{3.4}$$

$$\begin{aligned} I_p(\omega) =& I_0(\omega)e^{-\sigma_g(\omega)d(N_0-N_e)-\sigma_e(\omega)d(N_e)} = \\ =& I_0(\omega)e^{-\Delta\sigma(\omega)dN_e-\sigma_g(\omega)dN_0} = \\ =& I_u(\omega)e^{-\Delta\sigma(\omega)dN_e} \end{aligned} \tag{3.5}$$

$$\Delta\sigma(\omega) = -\frac{1}{dN_e}\ln\left(\frac{I_p(\omega)}{I_u(\omega)}\right) \tag{3.6}$$

$\Delta\sigma$ is directly related to the recorded TA signal which is the change of the absorption spectrum ($\Delta OD = \Delta\sigma dN_e/2.303$). In fact, the TA signal can be expressed as:

$$\Delta OD = OD_p - OD_u = -\frac{1}{2.303}ln\frac{I_p}{I_u} \tag{3.7}$$

considering that the variation of the absorption is low which means $I_p - I_u << I_u$, it is possible to linearize the Equation 3.7 and calculate the TA signal as:

$$\Delta OD = \frac{1}{2.303}\frac{I_u - I_p}{I_u} \tag{3.8}$$

In general, $\Delta OD(\omega)$ is the superposition of three contributions: ground state bleaching (GSB), stimulated emission (SE), and excited state absorption (ESA) (Figure 3.3).

GSB is a negative signal related to the depopulation of the ground state upon the pump pulse. In fact, photo-excited molecules are no more in the ground state and they can not contribute to the absorption at that specific wavelength, therefore the probe is less absorbed in that spectral range and this appears as a negative signal in the TA spectrum.

Also SE is a negative signal and it occurs because the probe pulse passing through the excited volume stimulates the emission of a photon from the excited state to the ground state. It produces a negative signal because the detector records an increase of intensity of the probe in the photo-excited system. Thus, its spectral profile is very similar to the fluorescence band except for its negative sign. However, it is worth noticing that SE intensity is proportional to the emission frequency, while the intensity of stationary fluorescence depends on the cube of emission frequency, as it is easy to see from Einstein's coefficients (section 2.1).

ESA is the only positive signal which is recorded in a TA experiment. It is due to the new electronic transitions that are possible after the photoexcitation from the excited state to other higher energy states [188].

It is important to notice that TA signal should be linear with the intensity of the pump which means that the photo-excited transition is not saturated and that only a small percentage ($< 10\%$) of the system is excited. But, this is not the only fundamental ingredient to perform useful TA experiments. Another crucial requirement of these experiments is time resolution, which should be good enough to resolve all the dynamics of interest (usually $<$ 100 fs). To achieve fs time resolution it is necessary to have short pulses (50-80 fs) which keep their duration along the setup (for example they should not traverse too much glass) and, moreover, it is necessary that the two

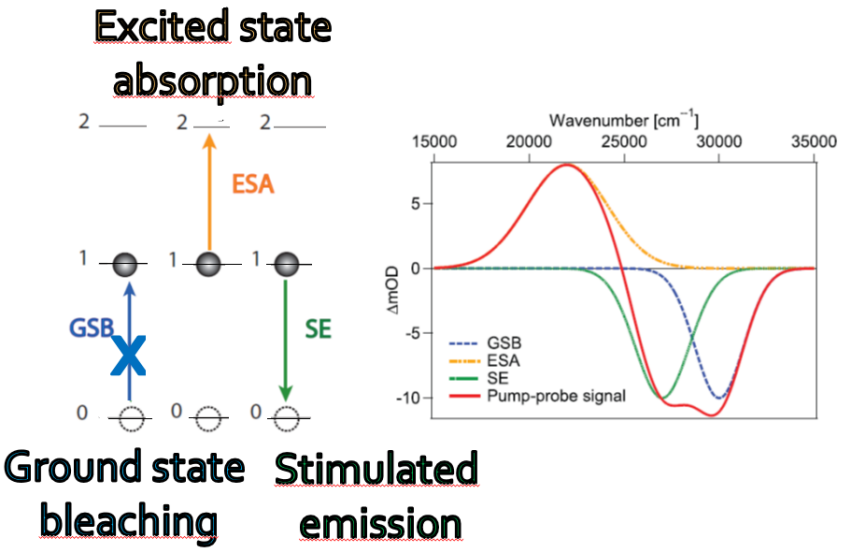

Figure 3.3: Diagram of the typical signals in a TA experiments: ground state bleaching (GSB), due to the decreasing absorption of the sample, stimulated emission (SE) due to the interaction with the probe which stimulates photon emission and the consequent decay of the excited system back to the ground state, and excited state absorption (ESA) related to the possibility of new transitions toward higher energy states. On the right panel a hypothetical signal with the three contributions.

pulses are synchronized down to the scale of a few fs. Synchronization on these time scales cannot be achieved by the use of electronics. The only way to achieve such a precision is to use optical strategies. In fact, a transient absorption setup typically exploits a *delay stage* in the optical path of one of the beams which allows to change the relative delay between two pulses increasing or decreasing the path of one of them. It is easy to calculate that an increase in the path of 3 mm corresponds to a delay of 10 ps.

Propagation of Ultrafast Pulses When dealing with optical pulses with femtosecond pulse durations, it is important to remember the concept of group velocity dispersion (GVD) and its effects on the temporal length of the pulse. The GVD, in fact, affects pulse duration which passes through any media. It is defined as:

$$GVD = \left(\frac{d^2k}{d\omega^2}\right)_{\omega_0} = \frac{d}{d\omega}\left(\frac{1}{v_g(\omega)}\right)_{\omega_0} \tag{3.9}$$

where v_g is the group velocity. This latter can be written as:

$$v_g \approx v_\phi\left(1 - \frac{\omega}{n(\omega)}\frac{dn(\omega)}{d(\omega)}\right) \tag{3.10}$$

and v_ϕ is the phase velocity of the pulse. During propagation, every spectral component of the pulse acquires a different delay (depending on the frequency and on the refractive index) and the result is a temporal broadening of the pulse without any spectral changes. Besides, the group velocities of two pulses (at different wavelengths) which pass through the same medium, are different (*group velocities mismatch* - GVM): if they are initially overlapping in time, after some propagation distance they are no longer overlapping. The GVM effect, for example, can be very

important in the generation of the pump pulse through nonlinear interactions because it can limit the interaction between two pulses.

To visualize the effect of GVD on a gaussian pulse passing through a medium, a simulation was performed. In Figure 3.4 three gaussian pulses are reported. The red pulse represents a gaussian

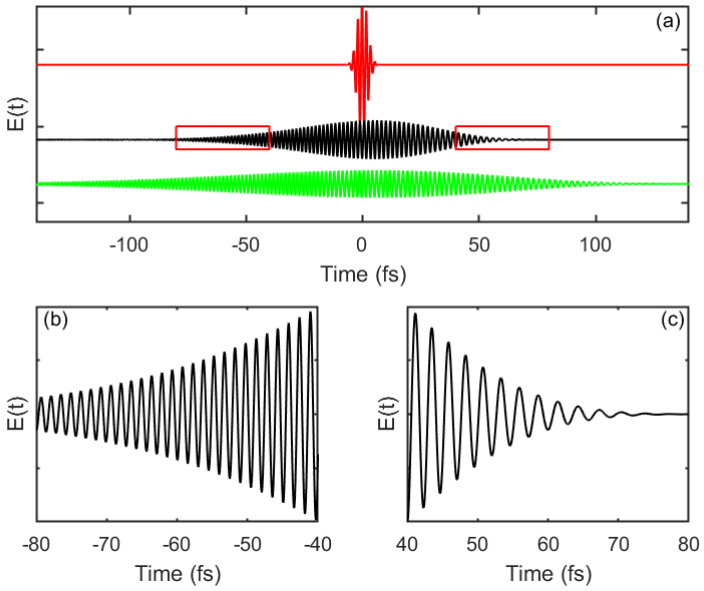

Figure 3.4: Panel a: Simulation of a gaussian pulse centred at 550 nm with FHWM= 5 fs after propagation through a SiO_2 medium of 1 mm thickness (black curve) and 2 mm (green curve). Panel b and c: zooms of the tails of the black pulse (red squares). Each wavelength is delayed by a different phase, resulting in a longer pulse with a positive chirp (the redder frequencies are faster than the bluer).

pulse with a FWHM=5 fs centred at 550 nm, the black and the green curves represent the same pulse after passing through a 1 mm or a 2 mm SiO_2 medium, respectively. GVD alters the pulse duration increasing it and causes a frequency *chirp* which means that the instantaneous frequency of the pulse depends on the time. In Figure 3.4a, it is evident that the duration of the pulse is extended on time, and the pulse is *chirped* as it is evident from the comparison of the frequencies of the two sides of the pulse as shown in bottom panels of Figure 3.4. The use of mirrors helps to diminish the effect of the GVD because the pulses do not pass through any medium being just reflected. The GVD effect is more relevant on the probe pulse than the pump pulse. Before passing through a medium, the duration of the probe pulse (trasform limited) is few fs, on the contrary, the duration of the pump pulse is 50-80 fs. As it is shown in the simulation in Figure 3.5, after 1 mm of SiO_2 the duration of the probe increased relatively more than the duration of the pump.

Some methods exist to manipulate the chirp. With the use of the so-called stretchers and compressors built by using a pair of prisms or gratings, it is possible to control the duration of the pulse adding positive or negative GVD. Positive GVD means $\frac{dn(\omega)}{d(\omega)} > 0$ and it is common for standard materials. Negative GVD means $\frac{dn(\omega)}{d(\omega)} < 0$ and it can be obtained by the use of a couple of prisms or gratings. With a negative GVD the redder part of a pulse is slower than the blue part, thus, adding negative GVD compensates the positive GVD and allows to have a compressed (shorter) pulse (Figure 3.6).

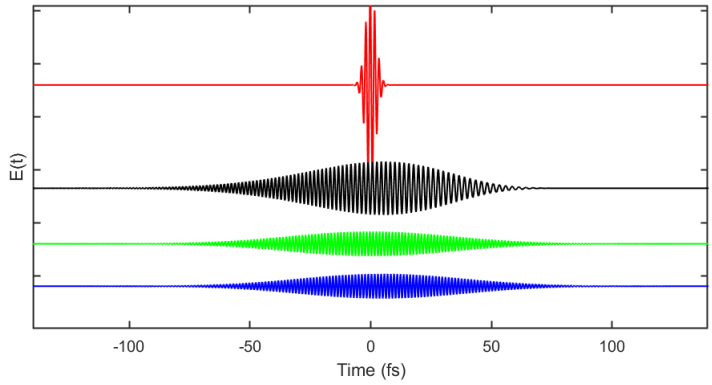

Figure 3.5: Simulation of a gaussian pulse centred at 550 nm with FHWM= 5 fs (red curve) after propagation through a SiO_2 medium of 1 mm thickness (black curve) and of a gaussian pulse centred at 400 nm with FHWM=80 fs (green curve) propagating in the same medium (blue curve).

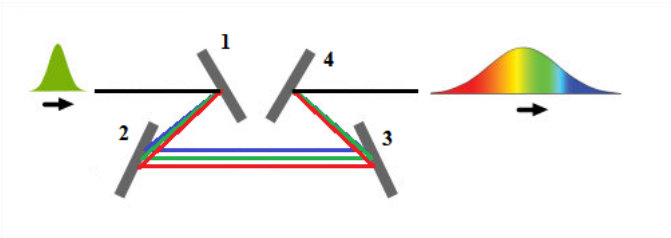

Figure 3.6: Compressor scheme: four gratings used to disperse a pulse and to give negative GVD to the pulse.

Generation of pump and probe pulses In a standard setup, both beams derive from a single laser (here, a Ti: sapphire laser), the original beam is split in two portions which are used to generate separately the pump and the probe. In general, both pump and probe derive from the same laser source because it would be harder to synchronize with femtosecond accuracy two beams originating from two different lasers.

Defining the experimental conditions, the operator selects the excitation wavelength and this decision establishes the generation methods of the pump beam. In particular, in this thesis, two different non linear phenomena were used: second harmonic generation (SHG) to generate a 400 nm beam from the fundamental Ti:Sapphire beam, centred at 800 nm, and optical parametric amplification used to generate a tunable pump in the spectral range of 490-760 nm. Both the processes are based on non-linear phenomena and are described in more detail hereafter.

The polarization of a medium upon irradiation with an electrical field $\vec{E}$ can be expressed as [189, 190]:

$$\frac{\vec{P}(\omega)}{\epsilon_0} = \chi^{(1)}(\omega)\vec{E}(\omega) + \chi^{(2)}(\omega)\vec{E}(\omega)\vec{E}(\omega) + \chi^{(3)}(\omega)\vec{E}(\omega)\vec{E}(\omega)\vec{E}(\omega) + ... \tag{3.11}$$

Where, in general, $\chi^{(n)}$ is a tensor. The first term of the equation describes the phenomena usually encountered in linear optics, while the other describe the nonlinear effects at different orders.

SHG is one of the simplest non-linear optical phenomenon which can be observed. Under certain conditions ($\chi^{(2)} \neq 0$, as generally occurs in a non-centrosymmetrical medium), two photons at the same frequency ω_1, passing through an appropriate medium, are combined to generate a

new photon with a doubled frequency ($2\omega_1$). The process follows the laws of energy and momentum conservation (as in Equation 3.3) and in not-depleted condition (negligible pump absorption) it is possible to describe the intensity of the new beam as [189, 190]:

$$I(2\omega_1) \propto \frac{\omega_1^2 \chi_{eff}^2 l^2}{n^3} I^2(\omega_1) \left(\frac{sin(\Delta k l/2)}{\Delta k l/2} \right)^2 \tag{3.12}$$

where n is the refractive index, l is the length of the material, $\Delta k = k_2 - 2k_1$ is the so-called phase mismatch, and χ_{eff} is the effective susceptibility which is a certain combination of the components of the $\chi^{(2)}$ tensor, which depends on the material and on its orientation (Figure 3.7). It is important to notice that the intensity of the new beam depends on the square of intensity of the incident beam but also on the square of the length of the material (blue curve in Figure 3.7-right panel). Moreover, the phase matching condition is important to optimize the intensity of doubled beam as displayed in Figure 3.7, and when $\Delta k = 0$ the doubling is maximally efficient (Figure 3.7). The phase matching condition $\Delta k = 0$ corresponds to the conservation of momentum in the SHG process. It can be seen as a situation in which two incident beams propagate in the medium with the same speed. In order to achieve this, the refractive index at those frequencies has to be the same. This is not possible in any isotropic media, but this limitation can be overcome by using birifrangent media in which the refractive index depends on light polarization and direction of propagation. For example, in an uniaxial crystal is possible to define the extraordinary (n_e) and the ordinary (n_o) refractive index, where the extraordinary index depends on the angle between the $\vec{k}$ of the beam and the optical axis. If the beam at ω propagates as an ordinary beam, while the beam at 2ω propagates as an extraordinry beam, changing the orientation of the crystal it is possible to obtain for only an angle $n_e(2\omega) = n_o(\omega)$, fulfilling the phase matching condition.

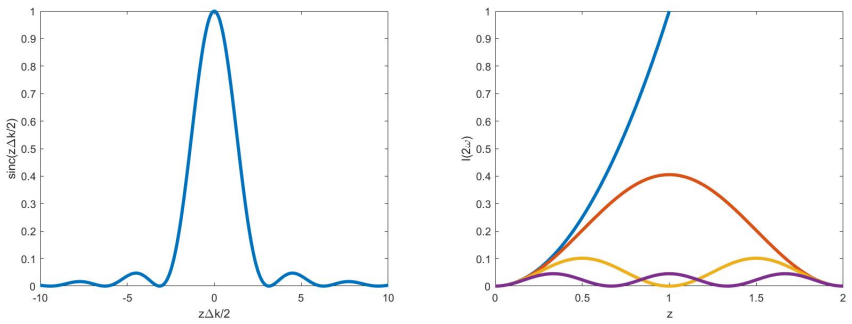

Figure 3.7: Left: Dependence of the SHG on the phase mismatch parameter. Right: Dependence of the SHG intensity as a function of distance at increasing ΔK values. Every maximum of the intensity is at $\pi/\Delta K$.

Another important parameter in SHG is the extent of spectral bandwidth which is doubled (acceptance bandwidth). In fact, the phase matching condition is exactly fulfilled only at a given wavelength, and therefore it cannot be exactly fulfilled across the entire pulse bandwidth. Considering that an ultrafast pulse has a wide spectral width (Heisenberg's indeterminacy principle $\Delta\omega\Delta t \geq 0.5$) only a part ($d\lambda_1$) of it is doubled ($d\lambda_2$) when the beam propagates through the crystal:

$$d\lambda_1 \propto \frac{\lambda_1}{l} \left(\frac{\partial n_o}{\partial \lambda_1}\bigg|_{\omega} - 0.5 \frac{\partial n_e}{\partial \lambda_2}\bigg|_{2\omega} \right) \tag{3.13}$$

Therefore to increase the broadening of the doubled beam, it is necessary to decrease the crystal thickness l, at the cost of SHG efficiency (proportional to l^2). Therefore, according to the experimental requirements one needs to find the right compromise between the two quantities.

The second way used in this thesis to generate a tunable pump pulse was to take advantage of a non-collinear optical parametric amplifier (NOPA) which makes possible to tune the excitation wavelength from 490 nm to 760 nm. Moreover, the visible beam can be doubled through SHG in order to obtain tunable pulses in the UV range. The output of a NOPA is obtained by the interaction of two beams in a $\beta-$BBO crystal: a strong pump (ω_p) and a weak and broadband *seed* ($\omega_s < \omega_p$). The pump is used to amplify the seed intensity and to create another beam named *idler* at ω_i, where $\omega_p = \omega_s + \omega_i$ for energy conservation. Considering that the seed is a broadband pulse, changing the orientation of the nonlinear crystal allows to amplify different wavelength which fulfills the phase matching condition. Optical parametric amplification can be obtained either in a collinear or non-collinear geometry. The NOPA configuration uses the latter, allowing to compensate for the GVM between the two pulses (Figure 3.8) which limits the interaction length and, therefore, the amplification of the seed.

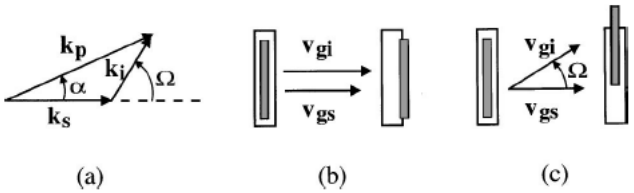

Figure 3.8: (a) Wavevectors of pump ($\vec{k}_p$), signal ($\vec{k}_s$) and idler ($\vec{k}_i$) in a non-collinear geometry; (b) Group velocity mismatch of signal and idler pulses in collinear geometry and (c) in non-collinear geometry. The interaction length between the pulses is longer in (c) than in (b). [191]

The advantages of a non-collinear configuration can be also explained in different terms: in a non-collinear configuration, the crystal orientation angle at which phase matching occurs for amplification of a given wavelength becomes dependent on the angle inside the crystal between the pump and signal α, as in Figure 3.9.

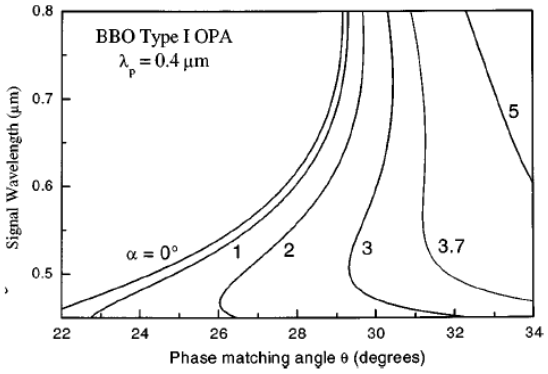

Figure 3.9: Phase-matching curves for a NOPA pumped at 400 nm, as a function of the pump-signal angle. [191]

In particular, as demonstrated in Figure 3.10, the phase matching condition is simultaneously achieved over a very broad wavelength range when $\alpha \sim 3.7°$. Usually, the output pulse is not broad as the continuous line in Figure 3.10 because the seed is temporally chirped and the interaction with the pump is with a narrower part of seed spectrum. Changing the alignment (spatially and temporally) between pump and signal allows to amplify different portions of the spectrum as the dashed lines in Figure 3.10.

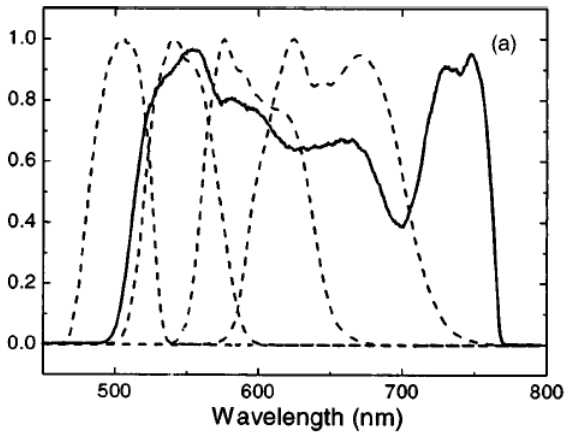

Figure 3.10: Solid curve: NOPA spectrum under optimum alignment conditions and a compressed seed; dashed line: sequence of spectra obtained by changing the white light chirp. [191]

The weak seed of a NOPA, usually, is a spectrally broad pulse. These pulses are called *white light* or *supercontinuum* pulse [192] and are generated by third order non-linear phenomenon which is the *Self-Phase Modulation* (SPM). It originates a spectrally broad and intense pulse useful for many applications and it is combined with another phenomenon called *Self-focusing* (SF) which increases the generation efficiency of the white light. Beside the NOPA seed, these white light pulses are also used as probe pulses for TA experiments. Their generation principle is explained hereafter.

Considering a centrosymmetric material ($\chi^{(2)} = 0$), the instantaneous polarization can be written as:

$$\frac{\vec{P}}{\epsilon_0} = \chi^{(1)}\vec{E} + \chi^{(3)}\vec{E}\vec{E}\vec{E} = \vec{E}(\chi^{(1)} + \chi^{(3)}|E|^2) \tag{3.14}$$

which makes possible to write the square of the refractive index n as:

$$n^2 = 1 + \chi^{(1)} + \chi^{(3)}|E|^2 = n_0^2 + \chi^{(3)}I \tag{3.15}$$

Therefore, a propagating pulse will produce a change of the refractive index related to its instantaneous intensity. In this situation, the instantaneous refractive index is given by the following equation where the intensity of the beam depends on the temporal and on the spatial distribution of the pulse:

$$n \approx n_0 + n_2 I(r,t) \tag{3.16}$$

Considering a Gaussian beam, the intensity depends on position and time. Therefore one may expect both spatial and temporal changes of the refractive index, which give rise, respectively, to SF and SPM. The SPM is the effect related to the temporal dependence of beam intensity and, in particular, to the variations of the phase of the pulse. The applied field can be written as:

$$E(t,x) = E_0 e^{-i(\omega_0 t - kx)} \quad \text{where} \quad k = \frac{\omega_0}{c} n(t) \tag{3.17}$$

therefore, the instantaneous phase of the pulse depends on time and as:

$$\phi(t) = \omega_0 t - \frac{\omega_0}{c} n(t) x = \\ = \omega_0 t - \frac{\omega_0 n_0}{c} x - \frac{\omega_0}{c} x n_2 I(t) \tag{3.18}$$

It is possible to introduce the instantaneous frequency $\omega(t)$ as:

$$\omega(t) = \frac{\partial}{\partial t}\phi(t) = \omega_0 - n_2 \frac{\omega_0 x}{c} \frac{\partial I(t)}{\partial t} \tag{3.19}$$

where the last term implies a change (self-modulation) of the frequency of the propagating light in a way controlled by the intensity envelope of the pulse itself. This implies the introduction of new frequencies in the spectrum of the pulse which are higher and lower than ω_0 in a symmetric way.

In parallel to SPM, another effect, that is self-focusing occurs because of the spatial dependence of the intensity in the pulse. Considering a gaussian beam, the intensity of the pulse depends on the spatial profile of the pulse. It is stronger in the centre of the beam than the sides. For this reason, the beam tends to modify the refractive index and this causes a focusing of the beam along its path. This self-focusing stops when the diameter of the beam, the *filament*, is so small that the linear diffraction is strong enough to balance the effect and prevent further self-focusing. This compromise should be reached before the damage threshold of the medium. Self focusing causes a dramatic increase of the local intensity of the electric field. SPM is strongly enhanced within the filament, contributing to the generation of an intense white light. Therefore, the formation of a stable filament is essential to have a stable and intense white light pulse. The output is a spectral

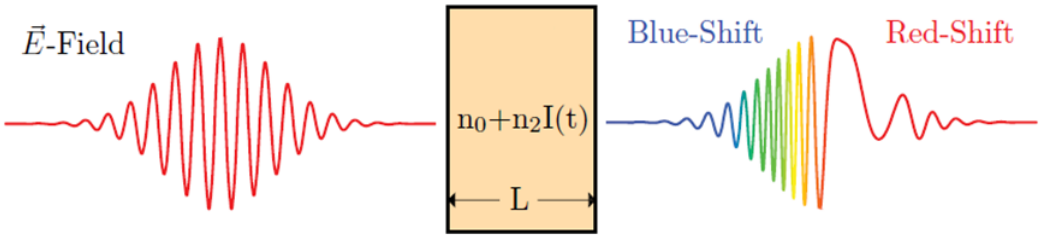

Figure 3.11: Generation of supercontinuum pulse (white light) from a red pulse propagating in a centrosymmetric medium.

broad pulse as a consequence of combination of SPM and SF, and it is also temporal broad and strongly chirped as a consequence of GVD, as depicted in Figure 3.11. For instance, if the white light is generated from 800 nm passing through a 2 mm cuvette of D_2O, the pulse covers a very broad range which is symmetric respect to 800 nm. In this thesis, the experiments are focused on the investigation of the visible and UV range, thus, with the use of suitable filters the white light pulse covers from 400 nm to 700 nm and its duration is about 800 fs.

Time resolution of TA experiments A transient absorption experiment consists in a temporal scan in which the delay between the two pulses is changed. The pump and probe pulses spatially overlap within the sample volume for the entire duration of the scan; in the time domain, the time zero of the experiment is identified when the overlap between the pulses is also temporal. If the pulses are transform-limited ($\Delta\omega\Delta t = 0.5$), the time resolution is given by the cross-correlation between the two pulses intensity profiles. In practice, this conclusion is still valid even if the probe pulse is chirped because of the effects of GVD. In fact, the effect of the GVD is to temporally

broaden the probe pulse and this implies a different temporal overlap between the pump and every wavelength of the probe. Inserting a spectral filter, as a grating, on the probe path after the sample allows to disperse spatially the probe beam and simultaneously to disperse it *temporally* on the detector guaranteeing the selection of a brief temporal slice for each spectral resolved range as shown in Figure 3.12. In this way the time resolution can be similar to the one of transform-limited pulses of the same spectral width of the unfiltered probe pulse [193]. Graphically, it is common to use the cross phase modulation to visualize the time resolution. The cross phase modulation (CPM) is an artifact related to the interaction of the probe with the variation of the refractive index induced by the pump inside the medium. It defines the time zero and helps to visualize the time resolution of the experiment Figure 3.12 .

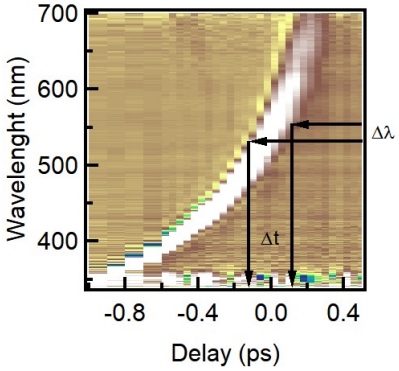

Figure 3.12: Example of cross phase modulation between pump and probe: the probe is temporally dispersed on the detector where a spectral slice ($\Delta\lambda$) is selected with the consequently temporal resolution (Δt).

Polarization-resolved transient absorption measurements

Anisotropy measurements are based on the principle of photoexcitation by polarized light. The excitation will be generated preferentially with transition dipole moment aligned parallel to the linearly polarized light.This selective excitation results in an oriented population of the system, and in a polarized fluorescence emission. With the flow of time, the random rotation of the system or the excitation migration on the surface would tend to randomize the electric dipole, randomizing also the signal polarization. Taking into account that also the probe beam is a linearly polarized pulse, as time proceeds, it is possible to follow the variation of the polarization of the signal. Performing experiments in two complementary relative polarizations of pump and probe pulses (parallel and perpendicular, respectively) allows to extract anisotropy defined in Equation 3.20 and its temporal dynamics:

$$r(t) = \frac{I_{para}(t) - I_{ortho}(t)}{I_{para}(t) + 2 \cdot I_{ortho}(t)} \tag{3.20}$$

where I is the signal intensity in the two different respective pump and probe polarizations (para = parallel and ortho = orthogonal). If before the photoexcitation the system is randomly oriented, anisotropy value can span from 0.4, when the dipoles are parallel, to -0.2, when the dipoles are perpendicular. This simple rule is not valid for pre-oriented system or if the photoexcitation involves more than one photon. It is possible to demonstrate that anisotropy is 0 at the so-called magic angle condition (54.7° between the pump and probe polarization) [178].

Transient absorption setup pumped at 400 nm

Part of this Ph.D. was devoted to built a transient absorption setup which is located in the laboratories of ATeN Center (Advanced Technologies Network Center) at University of Palermo.

The laser is a 5 kHz Ti:sapphire femtosecond amplifier (Spectra Physics Solstice-Ace). The system is composed by a *Mai Tai* seed laser, a pulse stretcher, a regenerative amplifier and pulse compressor, and a *Empower* pump laser (15 W) which pumps the amplifier.

The Mai Tai laser produces 35 fs pulses at 80 MHz.This pulse is used as the seed of the Ti:sapphire rod of the amplifier, although it is first broadened in time (through the use of a *stretcher*) from 35 fs to 500 ps, in order to avoid damage of the amplifier rod due to the excessive peak intensities that would be reached with a very short pulse. After stretching, the amplification occurs through multiple passages of the seed pulse through a Ti:Sapphire rod where a population inversion is achieved, just before amplification begins, by pumping a Ti:sapphire rod which is pumped at 5 kHz right before the passage of the seed. After its amplification, the pulse is recompressed in order to have again an ultrafast pulse with short duration and high peak intensity. This technique is called *Chirped pulse amplification* and produces a train of amplified pulses at the expense of the repetition rate, that decreases down from 80 MHz to 5 kHz.

The output after the compressor is nominally a 50 fs pulse peaking at 800 nm (FWHM=30 nm). The power of the beam is 3.5 W, therefore the energy per pulse is 700 μJ/pulse. From an SHG autocorrelation measurement, in the position where the sample will be for the measurement, the pulse duration was measured finding it lasts 75 fs. An autocorrelation measurement consists in measuring the interaction of two beams in a $\beta-$BBO in non-collinear geometry (Figure 3.13a). In

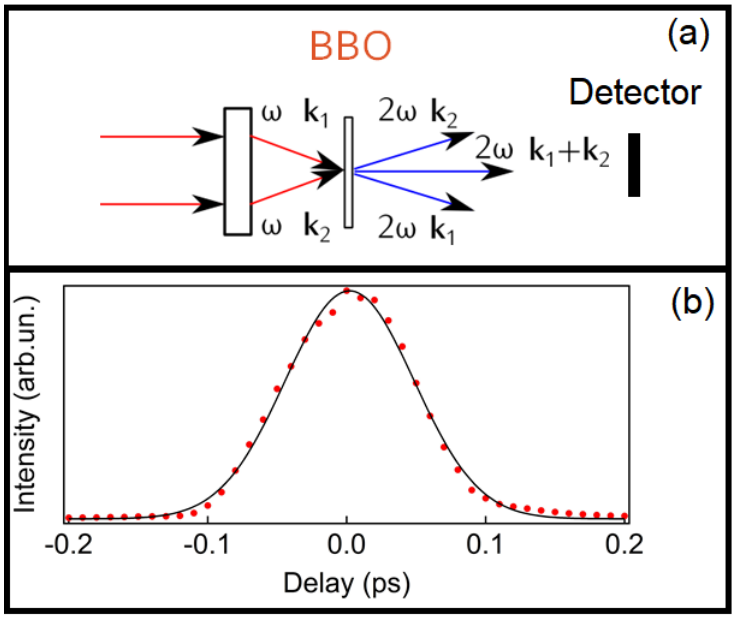

Figure 3.13: (a) Scheme of an autocorrelation experiment. (b) Temporal profile of the pulse measured by an autocorrelation measurement.

fact, when two 800 nm beams pass through a $\beta-$BBO, the results are two 400 nm beams with doubled wave-vectors respect to the original beam propagating in the same directions and, when the beams overlap temporally and spatially, a third 400 nm beam with a wave-vector which is the sum of the originals. The pulse duration is estimated from the measurement of the intensity of this third beam (Figure 3.13b) as a function of the relative delay, and estimated as the full width half maximum (FWHM) of the gaussian profile.

Only half power of this pulse is used to pump the transient absorption setup. This beam is split in two parts by a beam splitter (80%/20%) to generate the pump and the probe, respectively. The scheme of the setup is reported in Figure 3.14.

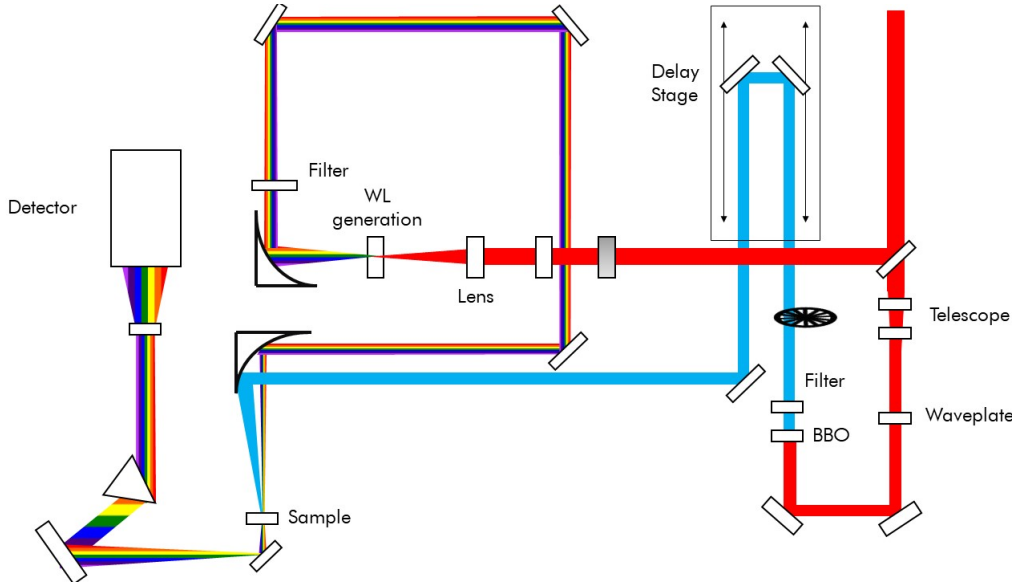

Figure 3.14: Scheme of the pump probe setup.

On the pump arm, the 800 nm beam passes through a telescope to decrease the size from 7 mm to 5 mm and to increase the power density from 10 GW$\cdot cm^{-2}$ to 17 GW$\cdot cm^{-2}$, in order to maximize the SHG generation efficiency while keeping the intensity below the $\beta-$BBO damage threshold. Because of the GVD introduced by the telescope (composed by a positive and a negative lens), the duration of the pulse increases from 50 fs to 75 fs. The central part of the spot is selected by an iris of 1 mm of diameter (this size reduction ultimately serves to increase the pump spot size on the sample) and then the 800 nm beam is frequency-doubled (type I phase-matching) by an ultrathin $\beta-$BBO crystal (250 μm) in order to create a 400 nm beam (20% efficiency) which is isolated from the fundamental by a Schott BG40 filter, the beam is chopped at 500 Hz and focused on the sample by a parabolic beam with f=150 mm. Pump spot on the sample has a gaussian spatial profile and $\approx 80\mu m$ diameter at $\frac{1}{e^2}$ level very close to the diffraction limit. The maximum energy per pulse of the pump at the sample position can reach 500 nJ/pulse. The polarization of the pump is controlled by a waveplate which changes the polarization of the fundamental 800 nm before the generation of the 400 nm beam.

On the second arm, the white light is generated focusing $\sim 300nJ/pulse$ of the 800 nm beam in a 2 mm quartz cuvette containing D_2O, generating $\sim 5nJ/pulse$ of a broadband pulse extending from 400 to 700 nm (Figure 3.15). The power of the 800 nm can be controlled by the use of two graduated filters and it is usually fixed at the value which creates a single stable filament in the cuvette when focused by a 150 mm lens.The spectral profile of the white light can be controlled by various filters as BG40 or BG28. After its generation, the white light beam is collimated by a 50 mm parabolic mirror to form a 4 mm diameter circular spot. The probe is focused on the sample by the same parabolic mirror used to focus the pump. Probe spot on the sample is gaussian and $\approx 45\ \mu m$ at $\frac{1}{e^2}$, and also in this case it is very close to the diffraction limit. Using a probe size which is about half in size than the pump size makes the system less sensitive to possible misalignments in the pump/probe overlap. It is possible to double the 800 nm before generating the white light, in this way the 400 nm is focused on the cuvette and the probe is extended to the UV, ranging in this case from 310 nm to 600 nm.

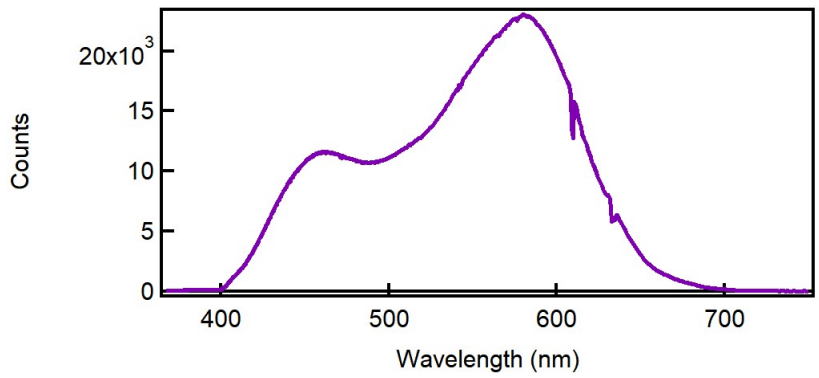

Figure 3.15: White light spectrum generated by 800 nm in a 2 mm cuvette of D_2O. Fundamental beam is cut by a BG40 filter.

Moreover, we implemented the possibility of performing pump probe measurements exciting at 266 nm generated by the third harmonic generation (THG) of 800 nm. To do this, after the generation of the 400 nm beam, both pulses (800 nm and 400 nm) are directed into a Calcite plate, and, then into a half-wave plate. The former allows to compensate the different group velocity of the two beams in order to temporally overlap them in the THG crystal. The latter rotates the polarization of the 800 nm in order to succeed in having a phase matching of type I. After these two components, the beams pass through a nonlinear crystal for the generation of the 266 nm. The efficiency of the process is about few percent. Therefore, it is possible to excite the sample with UV pulses at 150 nJ/pulse with a time resolution of 50-60 fs.

The pump-probe delay is controlled by a motorized delay stage. The probe and the pump overlap within the sample which continuously flows in a 200 μm thick flow cell upon the action of a peristaltic pump. The flow is regulated in order that every pump pulse hit a fresh portion of the sample (considering the repetition rate of the amplifier). The minimum amount of solution needed is about 2 mL.

After the sample, the probe beam is dispersed through a Brewster-angle silica prism and focused on the detector by a lens. The spectral resolution of this configuration is 3 nm. The temporal resolution is about 70 fs. Pump and probe are synchronously collected with a camera detector system with 1024 pixels (Glaz Linescan-I) with single-shot capability. To discriminate pumped from unpumped spectra a photodiode is positioned after the chopper and a portion of the 400 nm beam is sent on it. A typical signal is obtained by averaging 5000 pumped and 5000 unpumped spectra for each delay, and scanning over the pump–probe delay 10-20 times. In this conditions a single scan usually takes 4 minutes, and the entire measurement is about 40-80 minutes.

Changing the detector and using a photomultiplier allows to perform TA measurements in a single-wavelength detection. This configuration includes the use of a lock-in amplifier which allows to increase the signal-to-noise ratio despite of the spectral limitation.

Transient absorption setup pumped by a NOPA

This Ph.D. was a joint-Ph.D with the University of Bern where several transient absorption experiments were carried out. This setup is better explained somewhere else [194] and, here, just a general description is given. The scheme is in Figure 3.16. This TA setup is based on a 5 kHz Ti:sapphire regenerative amplifier system which generates 100 fs pulses at 800 nm with 0.5 mJ pulse energy. The seed of the amplifier is generated by the oscillator which is Ti: Sapphire oscillator by Kapteyn-Murnane laboratories, pumped by a CW 5 W pump at 532 nm (Finess by Laser

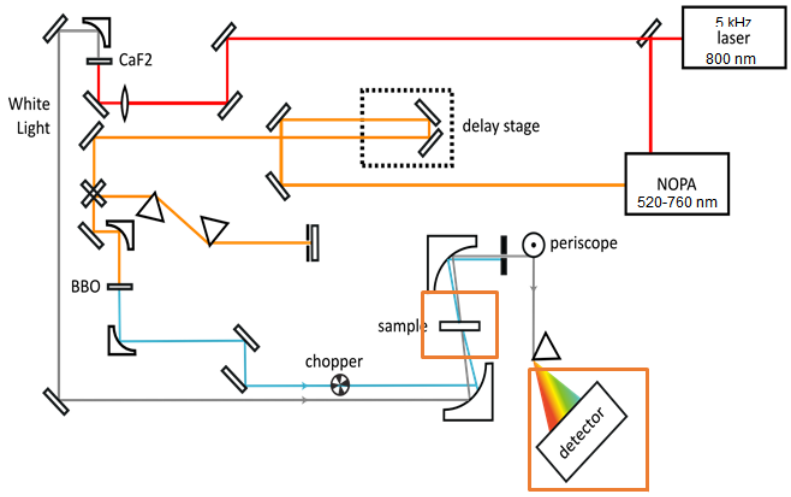

Figure 3.16: Scheme of the pump/probe setup.

Quantum). The output of the amplifier is sent to a commercial two stage NOPA (Topas white by Light conversion), tunable between 520nm and 750nm, a bandwidth variable from 10 nm to 200 nm, and an energy per pulse variable from 10 to 30 $\mu J/pulse$. Inside the NOPA, the residual of 800 nm is collected to generate also the probe pulse. The pump pulse can be visible (the output of the NOPA) or in the UV range (doubling with a $\beta-$BBO the output of the NOPA). The polarization of the pump is controlled by an achromatic waveplate.

The probe is generated by focusing $< 1\mu J$ of the 800 nm on a moving CaF_2 crystal, and the white light spectrum covers the spectral interval 320-750 nm.After the white light generation, the probe is split in two by a beamsplitter in order to have a reference beam of the probe which does not pass through the excited part of the sample and can be used to correct any artifacts coming from the probe distortions on a single shot basis. The pump and the probe are focused on the sample (which continuously circulates through a 200 μm flow cell) and the spot sizes are 50 μm and 40 μm, respectively. Their delay is controlled by a motorized delay stage. After the sample, the probe and the reference are spectrally dispersed by a prism and are focused on two Hamamatsu CMOS sensors with 512 pixels each. The spectral resolution is $\approx 1-2$ nm. The spectrum of probe and reference pulses is measured on a single-shot basis, and successive pumped and unpumped probe shots (due to the chopper) are compared to correct for the drift of transmission baseline over time. A typical signal is obtained by averaging 1000 pumped and 1000 unpumped spectra for each delay, and scanning over the pump–probe delay 20 times.

A third TA setup (details in [195]) was used to perform a portion of the experiments reported in this Thesis. It is similar to the one described now with the following differences: the system is based on a 1 kHz Ti:sapphire regenerative amplifier system which generates 90 fs pulses at 800 nm with 0.8 mJ pulse energy, the pump pulse is generated by a home-made two stage NOPA and it can be tuned from 480 nm to 750 nm, and the detectors are multi-camera detectors (Glaz Linescan-I) also in this case with singleshot capability.

Data Analysis

In this section, analysis of TA data is explained. In particular, preliminary data treatment (GVD and CPM correction) is shown, then, an example of analysis procedure on a set of data is illustrated.

A typical set of raw TA data is shown in Figure 3.17a where the consequences of GVD in the

probe pulse can be clearly seen. As mentioned before, the probe pulse is $\approx$ 1 ps long and the

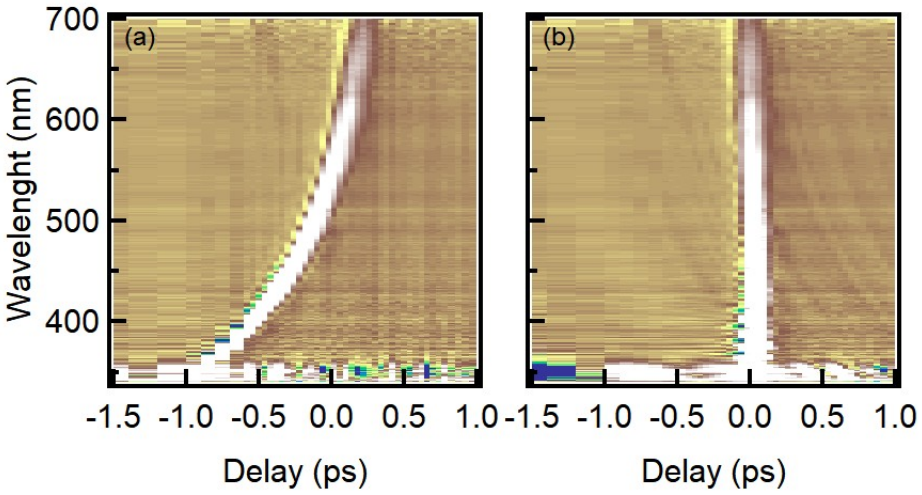

Figure 3.17: (a) Pump/probe measurement on pure solvent (ethanol) of the GVD effect on the temporal profile of the whitelight. (b) Effect of the GVD correction on the data. This procedure is applied to each recorded data.

time of the interaction with the pump depends on the wavelength. This causes an uncertainty on the definition of *zero-time* which is a crucial point in time resolved measurements. To solve this problem, one point at fixed wavelength is chosen as a pivoting point and all kinetic traces collected at other wavelengths are temporally shifted as in Figure 3.17b [188], in such a way to eliminate the wavelength-dependence of the zero-time. This procedure is helped by the presence of the CPM which is, as mentioned, an artifact related to the interaction of the probe with the variation of the refractive index induced by the pump inside every medium (also pure solvent). In Figure 3.17, the time interval in which the CPM occurs, due to the temporal overlap of the two pulses, is clearly visible as a coloured area. Since the measurement in Figure 3.17 was carried out on a pure solvent, this is the only signal observed in this case. Beside helping to locate the zero-time, the CPM is used to measure the instrumental response function (IRF) which is usually assumed gaussian and, therefore, the time resolution of the experiment (standard deviation of the IRF). The temporal span of the CPM in the presented example goes from -140 to 140 fs. Assuming a Gaussian pulse shape, and a temporal extension of the CPM equal to 6· standard deviation, this corresponds to a FWHM (K_B) of approximately 110 fs and a standard deviation of 45 fs. In practice, the spectra collected in the temporal window where CPM is observed are simply removed from the data.

After GVD correction, the following step is the extraction of the dynamics and the definition of the characteristic times. There are several different approaches to do this. Looking at spectra at various time delays and at the kinetic traces at different wavelengths can give an idea on the processes involved during the dynamics and on their timescales. Another approach used to perform the data analysis is is singular value decomposition (SVD) followed by a global analysis (GA). This is explained in the next paragraph.

Singular value decomposition

The SVD is a mathematical method by which data are decomposed to a minimum number of relevant kinetics and spectra, and at the same time, white noise is removed from the data. GA is combined with the SVD in order to find time constants which can describe the entire data providing a global model simultaneously fitting the kinetics at all wavelengths. From the SVD and the

global analysis, decay associated spectra (DAS) are extracted, which describe relevant changes of TA signal for each time constants found during GA. The last step consists of the check of critical differences between the real data and those reconstructed from the SVD and from GA.

Here, the theory of SVD and GA is explained step by step, and an example of the every step of the analysis is reported in order to clarify the practical use of the procedure.

The data, which will be considered for the example, concerns a TA experiment on an ethanol solution of 4-(Dicyanomethylene)-2-methyl-6-(4-dimethylaminostyryl)-4H-pyran (DCM), a dye used as a standard to check the proper operation of the setup.

The signal after GVD correction and the cut of CPM is shown in Figure 3.18.

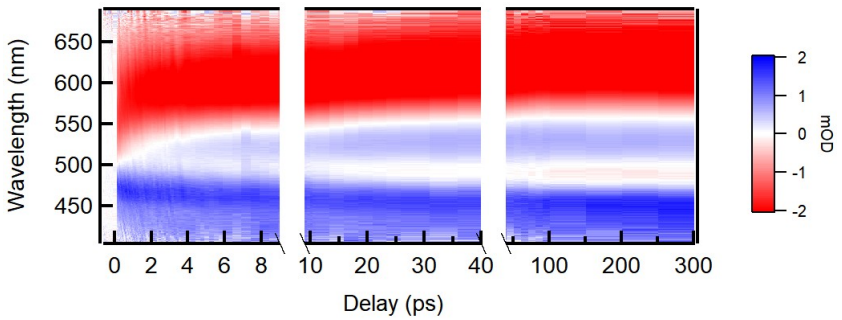

Figure 3.18: TA data of an ethanol solution of DCM pumped at 400 nm, after GVD correction and the removal of CPM.

Mathematically, an SVD analysis of TA data proceeds as described hereafter. The original matrix of the raw data, TA(λ, t), can be decomposed, as followed:

$$TA(\lambda,t)_{mxn} = U(\lambda)_{mxm} \times S_{mxn} \times V(t)^{T}_{nxn} \tag{3.21}$$

where S_{mxn} is a matrix with mxn elements (m=number of wavelength, and n= number of delays) where the diagonal elements are called eigenvalues or *singular values* and the other elements are zero. The other two matrices are composed by *eigenspectra* (U) and *eigentraces* (V). SVD procedure assumes the TA signal a linear combination of individual components with independent spectral and temporal functions. The single eigenspectrum or eigentrace has not a physical meaning if taken alone but, despite this, they help to describe the dynamics of the signal. To do this, the eigenvalues of S are initially used to discriminate between the components: if they describe a significant contribution to the dynamics of the signal, the eigenvalue is large, on the contrary, if the eigenvalue is small enough, one can assume that the related component is just associated to noise. Only the former components will be taken into account for further analysis and in this way, the number of spectra and kinetics vectors to describe TA data are reduced. Unfortunately, it can occur that some eigenvalues describe a mix between signal and noise where the ratio S/N is very low thus, the choice of the representative eigenvalues is very important to not lose part of the signal.

An SVD decomposition was performed on the data in Figure 3.18. The procedure returns the eigenvalues shown in Figure 3.19, where only three singular values (indicated by circles) contribute to the signal. Therefore, discarding all the others allows to substantially reduce the noise.

Then, the eigentraces associated to the selected (largest) eigenvalues are fitted with suitable functions describing the physical dynamics of the system, in order to extract the characteristic decay times (τ_i) with the related amplitudes (A_{il}). Equation 3.22 describes the convolution of multi-exponential decay function with the IRF. A multi-exponential decay is used to fit the data and to

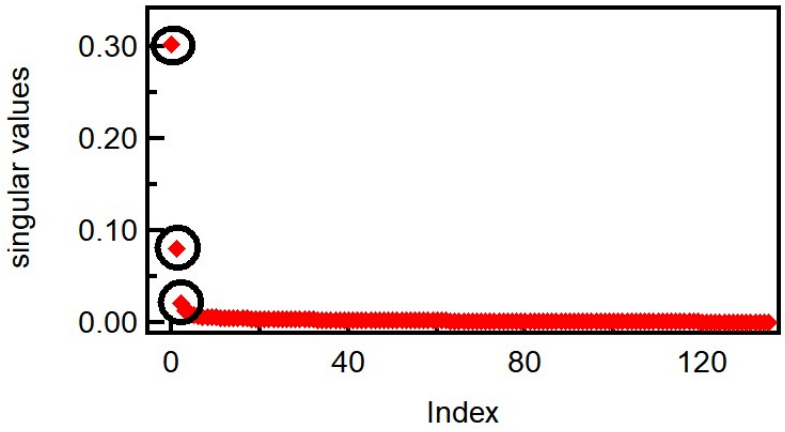

Figure 3.19: Singular values resulted from SVD decomposition.

describe the expected physical model which includes only incoherent relaxations (not oscillations or phase variations):

$$F_l(t) = \sum_i A_{il} e^{-\frac{t}{\tau_i}} u_0(t) \otimes IRF(K_b, t_0 = 0, t) = \sum_i A_{il} (e^{-\frac{t}{\tau_i}}_{t>0}|_{IRF}) \tag{3.22}$$

where i runs on the kinetic traces, τ_i and A_{il} are the characteristic times and the relative amplitudes, $u_0(t)$ is a Heaviside step function and IRF is the instrumental response function which is supposed to be a Gaussian function with a width ($\approx FWHM/2.35$) K_b and peaking $t_0 = 0$. The function in Equation 3.22 is used to perform the global analysis (GA), therefore, to fit the kinetic traces (the eigentraces) obtained by the SVD.

The IRF depends on the experimental setup, thus, it does not change during the single experiment. For this reason, during the GA, K_b and t_0 are fixed to be the same for all the kinetics traces. During the global fitting procedure also the time scales are fixed to be global variables, whereas the amplitudes are not the same for all the eigentraces.

In the analysis of the data for DCM shown in Figure 3.18, the eigentraces were fit by a four-exponential decay function (Figure 3.20) convoluted by a gaussian (IRF). The lifetimes were considered as global variables, while the amplitudes were considered as local variables.

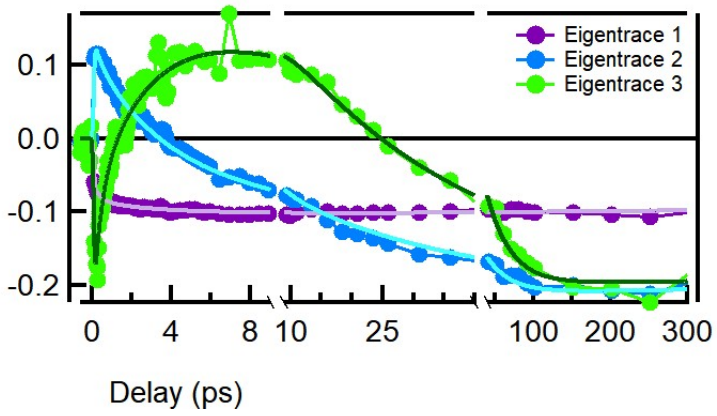

Figure 3.20: First three eigentraces from the SVD decomposition with the best-fit curves resulted from GA.

The resulting amplitudes are then used to calculate the DAS for every time constants [163]:

$$DAS_i(\lambda) = \sum_l A_{il} s_{ll} U_i(\lambda) \tag{3.23}$$

Taking the amplitudes obtained from the fit in Figure 3.20 and the associated singular values, it was possible to calculate the DASs applying Equation 3.23. The DAS are shown in Figure 3.21.

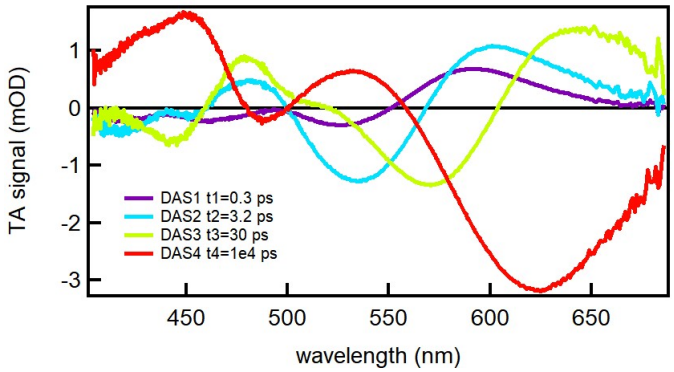

Figure 3.21: Calculated DASs with the respective time constants.

The DAS is as a function of wavelength and does not show any spectral evolution. Now, the data can be reconstructed by the following equation:

$$\Delta A(\lambda, t) = \sum_i DAS_i(\lambda)(e^{-\frac{t}{\tau_i}}_{t>0}|_{IRF}) \tag{3.24}$$

As last step, representative spectra of raw TA data were compared with the reconstructed data from Equation 3.24 (Figure 3.22). The very good match between the raw data and the reconstructed data guarantees the proper precision of the analysis.

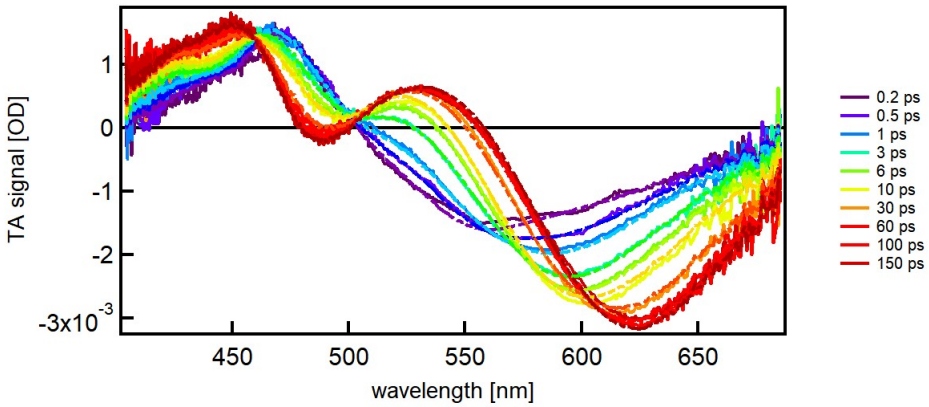

Figure 3.22: Comparison of selected spectra of raw data (continuous lines) with reconstructed data (dashed lines) after DAS calculation.

Comparing raw spectra and DASs gives the start for the interpretation of the data and helps to model the photo-physics of the system. If the intensity of the DAS is zero in a portion of the spectral range, this indicates that during its associated lifetimes there are no spectral evolution in that specific spectral region. If the sign of the DAS is negative (positive) and the sign of the raw TA

signal is negative (positive), this indicates a decay of a negative (positive) signal. On the contrary, if the sign of the DAS is opposite with respect to the sign of the signal, the latter is rising in those time scales.

In this experiment, in particular, the first two DAS (0.3 ps and 3.2 ps) describe a solvatochromic shift of the signal around 500-650 nm (negative sign of the DAS around 550 nm and positive sign of the DAS at 600 nm) which is evident also looking at the spectra from 0.2 ps to 6 ps. The identified time constants are typical of the solvation of a molecule in ethanol. The third DAS is associated to the formation of a new emissive state [196] which grows from the first one and emits with a time scale of nanosecond (forth DAS).

Fluorescence Upconversion

Another powerful ultrafast spectroscopic technique used in some of the experiments reported in this work is Fluorescence Upconversion (FlUC). It is a time-resolved spectroscopic technique capable of selectively detecting the (spontaneous) emission, with femtosecond time resolution, without any GSB or ESA. This provides a signal which is easier to interpret than that obtained by a TA experiment, although, at the same time, some information is hidden as the broadening of the ground state or the population of non-emissive states. The scheme of the setup is reported in Figure 3.23.

A FLUC experiment, as a TA experiment, requires the use of two pulses (here called *excitation* and *gate*) and the possibility of changing the time delay between them. The former excites the sample, and the fluorescence of which is captured by a parabolic mirror, and then is focused on a $\beta-$BBO crystal. The gate is focused on the same crystal and it is overlapped with the fluorescence spot. In this way, at a certain angle of the $\beta-$BBO, a third pulse (*upconverted* pulse) is generated by the nonlinear mixing of a spectral portion of the emission (the one that satisfies the specific phase-matching condition) and the gate. The non-linear process here involved is similar to the SHG, but with two generic frequencies and it is called sum frequency generation. It is described by the following equation: $\omega_{PL} + \omega_{gate} = \omega_{up}$, where the addends are the frequencies of the fluorescence of the sample (PL), of the gate and the frequency of the *upconverted* beam which usually is in the UV range. Because SFG occurs only within the temporal duration of the gate, SFG actually samples only a temporal "slice" of the emission, with duration of <100 fs, and the entire emission kinetics is then reconstructed by scanning the delay between the two pulses. The intensity of the generated pulse depends on the intensity of the emission and the intensity of the gate. Under certain approximations [190], the efficiency of the process, and in particular the intensity of the upconverted pulse is described by the following equation:

$$I(\omega_u) \propto \frac{\omega_{PL}\omega_g\chi^2_{eff}l^2}{n_0(\omega_e)n_{eff}(\theta,\omega_u)} I(\omega_{PL})I(\omega_g)\left(\frac{sin(\Delta kl/2)}{\Delta kl/2}\right)^2 \tag{3.25}$$

where the subscripts u, PL and g indicate the upconverted, the fluorescence and the gate beam, respectively.

Recording the upconverted pulse as a function of the gate delay allows to reconstruct the kinetics of the emission at a given wavelength, at variable delays from photo-excitation, with femtosecond time resolution. Rotating the $\beta-$BBO changes the phase-matching condition and allows to upconvert different spectral portions of the emission band in order to reconstruct the dynamics of the entire fluorescence as function of wavelengths.

The setup used in this Thesis has been built, as a part of this Ph.D., in the laboratories of ATeN Center (Advanced Technologies Network Center) at University of Palermo. The laser source is the same used in the TA setup used to perform experiments pumping at 400 nm.

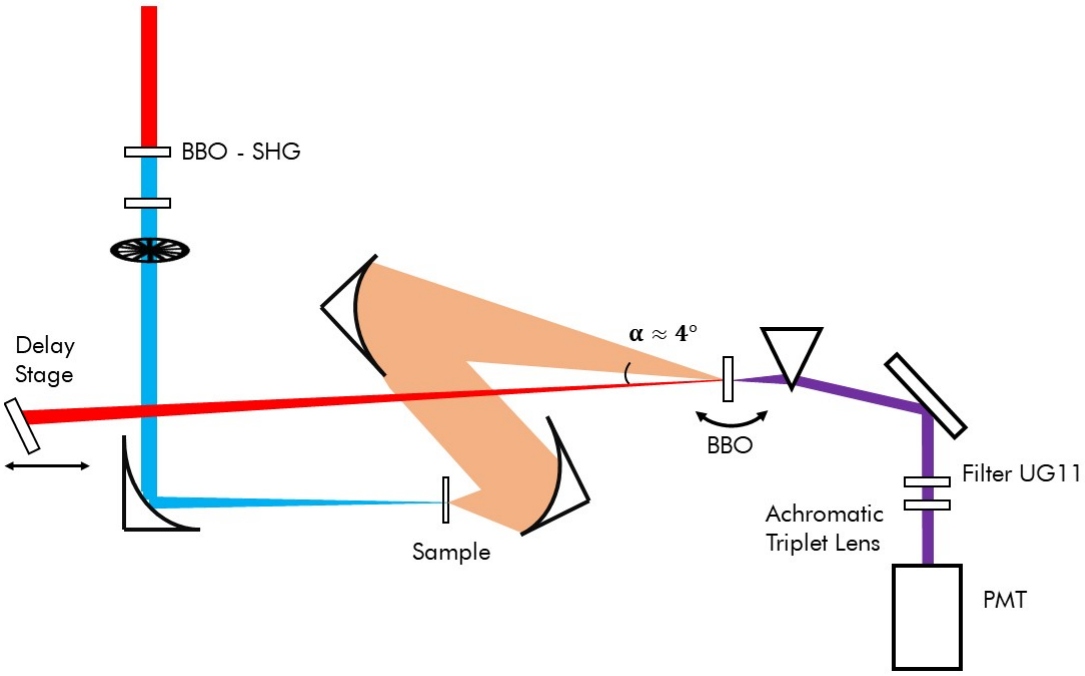

Figure 3.23: Scheme of the fluorescence upconversion setup .

Therefore, the laser is a 5 kHz Ti:sapphire femtosecond amplifier with an output beam at 3.5 W (50 fs pulse with 700 μJ/pulse) at 800 nm. Half of this beam is used to generate the excitation beam at 400 nm by passing through a $\beta-$BBO crystal. After removing the 800 nm with a BG40 filter, the 400 nm is chopped (500 Hz) and, then, it is focused on the sample (flow cell 200 μm thickness) by a parabolic mirror with a focal length of 200 mm. The spot on the sample has a diameter ($\frac{1}{e^2}$) of 50 μm. After excitation of the sample, the spontaneous emission is collected and collimated by second parabolic mirror with focal length of 50 mm and a diameter of two inches and, then, focused by a third parabolic mirror with the same diameter and a focal length of 250 mm into a 250 μm thick sum-frequency crystal where the gate finally overlaps to the fluorescence spot. The gate (800 nm) is focused on the same crystal with a lens having a focal length of 1 m. In these conditions, the sizes of the two spots are about 250 and 350 μm, respectively.The angle between the gate and the fluorescence is usually 4°.

The time delay is scanned in order to measure the fluorescence spectrum as a function of excitation-gate delay. On gate path there is a waveplate which allows to change the polarization of the beam in order to perform measurements in parallel, perpendicular or magic angle configuration. The upconverted emission after the non-linear crystal passes through a dispersive prism, and through a triplet achromatic lens. Then, it is detected by a photomultiplier (PMT) connected to a lock-in amplifier triggered by the chopper. In order to reduce the background during the measurement, there is an iris after the non linear crystal which helps to physically stop the visible beams. Besides, the upconverted beam, before reaching the PMT, passes through two UV band-pass filters (Schott UG11) in order to reduce the contribution of the excitation and of the gate to the measurements.

Data are collected as single-wavelength traces. The detected wavelength is determined by rotating the non-linear crystal, thus, determining a certain phase matching angle. The calibration of the setup is performed by a simulation which estimates the upconverted wavelength considering the ordinary and extraordinary refractive index of the crystal, therefore, the phase matching con-

ditions varying the angle between the emission and the gate as shown in Figure 3.24. After the

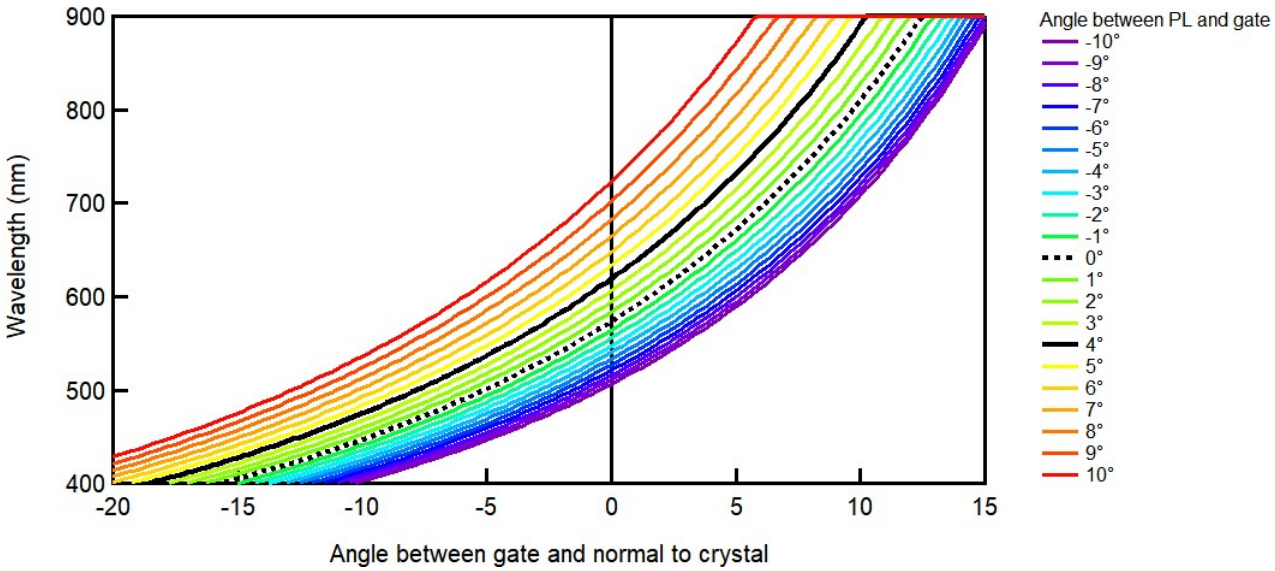

Figure 3.24: Simulated curves used to calibrate FLUC setup. The typical calibration curve is the black continuous curve (4° between the PL and the gate).

simulation, to calibrate every experiment, it is necessary to consider the zero angle (the gate beam is perpendicular to the crystal), and the angular position of the crystal with respect to the phase matching angle useful to generate 400 nm as SHG of the gate and with respect to the generation of 266 nm as SFG between 800 nm + 400 nm. Typical kinetic traces obtained in a FLUC experiment exciting at 400 nm are reported in Figure 3.25. The trace at 410 nm has been used to estimate the IRF of the experiment. The fitting procedure gives back an IRF $\approx$ 180 fs which corresponds to a time resolution of $\approx$ 70 fs which is limited by the non-collinear geometry and by GVM between the gate and the fluorescence occurring in the non linear crystal. The spectral resolution depends on the acceptance bandwidth of the crystal. We estimated it by Equation 3.13 and found that the acceptance bandwidth is about 13 nm at 550 nm and 26 nm at 700 nm.

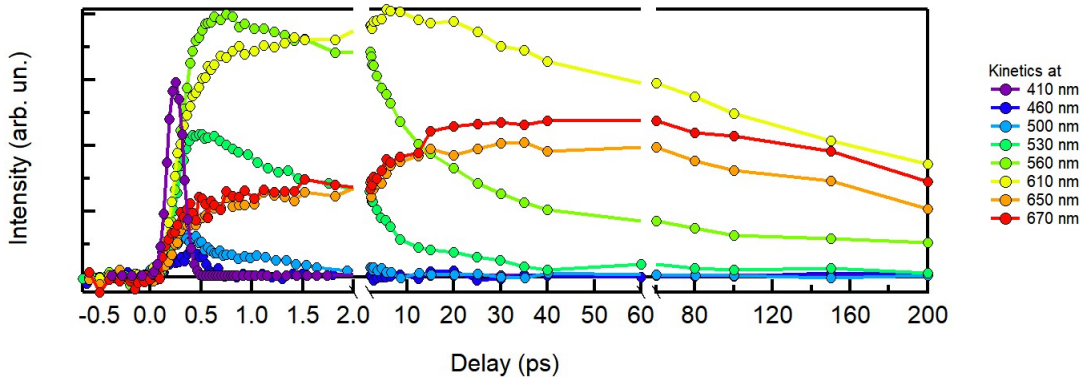

Figure 3.25: Kinetic traces obtained in a FLUC experiment exciting at 400 nm a solution of DCM in ethanol. The trace at 410 nm shows the IRF of the experiment.

3.3 Structural and Morphological Characterization

The CDs studied in this Thesis have been characterized by several morphological and structural techniques, whenever necessary. In particular, Atomic Force Microscopy has been used to study the morphology of the sample, Infrared Absorption has been used to investigate the surface of the CDs and Transmission Electron Microscopy has been used to investigate the core structure of the nanoparticles.

Atomic Force Microscopy

Atomic force microscopy (AFM) allows to study the surface morphology of a sample with nanometric resolution. The technique is based on the study of the interactions between the probe (tip) and the surface of the sample. These interactions depend on the distance between sample and tip and they can be attractive or repulsive. A morphologic study is perfomed by the use of a probe which starts to flex interacting with the surface. When scanning different points on the surface, the tip can feel the effects of a different interaction (if there is one) and will change its deflection. Scanning the surface and recording these changes, it is possible to obtain the morphology of the sample.

In general, the common operating modes of AFM are the contact mode and the tapping mode. In the former, the probe is in contact with the surface and the deflection of the probe is kept constant. The resolution is usually high but this mode is affected by some problems as the high friction and the possible damages on the surface of the sample. In the latter mode, the probe is forced to oscillate up and down with an amplitude fixed by the operator. If the tip feels deflection changes, it will change its distance from sample surface, in order to restore the pre-determined oscillation amplitude, and record the changes. This mode decreases the damage on sample surface [197].

During this thesis, to perform AFM measurements, a drop of solution conveniently diluted (about 1 mg/L) was deposited on a mica substrate and then dried in vacuum. AFM measurements were acquired in air by using a Bruker FAST-SCAN microscope. The scans were collected in soft tapping mode by using FAST-SCAN-A probes with apical radius of about 5 nm. The pixel resolution is comparable to the tip size. Each size distribution reported in the next chapters was estimated by evaluating the height of thousands of nanoparticles.

Infrared Absorption

As said in Chapter 1, the surface of CDs is dependent on the synthesis and passivation procedure. To get information on the chemical structure of CD surfaces, infrared absorption measurements were carried out on a N_2-purged, Bruker VERTEX-70 spectrophotometer, in transmission geometry.

The measurements were collected at room temperature under Nitrogen flux to avoid artifacts due to the residual water in the air. Samples were prepared by depositing drops of a concentrated CDs solution ($1\ g \cdot L^{-1}$) on a sapphire window and drying in vacuum.

Transmission Electron Microscopy

As said in Chapter 1, the core structure of CDs is synthesis dependent. In order to deeply characterize it, high resolution transmission electron microscopy (HRTEM) was used in collaboration with the Karlsruhe Institute of Technology using an aberration-corrected FEI Titan^3 80-300 microscope at 300 kV acceleration tension.

Transmission electron microscopy (TEM) is a technique in which a beam of electrons penetrates through an ultra-thin specimen and the electrons are then imaged by appropriate lenses. In this way, TEM is capable of recording magnified images of a sample with a magnification of $10^3 - 10^6$. In addition, the instrument can be used to produce electron-diffraction patterns, useful for analyzing the properties of a crystalline specimen. An imaging system is necessary to produce a magnified image (or a diffraction pattern) of the specimen on a fluorescent screen or on the monitor screen of an electronic camera system. It establishes the magnification of the image and the spatial resolution that can be obtained from the microscope. [198]

For each acquisition, the sample were prepared at room temperature in air by the deposition of a drop of aqueous solution of CDs on a commercial 400 μm mesh Cu-grid (Plano 01824) covered by a holey amorphous carbon film, with a nominal thickness of 3 nm.

HRTEM images were evaluated by calculating their two-dimensional Fourier transform, denoted as diffractogram, which yields information on the crystal structure (lattice parameters and crystal symmetry) of single nanoparticles. The analysis was performed by comparing the experimental diffractograms to calculated diffraction patterns with Miller indices.

Part II

Experimental Results

Chapter 4

Carbon Nanodots: Basic Characterization

In this chapter, the structural and optical characterization of home-synthesized CDs is presented. The synthesis is a widespread bottom up procedure described in section 3.1 which allows to dope the products in a controllable and easy way. The sample on which the great part of our studies have been conducted is presented as first. The study (section 4.1) was performed by the combination of various techniques which allow to carry out a complete structural and optical characterization of this sample. One of the main results of the study is the discovery of a new structure of CDs which had not been reported in the literature before. In the second part of the chapter some synthesis parameters are changed (section 4.2), and the investigation on the structure and on the optical properties of CDs varying the content of nitrogen during the synthesis is reported. The results demonstrate that N doping allows to tailor the emission colour and the structure of CDs in a controlled way.

4.1 Carbon Nanodots with Carbon Nitride Structure

Introduction

As already mentioned in chapter 1, many works report that the emission properties of nitrogen-containing CDs are rather peculiar with respect to undoped dots [20, 41–43, 49, 74]. Nitrogen-containing CDs (N-CDs) are particularly interesting because of their large fluorescence quantum yields [41, 74], the origin of which, however, is hardly understood. Rationalizing the structural variability of CDs and understanding the relationship between structure and optical properties are important and largely debated problems.

When CDs are doped with nitrogen, their surfaces usually host abundant amide and amine moieties [12,41,42,49]. Besides this, in some cases, nitrogen is also found in the core as a structural dopant (formation of defects in the core [43]) or as a key component of core structure as in g$-C_3N_4$ carbon dots [7, 59]. In all these cases, nitrogen is expected to have an influence on the electronic properties of the dots, although the mechanism is expected to be different depending on how nitrogen enters the structure of the dot.

In the course of our studies, a new variety of CDs with a $\beta - C_3N_4$ core structure has been found, which had not been reported before. A perfect $\beta - C_3N_4$ crystal consists of a hexagonal network of tetrahedral bonded (sp^3) carbon atoms connected to trigonal (sp^2) nitrogen atoms (Figure 4.1). These CDs, beyond the atypical core structure, display very unique optical characteristics as the intense tunable luminescence. We deeply investigated their characteristics with many different techniques as it is shown hereafter.

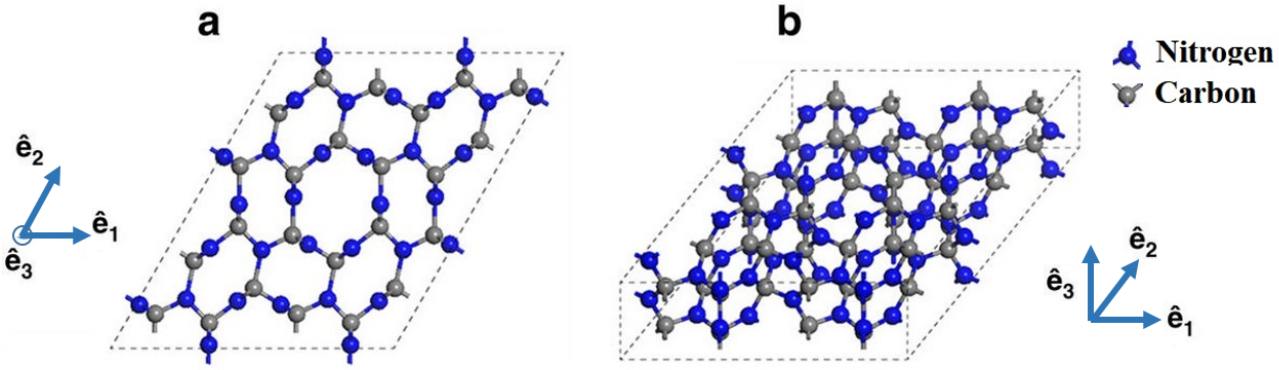

Figure 4.1: $\beta - C_3N4$ structure shown from two perspectives to illustrate the three-dimensional arrangement of the structure. [Adapted from [199]]

Structural Properties

$\beta - C_3N_4$ dots have been synthesized as explained in section 3.1. An aqueous solution of citric acid and urea (w/w=1/1) was exposed to microwave irradiation until the complete evaporation of the water. The black powder (CDs) collected after the drying of the sample has been characterized by the combined used of many structural and morphological techniques.

As the typical CDs reported in the literature, these CDs are very soluble in water and in polar solvents, remaining stable at large concentration (up to 5 g$\cdot$ L^{-1}) without collapsing for a long period of time.

Atomic force microscopy (AFM) revealed that the black powder consists of isolated spherical nanoparticles with an average diameter of 4 nm mixed with some larger aggregates. The distribution of CD heights obtained by AFM is shown in Figure 4.2.

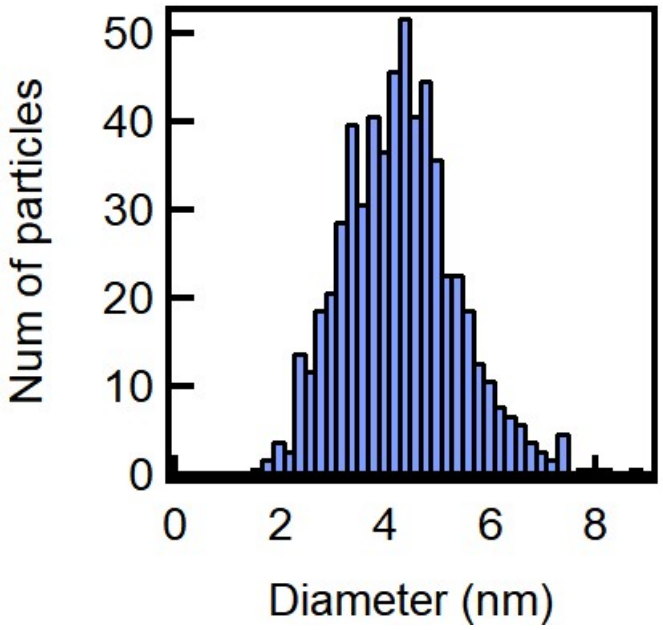

Figure 4.2: Size distribution of CDs measured by AFM.

High-Resolution Transmission Electron Microscopy (HRTEM) experiments, performed in col-

laboration with the Karlsruhe Institute of Technology, confirmed this result (Figure 4.3a) and added information on the core structure. In fact, zooming on single dot level by HRTEM, it is possible to see lattice fringes extending through the whole particle core (Figure 4.3b) demonstrating its quasi-perfect mono-crystalline structure. Sampling several single dots, HRTEM allows us

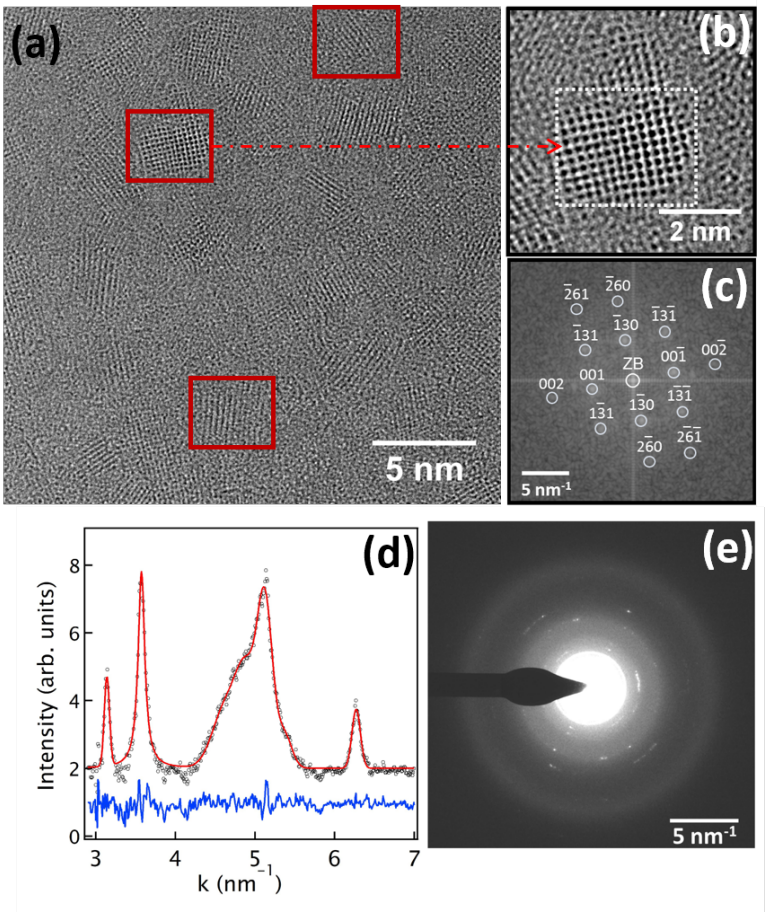

Figure 4.3: (a) HRTEM image of the sample, showing many small dots with crystalline structure and typical diameters of 3 nm. (b) Zoom of HRTEM image of a single CD and (c) experimental diffractogram of the nanoparticle shown in (b) and calculated diffraction pattern with Miller indices for hexagonal bulk $\beta - C_3N_4$ in the [310]-zone axis (white circles). The central spot indicates the zero-order beam (ZB). (d) Radial scan of the SAED pattern (open symbols), whole-pattern fit (red line) and residuals (blue line) used for the structure analysis and (e) SAED pattern of CDs [Adapted from [200]].

to identify the crystalline structure as a $\beta - C_3N_4$ crystal, as suggested by the good agreement between its diffractogram (Figure 4.3c) and the calculated diffraction pattern of hexagonal $\beta - C_3N_4$ (space group P63/m, space group number 176, with a = 6.380 Å and c = 2.395 Å) in the [310]-zone axis.

Besides HRTEM measurements, we also used Selected-Area Electron Diffraction (SAED) to investigate larger substrate areas. This approach allows to go beyond the single-dot level and sample a larger number of particles simultaneously. Thus, It allows to sample a greater number of particles and, thus, to obtain more accurate structural information. As a result, we find that all the observed Debye–Scherrer rings (Figure 4.3d-e) correpond to the hexagonal $\beta - C_3N_4$ crystal, strongly confirming the HRTEM results and excluding any further contributions from other pos-

sible CD crystalline structures. The analysis of these data yields the lattice parameters a = 6.37 $\pm$ 0.06 Å and c = 2.40 $\pm$ 0.02 Å, which are in good agreement with previous X-ray diffraction [201] and electron diffraction experiments [202] and with the results of theoretical simulations [203].

In order to investigate the surface of CDs, we used Fourier Transform Infrared Absorption spectroscopy (FTIR). In Figure 4.4 the IR spectrum is presented. The principal peaks appear at 1401, 1622, 1671 and 1716 cm^{-1}. Comparing with the experimental and computational literature of $\beta - C_3N_4$ [203, 204], we attribute the peak at 1401 cm^{-1} to a C-N vibration within the $\beta - C_3N_4$ core. The higher frequency peaks (until 1800 cm^{-1}) indicate the presence of a large variety of surface groups which decorate the crystalline core. It is possible to associate the peaks at 1622 and 1671 cm^{-1} to amide (amide I and II modes, respectively) and the peak at 1716 cm^{-1} to carboxylic moieties. At higher frequency the absorption spectrum displays other peaks between 2600 and 3600 cm^{-1} due to O-H, N-H, and possibly C-H stretching vibrations.

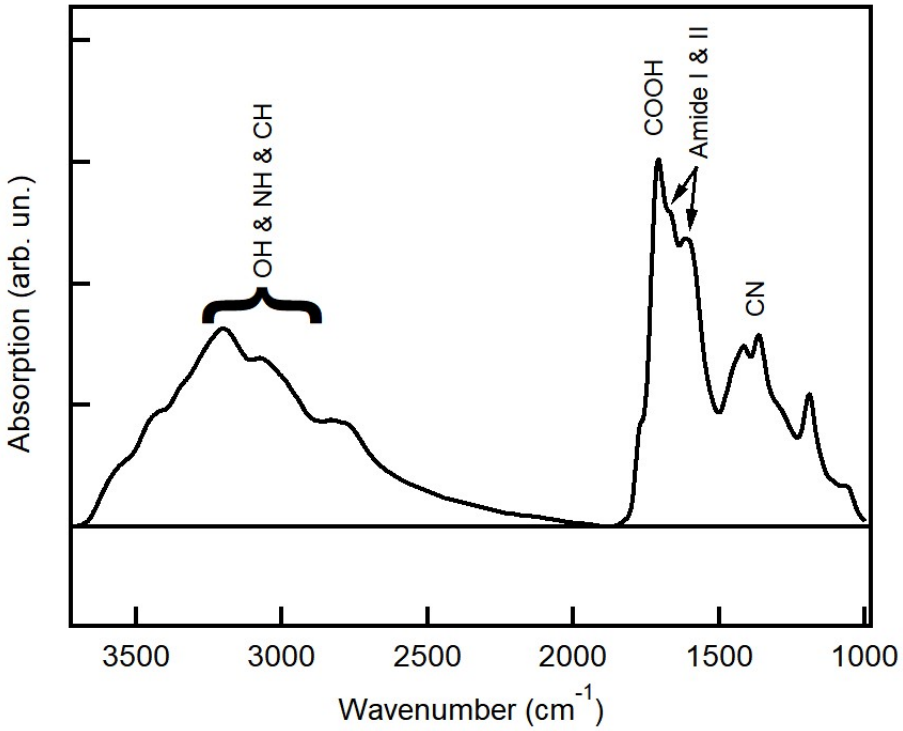

Figure 4.4: Typical infrared absorption spectrum of CDs. The labels indicate attributions we propose for the observed absorption peaks. The main vibrational signals associated to the surface structure of these CDs are due to amide (1622 and 1671 cm^{-1}), carboxylic groups (1716 cm^{-1}), and hydroxyl groups and N-H (around 3200 cm^{-1}).

The $\beta - C_3N_4$ structure we find here is uncommon in the literature. Based on previous works, macroscopic crystals with a C_3N_4 stoichiometry occur in graphitic (g-C_3N_4), cubic (γ-C_3N_4) and hexagonal (β-C_3N_4) phases [199, 203]. Even if g-C_3N_4 is considered the most stable allotrope of the carbon nitride family [205], recent theoretical studies suggest nanosized β-C_3N_4 form can be synthesized upon specific conditions [204]. However, relatively a few experiments reported the successful synthesis of nanosized β-C_3N_4 [202].

In the literature fluorescent CDs are mostly described as sp^2-carbon nanomaterials [1, 20, 25, 49, 50, 54–57], although only a few HRTEM studies clearly proved them to have the crystalline structure of graphite [3, 57]. When CDs are doped with nitrogen, the latter is usually found on the surface as a component of amide and amine moieties [41, 42], but in few exceptional cases

it is also found in the core as a structural dopant altering the very crystalline structure of the dot as in graphitic carbon nitride (g-C_3N_4) dots [7, 59]. g-C_3N_4 is again an sp^2 carbon material, quite different from the β-C_3N_4 core structure we found for our sample, where carbon is in sp^3 hybridization. β-C_3N_4 dots are also obviously different from nanodiamonds, [132] which have almost pure sp^3-carbon cores associated with very large (>5 eV) electronic bandgaps, and emit luminescence only in the presence of point defects, yielding comparatively narrow emission with well-defined and non-tunable spectral features [132].

All the measurements described so far were conducted on the as-synthesized sample. The latter is expected to contain a certain amount of impurities produced along with CDs in the synthesis as suggested in other works [45–47]. Besides, the size distribution of CDs is rather broad, as can be seen from Figure 4.2. Therefore, to purify the sample, we use size exclusion chromatography (SEC), which allows us also to separate the sample in different subsets (section 3.1). During the SEC procedure, 5 ml of the sample were added on the stationary phase and, after the complete absorption, ultrapure water was added on the top as eluant (flow = 2.5 ml·min^{-1}). Several (18) fractions of the eluate (5 ml) were collected (Figure 4.5). Investigating the optical and morphological properties of all of the fractions, it was possible to identify four different fractions of CDs with distinct properties and unify them as indicated by the coloured brackets in Figure 4.5. Some subsets of the sample contain just product of waste from the synthesis and they have been excluded from further characterization. The four subsets indicated in Figure 4.5 were characterized

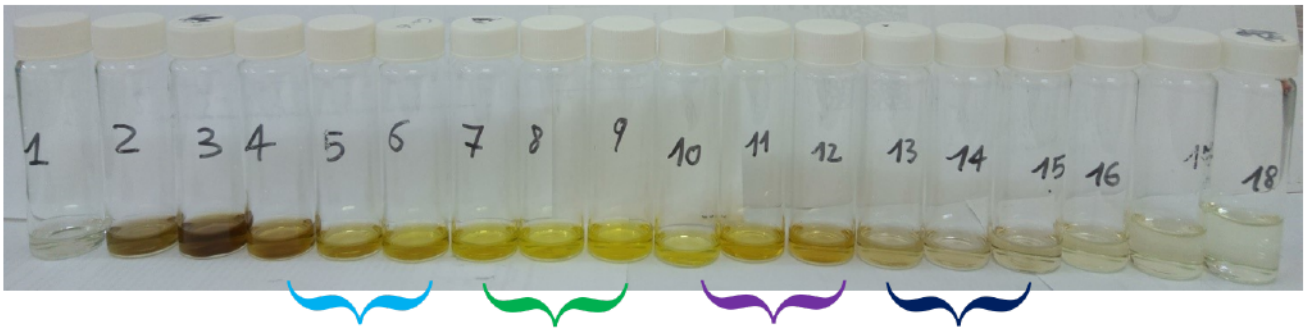

Figure 4.5: Photograph of the fractions after the size exclusion chromatography. The four fractions investigated in more detail are indicated by the coloured parenthesis.

by many techniques in order to compare the morphological and structural properties and, then, the optical properties.

AFM measurements on these fractions allow to identify the morphological differences. In Figure 4.6 the AFM images and the respective height histograms are reported. SEC procedure purifies the initial sample from very large aggregates and impurities. In fact, when each of the four subsets is deposited on a substrate and observed by AFM, we find thousands of nanoparticles which appear very well isolated from each other after deposition, very differently from the unfractionated sample which contains plenty of aggregates. Moreover, SEC procedure succeeds in separating CDs with respect to their size. In fact, AFM reveals that the four fractions in Figure 4.5 display very different size distributions, as seen from Figure 4.6: a very small fraction with a diameter of 2.6 nm, a bigger fraction with a diameter of 6 nm and narrow height distribution, an intermediate fraction of 4 nm, and a more complex subset which is characterized by two typical sizes of 2.5 nm and 3.5 nm.

As a matter of fact, although the fractions have very different size distributions, they are found to have very similar crystalline and surface structures. HRTEM investigation shows that all of them display a $\beta - C_3N_4$ core regardless the size (few examples in Figure 4.7). FTIR experiments show that the spectra collected from the fractions are similar to the unfractionated sample (Fig-

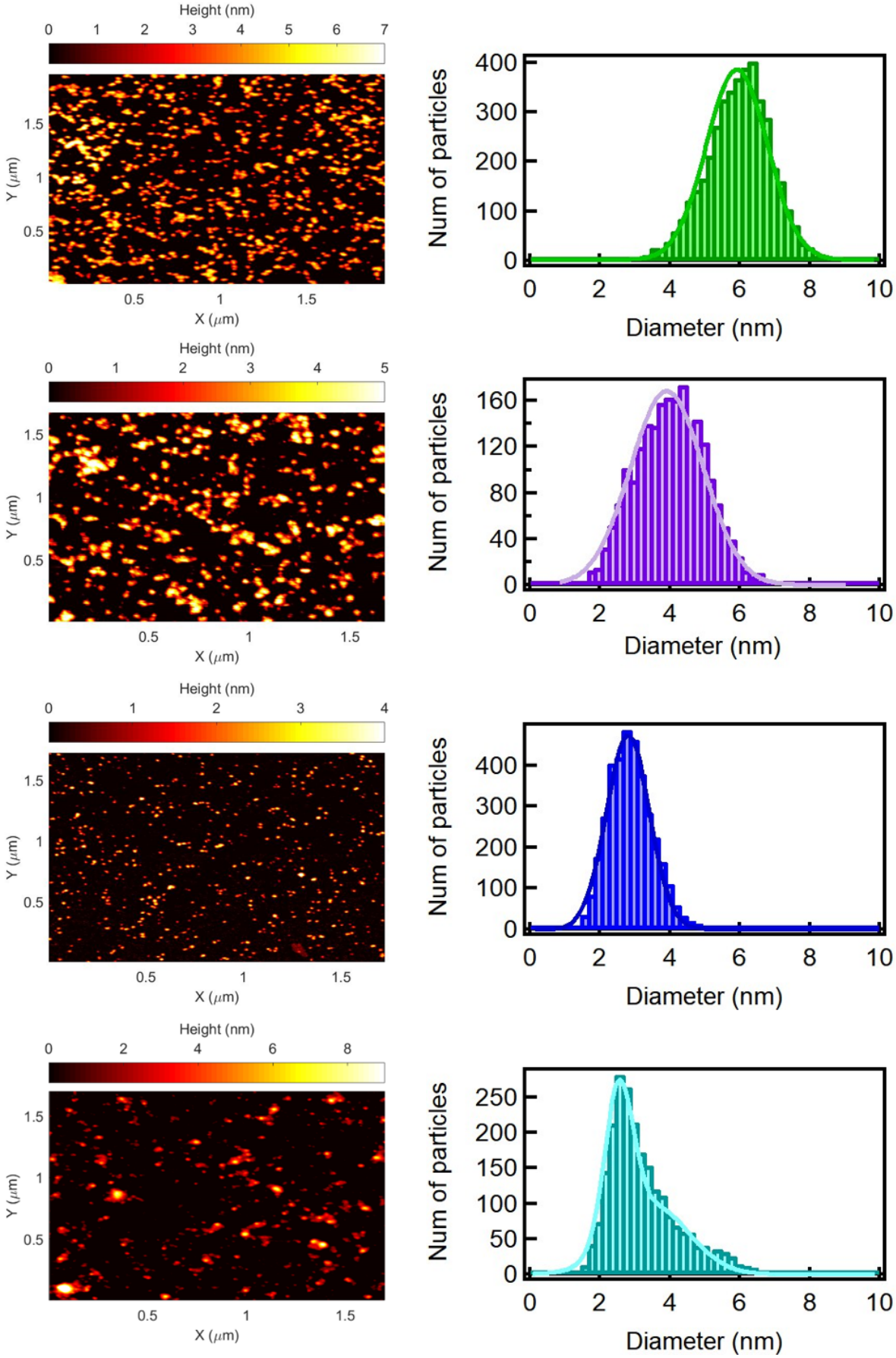

Figure 4.6: AFM images and height histograms of the four fractions.

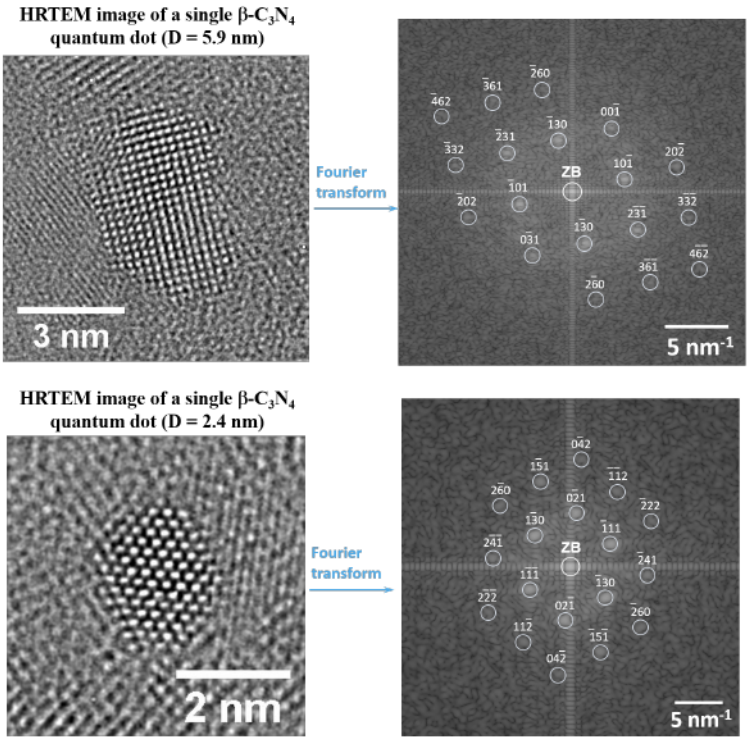

Figure 4.7: HRTEM images of single CD belonging to different chromatographic fractions, with different size and the experimental diffractogram of the nanoparticles and calculated diffraction pattern with Miller indices for hexagonal bulk $\beta - C_3N_4$ in the [310]-zone axis (white circles). The central spot indicates the zero-order beam (ZB).

ure 4.8): they contain the same vibrational fingerprints (e.g. C=O vibration around 1700 cm^{-1}, amide around 1600 cm^{-1}, C-N around 1400 cm^{-1}), although in different relative ratios. The

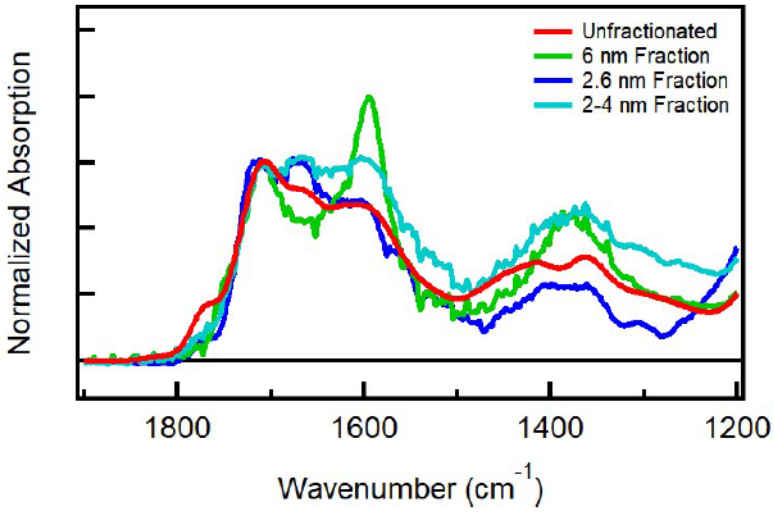

Figure 4.8: Mid-IR absorption spectra of fractions obtained after SEC procedure. They show the same peaks, although in different ratio.

present evidences of fluorescent N-CDs with a β-C_3N_4 core and their behavior as efficient emitters

(see nexgt paragraph for further details) are rather unanticipated by the literature, despite many studies synthesized CDs using similar procedures [20].

Optical Properties

Here, a complete optical characterization of the (unfractionated and fractionated) samples dispersed in water is presented in order to give the general characteristics. The investigation of the emission mechanism will be better analyzed and explained in the next chapter.

The absorption spectrum of $\beta - C_3N_4$ in water is shown in Figure 4.9. The spectrum displays

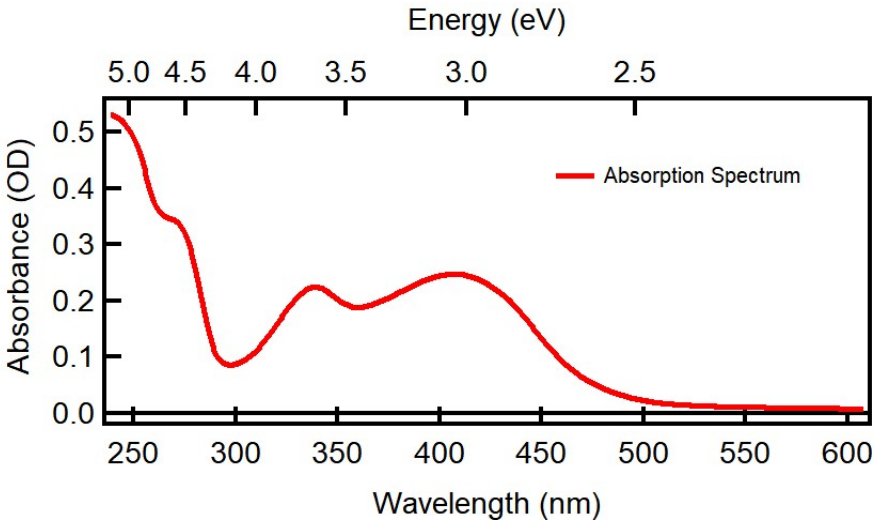

Figure 4.9: Absorption spectrum of an aqueous solution of $\beta - C_3N_4$ in a concentration of 0.02 $g \cdot L^{-1}$ in a 1 cm cuvette.

four well-defined peaks at 250 and 270 nm, at 340 nm and at 410 nm. The latter displays a long tail which extends in the visible range. When the sample is photoexcited varying the wavelength (Figure 4.10), it shows a dual emission, that is the presence of two different emission bands which we call the *blue band* (emission peak at 440 nm) and the *visible band* (tunable emission).

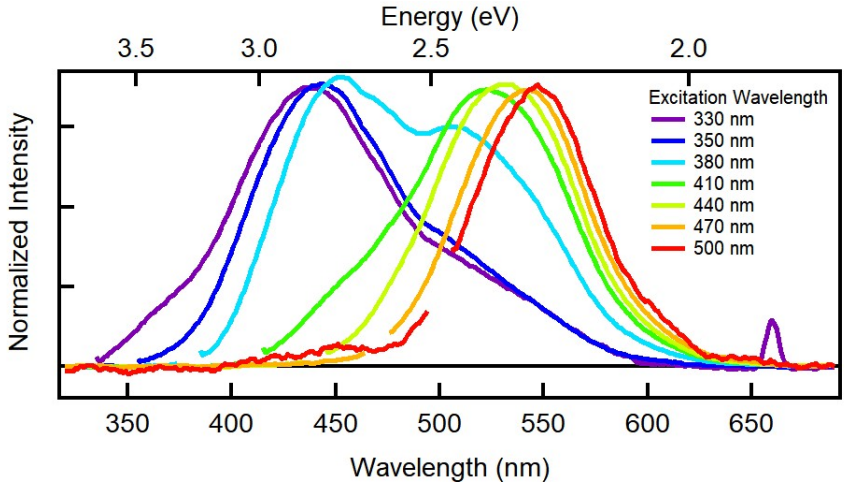

Figure 4.10: Normalized emission spectra of an aqueous solution of $\beta - C_3N_4$ at different excitation wavelengths.

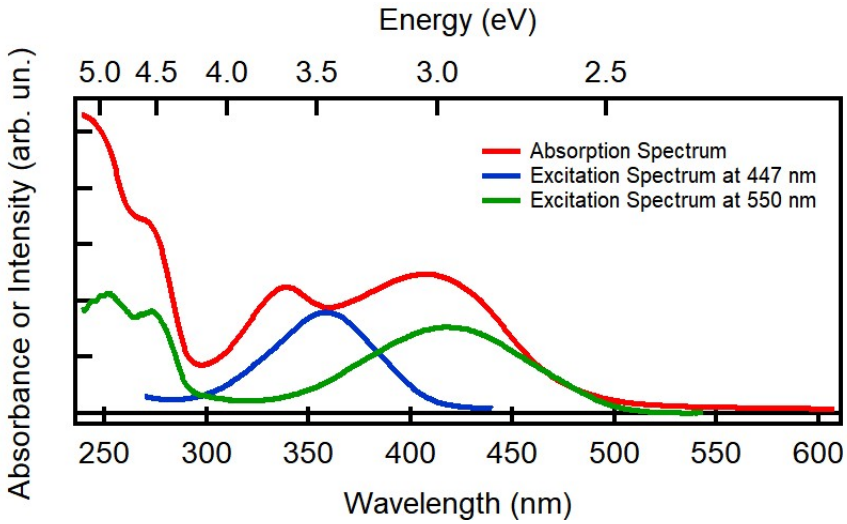

Figure 4.11: Comparison between absorption spectrum (red curve) and the excitation spectra of the emission at 440 nm (blue curve) and 550 nm (green curve) of an aqueous solution of $\beta - C_3N_4$.

The so-called blue band can be excited from 320-410 as the excitation spectrum shows (Figure 4.11). The emission of the blue band peaks at 440 nm, and is almost excitation-independent (no fluorescence tunability) (Figure 4.10). By time resolved nanosecond measurements, the decay of the band is recorded and in Figure 4.12 it is possible to see that the band decays without any spectral changes , while its decay kinetics can be described as a mono-exponential decay with a lifetime of 10 ns.

On the contrary, the visible band is tunable in a large spectral range. In fact, its emission peak spans from 510 nm when excited at 400 nm to 560 nm when photo-excited at 550 nm (Figure 4.10). The PLE shows (Figure 4.11) three peaks which stem from the transitions displayed in the absorption spectrum (400 nm, 270 nm and 250 nm), which tentatively represent the first, the second and the third excited states of the chromophore. As the blue band, also the visible emission decays without any spectral changes, although its decay kinetics can be described as a stretched-exponential decay with a lifetime of 5 ns and a stretching parameter of $b = 0.8$ (Figure 4.13). The presence of a stretching in the decay kinetics is symptom of the presence of a distribution of chromophores, thus, of inhomogeneity of the sample, which is consistent with the tunability of the emission peak as a function of excitation wavelength.

We measured the Quantum Yield (QY), when the sample is dispersed in water, and found it to be about 13%.

After SEC procedure, we studied the optical properties of the differently-sized fractions, and we see a clear size trend on the OA spectra (Figure 4.14): the feature peaking at 400 nm in the OA spectrum becomes broader and more asymmetric towards the red for smaller sizes, with a strong change from 6 nm- to 4 nm-diameter dots, and only minor variations when further reducing the size to 2.6 nm. This behaviour excludes a quantum confinement effect, which would cause a regular blue shift of the OA when size is reduced. The fraction which contains particles with a size from 2-4 nm (Figure 4.6) displays a very prominent absorption peak at 330 nm (Figure 4.14) which should be essentially related to the blue band as demonstrated by the PLE spectrum in Figure 4.11. Besides, the comparison between the OA spectrum of the unfractionated sample (red curve in Figure 4.14) with the OA of the various fractions highlights another important evidence: the 6 nm fraction is the only subset which does not displayed an intense absorption at 330 nm. This indicates that a portion of the initial sample does not contain the blue band and, thus, that it is possible to separate the blue from the visible emission. This finding is quite rare in the literature, in

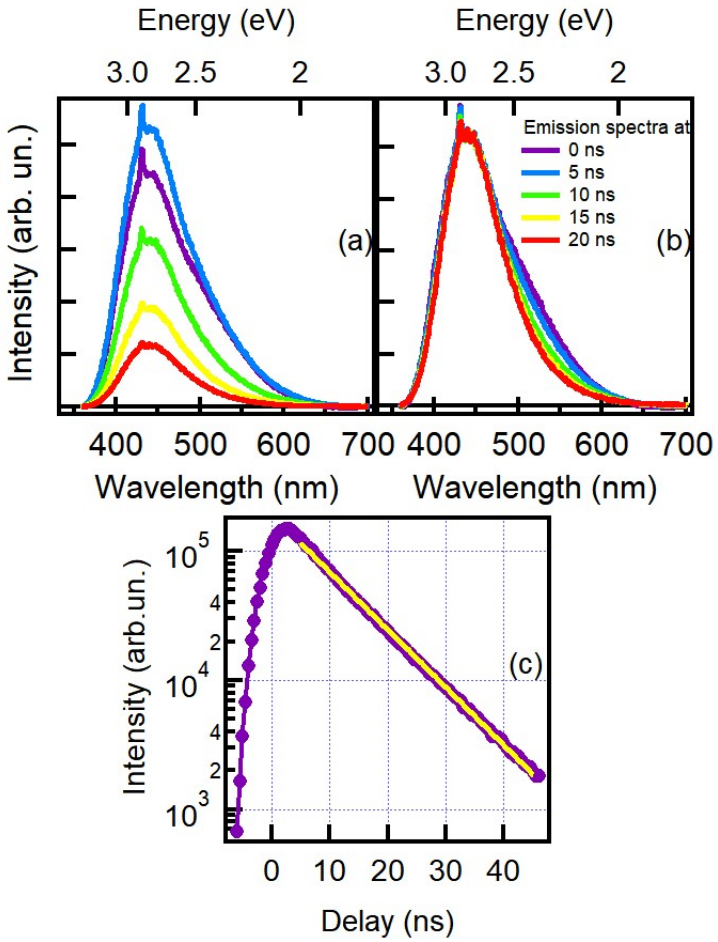

Figure 4.12: (a) Emission spectra and (b) Normalized emission spectra at different delay time after pulsed laser excitation at 350 nm. The evolution at 500 nm is related to the presence of a small additional contribution of the green band, which decays with a different time scale than the blue band provoking a spectral change. (c) Decay kinetics of the blue band recorded at 400 nm in order to avoid the contribution of the green band.

fact, only few works through SEC procedure succeeded in the separation of the dual emission [48].

The complete photoluminescence study of the visible band, as observed in the differerent fractions, is reported in Figure 4.15 and in Figure 4.16. The data highlight the presence of the same emission but with different degree of tunability. In fact, although in all samples the redshift of the emission is observed when exciting more into the red, it is accompanied by an intensity decrease, the latter occurs very differently in the various samples (Figure 4.16), for instance, exciting at 560 nm, the intensity of the emission band of 6 nm sized fraction is three times less than the intensity of the same band for the smallest fraction.

However, the tunability is always preserved in our fractions, and this evidence contrasts with the literature where every chromatographic fractions typically displayed a non-tunable emission display [27, 52, 207], except in few cases [51].

Among the fractions obtained by SEC, we found that the 6 nm-sized one (Figure 4.6) displays especially interesting characteristics. In fact, this fraction is the one displaying the most homogeneous optical characteristics. On one hand, displays the visible band only, with no appreciable contributions from the blue emission. Besides, the absorption band at 400 nm is the narrowest

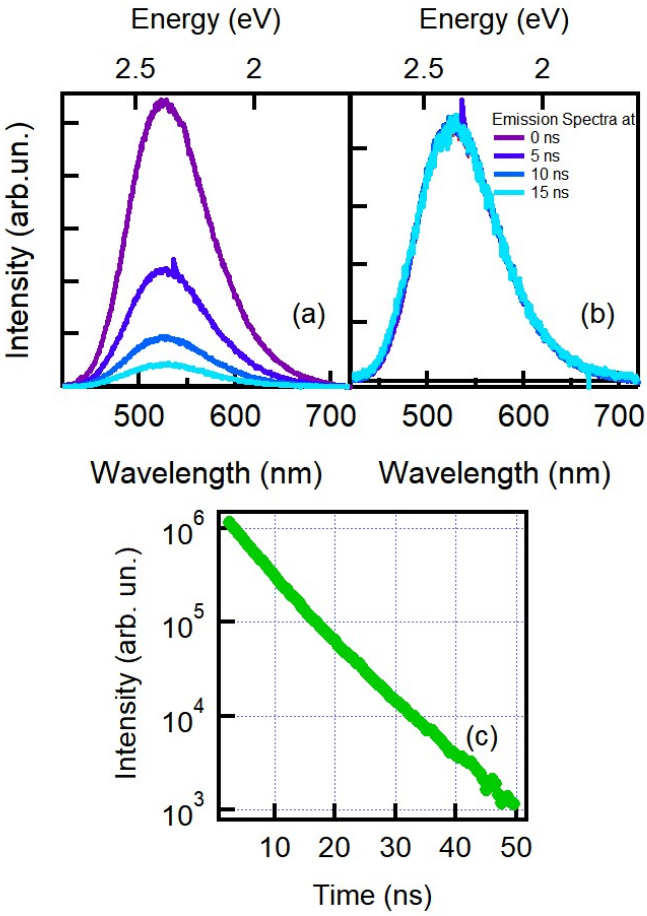

Figure 4.13: (a) Emission spectra and (b) Normalized emission spectra at different delay time after pulses excitation at 440 nm. (c) Decay kinetics of the green band extracted at 550 nm.

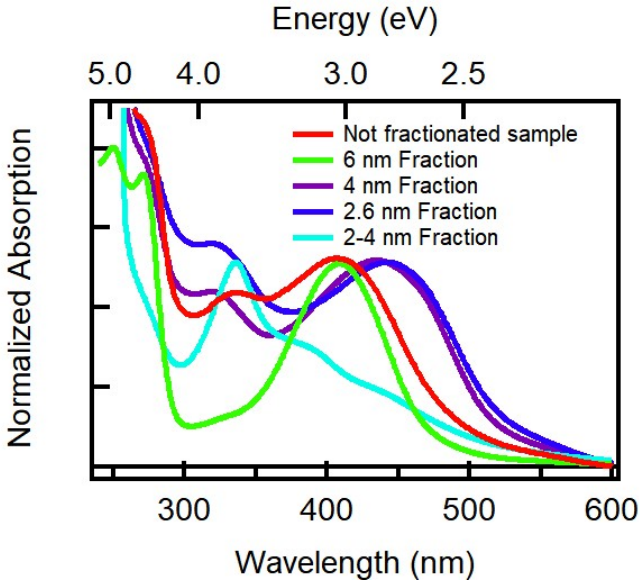

Figure 4.14: Absorption spectra of the four fractions obtained by SEC procedure [Adapted from [206]].

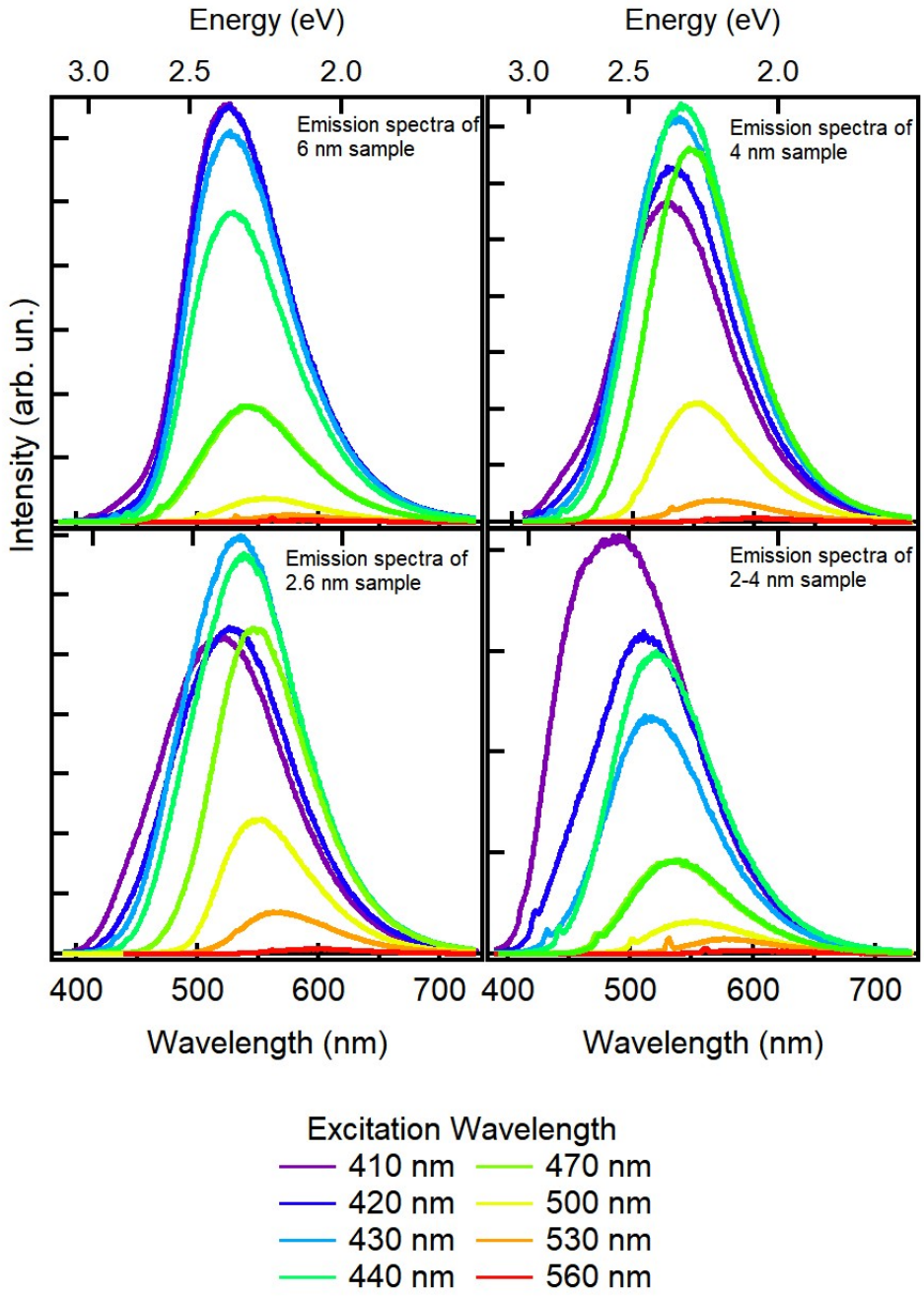

Figure 4.15: Emission spectra of the four fractions obtained by SEC procedure. The excitation wavelengths are indicated in the legend [Adapted from [206]].

(Figure 4.14) and the fluorescence is much less tunable than the other fractions and than the original sample. Considering that such a homogeneity is rare in literature and that the characteristic can be very useful in several applications, the optical properties of this fraction have been investigated in detail and we demonstrate the possible use of it as an active medium in a laser cavity. The molar extinction coefficient ϵ was estimated considering the size (6 nm) and the density of the $\beta - C_3N_4$ (3.57 $g \cdot cm^{-3}$ [208]). We obtained an extremely high $\epsilon = 3.4 \cdot 10^6 M(dot)^{-1} cm^{-1}$ at 400 nm, corresponding to an absorption cross section of $\sigma = 1.3 \cdot 10^{-14} cm^2$. This is an extremely high value as compared with previous reports on carbon nanodots [12, 209]. Moreover, this absorption

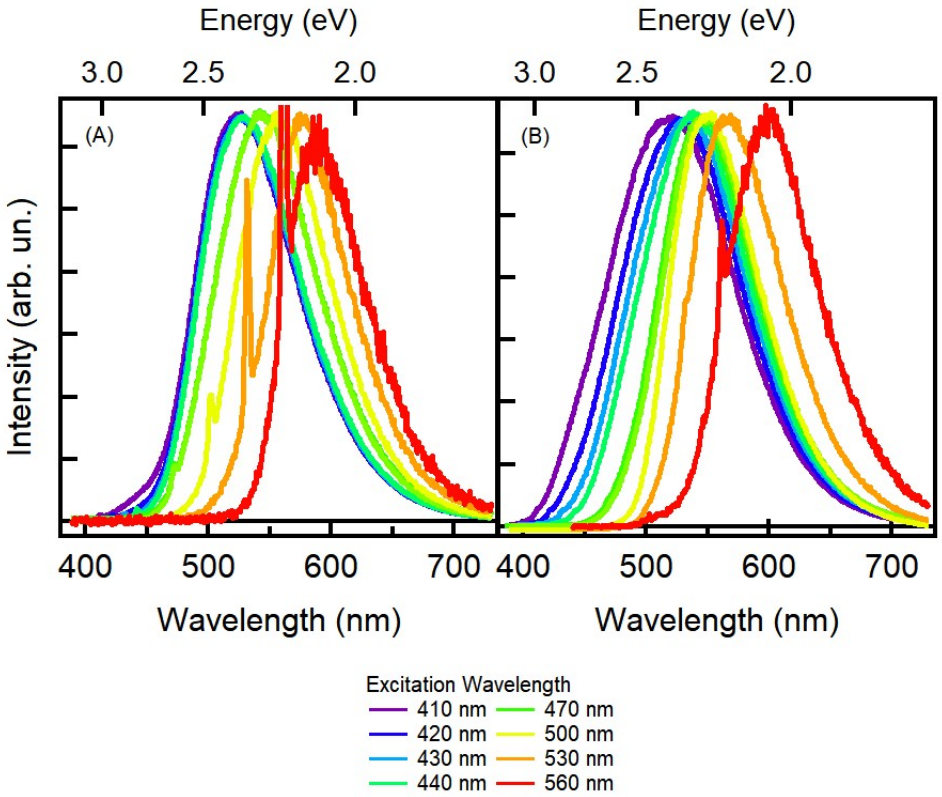

Figure 4.16: Normalized emission spectra of the 6 nm-sized (A) and of the 2.6 nm-sized (B) fractions obtained by SEC procedure. The excitation wavelengths are indicated in the legend.

strength is more than one order of magnitude higher than typical fluorescent molecular dyes [210] and even higher than CdSe or CdTe quantum dots of the same size [211,212] (e.g. $\sigma \approx 4 \cdot 10^{-15} cm^2$ for 6.8 nm-sized CdSe dots on the peak of the lowest-energy transition [212]). The emission quantum yield of this fraction is doubled (25%) with respect to the unfractionated sample. Varying the solvent in which CDs are dissolved changes the QY value (as it is reported in the next chapter), and if this fraction is dissolved in dimethyl sulfoxide, the quantum efficiency reaches the value of 73%. In addition, time resolved measurements show that the decay of the band is independent of the emission wavelength and that it can be described as a mono-exponential decay (not stretched) with a $\tau = 5.0$ ns (not shown), highlighting the reduction of disorder in this fraction, with respect to the unfractionated samples.

The large QY, the homogeneity of the emission and the large absorption reflect on a very efficient laser capability. In fact, pumping an aqueous solution of the sample, inside a home-made laser cavity, by nanosecond laser pulses at 440 nm, a laser emission is generated from the sample peaking at 568 nm (Figure 4.17). The laser cavity used for this test simply consisted in a 1 cm quartz cuvette containing the concentrated (1 g/L) CD solution, enclosed within two parallel flat mirrors and pumped through a cylindrical lens (f=150 mm) perpendicularly to the cavity axis. In such configuration, we found that lasing condition occurs when the pump reaches at least 1.5 mJ/pulse (as shown in the inset of Figure 4.17). In fact, above this threshold the bandwidth of the emission decreases with respect to photoluminescence, as expected due to the onset of laser amplification. Well above lasing threshold, we found that the lasing emission FWHM is $\Delta\lambda \approx 10nm$, a rather large value likely due to the involvement of several longitudinal modes, because of the absence of wavelength-selective elements in the laser cavity. The previous few works where CD-based lasing was achieved generally did not study the excitation-wavelength dependence of the laser emission

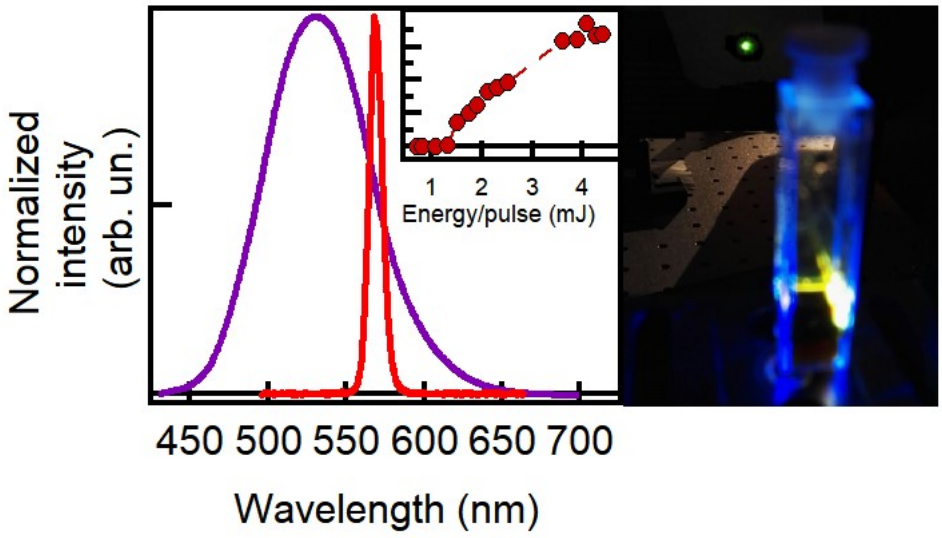

Figure 4.17: Left: Photoluminescence spectrum (purple curve) and lasing emission spectrum (red curve) of 6 nm fraction excited at 440 nm. Right: Photo of the laser emission generated from the CDs fraction. The lasing cuvette appears out of focus in the foreground of the photograph, while the green spot visible at the top center is the laser beam as it appears on a wall located at ≈ 1 m from the cuvette [Adapted from [206]].

and typically achieved lasing under UV excitation at a fixed wavelength [12, 213–215]. Here, we found that the lasing emission can be detected if the excitation wavelength spans the $410-440$ nm range and the peak and the FWHM are practically independent of pump wavelength and intensity.

4.2 Carbon Nanodots: Structural and Optical Properties vs Nitrogen Content

Introduction

As already mentioned, nitrogen content in CDs plays a crucial role both on the structure and on the optical properties. After studying in detail the properties of $\beta - C_3N_4$ dots, in a further experiment we studied structural and optical properties of CDs changing the content of nitrogen and found regular behaviour in the optical properties as a function of increasing nitrogen doping. In particular, we identified a sharp transition between two different crystalline structures of the dots which is observed when nitrogen content overcomes a well-defined threshold.

Structural Properties vs Optical Properties

We prepared CDs by the same microwave decomposition used for synthesis of $\beta - C_3N_4$, except we now tested different nominal atomic ratios between nitrogen and carbon (N/C). In particular, we synthesized four samples with a N/C values of 0.14 (sample named N1), 0.34 (N2), 0.58 (N3) and 0.74 (N4). The maximum ratio is the value used in the synthesis of $\beta - C_3N_4$, already described in detail in the previous section.

The normalized optical absorption spectra recorded in the four samples are displayed in Figure 4.18, and show two prominent transitions at 340 nm (3.65 eV) and 410 nm (3.02 eV). The black

curve in Figure 4.18 represents the absorption spectrum of $\beta - C_3N_4$ shown in Figure 4.9. Visible

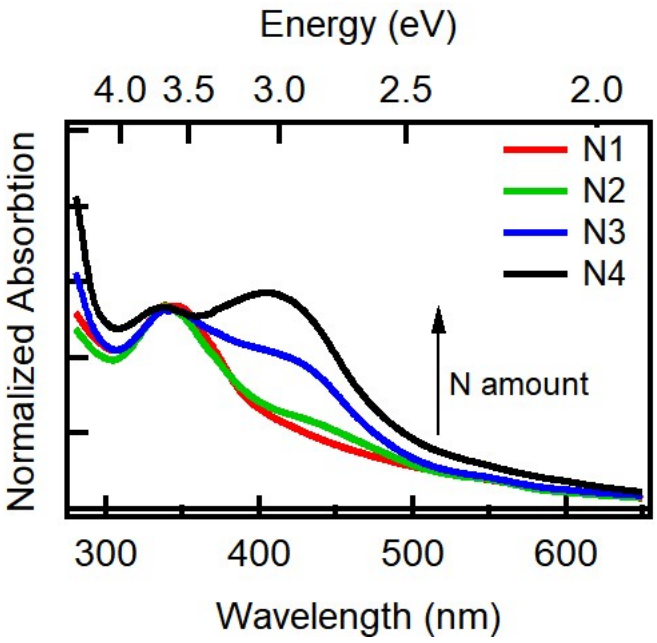

Figure 4.18: Normalized optical absorption spectra at 340 nm of sample N1 (red line), N2 (green line), N3 (blue line), N4 (black line), obtained with different degrees of N doping as explained in the text. The arrow highlights the increase of the amount of nitrogen [216].

transitions such as the one we observe at 410 nm have been reported before only in CDs doped with nitrogen [20, 161]. Our spectra in Figure 4.18 point out explicitly the increase of this band as the amount of nitrogen raises, clearly confirming its connection to nitrogen content. Even though the spectra are different, they can be grouped in pairs: N1 and N2 spectra on one hand, and N3 and N4 on the other. In fact, they are structurally similar both in the UV and in the visible region. In particular, only N3 and N4 show a relevant band at 410 nm, which is almost absent in the N1 and N2 absorption spectra. In the same way, it is possible to couple the samples based on their emission-excitation spectra (Figure 4.19): all the samples display two fluorescence bands, which resemble the blue and visible band characterized in the previous section, but the decrease of the amount of nitrogen controls the decrease of the visible band activity, with respect to the blue band, up to the almost disappearance of this emission in N1 and N2, which practically display the blue band only.

These evidences can be connected to some results found in the literature. The presence of an absorption transition peaking at 400 nm and of visible and tunable emission with high QY is usually related to nitrogen doping [7, 8, 41, 42], whereas a blue emission with almost no tunability is quite common in CDs produced from citric acid by a bottom up procedure and it is associated to molecular transitions [50, 139, 140]. In addition, the relative yield of the two bands was found to be dependent on synthesis conditions [128, 142] , particularly the synthesis temperature. Here we see that also the ratio between the precursor controls the ratio between the two transitions. In particular, from the optical characterization, it is evident the presence of a demarcation line which separates the samples in two groups: low nitrogen content-blue emitters (N1 and N2), and high nitrogen content-dual emitters (N3 and N4).

In order to correlate the optical characteristics to the structure, we performed IR and HRTEM measurements. HRTEM analysis of the two higher N-doped samples (N3 and N4) shows that both samples consist in monocrystalline nanoparticles with diameters less than 7 nm (third and

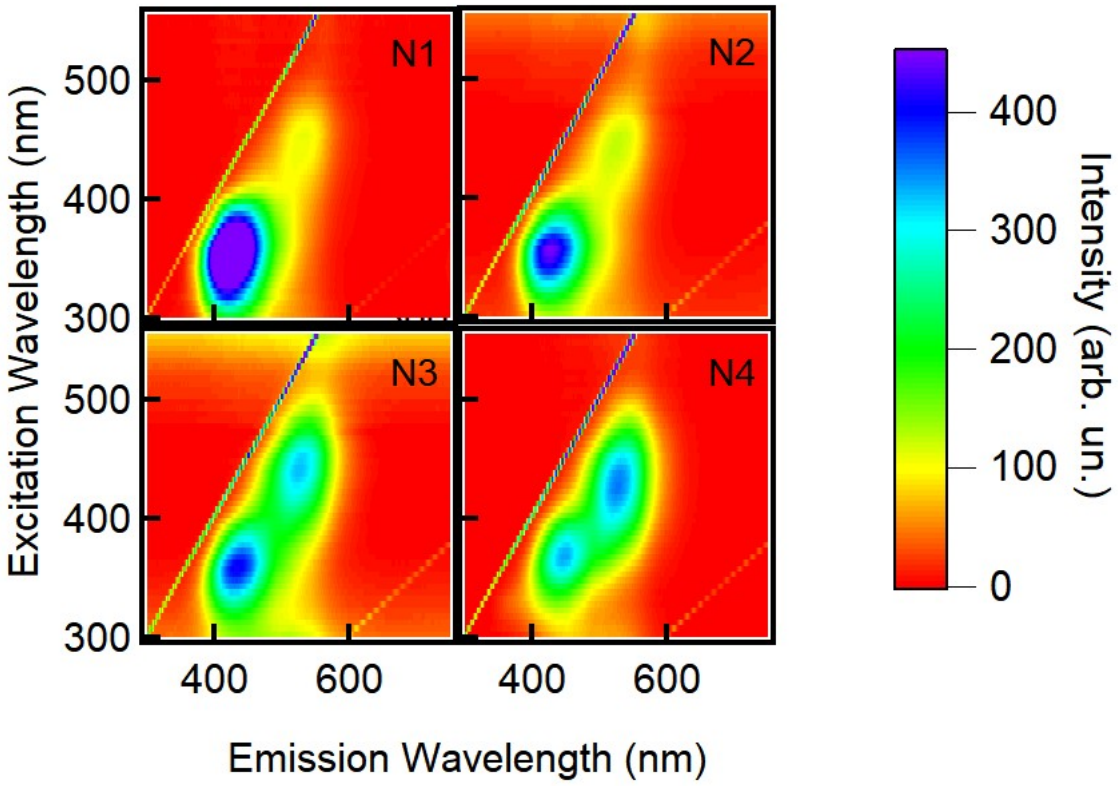

Figure 4.19: 2D excitation-emission fluorescence maps of N1-N2-N3-N4 samples [216].

fourth coloumns in Figure 4.20). The CD core investigation shows the presence only of $\beta - C_3N_4$ monocrystals demonstrated by the agreement of the Fourier Transform with the calculated diffraction pattern of bulk hexagonal $\beta - C_3N_4$ (space group P63/m, space group number 176, a=b=6.38 Å, c=2.395 Å) 36 in the [320]-zone axis (third and fourth coloumns in Figure 4.20). The same investigation on the low nitrogen-content samples shows a completely different scenario. Also in this case, the nanoparticles have a size less than 7 nm but the core structure consists in a monocrystal with a graphite structure (first and second columns in Figure 4.20). Looking more deeply into the Fourier Transforms obtained from HRTEM images (Figure 4.20), some forbidden reflections can be recognized (orange circles in Figure 4.20). In case of the ideal bulk *hcp* C-graphite crystalline structure, the structure factors of the (213), (303), and (113) reflections are zero, but these can be observed only if some carbon atoms are substituted by nitrogen atoms within the ideal C-graphite structure of cores. Therefore, this result confirms the N-doping influences the core of CDs, although this amount of nitrogen is not enough to modify the C-graphite crystalline structure itself. Although previous works have highlighted that the level of N-doping can be used to control the optical properties of CDs [43], ours is the first evidence of a clear, and abrupt transition between two different structural families of CDs when the level of N doping overcomes a defined threshold.

IR spectra shown in Figure 4.21 highlight the presence of several organic moieties on the surface as amide, carboxyl, and ester groups, albeit in different amounts. Nitrogen-content groups are recognizable in all samples, but N1 and N2 display low amounts of surface amide groups. In contrast, a very strong increase of surface amide is observed only when further increasing the nitrogen above a certain threshold, between N2 and N3, and another strong increase from N3 to N4.

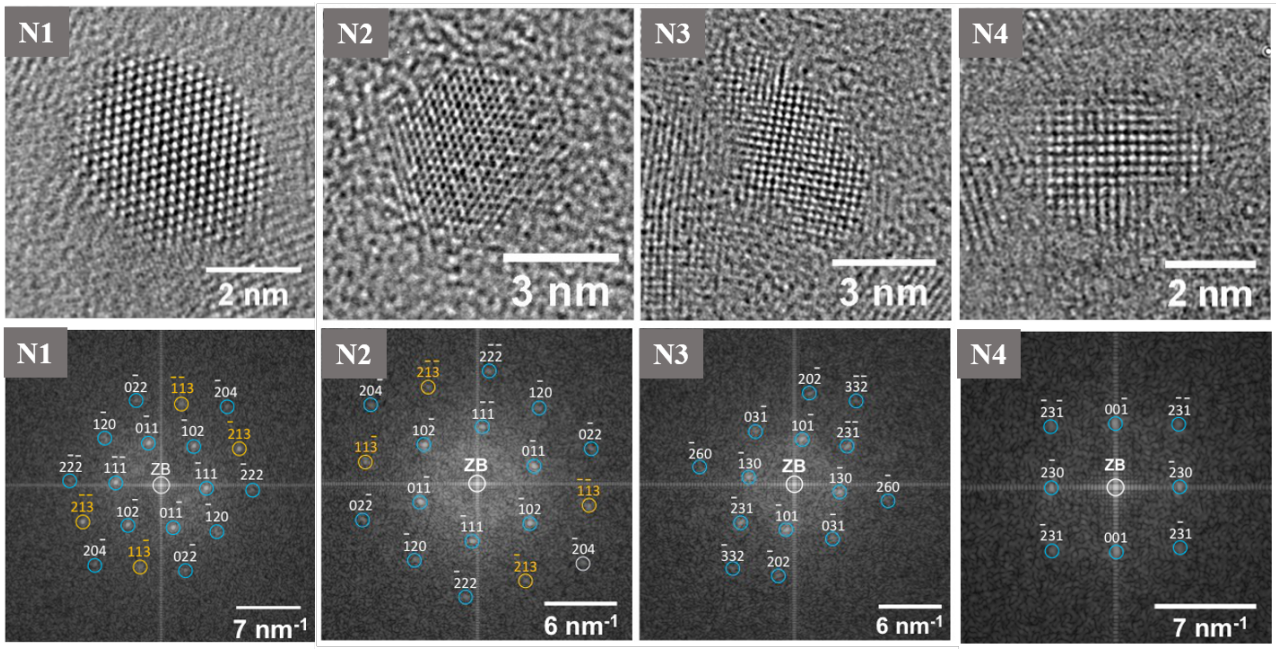

Figure 4.20: Top panels: HRTEM images of single CD N1, N2, N3, N4 samples (from left to right). Bottom panels: experimental FT of the nanoparticle shown in top panels and calculated diffraction pattern with Miller indices for a hcp C-graphite structure (N1 and N2 samples) in the [211]-zone axis (blue and orange circles), where orange circles mark forbidden reflections, and experimental FT of the nanoparticle in top panels and calculated diffraction pattern with Miller indices for a hexagonal $\beta - C_3N_4$ structure (N3 and N4) in the [320]-zone axis (blue circles). The white circle indicates the zero-order beam (ZB) [216].

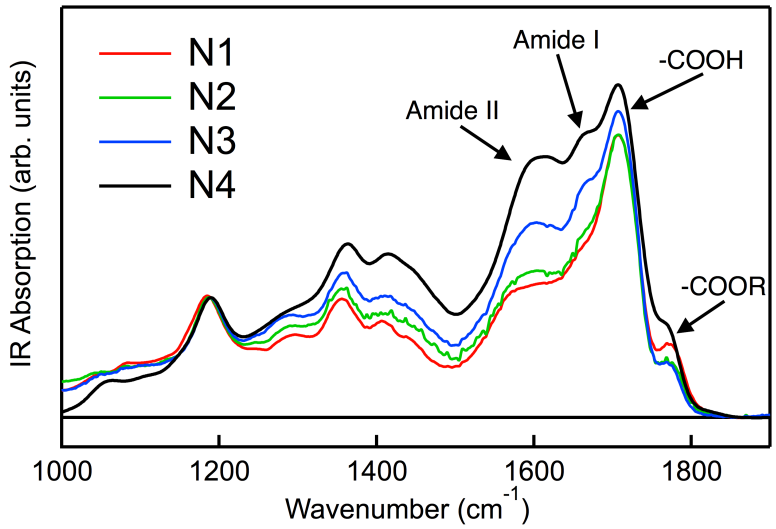

Figure 4.21: Mid-IR absorption spectra of sample N1 (red line), N2 (green line), N3 (blue line), and N4 (black line); the arrows highlight the signal attributions [216].

A clear picture of the structural changes can be obtained by the combination of all the results. The microwave synthesis produces C-graphite CDs with some nitrogen atoms in the core (Figure 4.20) as structural defects, and more on the surface as a component of amide groups (Fig-

ure 4.21). Increasing the amount of Nitrogen, at the beginning, increases the number of structural defects in the core. Because the latter can host a large fraction of N atoms in this phase, the number of surface amides grows only very slowly. . Further increasing the amount of nitrogen above a certain threshold (nominally N/C$\approx 0.4 - 0.5$) leads to an abrupt change of the crystalline structure of the core leading to a completely different type of CDs, which consist in $\beta - C_3N_4$ nanocrystals (Figure 4.20). Such a transition is probably due to the fact that the graphite structure host too many nitrogen defects to remain thermodinamically stable, and it is forced to rearrange to a carbon nitride structure. Once $\beta - C_3N_4$ is formed, the core cannot accommodate any more nitrogen. Therefore, all additional N atoms accumulate on the surface giving rise to an enhancement of the amount of the amide moieties in the N3 sample and even more in the N4 sample (Figure 4.21).

4.3 Conclusions

Summarizing, our experiments point out that the role of nitrogen is crucial on the core and surface structure of CDs. In particular, we demonstrate for the first time that the addition of large amounts of N changes the structure of CDs from N-doped graphitic to an entirely new type of CDs, the $\beta - C_3N_4$. This analysis shows that the N-content is fundamental to control the electronic properties, transforming the sample from a blue emitter to a dual emitter.

The investigation on $\beta - C_3N_4$ dots revealed that these dots consist of a monocrystal core with $\beta - C_3N_4$ structure and a disordered surface corona hosting a collection of polar functional groups. The optical activity is a dual emission characterized by a blue non-tunable band and a visible tunable band.

Fractionating the sample, it is possible to collect different sub-types of dots which display the same core structure, and similar surface structure but very different morphologic distribution. This allows to isolate different optical behaviours and, in particular, to separate the contribution of two different optical activities.

A detailed analysis of the photo-physics of these emission bands is presented in the next chapter. In addition, to have a complete view on the possible emission mechanisms of CDs, these samples will be compared with different CDs synthesized by top down methods.

Chapter 5

Emission Mechanisms of Carbon Nanodots

In this chapter, the emission mechanisms of different CDs are deeply investigated. Some of these CDs are those described in the previous chapter, produced in-house by thermal decomposition of small molecules. However, we also analysed other CDs obtained by completely different methods and provided by external collaborations. The aim of the chapter is to compare different types of CDs and their emission mechanisms giving a comprehensive view on the possible transition mechanisms which involve CDs.

The samples are classified based on the synthesis approaches (Bottom up or Top down) and then the electronic transitions are categorized based on the different emission mechanisms. First, the typical electronic transitions of the $\beta - C_3N_4$ and of the nitrogen doped graphitic CDs, obtained by the bottom up approaches described in chapter 4 are analysed. In particular, the characterization of the visible emission of the $\beta - C_3N_4$ is first investigated in detail, followed by an analysis of and, then, the analysis of the blue emission typical of the bottom up samples.

The second part of the chapter is focused on the emission mechanisms of amorphous and graphitic CDs synthesized by Top down methods (described in section 3.1) which are found to display substantially emission mechanisms with respect to bottom-up-produced CDs.

5.1 Carbon Nanodots from Bottom Up Synthesis

Introduction

The debate on CDs emission mechanism is still open, as discussed in section 1.2. Understanding if CDs emission is affected by quantum confinement effects or if only surface states play a key role on the emission is one of the most important questions in the literature. Here, the emission of bottom up synthesized CDs is presented. From the previous paragraph, it should be clear that the samples can be divided in two groups based on the core structure but also based on the emission bands: visible and blue. First of all, the typical band of $\beta - C_3N_4$ named in the previous chapter as the visible emission, which was at the centre of several of our studies, is presented and its emission mechanism analysed in detail. Then, the blue activity, typical of several bottom up samples, is analysed.

The results of size exclusion chromatography in section 4.1 point out that $\beta - C_3N_4$ does not present any quantum confinement effect. Indeed, the smallest fraction displays the most red-shifted transition in the absorption spectrum (Figure 4.14), which is the exact opposite of the behaviour that would be observed in a quantum confinement regime. Thus, in $\beta - C_3N_4$ the emission should stem from electronic transitions which surely involve the surface of the nanoparticle.

To deeply investigate the problem and to understand which is the real role of the surface in the emission mechanism, we studied the solvatochromic behaviour of the visible fluorescence. In fact, if surface states are involved in the emission mechanism, the interactions of CDs with the surrounding solvent should be essential in determining their optical properties. Conversely, solvation could be used to interrogate the photo-physics of CDs and to clarify the characteristics of their fluorescent transitions, especially if site-specific interactions are involved. This method allows us to elucidate the nature of the visible fluorescence finding a systematic dependence of the emission peak and decay kinetics on solvent properties, directly highlighting the crucial role of surface moieties. Our results point to a model in which absorption and emission transitions couple core and surface states through a transfer of electronic charge from the crystalline core to surface groups and back.

To investigate the electronic transition related to the blue band, we carried out a similar solvatochromic study combined with photobleaching (and successive recovery) experiments.

The results on the two bands are different: while the visible band is associated to the entire dot, involving a coupling between core and surface, the blue band seems to be associated to a small molecule which is synthesized together with the CDs.

Visible Emission

To investigate CD−solvent interactions, we dispersed the dots in a wide range of solvents with different solvation capabilities (Table 5.1). These capabilities can be described by different parameters such as the dielectric constant (ϵ) which describes the dielectric solvation, or the Kamlet-Taft parameters, which describe the solvent polarity separating the contributions of the hydrogen bond donor (α), hydrogen bond acceptor (β), and dipolarity/polarizability (π^*) properties of the solvent [217], or the E_T^N parameter, that is a normalized parameter measuring the overall solvation capability of solvents as a combination of nonspecific (e.g. dipole-dipole) and specific (Hydrogen bond) interactions [218].

Solvent	ϵ	E_T^N	α	β	π^*
H_2O	80	1.00	1.17	0.47	1.09
D_2O	79	1.00	1.09	0.18	1.09
Glycerol	43	0.81	1.21	0.51	0.62
Ethylene Glycol (EG)	37	0.79	0.9	0.52	0.92
Methanol (MeOH)	33	0.76	0.98	0.66	0.6
Ethanol (EtOH)	24	0.65	0.86	0.75	0.54
2-propanol (IsOH)	18	0.55	0.76	0.84	0.48
PEG400	14	0.57	0.31	0.75	0.75
Dimethyl sulfoxide (DMSO)	47	0.76	0	0.76	1
Acetonitrile (ACN)	38	0.47	0.19	0.4	0.75
Acetone	21	0.35	0.08	0.43	0.71
Dichloromethane (DCM)	9.1	0.32	0.13	0.1	0.82
Toluene	2.4	0.10	0	0.11	0.54
1,4-Dioxane	2.3	0.16	0	0.37	0.55

Table 5.1: Protic (upper part of the table) and aprotic (lower part) solvents used in this study. Dielectric constant, E_T^N polarity parameter, and Kamlet-Taft polarity parameters of the solvents (second to sixth column).

Each solution of CDs was studied with steady state and time resolved optical techniques. The

resulting emission spectra excited at 440 nm exhibit a strong solvent-dependent shift as shown in Figure 5.1.

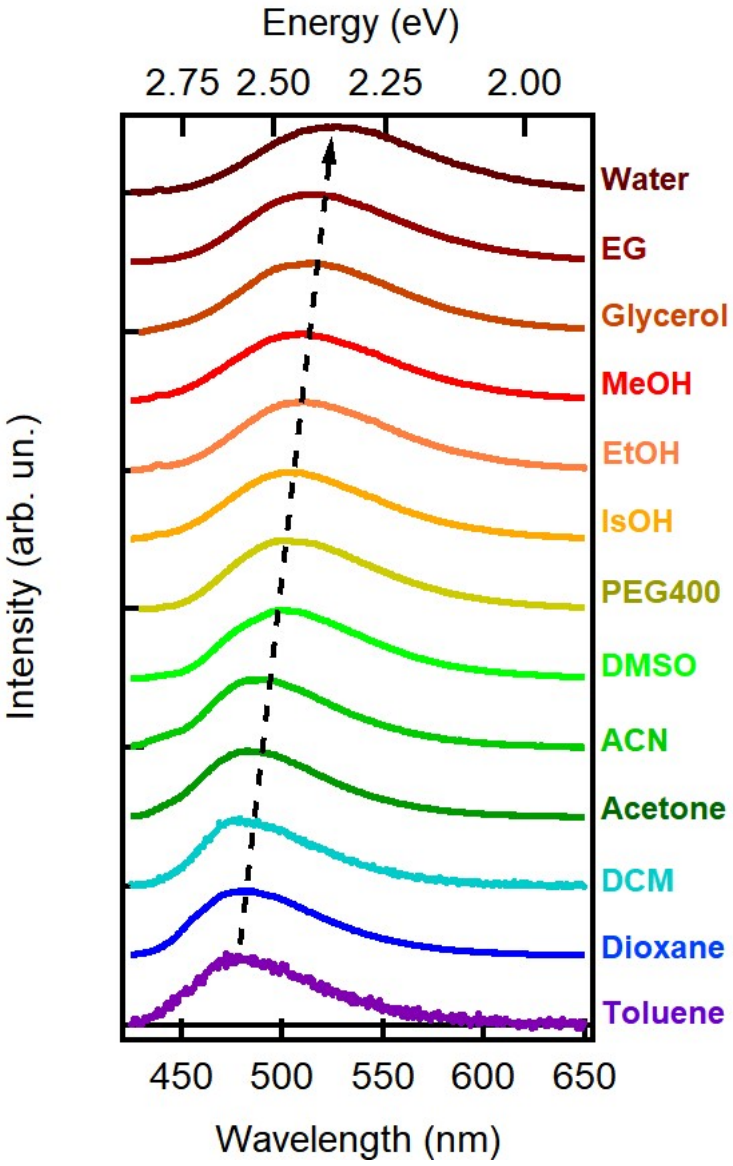

Figure 5.1: Normalized emission of CDs excited at 440 nm in different solvents. Spectra were vertically shifted for the sake of clarity. Acronyms are defined in Table 5.1.

The fluorescence redshifts with increasing solvent polarity from 482 nm (2.57 eV) in toluene, the bluemost fluorescence, to 534 nm (2.32 eV) in H_2O, therefore showing a maximum shift of 52 nm (0.25 eV) associated with the stabilization of the excited state by solvation. As shown in Figure 5.2, the emission peak position displays an approximate linear dependence (r = 0.95) on solvent polarity as estimated by E_T^N, confirming the regular solvatochromic shift of the fluorescence. Similar solvatochromic behaviour is preserved at any excitation wavelength and in every solvent (e.g. in Figure 5.3). The trend in Figure 5.1 and 5.2 is systematic and without substantial changes of the emission shape (Figure 5.4), differently from the few previous solvatochromic studies, where no clear trend of the emission peak was found [220] or rather dramatical shape changes were observed [76].

These results are also demonstrated by low temperature steady state measurements (Figure 5.5)

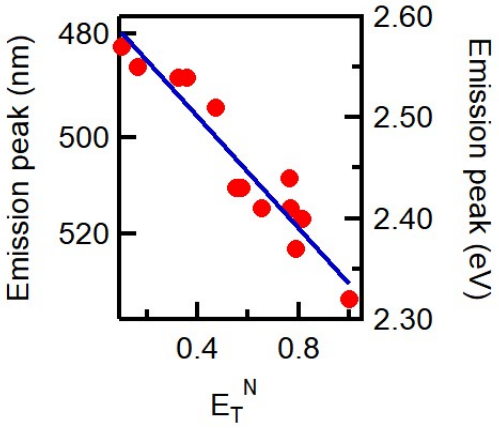

Figure 5.2: Emission peak of spectra from Figure 5.1 as a function of E_T^N solvent polarity parameter; the line is a linear fit of the data [Adapted from [219]].

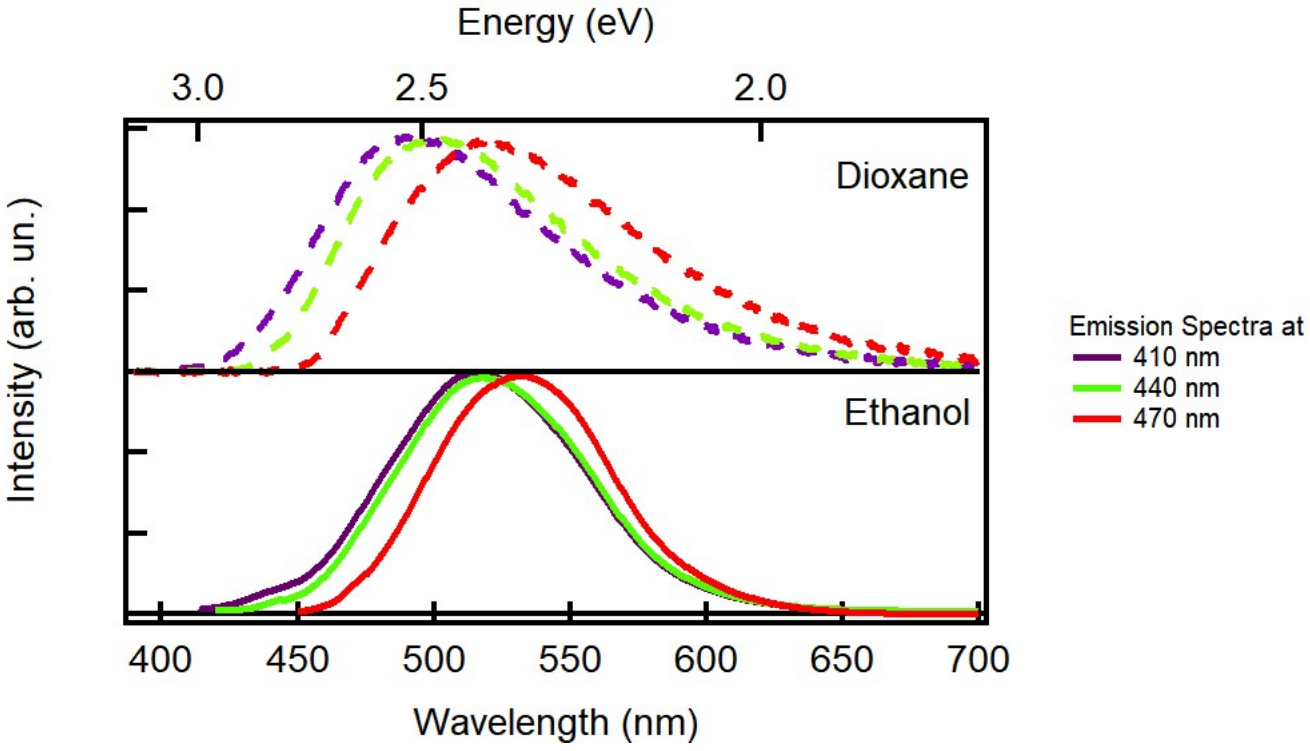

Figure 5.3: Emission spectra in dioxane (top) and in ethanol (bottom) of CDs excited at different wavelengths [Adapted from [219]].

where the emission peak dependence is evident. In fact, at low temperature every inhomogeneity effect due to the solvation should be prevented because the excited state is frozen in a non-relaxed configuration. In Figure 5.5 the emission spectra at two different temperatures confirm these hypothesis: the solvatochromic shift is almost absent at low temperature as when CDs are dissolved in Dioxane.

The results suggest that the excited state is very sensitive to the external environment and confirm that the surface is involved in the emission mechanism. To distinguish which is the contribution to the Stokes shift of nonspecific from specific interactions, the emission spectra of CDs

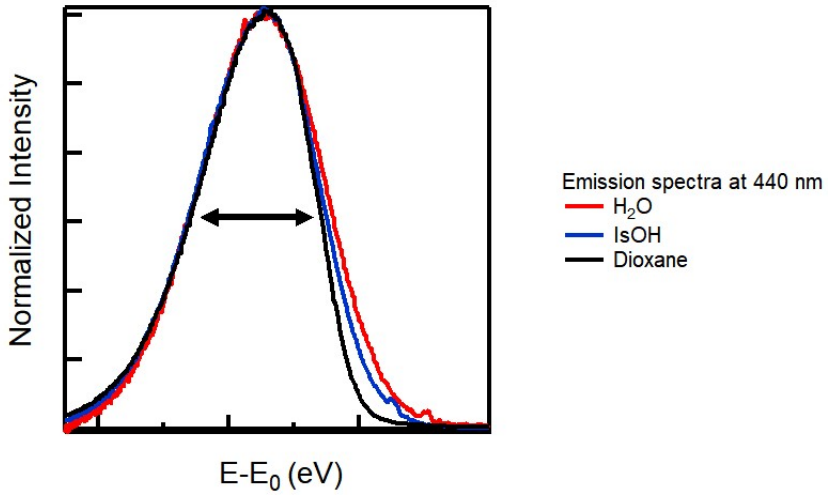

Figure 5.4: Normalized emission spectra of CDs in dioxane (black), 2-propanol (blue) and water (red). The spectra have been horizontally shifted in order to compare their widths. The arrow is a guide to the eye to emphasize the almost complete absence of solvatochromic broadenings. [219]

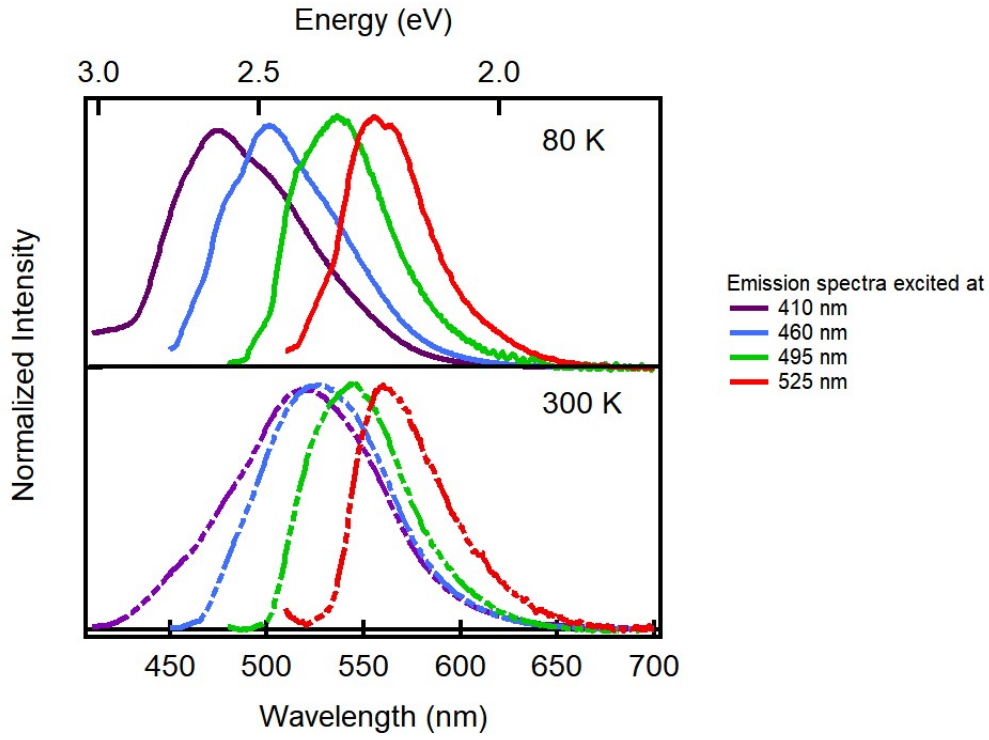

Figure 5.5: Emission spectra recorded at different excitation wavelengths of CDs dispersed in glycerol at 80 K (Top) and at 300 K (Bottom).

in dioxane ($\epsilon = 2.3$ and $\alpha = 0$), acetone ($\epsilon = 21$ and $\alpha = 0.08$), acetonitrile ($\epsilon = 38$ and $\alpha = 0.19$), 2-propanol ($\epsilon = 18$ and $\alpha = 0.76$) and methanol ($\epsilon = 33$ and $\alpha = 0.98$) are compared in Figure 5.6. Dioxane has been chosen as a reference point in which the solvation is almost null ($\epsilon = 2.3$ and $\alpha = 0$). Acetone ($\epsilon = 21$ and $\alpha = 0.08$) and 2-propanol ($\epsilon = 18$ and $\alpha = 0.76$) have been chosen because they have similar dielectric constant but different hydrogen bond donor capability

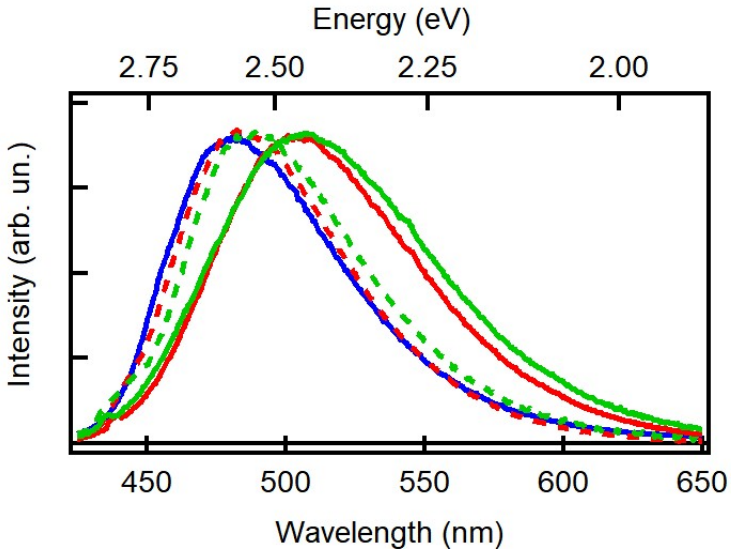

Figure 5.6: Spectra from Figure 5.1 in selected solvents: dioxane (blue line), acetone (green dashed line), acetonitrile (red dashed line), 2-propanol (red continuous line), methanol (green continuous line) [Adapted from [219]].

(acetone is an aprotic solvent), and, for the same reason, acetonitrile ($\epsilon = 38$ and $\alpha = 0.19$) and methanol ($\epsilon = 33$ and $\alpha = 0.98$) are compared. In Figure 5.6, the emission of CDs dispersed in nonpolar dioxane peaking at 482 nm (2.56 eV) is compared with the emission in the other two aprotic solvents having larger dielectric constants. The fluorescence shifts only about 0.01 eV in acetone, or 0.04 eV in acetonitrile, which are very small redshifts if we consider the substantial increase in polarity. In contrast, protic solvents with almost the same two dielectric constants, 2-propanol and methanol, induce an additional emission red shift, much larger than the first (0.10 eV in 2-propanol and 0.12 eV in methanol). Hence, the strongest solvation effect on CDs can be clearly attributed to Hydrogen bond between the protic solvents and the CDs. In particular, the contribution comes from the capability of the solvent to act as a donor of hydrogen. In fact, almost no shift is observed when comparing CD-dioxane ($\epsilon = 2.3$, $\alpha = 0$ and $\beta = 0.37$) and CD-toluene ($\epsilon = 2.4$, $\alpha = 0$ and $\beta = 0.11$) emission as shown in Figure 5.7 despite the different β parameter. This parameter probably does not influence the emission but still bears a great impact on the solubility of CDs in the solvent: in fact, CDs are much more soluble in dioxane with respect to the other apolar solvents.

Hydrogen bond is a short range interaction, thus, its strong effect provides direct evidence of the involvement of surface states in the emission mechanism. To further highlight this point, we dispersed CDs powder in D_2O to directly study the influence of isotopic exchange on CD surface groups, without changing the hydrogen bond capability (α parameter of D_2O is almost the same than water). As a result, we measured a doubling of QY from water (0.09) to heavy water (0.18), whereas the emission peak position remains unchanged (Figure 5.8). The remarkable influence of isotopic exchange on the QY further confirms a deep involvement of surface moieties in the emission mechanism. As already shown by IR measurements (Figure 4.4), the surface of these $\beta - C_3N_4$ is rich of amide and carboxylic groups that can both act as efficient Hydrogen bond acceptors because of their electron lone pairs, and potentially respond to hydrogen−deuterium substitution because they contain one or more hydrogen atoms. Therefore, we conclude that the fluorescence mechanism of these CDs closely involves amide and/or carboxylic groups which decorate the surface of CDs.

After their publication [219], our results have been confirmed by following studies which con-

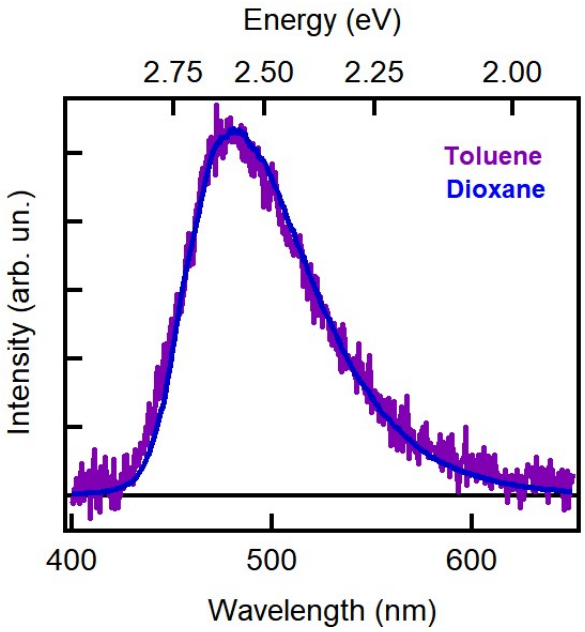

Figure 5.7: Emission spectra of CDs in toluene (purple line) and in dioxane (blue line) excited at 440 nm.

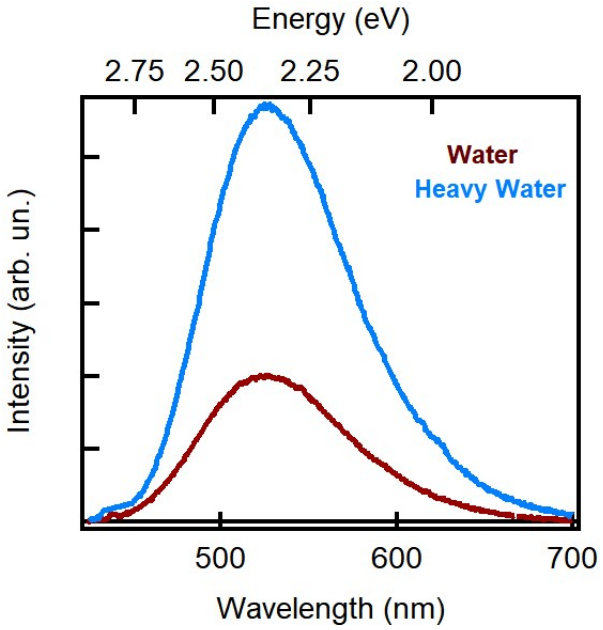

Figure 5.8: Emission spectra of CDs in H_2O (dark red line) and D_2O (blue line) excited at 440 nm in the same experimental conditions of absorption and excitation power [Adapted from [219]].

firm that the fluorescence peak depends not only on the dielectric constant of the solvent but also on its capacity to create a hydrogen bond with the surface of the dots having a crucial influence on the emission [221]. To model this, the authors combine Lippert-Mataga model with a Kamlet-Taft model [64, 221–223] confirming our results.

Beside the emission, we also compared the photoluminescence excitation spectra in different solvents. From this experiment we find that the excitation spectra are not as sensitive as the luminescence spectra. The PLEs are all slightly blueshifted from apolar dioxane (Figure 5.9), and

they almost coincide whatever the solvent is, with the notable exception of dioxane. Despite Dioxane is an apolar solvent, CDs are quite soluble in it. Looking at Kamlet-Taft parameters (Table 5.1), Dioxane shows a $\beta = 0.37$ which indicates the capabilities of acting as an acceptor of hydrogen bonding. This indicates that CDs can interact with it in a 'non-standard' way, involving the donation of a H-Bond from CDs to the solvent, explaining the high solubility, and the different behaviour recorded in PLE spectra.

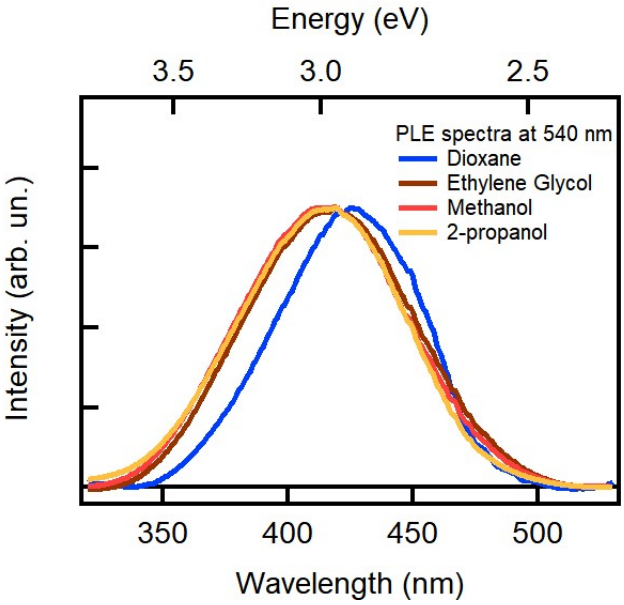

Figure 5.9: Excitation spectra at 540 nm of CDs in selected solvents: dioxane (blue line), Ethylene Glycol (brown line), Methanol (red line) and 2-propanol (orange line) [Adapted from [219]].

Besides dioxane, PLEs detected in the other solvents are identical, indicating that unlike the excited state that depends sensitively on the solvent environment, the ground-state of CDs is much less affected by the it.

Time resolved fluorescence experiments were performed to examine the emission kinetics (Figure 5.10). In all solvents, the fluorescence displays no spectral migration during the decay and behaves as a single band that keeps the same shape (as in Figure 4.13). In contrast with previous reports of multiexponential kinetics [146, 220], the detected fluorescence, here, almost behaves as a mono-exponential decay (with a small stretching which depends on the solvent) with a lifetime that changes significantly in different solvents (Figure 5.10 and Table 5.2).

Single-exponential decay suggests a single, well-defined electronic transition to be responsible of the observed fluorescence. On the basis of the measured values of QY and lifetime (Table 5.2), we estimate the radiative (K_R) and non-radiative (K_{NR}) rates according to Equation 2.23 and 2.24. The non-radiative rates regularly increase with E_T^N parameter in protic solvents (Figure 5.11), unlike in aprotic solutions, where an obvious trend cannot be recognized. The rise of K_{NR} in protic solvents causes a progressive reduction of the QY (and lifetime) of CDs from 0.41 in PEG400 ($E_T^N = 0.57$) to 0.09 in water ($E_T^N = 1$). Hence, the redshift which indicates a reduction of the energy gap, with increasing solvent polarity (Figure 5.1) favours nonradiative decay back to the ground state. In contrast, the radiative lifetimes $1/K_R$ are hardly solvent-dependent and are of the order of tens of nanoseconds. Following studies agree with our results, showing that the emission quantum yield changes with the solvent, mostly due to a modulation of the non-radiative decay rate [222].

Our results unravel the emission mechanism of CDs. Although the solvation dependence

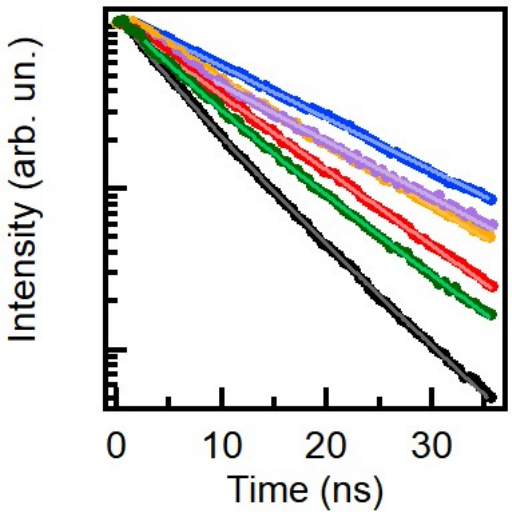

Figure 5.10: Normalized decay kinetics of CDs excited at 440 in water (black), ACN (green), methanol (red), 2-propanol (orange), DMSO (purple), PEG400 (blue), with their least-squares fitting curves (continuous lines) [Adapted from [219]].

Solvent	E_T^N	QY	τ (ns)	$1/K_R$ (ns)	$1/K_{NR}$ (ns)
H_2O	1.00	0.09	4.8 (b=0.85)	53	5
D_2O	1.00	0.18	10.7	61	13
Glycerol	0.81	0.25	8.0	31	10
Ethylene Glycol	0.79	0.27	9.0	33	12
Methanol	0.76	0.22	9.7	45	12
Ethanol	0.65	0.28	10.5	38	14
2-propanol	0.55	0.33	11.5	34	17
PEG400	0.57	0.41	13.5	33	23
DMSO	0.76	0.44	12.5	29	22
Acetonitrile	0.47	0.24	5.7 (b=0.85)	24	8
Acetone	0.35	0.45	9.5	21	17
Dichloromethane	0.32	ND	5.2 (b=0.75)	ND	ND
Toluene	0.10	ND	5.7 (b=0.54)	ND	ND
1,4-Dioxane	0.16	0.13	7.6	58	9

Table 5.2: Protic (upper part of the table) and aprotic (lower part) solvents used in this study. Fluorescence quantum yield, decay lifetime (b is the stretching parameter, if smaller than one), radiative and non-radiative decay rate measured for CDs dispersed in each solvent and excited at 2.82 eV (seventh to last column). QY measurements (and, in turn, K_R and K_{NR}) were not possible in some of the most apolar solvents where a low solubility hindered a reliable estimate of the absorption coefficient, needed to calculate the QY. In the table, these cases are indicated as ND - not determined.

directly evidences the central role of surface groups in the emissive transitions, the amide and carboxylic surface moieties are not expected in themselves to undergo transitions at these low energies ($2-3$ eV). Instead, we propose a transition which involves a coupling between surface-localized states and those of the crystalline carbon-nitride core, which has a bandgap $>$ 3.50 eV [224]. Considering that the CDs appear much more solvent-sensitive in the excited state than in ground-state, it is possible to suppose that the hydrogen bond accepting capability of CDs is strongly enhanced by photo-excitation, due to an increase of the negative charge localized on

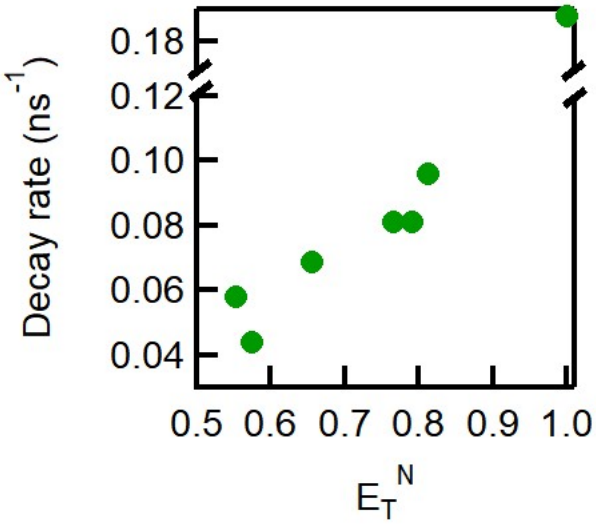

Figure 5.11: Non-radiative decay rates in protic solvents as a function of E_T^N parameter; there is a break on the vertical axis [Adapted from [219]].

surface HB-accepting groups. Indeed, similar situations where an increase of the Hydrogen bond propensity of a certain site is caused by the charge transfer character of the electronic transition are common for optically active systems [225, 226] Thus, this electronic transition can be schematized as a transition from the valence band of the core to a manifold of midgap empty states localized on surface carboxylic or amide groups, whereas the fluorescence arises from the radiative recombination of the photo-excited electron with the hole left in the core. This interpretation, which, for the first time, invokes a coupling between core and surface states to explain the fluorescence, contrasts with other common views which explain the electronic transitions involving the quantum confinement effect [27, 134–136, 207] or some surface states [133, 137].

Blue Emission

In the literature, the blue emission of CDs synthesized by a bottom up approach with citric acid as a precursor has been attributed to an electronic transition which involves a small fluorescent molecule such as a 2-pyridone derivative [50, 63, 139–141] which can be free in solution or connected to CD surface. Every sample synthesized here by microwave method presents a blue emission which has similar spectral characteristics. To understand the nature of this emission peaking at 440 nm (2.82 eV), a solvatochromic investigation was performed. The blue emission displays a bathochromic shift increasing the polarity and the hydrogen bond capability of the solvent (Figure 5.12). Comparing the PL spectra in Figure 5.12, it is evident that the blue band is more sensitive to the presence of hydrogen bonding (Acetone vs Ethanol) than to the variation of dielectric constant (ACN vs Ethanol).

Also the excitation spectra show a solvatochromic behaviour, and, in particular, the excitation band blueshifts with the increasing of polarity and of the hydrogen bond donor capability of the solvent (Figure 5.13). This behaviour was not present in the visible band and suggests that this band has a different emission mechanism than the core-to-surface coupling. In this case, in fact, both the ground state and the excited state are sensitive to the surrounding solvents suggesting the involvement of the surface or of free molecules in solution.

With this investigation it is not possible to disentangle the presence of small molecules, either

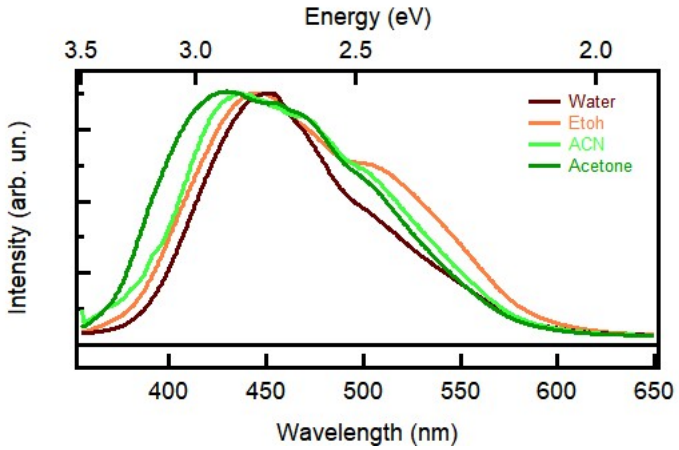

Figure 5.12: Emission spectra of CDs excited at 350 nm in Water (brown line), ethanol (orange line), Acetonitrile (ACN) (light green) and Acetone (dark green).

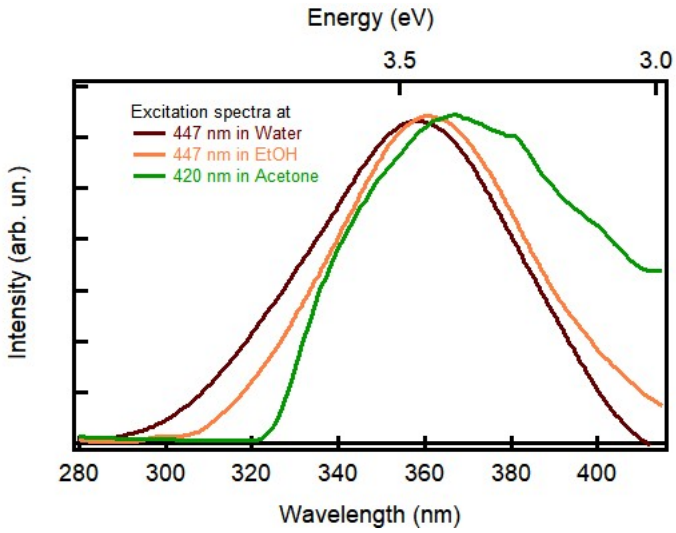

Figure 5.13: Excitation spectra of CDs in water (brown curve), ethanol (orange curve) and acetone (green curve).

free or linked to the surface of the dots. Thus, a further method used to investigate the two bands was a photobleaching experiment. In fact, when CD sample is exposed to high power UV irradiation, the emission (and the absorption) tends to decrease in intensity. This phenomenon (the photobleaching) occurs both for the visible band and for the blue band but with different efficiency. In fact, after 500 pulses (5 ns) at 355 nm at 10mJ/pulse, the intensity of the blue band decreases of 90%, on the contrary, the intensity of visible band decreases only of 30% , as shown in the two panels of Figure 5.14. This result confirms that the nature of the two transitions is different.

A correlated effect is recorded for the absorption spectrum where the peaks at 330 nm and at 400 nm are bleached by the UV exposure. Besides, the photobleaching effect is not only observed for $\beta - C_3N_4$ dots. In fact, the same experiment has been performed on the N-doped sample with a graphitic core structure described in section 4.2 and the results are the same. This suggests that the chromophores in the two samples are similar. Here, for simplicity's sake, considering that the blue band is almost isolated in the graphitic sample, only the data on it are reported. In order

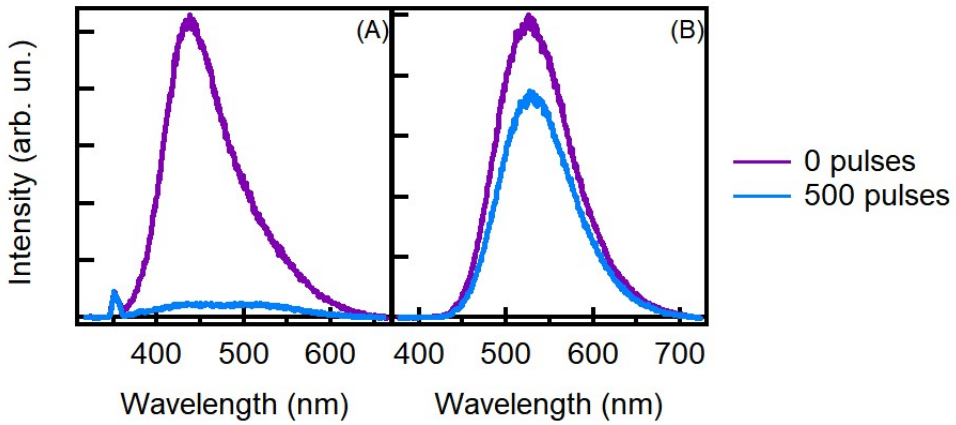

Figure 5.14: Emission Spectra of CDs excited at 350 nm (panel A) and at 440 nm (panel B) before the photobleaching and after 500 pulses of 350 nm at 10 mJ/pulse.

to investigate the nature of the blue activity, we performed an experiment specifically aimed at revealing any post-irradiation kinetics of the absorption related to the blue band (peak at 330 nm) after a photobleaching in non-uniform conditions. To perform the experiment a 1 cm cuvette was exposed to UV irradiation by a pulsed laser (355 nm, 10 mJ/pulse, 3 mm spot diameter) for approximately 100 s. Because the spot diameter is smaller than the size of the cuvette, the photobleaching is deliberately non-uniform, that is, only a portion of the sample is photobleached. Before, during and after the photobleaching the absorption spectrum of the exposed part of the sample was monitored (Figure 5.15) in situ during time.

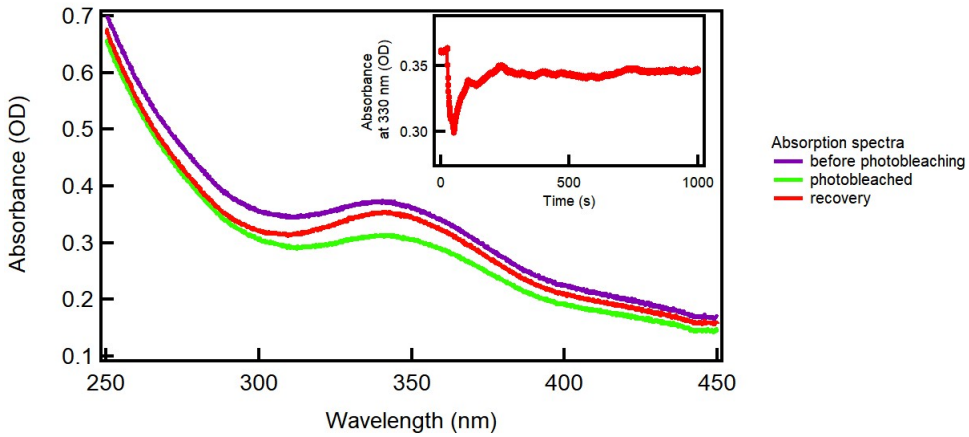

Figure 5.15: Absorption spectra of the sample before (purple curve), during (green curve) and after (red curve) photobleaching at 355 nm. Inset: Kinetics of the peak at 330 nm which shows the decrease of the absorption due to the UV irradiation and the following recovery of the absorbance when the UV irradiation is stopped.

In the experiment, the sample is initially exposed to 200 shots, causing a decrease of the absorption due to photobleaching, from 0.35 OD to 0.30 OD, as in the inset of Figure 5.15. However, we find that the effect is partially reversible: once the sample is not exposed anymore to UV irradiation, the absorbance increases again and almost recovers the initial value. The kinetics at 330 nm is extracted from the data and shown in the inset of Figure 5.15. The recovery kinetics is simple: the absorption peak starts to recover the intensity until a saturation value which corresponds

to the 95% of the initial absorption within a few 100s of seconds. Following the idea of an emissive state related to a small fluorescent molecule [47, 143], and considering the non-uniformity of the UV exposure, the recovery in the inset of Figure 5.15 suggests the involvement of small free molecules which re-enter the photobleached volume via diffusion, from other parts of the cuvette which were never photobleached. Because the probed region coincides with the initially photobleached volume, this effect is seen as a post-irradiation recovery within the probed region. In fact, considering Einstein's equation $\Delta x^2 = 2D\tau$ [178], where $x = 1.5$ mm (radius of the bleached spot) and $D \approx 2 \cdot 10^{-3} mm^2/s$ (diffusion coefficient in water of a small molecule as O_2) only a small molecule can diffuse in such fast time (hundreds of seconds) in this volume, and on the contrary an entire dot (3 nm of diameter) should need more time (at least 10 times more). Therefore, the observation of a recovery after photobleaching is a strong point in favour of the attribution of this blue fluorescence to small molecular chromophores (1 nm or below), capable to freely diffuse in solution within the time scale of the experiment, rather than to the bulkier carbon dots.

Thus, these results are consistent with the literature [47, 50, 141, 143], where several authors have recently suggested that the blue emission is related to the presence of small fluorescent molecules synthesized simultaneously to CDs either free in solution or linked to surface of the CDs. While our data clarify that that the blue band is related to a small molecule which can diffuse rapidly in a small volume, but more studies are compulsory to understand the emission mechanism or to find the specific nature of these molecules.

5.2 Carbon Nanodots from Top Down Synthesis

Introduction

In the previous section, the emission mechanism of bottom up CDs was presented. Here, other types of CDs, synthesized by top down approaches, are analysed and their emission mechanisms is unravelled. On one hand, these CDs eliminate the interference from small fluorescent molecules in the study of the emission mechanism. In fact, CDs synthesized by these methods should not affected by the "small molecules" problem considering that during the synthesis they cannot be produced. Besides, our experiments on these dots allowed to perform a comparative optical study on the effects of different core structures (from crystalline to amorphous) and of different surface structure. This investigation helps to understand the nature of electronic transitions, and to disentangle the role of the core from that of the surface. The results highlight that the emission mechanism of the tunable visible fluorescence is identical for crystalline and amorphous samples, indicating the independence of the emission from the core structure.

Furthermore, various surface functionalization weakly influence the emission peak position, but have large consequences on their interaction with the surroundings as suggested by specific experiments which address the influence of metal ions and pH. The tunable visible emission of these dots cannot be specifically attributed to any given kind of surface functional group, and rather appears to involve quasi-degenerate electronic states originating from the high density of different interacting groups on the surface.

Disentangling the role of core and surface structure in CD emission

The samples are synthesized at University of Cordoba by the synthesis procedure described in section 3.1. They are two types of CDs: amorphous CDs named c-CNDs, and crystalline graphitic CDs named x-CQDs where x indicates the passivation of the surface (x can be r=raw, p= rich of carboxylic groups, t= rich of thiol groups, a= rich of amine groups). r-CQDs is the as-synthesized graphitic sample, and does not display any steady state emission. Only after the passivation of the

surface with carboxylic groups (explained in section 3.1), the sample, p-CQDs, shows a tunable emission with a QY of ≈10 %. Thus, the surface groups are compulsory to have an emission. On the contrary, the amorphous sample directly after the synthesis shows a tunable emission with a QY=19 %. The surface of both p-CQDs and c-CNDs is characterized by abundant C=O and -COOH surface moieties, although their surfaces are actually quite complex and –OH and $–CH_3$ contributions can be equally recognized from the FTIR spectra (Figure 5.16).

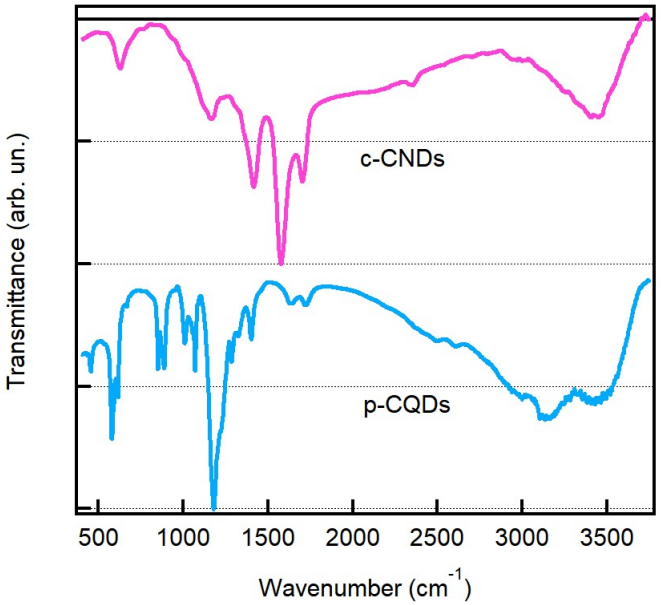

Figure 5.16: IR spectra of carbon-based nanodots with different core: amorphous (pink curve), and graphitic (blue curve) [Adapted from [227]].

The absorption spectrum of p-CQDs and c-CNDs (Figure 5.17) is mostly unstructured and displays no obvious absorption peaks. Both samples show a steep increase of the absorption

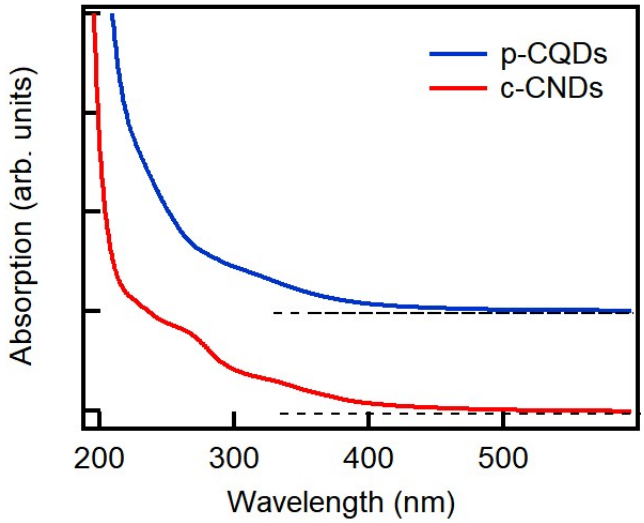

Figure 5.17: Absorption spectra of carbon-based nanodots with different core: amorphous (red curve), and graphitic (blue curve) [Adapted from [227]].

coefficient only below 280 nm (p-CQDs) or 220 nm (c-CNDs), due to the onset of $\pi - \pi^*$ transitions within their sp^2-carbon inner cores. The blue shift of this threshold in c-CNDs, as compared to p-CQDs, suggests a significantly smaller average size of sp^2-domains in the amorphous dots, not surprising because of their disordered core structure. Both samples display a very broad and degrading absorption band in the red, peaking around 330 nm with a long tail down into the visible range. Besides, an additional shoulder around 270 nm, slightly more defined, can be noticed for c-CNDs only.

Both samples display a visible tunable emission which can be excited across a very broad wavelength range spanning from near-UV to visible (Figure 5.18).

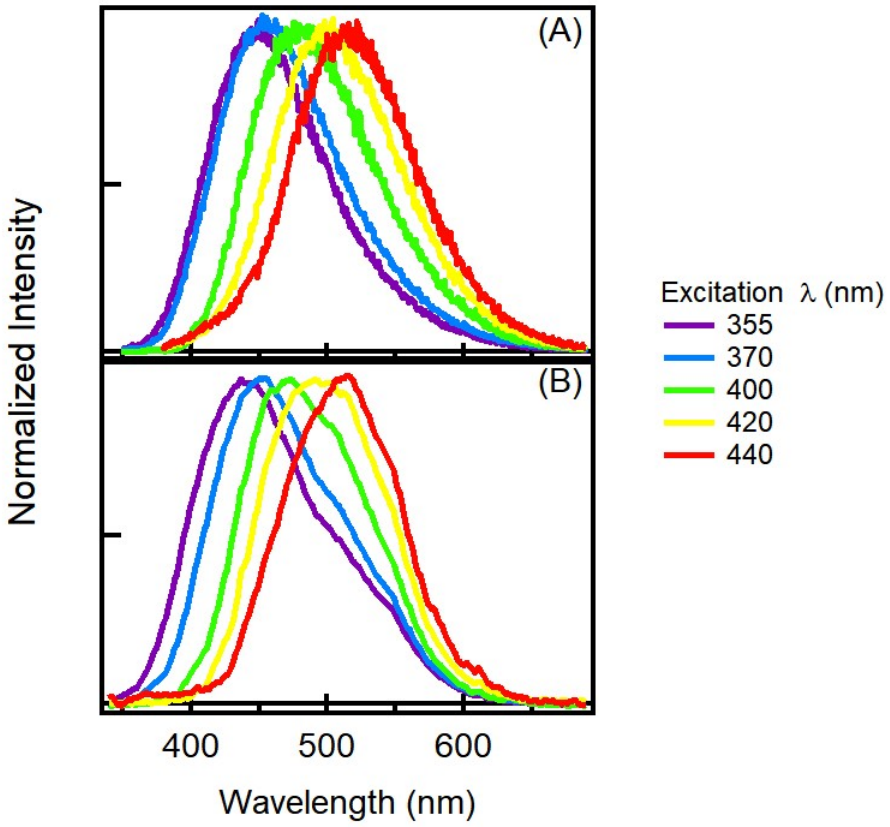

Figure 5.18: Emission spectra of c-CNDs (panel A) and p-CQDs excited at different wavelengths indicated in the legend [Adapted from [227]].

Comparing the steady-state fluorescence excited at 350 nm and 266 nm, which should be two representative spectral positions of the main features observed in absorption, it is evident that the emission from both samples excited in the near-UV are almost identical, and consist of a broad and intense emission band peaking at 450 nm (Figure 5.19a). While these measurements were carried out at pH = 4, very similar spectra are recorded in a wide pH range spanning from 2 to 9 ([5,54]). Exciting at 266 nm the emission at 450 nm is still observed, with very similar characteristics to near-UV excitation, and additionally in c-CND sample it is possible to detect an UV band peaking at 350 nm, which is absent in p-CQDs (Figure 5.19b).

To deeply investigate the nature of the tunable visible transition in both samples, time resolved experiments were performed exciting the samples at 350 nm and at 266 nm. The fluorescence kinetics display a bi-exponential behavior with a short lifetime of 3.7 ns and a slower one of 12.5 ns (Figure 5.20). The similarity of the decays in c-CNDs and p-CQDs, together with the identical

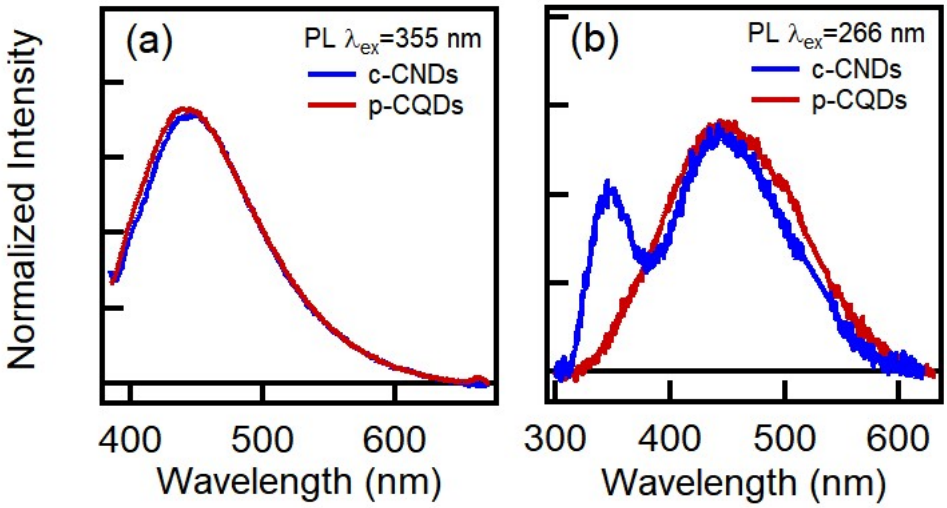

Figure 5.19: Emission spectra excited at 355 nm (a) and 266 nm (b) of carbon-based nanodots with different core: amorphous (red curve), and graphitic (blue curve) [Adapted from [227]].

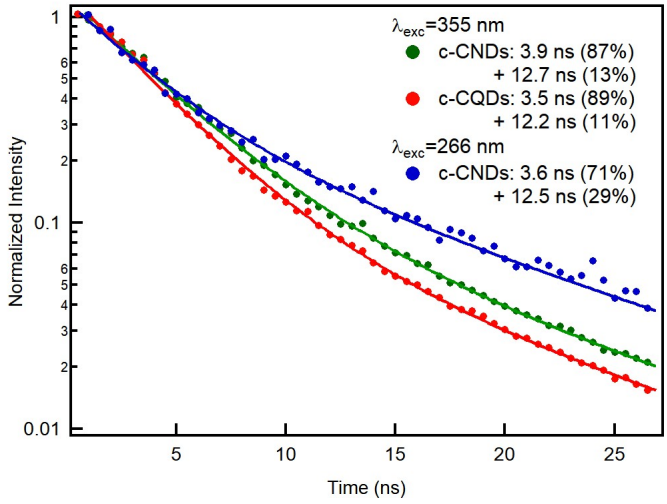

Figure 5.20: Photoluminescence decay kinetics of the emission at 450 nm, as measured in c-CNDs and p-CQDs upon excitation at 355 nm or 266 nm. Experimental data are fitted with bi-exponential decay functions. The fitting parameters are reported in the legend [Adapted from [227]].

spectral shape (Figure 5.19a), conclusively confirms that the origin of this emission has to be the same in both the samples. Thus, the emission process is insensitive to the very different core structure suggesting the association of this fluorescence band to a type of surface transition, or state, common to the two types of dots. The surface localization of this transition is further confirmed by the quenching of the emission provoked by short-range interaction of these dots with metal ions (p-CQDs) or other nanomaterials (c-CNDs) in solution, as demonstrated in previous studies from our collaborating group in Cordoba [5, 54]. Their different response is probably the consequence of different geometrical arrangements of the groups on the surface, and variations of the relative densities between different types of groups allowing, in each case, efficient binding of different analytes through different chemical mechanisms.

Thus, the surface hosts the origin of this emission, but it is still unclear which is the group or which are the groups involved in the electronic transition. To investigate it, the same optical experiments have been performed on samples having exactly the same graphitic crystalline core structure, but passivated with a different moieties on the surface: amine- (a-CQDs) and thiol (t-CQDs) sample. The result of the optical characterization is a very similar emission band (Figure 5.21) in the three samples (similar emission peak, shape of the band and lifetime), despite the change in the functional groups, clearly confirmed by the appearance in the FTIR spectra (Figure 5.22) of the 2506 cm^{-1} vibrational peak of S–H stretching in t-CQDs, and 1675 cm^{-1} ($C{=}O_{amide}$) for a-CQDs.

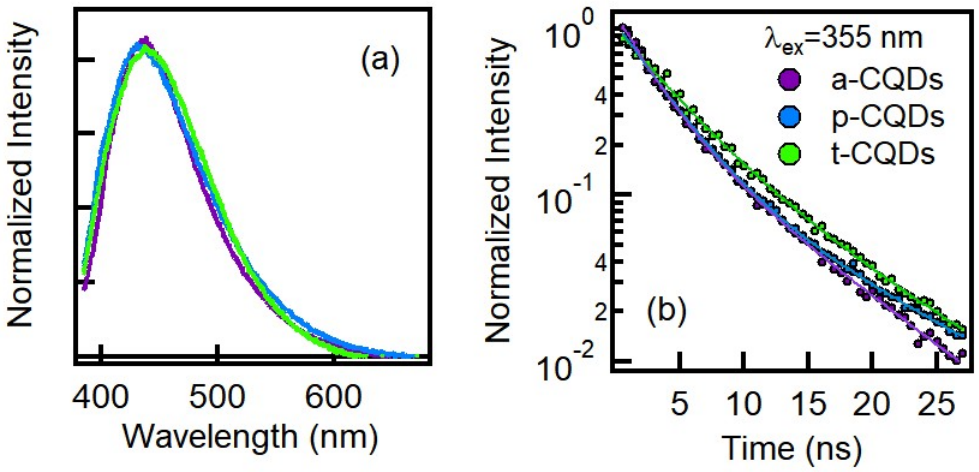

Figure 5.21: Normalized steady-state emission (a) and nanosecond decay kinetics (b) of CQDs with three different surface functionalizations, as excited at 355 nm under identical conditions [Adapted from [227]].

Furthermore, p-CQDs, a-CQDs, and t-CQDs display quite different responses to metal ions (Figure 5.23), probably depending on their different surface affinities to the various functional groups [228].

This finding demonstrates that this fluorescence cannot be associated with a specific kind of functional group, and has to involve different combinations of surface moieties depending on the passivation. On these grounds, we suggest that the electronic wavefunctions involved in the fluorescence transition are delocalized over the entire surface shell of the dots, or a large portion of it, thus involving several different functional groups at the same time.

Looking at Figure 5.19b, co-existing to the main visible emission band discussed so far, the presence of an UV fluorescence is evident when the amorphous dots are excited at 266 nm. An UV emission is quite an unusual finding for CDs which, according to the literature, emit rather ubiquitously in the visible range. Notably, the UV emission is much narrower than the visible band (Figure 5.19b), and can only be excited around 266 nm. In fact, its excitation spectrum roughly matches the absorption shoulder at 270 mn observed only in c-CNDs (Figure 5.24). Based on the fact that it is only observed in the amorphous sample, it seems that such a transition is sensitive to the inner structure of the dots, and the associated chromophore most likely extends somehow into the core. However, a study of the emission as a function of pH value of the solution show that this emission is dramatically sensitive to pH (Figure 5.25). Its lifetime shortens from 8.1 ns to 2.1 when pH increases from 4 to 7, indicating that the chromophore involves surface functional groups within its structure. In particular, the changes observed between pH = 4 and pH = 7 suggest the role of surface COOH groups responding to such a pH variation. Therefore, this UV-band

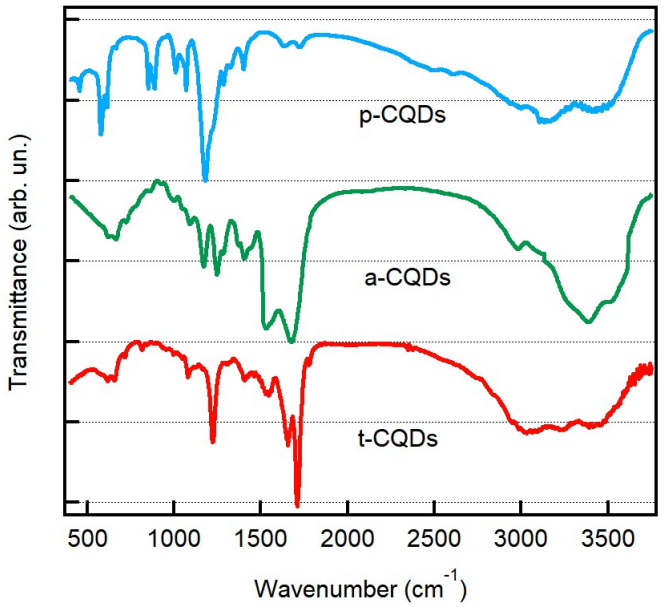

Figure 5.22: IR spectra of carbon-based nanodots with different core and superficial functional groups [Adapted from [227]].

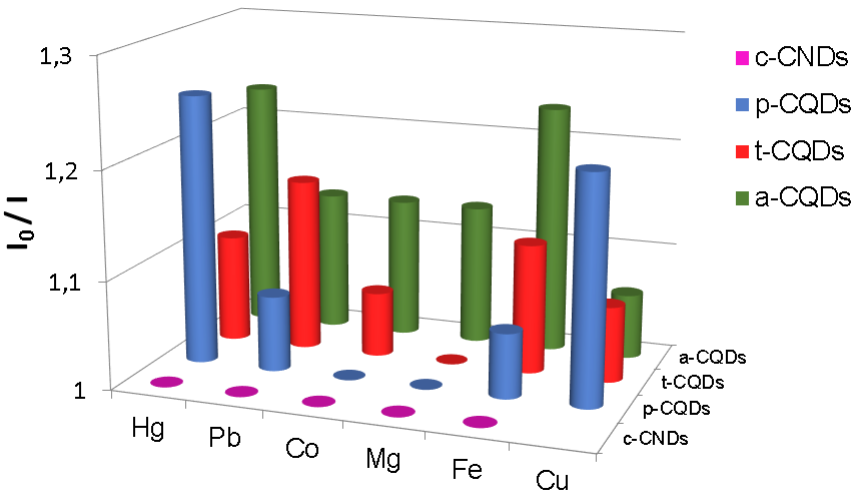

Figure 5.23: Sensing behavior of different subtypes of CDs towards a variety of metal ions (Hg^{2+}, Pb^{2+}, Co^{2+}, Mg^{2+}, Fe^{2+}, Cu^{2+}). The degree of quenching (I_0/I) is reported on the vertical axis as a function of the type of dots and metal ion [Adapted from [227]].

is tentatively associated to localized molecular-type chromophores on the surface with carboxyl ends.

5.3 Conclusions

In summary, we investigated various sub-types of CDs characterized by different synthesis routes, core structure and surface structure. All of our results show that the emission mechanism is widely variable and largely depends on the specific characteristics of the sample.

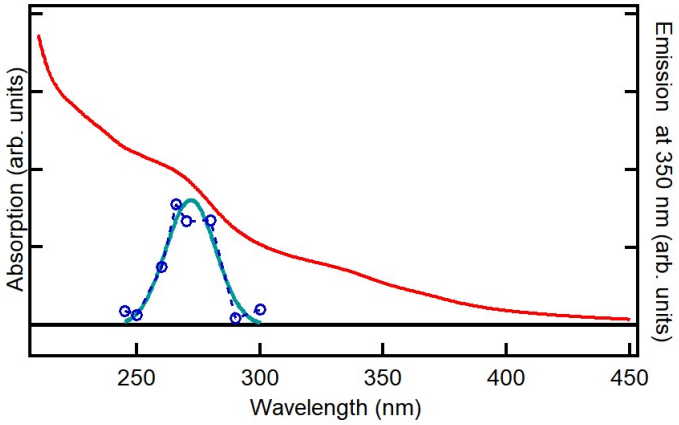

Figure 5.24: Excitation spectrum of the UV emission at 350 nm (blue dots) observed in c-CNDs and a fit as a guide to the eyes, as compared to their absorption spectrum [Adapted from [227]].

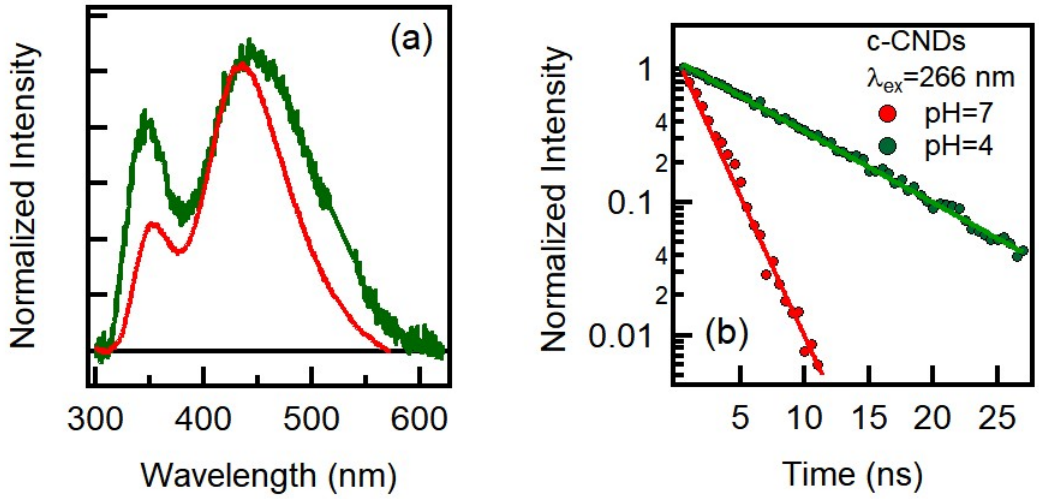

Figure 5.25: (a) Normalized steady-state photoluminescence observed from c-CNDs at pH = 7 (red) and pH = 4 (green) and (b) their decay kinetics fitted by single-exponential functions. Data around 532 nm were removed because of the distortions by the second order of the pump wavelength [Adapted from [227]].

We compared various types of CDs: carbon dots obtained by top-down synthesis routes, allowing to control the core structure from amorphous to graphitic, samples with a N-doped graphitic core structure, obtained by bottom-up routes, and a special type of CD with a $\beta - C_3N_4$ core structure, first reported by this work. These three sub-types of CDs are found to emit through different fundamental mechanisms. However, a very general finding of our study is that the emission mechanism involves only the surface structure of any of these dots, or, in particular cases, involves a coupling between core and surface. Therefore, surface states are found to be always crucial, ruling out the role of a quantum confinement effect and claimed with some works [27, 133, 136].

Here, the emission mechanisms associated to different electronic transitions of CDs were unravelled by various investigation methods. In particular, with a solvatochromic approach, it was

possible to disclose the emission mechanism of the visible tunable band in $\beta - C_3N_4$ nanodots. Its excited state is very sensitive to changes in the polarity of the solvent and, in particular, it is strongly affected by the presence of hydrogen bonds. Thus, the electronic transition is modelled as involving a coupling between core and surface. The photo-excitation provokes an electron transfer from the core to localized states on the surface, and the fluorescence stems from the radiative recombination of this electron with the hole left in the core.

CDs produced by bottom-up routes display also a blue emission peaking at 440 nm, which, instead, is not associated with the entire dot. In fact, photobleaching and recovery data suggest that this type of emission stems from an electronic transition which involves small molecules generated as side-products of CDs through these synthesis protocols, confirming many findings in the literature [47, 50, 141, 143].

Last but not least, we demonstrate that amorphous and graphitic CDs synthesized by top down methods emit fluorescence through another, fundamentally different mechanism. In fact, despite they show a different core structure, the tunable emission is very similar (emission peak and lifetime) in the two samples, suggesting that the emission entirely comes from the surface corona, with no involvement of the core. Indeed, surface passivation is found to be necessary to have an emission.Most importantly, we also found for the first time that passivating graphitic CDs by various types of surface groups does not change the main spectroscopic characteristics of the emission. This result leads to propose a model in which the chromophore is not sufficiently localized to be associated to only one type of functional groups but comes from a large part of the surface which encompasses several types of groups.

Chapter 6

The Photocycle of Carbon Dots

After steady-state and nanosecond-resolved studies have allowed (chapter 5) to formulate several hypoteses on the emission mechanism of different types of CDs, an ultrafast approach is mandatory to investigate in more detail the photocycle of CDs, in order to observe and study phenomena which can occur on a ps or sub-ps time scale.

Both bottom up and top down samples have been investigated here by ultrafast approaches. In the case of $\beta - C_3N_4$ dots, the information gained by ultrafast experiments allowed to fully unravel the photocycle down to the femtosecond time scale. In the case of graphitic dots described in section 5.2 (N-doped or not), ultrafast experiments allowed to disentangle the role of the core and of the surface in the emission mechanism, ultimately addressing the role of surface passivation.

6.1 The Photocycle of N-rich Bottom Up CDs

Introduction

To investigate the physics of photoexcited $\beta - C_3N_4$, femtosecond transient absorption and fluorescence upconversion techniques (chapter 3) have been used. Dispersions of CDs were photoexcited at 400 nm and 270 nm to study the so-called visible band, and at 350 nm which allows to photoexcite the so-called blue band. The photocycle of the visible emission has been entirely unravelled by the combined use of polarization-resolved transient absorption measurements and fluorescence upconversion experiments. On the contrary, the photocycle of the blue band remained unclear because of the complexity of the signal.

The photocycle of the visible band

TA data of an aqueous solution of CDs excited at 400 nm in magic angle (MA) polarization condition are reported in Figure 6.1a, and in Figure 6.1b-c representative spectra have been extracted from panel a. The so-called MA configuration corresponds to a relative angle of 54.7° between the linear polarization of pump and probe beams . It can be shown that these experimental conditions allow to have a signal which does not contain influence of rotational diffusion but reflects the pure population dynamics [178].

Based on the results of chapter 4, the steady-state emission of $\beta - C_3N_4$ excited at 400 nm essentially consists in what we have named the visible fluorescence (here peaking in the green), and a small contribution from the blue band, peaking around 420 nm. These observations provide a good starting point for the interpretation of the TA data. Considering this and looking at the TA spectra in Figure 6.1b-c, three contributions to the signal are well recognizable: i) a negative contribution around the pump wavelength, mostly due to ground state bleaching (GSB) associated with

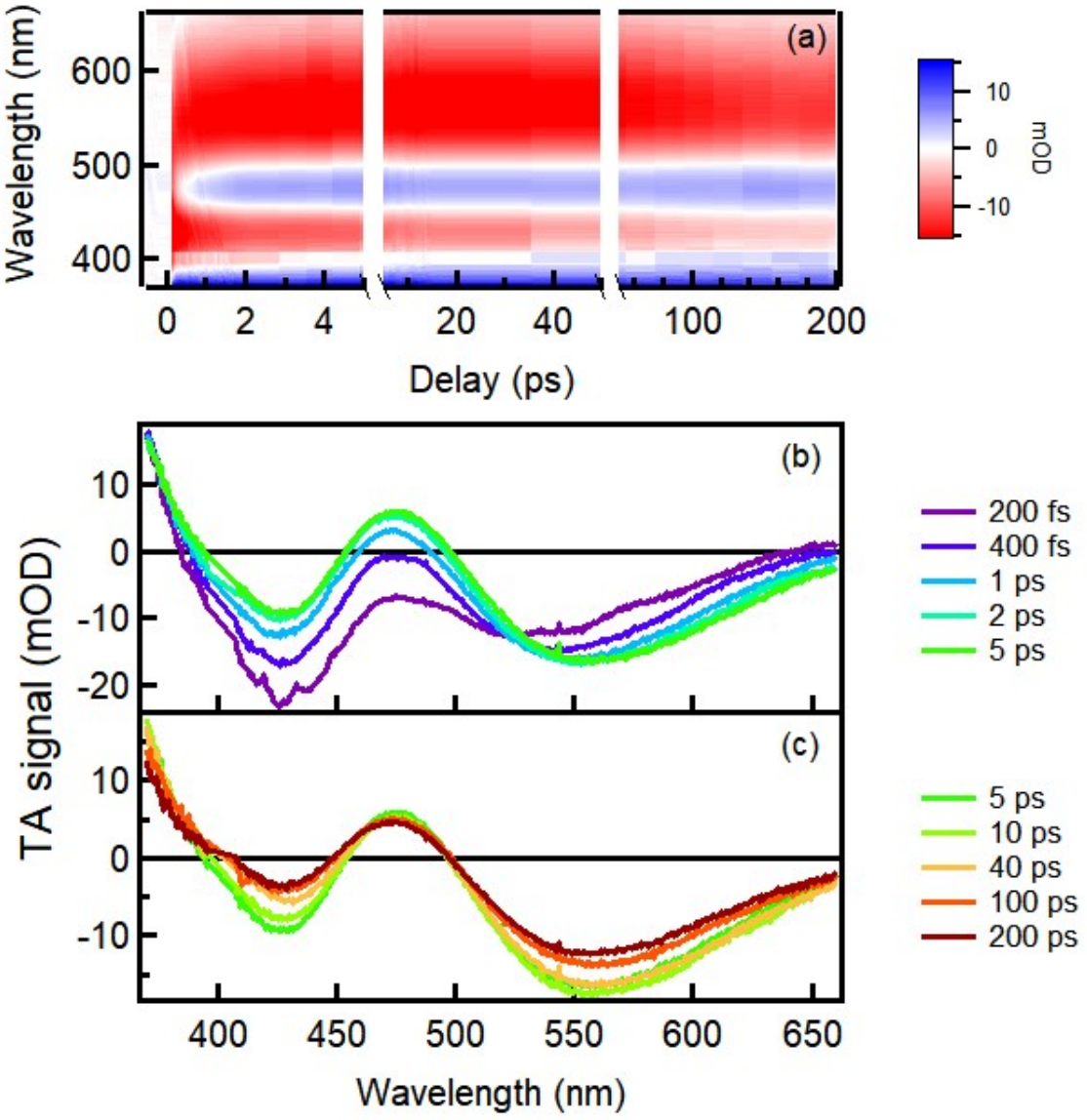

Figure 6.1: (a) Transient absorption 2D-plot of an aqueous solution of CDs excited at 400 nm. (b) and (c) Transient absorption spectra of CDs recorded at various time delays after photoexcitation, as obtained by vertical cuts of the 2D-plots in panel (a). Data between 388 nm and 405 nm were removed because of distortions by pump scattering around 400 nm.

the depopulation of the ground state via photo-excitation, probably combined with a stimulated emission due to a fluorescence signal peaking at 420 nm (the blue band of these dots, described in chapter 4); ii) a strong stimulated emission (SE) in the green (520–550 nm), corresponding to an ordinary fluorescence signal of the visible emission band of these dots (chapter 4) except for its negative sign. In fact, the spectral features of this signal are consistent with the steady-state visible fluorescence excited at 400 nm; iii) several positive excited state absorption (ESA) signals, at $\lambda < 400$ nm, $\lambda \approx 470$ nm and $\lambda > 600$ nm, respectively, due to electronic transitions from the excited state towards higher excited states.

Looking at the spectral range around the pump wavelength, the negative signal decays rapidly in less than 5 ps (Figure 6.1b) and, then, the signal is almost constant in the range of several

hundreds ps (Figure 6.1c). Considering that exciting at 400 nm, beyond the visible emission, this sample displays a blue emission peaking at 430-440 nm, it is reasonable to interpret this negative signal as the superposition of a SE (associated with the blue band) and a GSB (associated with the visible band). To disentangle the behaviour of these two contributions to the overall dynamics, it is necessary to look at the dynamics of the green SE at 520-550 nm, which is fairly isolated and easier to interpret. The SE signal in Figure 6.1b is present since the time zero and it seems to undergo a small intensity increase in the first few ps, and simultaneously a redshift. This shift is compatible with solvation dynamics of water which, as already shown in the previous chapter, redshifts dramatically the emission. Considering that this SE undergoes essentially no decay, we can conclude that the system is still in an excited state for the entire duration of the measurement. Therefore, no decay of the GSB is expected in the same time range, because the GSB at 400 nm is associated to the same transition, that is the green-emitting chromophore. Thus, the decay of the negative signal around 400-440 nm in Figure 6.1b is hardly due to the GSB contribution, and should mostly stem from a fast decay of the Blue band which covers the GSB. After 5 ps, the signal should be interpreted as a pure GSB which represents the depopulation of the ground state after the photo-excitation. Simultaneously to the decay of the blue SE, the ESA signals at 470 nm and at 680 nm decay. This suggests that these ESAs are associated with the same chromophore responsible of the blue optical activity.

All the interpretation is supported by comparing the dynamics with another solvent, and by an SVD analysis which allows to decompose all the time-wavelength data into a minimal number of spectra (DAS) each undergoing an exponential decay with different time scale, and by fluorescence upconversion measurements (FLUC).

The data were spectrally decomposed into four DAS with lifetime 0.2 ps, 2.1 ps, and several nanoseconds (Figure 6.2). DAS1 and DAS2 (0.2 and 2.1 ps) fundamentally describe the redshift of

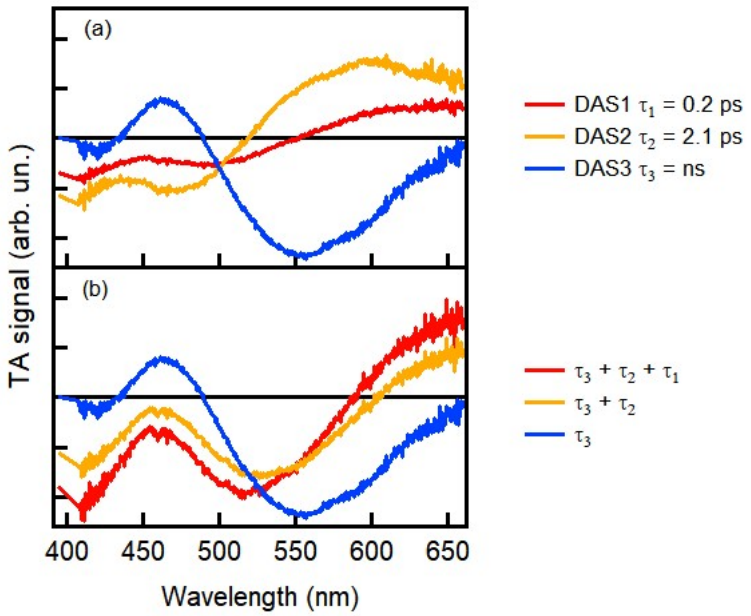

Figure 6.2: (a) Decay-associated spectra (DAS), and the respective characteristic times, as obtained with a global analysis by the SVD method of the TA data in Figure 6.1 describing the dynamics. (b) Sums of DASs which represent spectra after each time associated with the single DAS.

the green SE (derivative-like shape), the simultaneous decrease of the negative signal at 420 nm and the disappearance of the ESA signal at long wavelengths. DAS3 describes the decay of the

entire signal with a timescale of several nanoseconds, hence describes the nanosecond long-lived signal, fully consistent with the observation of this band in steady-state measurements (chapter 4) excited at 400 nm.

Overall, one aspect of these data is a small, but appreciable contribution of the blue fluorescence (SE at 420 nm), which disappears within a few ps. Because the excitation peak of the blue fluorescence is located around 350 nm (see chapter 4), the photocycle of this chromophore will be discussed in some more detail in the next paragraph, where TA data excited at 350 nm are analyzed. In the rest of this paragraph we will discuss the main contribution to the signal in Figure 6.1, which is due to the visible fluorescence.

The redshift of the green SE which occurs in 0.2+2.1 ps matches a solvatochromic relaxation. In order to check this aspect, the same measurements have been conducted on a solution of CDs in ethanol which shows different (slower) solvation time scales than water. The main results are

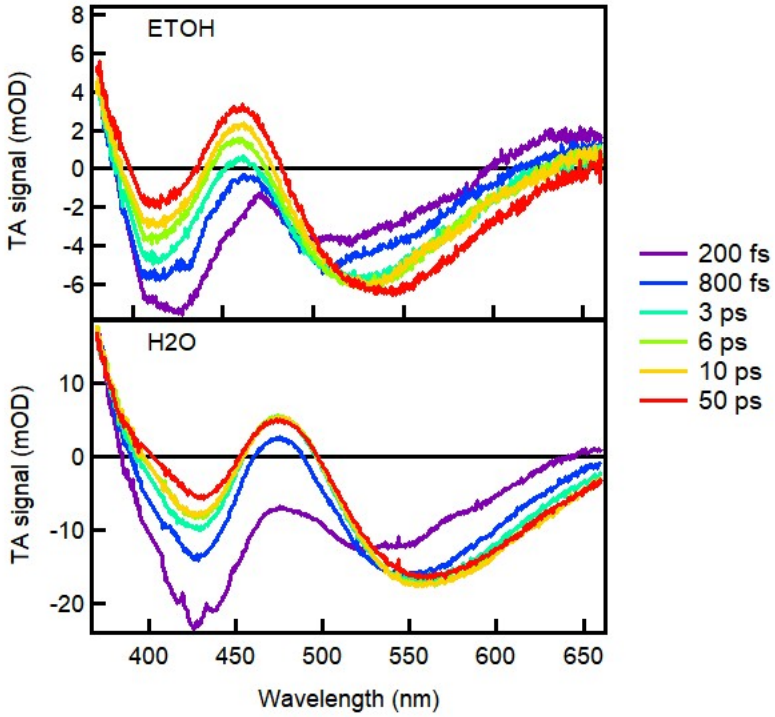

Figure 6.3: TA spectra at different delay time after the photoexcitation of CDs in water and ethanol.

shown in Figure 6.3 and 6.4 where some spectra at different delays and kinetics at 550 nm are compared. The shift of the SE signal is due to solvation relaxation as it is suggested by the time constants obtained by fitting the kinetics at 550 nm with a multi-exponential function (Table 6.1), and it ends in few picoseconds. In Figure 6.4, this shift appears as a rise of the TA signal intensity because the kinetic trace was taken at a wavelength on the red side of the fluorescence band, where the signal grows due to a redshift. Similar results have been reported in other recent works [161]. Other works obtain different results [146, 229]. Khan et al. [146] detect a very slow solvation process in the nanosecond range. Strauss et al. [229], despite the emission and its dynamics is slightly different in various solvents, do not explain the variation as due to solvent relaxation but, on the contrary, relate it to solvent-controlled population of the excited state, which lasts ten of ps. Instead, here we find that the population of the excited state is instantaneous with the photoexcitation of the system, as in other works [165].

To separate the emission contribution from the rest of the signal, FLUC measurements with

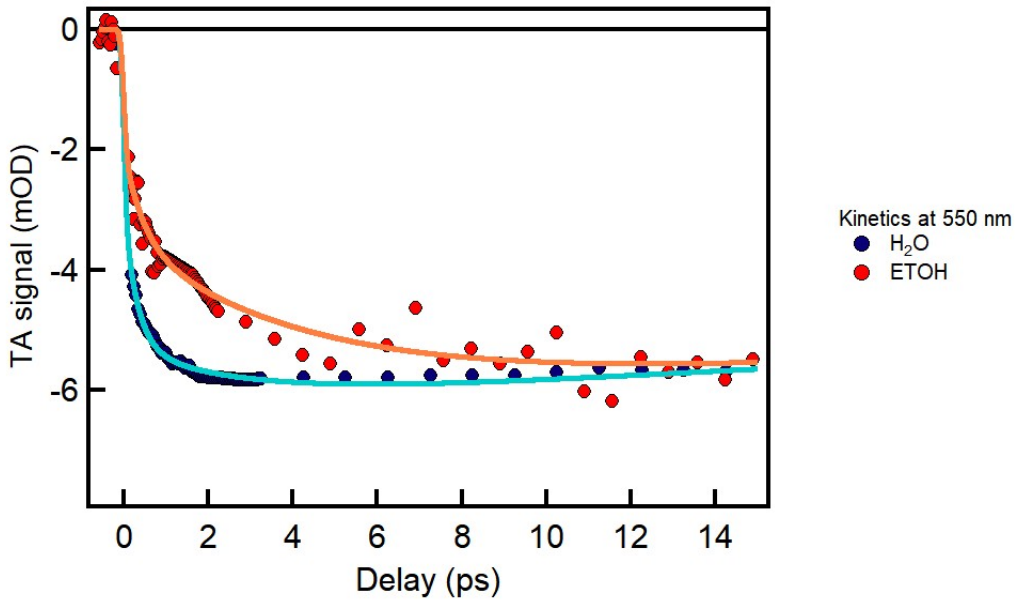

Figure 6.4: Kinetics at 550 (SE peak) of CDs in water and ethanol with the corresponding fitting function.

Solvent	τ_1 (ps)	τ_2 (ps)
H_2O	0.19 $\pm$0.05	2.1$\pm$0.1
ETOH	0.4 $\pm$ 0.1	4.5 $\pm$0.1

Table 6.1: Summary of the characteristic time scales of the kinetic of CDs in water and ethanol as obtained by the fitting procedure.

single-wavelength detection have been performed on solution of CDs in water (Figure 6.5). The

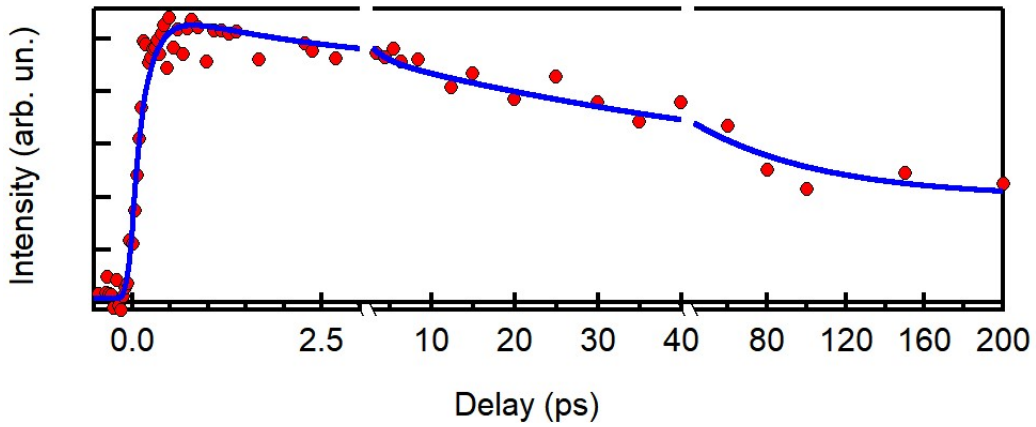

Figure 6.5: Kinetics trace at 550 nm of CDs in water from Fluorescence upconversion experiments and the least-squares fitting curve.

kinetic of the emission at its peak (550 nm) has been recorded and it shows that the signal is present from the time zero as already found in TA, ruling out the presence of any rise. This finding

demonstrates that the excited state which produces the steady state emission is directly populated after photoexcitation, meaning that the visible band is simply the inverse transition of the OA band peaking at 400 nm. This kinetic traces has been recorded in parallel configuration. This adds a new time scale to the dynamics which will be better analyzed in the anisotropy transient absorption measurements. In any cases, the time scales obtained by the fitting procedure are in good agreement with those obtained in the TA analysis.

In addition, anisotropy transient absorption measurements at 400 nm were performed on solution of CDs in water. The anisotropy study provides supplementary information on relative orientation of the transition dipole moments for absorption and emission, which can lie along different directions within the fluorophore structure and, in this case, on the dynamics and mobility of the photoexcited electron.

Performing these experiments, it turns up that the anisotropy value of SE signal in water at time zero is 0.4, but then decrease to 0 in 200 ps (Figure 6.6). Fitting the anisotropy kinetics at 540

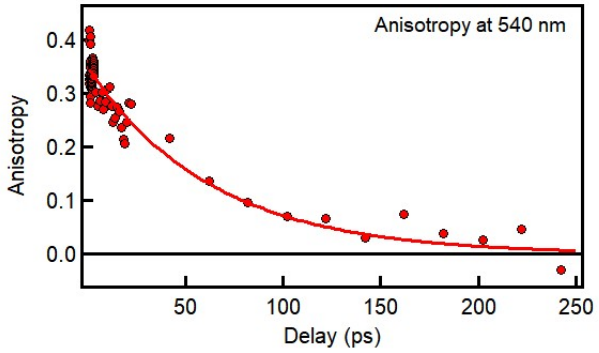

Figure 6.6: Kinetics of anisotropy at 540 and the least-squares fitting curve.

nm with single exponential decay returns a time constant of τ=60 ps $\pm$ 5. Such type of depolarization is typically observed for fluorescent molecules due to their rotational diffusion after photoexcitation. However, the time constant of 60 ps we find here is too fast to be consistent with the effect of rotational diffusion of the entire dot, much bulkier than a typical molecular fluorophore. In fact, by Perrin equation [178] it is possible to estimate that the time constant for the rotational diffusion of a dot with a diameter of 6 nm is cca 20 ns. Similar results on anisotropy are shown in other works [161, 167], where the depolarization time of CDs in water is in sub-nanosecond range. Despite the similar time constants, the interpretation of the data or remains unclear [167]. To explain our results, here we propose that the migrated electron on CDs surface has the possibility to move around the surface by, for instance, thermal hopping or tunnelling across the surface, randomizing the initial orientation. This suggests the degeneracy of several energy levels on the surface of the dots which allows the mobility of the electron across the surface.

To have a deeper understanding in the photocycle, additional pump probe experiments have been performed on the aqueous solution of CDs exciting at 270 nm (MA conditions). This wavelength corresponds to a further peak in the absorption profile and to the second peak of green band excitation spectrum showed in chapter 4 in Figure 5.9. Furthermore, the energy gap of the bulk $\beta - C_3N_4$ is 3.5-4 eV [224], and considering the small size of the system, the gap may be higher because of quantum confinement effects. Thus, exciting at 270 nm means exciting at 4.6 eV which probably corresponds to an excitation of the core. Therefore, it is interesting to find out the mechanism by which the green band is populated upon the initial photo-excitation of these higher-lying states, likely involving the core.

The overall TA signal is similar to the one obtained at 400 nm excitation (Figure 6.7) with slight differences. In particular also in this case, the SE signal at long time delays (200 ps in Figure 6.8)

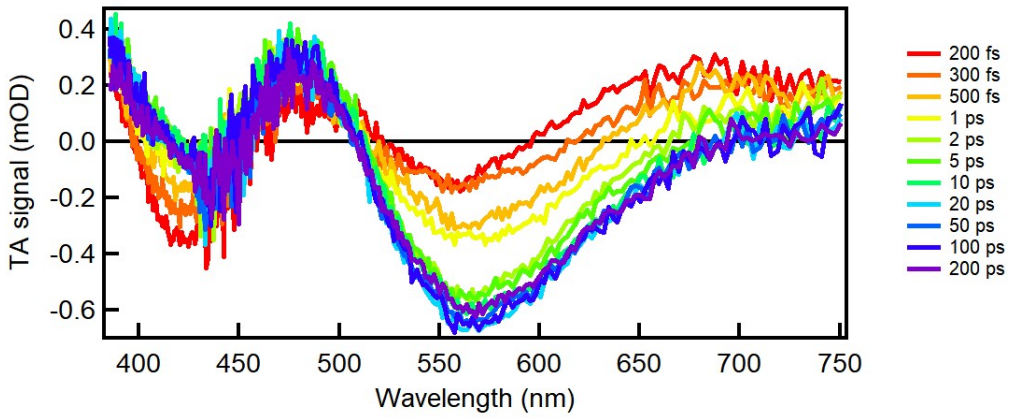

Figure 6.7: TA spectra of CDs in water excited at 270 nm after various delays after the photoexcitation.

overlaps with the SE signal excited at 400 nm, proving again that the photo-excited transition is a higher transition leading to the same emission. However, there are two important differences

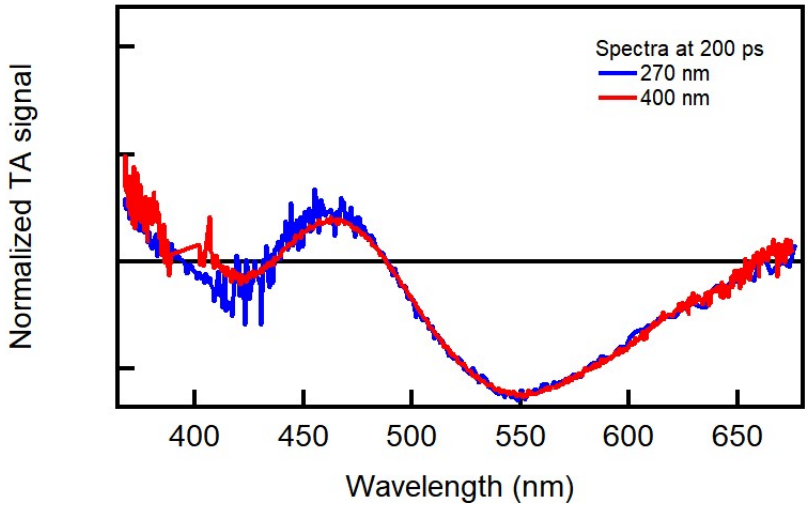

Figure 6.8: Comparison between the TA spectra at 200 ps excited at 400 nm (red curve) and 270 nm (blue curve).

with respect to the case of 400 nm excitation. First, solvation is almost absent in 270 nm data respect to the 400 nm data as it is shown in Figure 6.7, as from the absence of any dynamical Stokes shift in the data. Second, another difference between the two experiments is the slow rise of the SE lasting 1.2 ps as extracted by a fitting procedure of the kinetic at 550 nm (Figure 6.9), whereas at 400 nm there is no rise of the SE, as demonstrated both by the TA data (Figure 6.1) and by the FLUC kinetics (Figure 6.5). These data indicate that the emissive state is directly populated by excitation at 400 nm, whereas the population of the same state takes place only after a 1.2 ps delay if the dots are initially photo-excited at 270 nm. If the photo-excited state is the higher state of the same transition excited at 400 nm it would expect a fast internal conversion within 100 fs. In fact, molecular internal conversion typically occurs well within 100 fs [230], in contrast with our data, which demonstrate that the rise of the SE is much slower (1.2 ps). Therefore we proposed a different interpretation. In our model when CDs are excited at 270 nm, core states

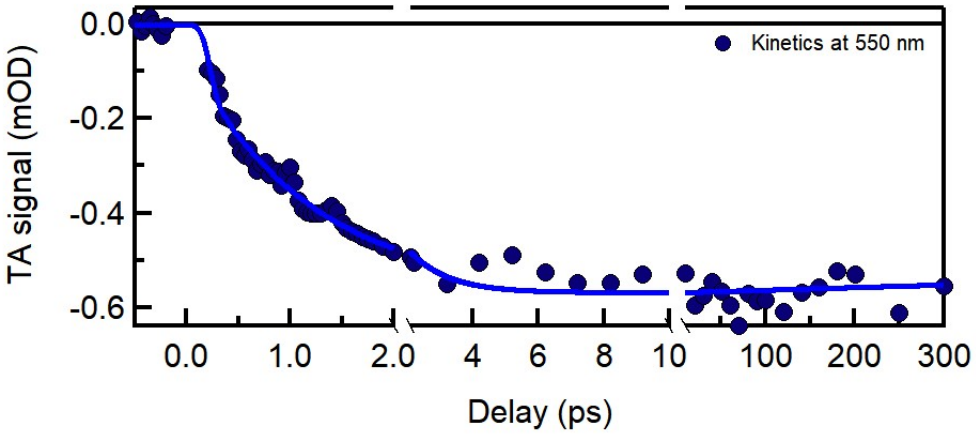

Figure 6.9: Kinetics trace extracted from Figure 6.7 at 550 nm with the least-fitting curve.

inside the dots are initially involved, after which a charge separation occurs inside the core, and an electron is transferred to a surface state forming the charge-separated state responsible of the green fluorescence (chapter 5). In this vision, while the core is transferring the electron to the surface in 1.2 ps, the solvent has the time to adiabatically reorganize itself. The major part of solvation is, in this case, a rate limited process (it should last 0.19 ps as already mentioned) hidden by the slow electron transfer from the core to surface. After the electron is on the surface, it can recombine radiatively with the positive charge left in the core. This result suggests again a strong coupling between core and surface where the core transfers the excitation in 1.2 ps to surface state. This time scale is quite slow with respect to other works in the literature [21] where a similar transfer was proposed to occur in 400 fs. In any case, although many works proposed CD transition as occurring through the initial photoexcitation of the core and the following excitation transfer to the surface [21, 70, 71, 133, 229], only one directly detects this phenomenon [229], as in our case, as a rise of the stimulated emission related to the surface fluorescence, even if the time scale is slower than our findings.

Summarizing the results obtained by several spectroscopic techniques on the fluorescence visible band, it is possible to describe it as the transition of the absorption band peaking at 400 nm. The entire dynamics of this optical activity, after it is directly excited at 400 nm, can be described as a simple solvation (occurring in 0.21 and 1.9 ps time scales in water) from the very initial photoexcitation. This establishes that there is not a sub-nanosecond depopulation of the excited state bringing the loss of the quantum yield in the nanosecond regime as demonstrated in chapter 5. This excited state can be modelled, as already mentioned in chapter 5, as a charge-separated state coupling the core and the surface. From the presented femtosecond study, it is possible to affirm that this charge separation is instantaneous with the photo-excitation at 400 nm. Besides, from anisotropy-resolved TA we found that the electron on the surface is mobile by hopping (thermally or by tunnelling process) through a manifold of quasi-degenerate surface states. Exciting at higher energy produces the same result (an electron exposed to the solvent) but, in this case, the electron is initially born in the core and, only after that, is transferred on the surface. In this case, no solvation is observed because solvent rearrangement follows adiabatically the electron transfer from the core to surface.

The photocycle of the blue band

As mentioned in the introduction of this chapter, the photocycle of the blue band has been investigated by TA measurements, but further experiments are needed to unravel it. Despite of this, it is worth making some considerations on the collected data.

TA measurements in MA condition at 350 nm (Figure 6.10) have been performed on aqueous solution of $\beta - C_3N_4$ and of N-doped graphitic sample (N1 in section 4.2) . Both samples, in fact, display similar absorption (peak at 340 nm) and emission features when excited at 330-350 nm. Thus, as already discussed in the previous chapter, our hypothesis is that the blue band is related to the same molecular species in both samples.

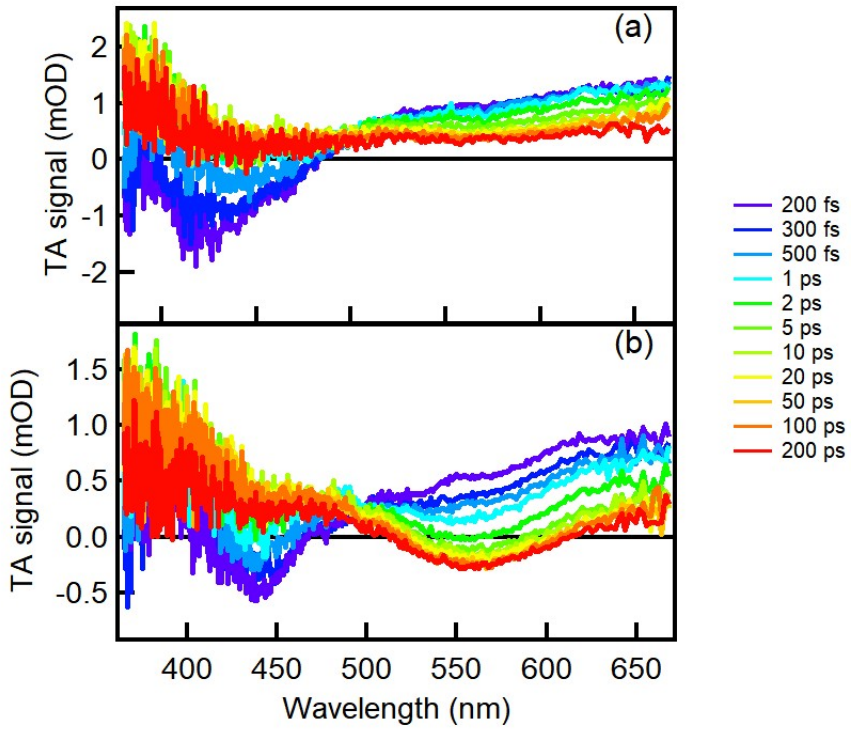

Figure 6.10: TA spectra of (a) N-rich graphitic CDs and (b) $\beta - C_3N_4$ in water excited at 350 nm at different delay after photoexcitation.

Indeed, the TA signal observed upon photo-excitation at 350 nm is similar in both samples. There is a negative signal (SE) peaking at 420 nm and an almost flat ESA which covers the entire explored spectral range (380-670 nm). Both the signals decay: the SE decays with two time scales, 0.4 ps and 1.70 ps, time constants obtained by a fitting procedure, and the ESA decays in 4.5 ps plus a long-lived component. Considering that in the steady state experiments it is possible to detect the blue emission, the SE associated to the blue band is not expected to disappear on a sub-nanosecond time scale. Therefore, the disappearance of the blue SE should be attributed to the growth of a positive signal (ESA) at 440 nm which completely covers the SE. In both samples, the measured signal and its dynamics are very similar, except for the presence of an additional contribution in the case of $\beta - C_3N_4$, which is the SE related to the green band as displayed in Figure 6.10.

Despite the photocycle is not yet clear, these results suggest two ideas: i) on one hand, the similarity of the signal in both samples suggests that the excited transition is the same in both CDs and, considering the results for the blue band reported in chapter 5, it is possible to suppose

the formation of fluorescent molecules during the synthesis of both the samples; ii) on the other hand, a flat ESA, beyond covering the rest of the signal, is usually related to electronic transitions towards a continuum as the transitions of free charges in the conduction band of the material. Therefore, the data provide evidence of a photo-generation of conduction electron, which may occur through an electron injection from the adsorbed molecules on CD surfaces to the conduction band.

More experiments will be required to clarify it, such as fluorescence upconversion experiments exciting at 350 nm, and 2-Dimensional transient absorption measurements.

6.2 The Photocycle of Top Down Graphitic CDs

Introduction

As already mentioned in chapter 1, the respective roles of the surface and of the core in the photocycle of CDs are not clear. Several authors demonstrated the need of passivating the surface of nanoparticles to obtain an efficient emission [16] and it is not yet clear if the passivation introduces new surface emitting states or if it stabilizes existing states making them fluorescent. Moreover, it is not clear if the photocycle and fluorescence involves the entire dot, in the sense that the photoexcitation excites the core of the dot which transfers the excitation to the surface [133, 138], or if the photoexcited state involves only part of the surface [1,9,137]. To shed a light on these questions, we investigate by an ultrafast approach the photocycle of the graphitic CDs analyzed in section 5.2. In particular, we chose to compare the properties of p-CQDs sample (graphitic core passivated by carboxylic groups) to its *raw*-version (without any passivation, named r-CQDs) demonstrating which is the role of the passivation on the emission mechanism.

The role of passivation of the surface investigated by ultrafast approaches

r-CQDs are the dots retrieved immediately after the top-down synthesis described in section 3.1, which, as-synthesized, do not display any steady-state emission. To have emissive CQDs it is necessary, as already mentioned in the previous chapter, to passivate the surface of the dots with different functional groups.

Infrared absorption spectra confirm that the passivation of the surface occurred (Figure 6.11b). In fact, r-CQDs shows a single and narrow absorption band at 3460 cm^{-1} for vibration of isolated -OH, which may be associated to the stretching vibration of non-hydrogen bonded hydroxyl groups. After the passivation of the surface by acetone, p-CQDs show broad bands at 3431 cm^{-1} and 3136 cm^{-1}, associated with hydrogen bonded OH from carboxyl and hydroxyl groups. Besides, passivated sample displays peaks associated to -CH (2995 cm^{-1}) and to -C=O vibrations of carboxyl groups (1710 cm^{-1} and 1644 cm^{-1}). These changes in the FTIR spectrum are the sign of a succesful passivation, which introduces a high density of carboxylic and hydroxyl groups on the surface of p-CQDs, with respect to r-CQDs.

The absorption spectra of aqueous solutions of raw and passivated CQDs (r-CQDs and p-CQDs, respectively) are compared in Figure 6.11a. Both spectra present an intense and similar absorption below 270 nm which grows at shorter wavelengths. Considering that the core of both r-CQDs and p-CQDs is the same (in fact, the passivation does not modify the core), as already suggested in section 5.2, the absorbance at high energies probably corresponds to electronic transitions related to the core of the CDs. At longer wavelengths, the absorption spectra display different profiles, probably related to surface states. In fact, the p-CQDs display very broad band (barely visible from the shoulder at 300 nm) which excites the tunable emission displayed in Figure 6.12, which we already attributed to the surface in section 5.2, and the r-CQDs absorption shows two

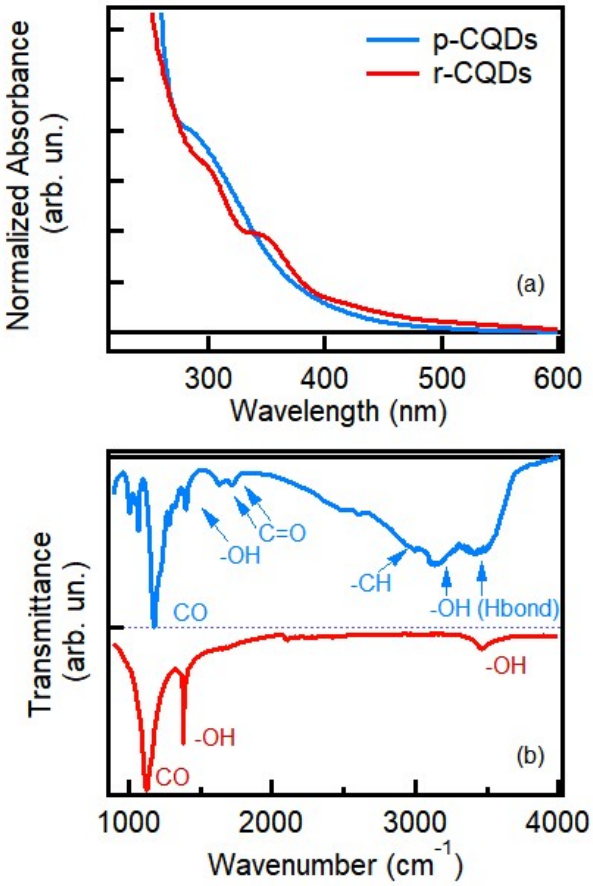

Figure 6.11: (a) Normalized absorption spectra of aqueous solution of r-CQDs (red curve) and p-CQDs (blue curve). (b) IR spectra of r-CQDs and p-CQDs.

more defined bands peaking at 300 nm and 350 nm which probably correspond to non-emitting surface states, considering that r-CQDs are non-fluorescent.

The emission band of p-CQDs photoexcited at 400 nm peaks at 470 nm and the QY is about 4%. To investigate the electronic transition involved in the emission from the initial photo-excitation, we performed fluorescence upconversion measurements. The fluorescence is observable from the very earliest times after photoexcitation as it is displayed in Figure 6.13 demonstrating that the emitting state is populated in a very short time (below experimental time resolution $\approx$ 70 fs). This suggests the direct population of a surface state avoiding the involvement of a core which would transfer the excitation to the surface in a longer interval of time as in the previous paragraph. By FLUC experiments, the direct population of surface state has been already detected in other CDs [165] confirming our results. The dynamics appear to be essentially independent of the emission wavelength, and essentially consist in a strong decaying signal at all wavelenghts. Beside the strong decay, a closer inspection of the traces reveals a fast redshift (150-200 fs), where the decay in the blue region correlates with a rise in the red region, which can be tentatively associated to solvation.

To increase the signal-to-noise ratio, the kinetics at different wavelengths have been averaged and analyzed by least-squares fitting with multi-exponential function. The averaged kinetics with the fitting function are reported in Figure 6.14. The trace can be reproduced by a rise with time scale of 0.18 ps, and 4 decays with different timescales: τ_1 =0.3 $\pm$ 0.1 ps, τ_2 =2.5 $\pm$ 0.1 ps, τ_3 =70

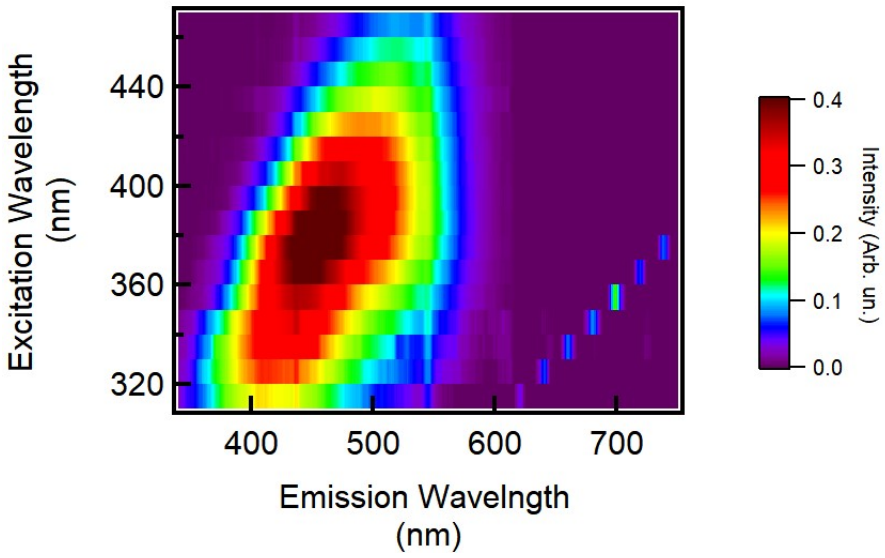

Figure 6.12: 2D excitation-emission fluorescence maps of p-CQDs.

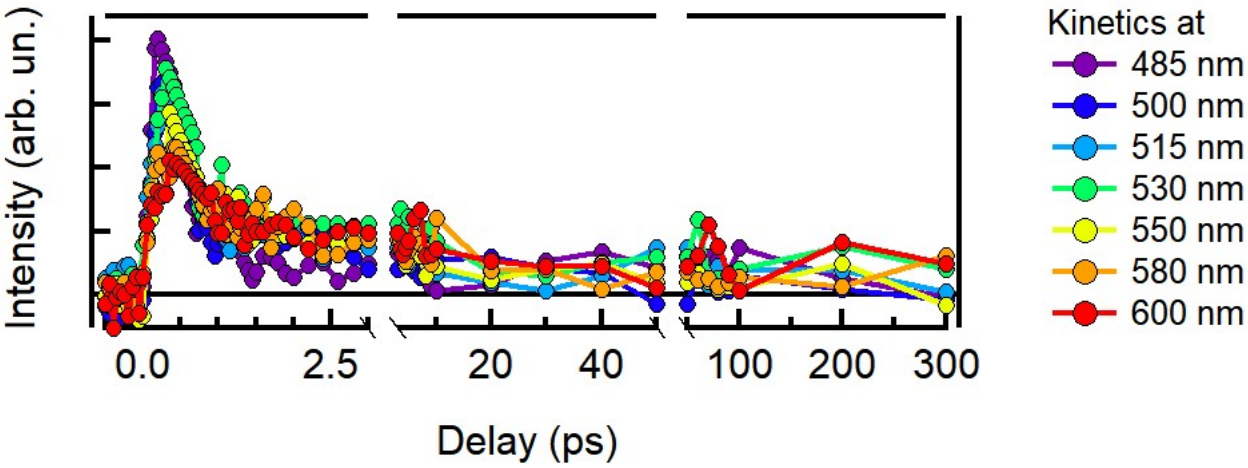

Figure 6.13: Kinetic traces recorded in a fluorescence upconversion experiment at different emission wavelengths of an aqueous solution of p-CQDs excited at 400 nm.

$\pm$ 10 ps and $\tau_4 > 1$ ns, as reported in Table 6.2.

The four decays describe the multi-exponential depopulation of the photoexcited state until the formation of a long-lived state which only accounts for 2-4% (the amplitude of the longest component) of the initial population. The agreement between the results of ultrafast and steady state techniques suggests not only that the photoexcitation involves a single transition, which, in this particular case, affects only the surface of the dot, but also that all the non-radiative losses occur in the sub-nanosecond regime, whereas the nanosecond decay (section 5.2) is entirely radiative.

Beside the decay, it was necessary to include in the fitting function a fast component ($\approx$180 fs) which describes a rise of the signal, this component is associated to the solvation of the band which is visible in the averaged kinetics only because the investigated spectral range mostly involves the redder part of the band and avoids its blue tail, because it is too close to the excitation wavelength

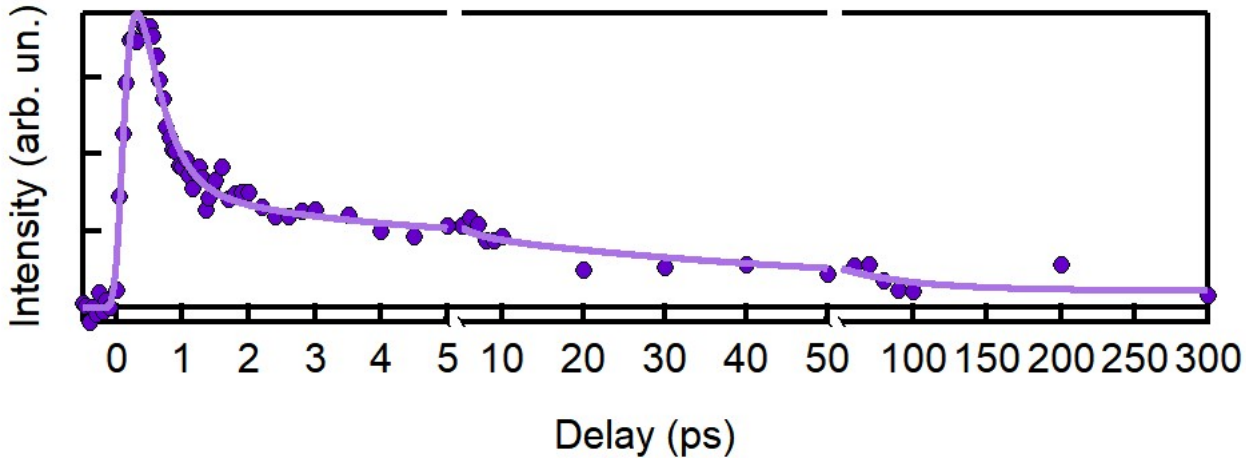

Figure 6.14: Kinetic trace which represents the decay of the emission band detected in a FLUC experiment (as obtained by averaging single-wavelength traces) with the least-squares fitting curve. Before GVD correction, some points have been removed (0.3-0.7 ps) because of pump scattering.

τ (ps)	Amplitude
0.3 $\pm$0.1	87%
2.5 $\pm$0.1	6%
70 $\pm$ 10	6%
nanosecond	2%

Table 6.2: Parameters obtained in the fitting procedure of FLUC kinetic trace. The relative amplitude of the fourth component (2%) explains the low value of the steady state QY.

and affected by scattering.

In parallel to upconversion measurements, transient absorption experiments at 400 nm have been carried out. Selected pump probe spectra and kinetics are reported in Figure 6.15.

The signal in Figure 6.15 can be described as a GSB signal around the pump wavelength and an ESA which involves almost the entire spectral range. This broad ESA spectrally overlaps the fluorescence hiding the presence of a stimulated emission signal. Despite of this, selected kinetic traces can be analyzed and fitted by a multi-exponential function obtaining almost the same decay times collected in the analysis of FLUC experiment: 0.3 $\pm$ 0.1 ps, 2.6 $\pm$ 0.1 ps, 50 $\pm$ 10 ps and a nanosecond time scale (fitting parameters in Table 6.3). Besides, all the signals detected in TA measurements do not almost change their shape and, therefore, their dynamics arise from the partial depopulation of the same emitting excited state detected in FLUC. The very earliest component revealed by FLUC (150-200 fs, tentatively ascribed to solvation) is hardly visible in TA due to the worse time resolution.

Fluorescence upconversion and transient absorption measurements allow to describe the system from two different points of view. The former detects the direct emission from the first excited state without any other contributions. While, the latter discloses the same dynamics via ground and higher energy states dynamics. Both concur to picture the photo-cycle of p-CQDs as a very simple one: the direct photo-excitation of the emissive state is followed by a strong sub-nanosecond population loss, which explains the low steady-state QY.

Since the fluorescence of p-CQDs is tunable in the visible range as displayed in Figure 6.12 pump probe measurements at two different excitation wavelengths have been performed. In Fig-

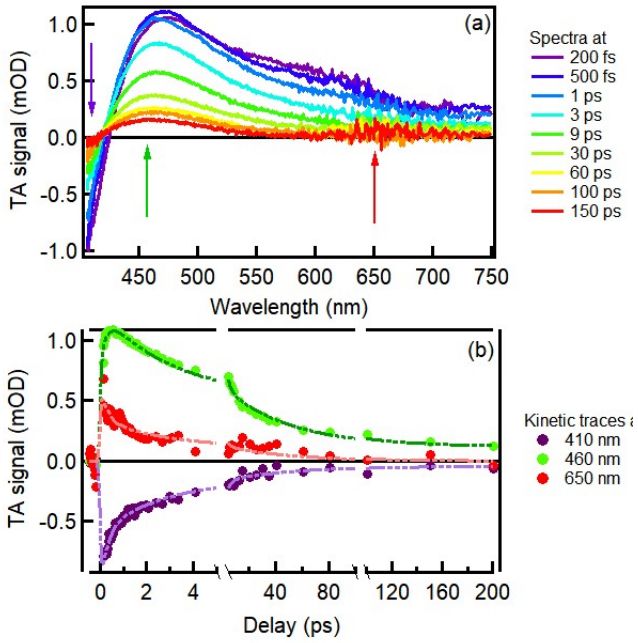

Figure 6.15: (a) TA spectra of p-CQDs in water excited at 400 nm after various delays after the photoexcitation and (b) kinetic traces at different wavelengths.

τ (ps)	Amplitude @ 410 nm (10^{-4} OD)	Amplitude @ 460 nm (10^{-4} OD)	Amplitude @ 650 nm (10^{-4} OD)
0.3 ± 0.1	5.0	-5.0	3.0
2.6 ± 0.1	4.0	6.0	2.0
50 ± 10	1.3	5.0	1.3
nanosecond	0.4	1.0	0

Table 6.3: Parameters obtained in the fitting procedure of TA kinetic traces.

ure 6.16 spectra excited at 400 nm and 350 nm at 100 ps are compared. It is evident that the pump probe spectra reflect the tunability of the emission showing the tunability of the GSB and of the ESA. Considering that the tunable emission is related to electronic transitions involving the surface as explained in chapter 5, this, indeed, suggests that the GSB and the ESA are both associated with surface states and that these states can be described as a manifold of surface states with continuous variable energy. Similar results, without any interpretation are reported in the literature [231]. The tunability can be associated to a static inhomogeneity probably related to structural inhomogeneity. Looking in details the spectra, it is possible to notice that the shape of the signal is not perfectly identical. In fact, in the spectrum excited at 350 nm, it is evident the presence of an extended ESA at longer wavelengths respect to the spectral range involved in the surface emission Figure 6.12. This suggests that there is an additional contribution to the signal at 350 nm which can be tentatively associated with the excitation of the core. Anyway, considering that the emission mechanism involves the surface (as explained in section 5.2) and that the shape of the TA spectra is quite similar changing the excitation wavelength, it is suggested that the photoexcitation involves mostly the surface of the dots, with only a minor contribution from core transitions.

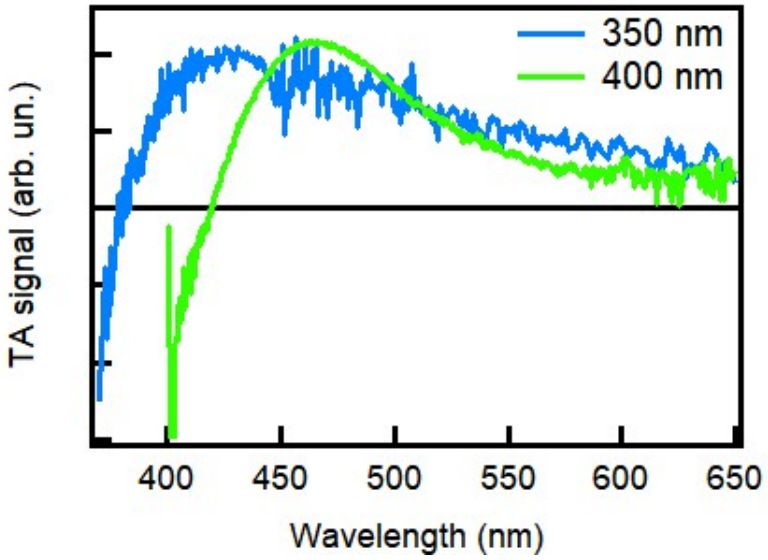

Figure 6.16: TA spectra of p-CQDs in water excited at 350 nm (blue curve) and at 400 nm (green curve) after 100 ps after the photoexcitation.

Comparison between raw and passivated CQDs

In order to further disentangle the role of the core from that of the surface we performed comparative pump probe measurements at 350 nm on p-CQDs and r-CQDs. Indeed, both samples have the same core structure and, if core transitions and surface transitions do not interplay with each other, it is expected that the TA signal associated to the core should not change with the passivation. The different results for the two samples are shown in Figure 6.17 where selected spectra and kinetic traces are reported, and are reported in Table 6.4 where the time scales extracted from fitting procedure are summarized.

Time scale	p-CQDs	r-CQDs
τ_1 (ps)	0.35 ± 0.05	0.5 ± 0.1
τ_2 (ps)	2.2 ± 0.1	1.5 ± 0.1
τ_3 (ps)	140 ± 10	25 ± 1
τ_4	few ns	few ns

Table 6.4: Summary of the characteristic time scales of the kinetics from Figure 6.17.

From Table 6.4 it is evident that the time scales which describe the signal are quite different in the two samples. We first discuss in detail the data on p-CQDs excited at 350 nm. The time scales and the dynamics are very similar to the one recorded exciting at 400 nm. The entire signal can be described as a GSB around the pump wavelength and a broad ESA which covers the entire spectral range. The total signal undergoes a multi-exponential decay, therefore the excited state undergoes a depopulation after the initial photoexcitation. If there is in the signal a contribution stemming from the core, it should be in the red part of the spectral range (around 600-650 nm) as already mentioned, and it should be very weak with respect to the surface contribution considering that 350 nm fairly matches the peak of the steady-state absorption band that we already attributed to surface transitions. Comparing the time scales in Table 6.4 and in 6.2, it is evident that they are almost the same regardless the excitation wavelength confirming again that the excited

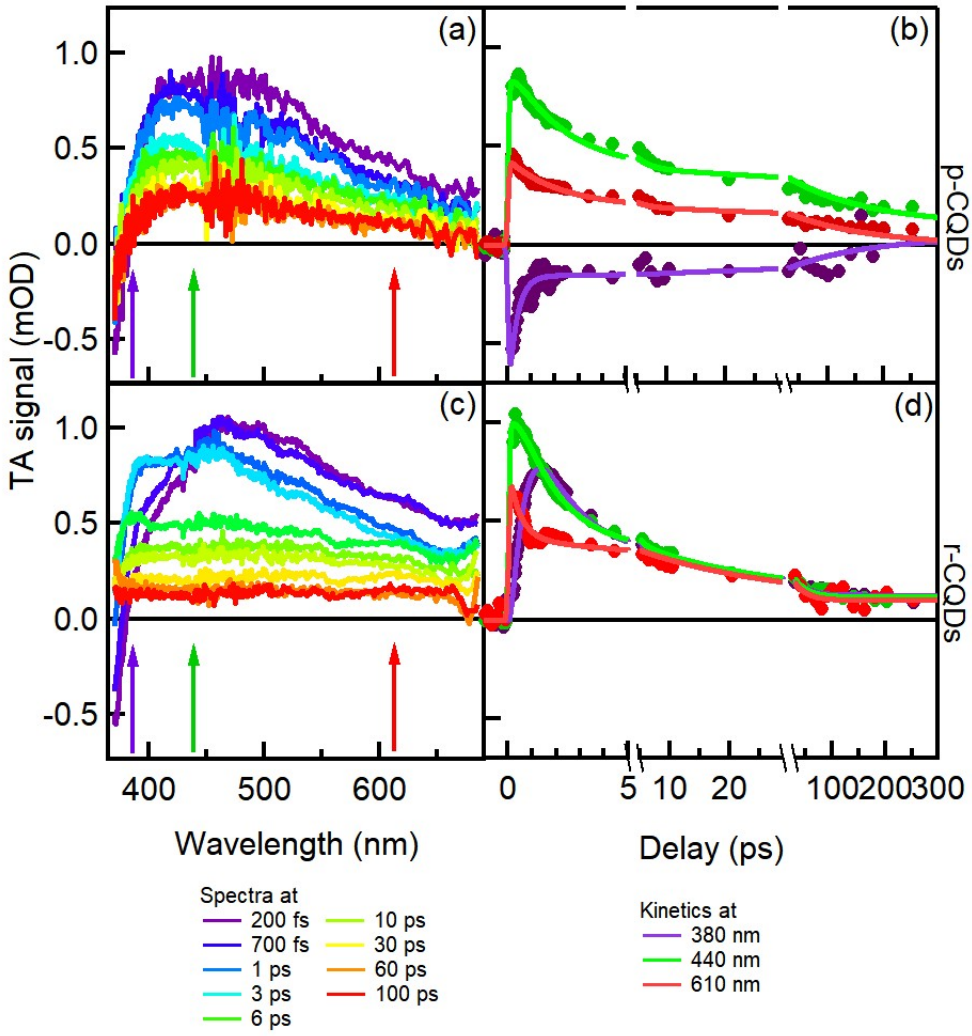

Figure 6.17: TA spectra of p-CQDs (a) and r-CQDs (c) in water excited at 350 nm after various delays after the photoexcitation. TA kinetic traces of p-CQDs (b) and r-CQDs (d) at different wavelengths indicated by the arrows.

chromophore belongs to the same manifold of states having very similar spectroscopic characteristics (shape of the TA signal, ultrafast dynamics, ...). To further confirm the major involvement of the surface in these dynamics, pump probe experiments were conducted on solutions of p-CQDs in presence of 80 μM of Cu^{2+} and of Fe^{2+}. The appearance of a new decay component ($\tau = 0.4$ ps) in the kinetics (Figure 6.18) confirms that the signal is associated to the depopulation of a state which involves the surface, because, for instance, an electron transfer from the dot to the ion requires the close contact between the donor and the acceptor, therefore, only the surface is expected to interact with the ions. Moreover, the increase of the signal at time zero shown in Figure 6.18 suggests some modifications which occur with a time scale lower than the experimental time resolution. Therefore, a close analysis of the data collected on p-CQDs excited at 350 nm fully confirm the conclusions obtained at 400 nm excitation.

We move now to compare the behaviour of p-CQDs and r-CQDs. Considering panels (c) and (d) in Figure 6.17 and the time scales reported in Table 6.4, it is possible to state that exciting r-CQDs sample produces a signal with a different shape and dynamics. Also in this case, at a first

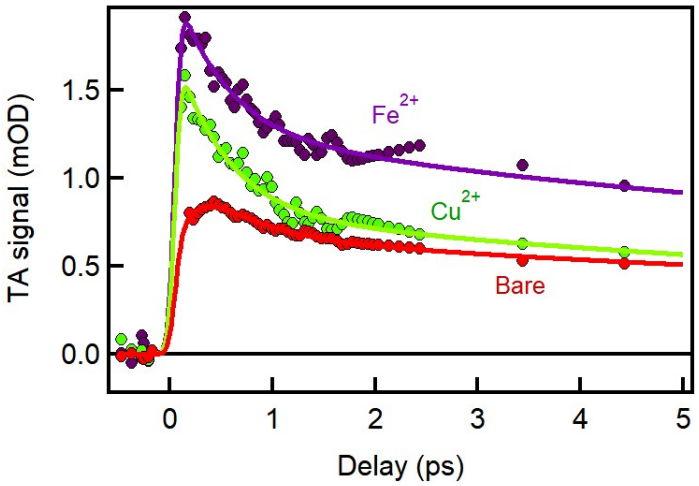

Figure 6.18: TA kinetic traces at 420 nm of bare p-CQDs (red curve), p-CQDs with 80 μM of Cu^{2+} (green curve) and with 80 μM of Fe^{2+} (purple curve) with the respective least-fitting curves.

glance the signal is composed by a GSB around the pump wavelength and a very broad ESA. However, the GSB signal decays completely in few ps (in contrast to p-CQDs dynamics). After that, only an ESA remains. This ESA is very differently from that observed in p-CQDs. In fact, the ESA signal of r-CQDs displays a very flat shape, covering the entire spectral range. Besides, such a signal decays with longer time scales (25 ps + nanoseconds) which are completely different from the passivated sample.

In this type of experiments, a flat ESA is usually associated with the presence of delocalized free charges (probably electrons) in the conduction band of the core. This flat ESA resembles also the ESA at long delays in Figure 6.10 where TA spectra of bottom up graphitic CDs are reported. Despite the different synthesis procedure, the shape of the signal is similar for the two samples, and considering that the core is graphitic in both cases (even if one is N-doped) the data suggest the involvement of core transitions, a very different result from p-CQDs.

Focusing on the firsts picoseconds, in addition to the disappearance of the GSB, it is possible to notice in the spectral region below 420 nm another fast change of the signal. This spectral evolution could be due to a fast decaying emission or a solvation driven spectral shift of a positive signal. To have an insight on its origin, the difference between the spectra at 1 ps and 200 fs was calculated, after normalizing the spectra in the red spectral region. The difference spectrum was finally compared with the absorption spectrum, as shown in Figure 6.19. From this comparison, the shape of the absorption band and of the signal is almost mirror symmetric to the absorption transition. Therefore, this fast emission peaking at 380 nm is the inverse transition of the absorption band peaking at 350 nm. This result is fully in line with the absence of a steady state emission from r-CQDs. In fact, considering that the absorption spectrum shows some structured bands related to the surface, these should correspond to some electronic transitions which involve the surface but which decay through very efficient non-radiative recombination channels, as inferred from the absence of any steady-state emission. Moreover, the dynamics of the fast emission and that of the flat ESA seem to occur in a completely different time scales suggesting that these two transitions do not interact between themselves. These data suggest that in r-CQDs there are some surface states but their dynamics last few ps, while the dynamics of the core is long lived but does not give rise to any steady state emission, and that core and surface transitions are completely independent from each other. Similar results are found in other works [165], where TA measurements help to disentangle and to separate the dynamics of the core from the dynamics of

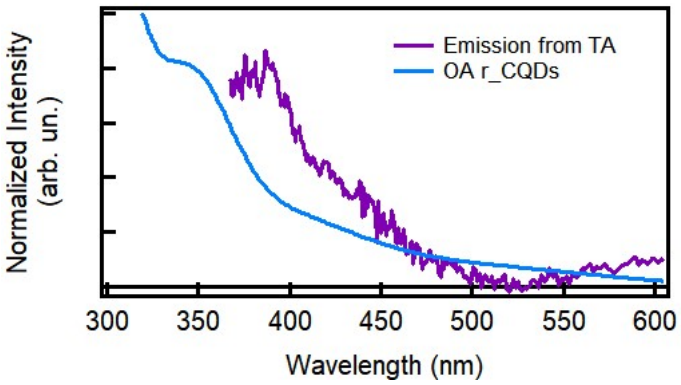

Figure 6.19: Comparison between the absorption spectrum of r-CQDs (blue curve) and the emission obtained from the difference between the TA spectra at 1 ps and 200 fs (purple curve).

the surface. At the same time, other authors proposed arguments in favor of an interplay between core and surface transitions [70,71]. The question is still debated and, probably, the real interaction between core and surface is synthesis dependent.

Summarizing the obtained results on raw and on passivated samples, it is possible to schematize the differences between them and the effects of the passivation procedure. In raw CDs there are two different channels which can be photoexcited: the surface and the core. These two transitions are completely independent from each other: excited core states show up as a flat ESA signal which undergoes a slow decay, indicating a depopulation of the excited states through band to band recombination. In contrast, surface dynamics are characterized by the very fast decay of a stimulated emission showing a mirror symmetry with respect to the OA profile. The presence of this emission band, despite the very fast recombination, suggests that the surface of raw dots hosts electronic states which would be theoretically capable of fluorescence, but recombine too fast to be observable in a steady state experiment. Once the surface is passivated, the situation is quite different. Passivation introduces, in fact, new electronic states on the surface which are capable of emitting fluorescence in the visible range. This is demonstrated by the appearance of an entirely new OA band which now excites a steady-state emission, by the results of FLUC, and by the substantial change of shape of the TA spectra induced by passivation. Moreover, ultrafast experiments allow to picture the dynamics of the excited state as the instantaneous population of surface emissive state followed by its partial sub-nanosecond depopulation which, as demonstrated by the comparison with the nanosecond and steady state data, is the main limiting factor of the steady state emission efficiency. Despite the core of p-CQDs and r-CQDs is the same, these ultrafast experiments suggest that the core is not involved in the dynamics of the p-CQDs or its contribution to the dynamics is very low. Based on the results, it can be supposed that the main contribution in the OA transition in p-CQDs is associated to the surface, due to the fact that surface states of the passivated sample are strongly absorbing, and, then, that we excite above the surface respect to the core. On the contrary, the major part of absorption of the r-CQDs stems from core transitions, therefore, the photoexcitation reveals core dynamics in the ultrafast experiments.

6.3 Conclusions

By an ultrafast approach, we unravelled the photocycle of different families of CDs: bottom up $\beta - C_3N_4$, bottom up graphitic dots, and top down graphitic dots.

Excitation of $\beta - C_3N_4$, as inferred by steady state and nanosecond approaches, involves the coupling between core and surface. When the excitation of the visible band is direct, the dynamics are only due to a solvation relaxation. The excited state does not depopulate in the sub-nanosecond regime confirming the results of chapter 5. Moreover, the charge exposed to the solvent is free to move on the surface because the latter hosts a manifold of degenerate states. Exciting at higher energy allows to excite core transitions. This creates a hole-electron pair in the core and, then, an electron is spontaneously transferred to the surface within 1.2 ps. The rise of the emission, we observed here after photo-excitation at 266 nm, is the first direct evidence of this core-to-surface population mechanism for CDs.

The photocycle of bottom up graphitic dots is more complex but, comparing it with the literature, it is possible to speculate that the emission stems from a molecular-like transition which involves small molecules (2-pyridone derivatives) created during the synthesis.

Regarding the top down graphitic dots, we disclosed the role of passivation and the interplay between core and surface. As many works suggested, the passivation is crucial for the emission of the dots. Here, with femtosecond approaches we confirmed that it is fundamental for the fluorescence and, in addition, we found that the role of passivation is to create a manifold of emissive states on the surface characterized by a continuum of different energies. Despite this, the emission quantum yield is very low caused by sub-nanosecond depopulations of the excited state. Moreover, we demonstrate for the first time that even the non-passivated sample hosts emissive states, they decay in a very short time limiting an observable long-lived emission. Thanks to this very fast decays, it is possible to observe a signal which derives from the core states which usually are hidden under the surface states signatures.

Chapter 7

Interaction With Metal Ions

In this chapter, the interactions between $\beta - C_3N_4$ CDs and metal ions in solution are investigated. In particular, the visible transition with a charge transfer character is analysed by steady state and time resolved spectroscopic techniques when CDs are dispersed in aqueous solution together with different ions. This characterization demonstrates the influence of ions on the fluorescence and suggests that different interaction mechanisms can occur with different ions. Then, ultrafast experiments were carried out on specific samples with the aim of fully unravelling the interaction mechanisms which can occur, such as charge or energy transfer phenomena. By ultrafast techniques, it is possible to study these mechanisms in real time, down to the femtosecond time scale, overcoming the severe limitation of steady-state studies.

7.1 Ions-CDs Complexes Investigated Down to the Femtosecond Scale

Introduction

One of the remarkable properties of CDs is their strong sensitivity to local environment as already demonstrated in chapter 5. This sensitivity is very evident when CDs are interacting with metal ions in solution highlighting their marked photochemical properties which have been usually associated to charge transfer events. This sensitivity is usually detected as a variation (quenching or enhancement) of their luminescence, which can be very selective with respect to specific ions and fully reversible. Moreover, the surface of CDs is usually negatively charged in solution because of the dissociation of carboxylic groups (COO-). Therefore, one may expect especially favourable interactions with positive ions, such as metal cations.

Here, the emission of CDs has been studied in presence of different ions, and different mechanisms of interaction, which cause the quenching or the enhancement of the emission, are proposed. The use of several optical techniques, down to femtosecond time resolution, has allowed us to fully resolve in time the photocycle of CD+ion complexes. An important finding of our studies is that solvent molecules drive CD-ion interaction and play a crucial role in the photochemical behaviour of CDs.

Steady State and Time Resolved Experiments

$\beta - C_3N_4$ dots were dispersed in aqueous solution with different amount of various cations. In particular, a preliminary steady state optical study was performed on the influence of Fe^{3+}, Co^{2+}, Cu^{2+}, Zn^{2+}, Ag^{+}, Na^{+}, and K^{+} (electronic configurations in Table 7.1) to assess the visible emission. Considering the electron transfer character of the transition (chapter 5), the aim of the study

Ion	Electronic Configuration
Na^+	$[Ne]3s^1$
K^+	$[Ar]4s^1$
Fe^{3+}	$[Ar]3d^5$
Co^{2+}	$[Ar]3d^7$
Cu^{2+}	$[Ar]3d^9$
Zn^{2+}	$[Ar]3d^{10}$
Ag^+	$[Kr]4d^{10}$

Table 7.1: Summary of electronic configurations of used ions.

was to investigate CD-ion interaction changing the electronic configuration of the ion focusing, in particular, on the variation of its capability to accept an electron.

In a first explorative experiment, we measured the intensity of the green emission band in the presence of 4-10 mM concentration of ions, the results are reported in Figure 7.1. As it is

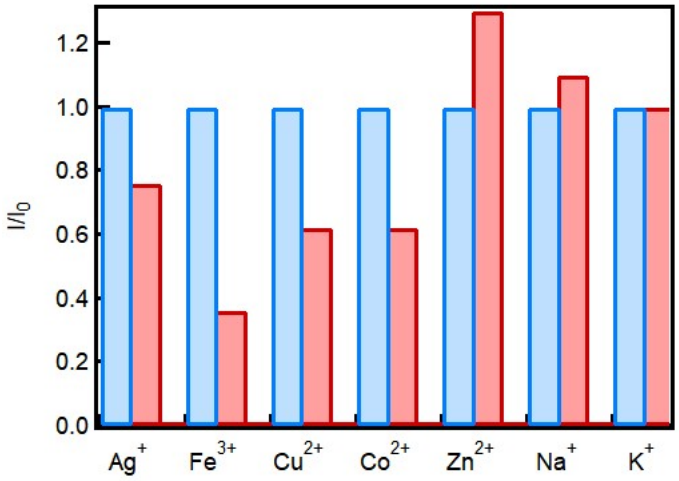

Figure 7.1: Intensity of the green band of CDs with 4 or 10 mM of ions (red bars) as compared to the intensity of bare CDs which corresponds to the value of 1 (blue bars).

evident, the emission is quenched by every ion we tested except for Zn^{2+}, K^+ and, Na^+ which, on the contrary, can produce an enhancement of the photoluminescence. Interestingly, despite the electronic configuration of Zn^{2+} and of Ag^+ is a completely full d-shell, their influence on the emission is opposite. This suggests that the outer electronic configuration cannot be simply related to the quenching efficacy. In fact, the important parameter is the capability of accepting an electron from the dots, as already suggested by some authors [160]. This capability is described by the so-called redox potential which is a measure of the tendency of a chemical species to accept electrons and hence to be reduced. In other words, the more positive the redox potential, the stronger ability of the species to behave as an oxidant.

Thus, looking at the redox potential values of the semireactions involving the ions (Table 7.2) and considering the behaviour in Figure 7.1, one can infer that there is a threshold value in the redox potential scale which defines the favourable condition to allow an electron transfer from the dot to the ion causing the quenching of the emission. In particular, this redox potential should be between the value of the semireactions which involve zinc and cobalt ions considering the effects

in Figure 7.1. The redox potential of the semireaction $Zn^{2+}(aq) + 2e^- -> Zn(s)$ is $-0.76V$ and the emission of CDs in presence of Zn^{2+} ions is not quenched, thereby, it turns out that the electron transfer from the photo-excited dot to these ions is energetically forbidden. In contrast, CDs are effectively quenched by Co^{2+} ions, characterized by the semireaction $Co^{2+} + 2e^- -> Co(s)$, with slightly higher redox potential ($-0.28V$). As can be seen from Figure 7.1, the response of CDs (quenching or not) to all the other ions we tested is consistent with this simple interpretation. Therefore, the threshold value is somewhere in between -0.28 V and -0.76 eV, and represents the redox potential for the reduction of the weakest oxidant capable to extract an electron from the excited state of these CDs.

Ion	Redox Potential (V)
$Ag^+ + e^- \rightleftharpoons Ag$	0.8
$Fe^{3+} + e^- \rightleftharpoons Fe^{2+}$	0.77
$Cu^{2+} + e^- \rightleftharpoons Cu^+$	0.16
$Co^{2+} + 2e^- \rightleftharpoons Co$	-0.28
$Zn^{2+} + 2e^- \rightleftharpoons Zn$	-0.76
$Na^+ + e^- \rightleftharpoons Na$	-2.71
$K^+ + e^- \rightleftharpoons K$	-2.93

Table 7.2: Summary of Redox Potential values of used ions.

Thus, the response of our dots to metal ions is not expected to be selective for a single type of ions as sometimes happens [110, 154, 157]. Anyway, our finding that the response of CD emission to different ions can be explained by their redox potential is a very strong indication of the electron transfer nature of the quenching interaction with metal cations. Although the redox potential allows to predict if a given ion can or cannot quench excited CDs, it is not expected that the fluorescence decrease induced by a given quencher concentration is a regular function of the redox potential, in fact, several other ingredients should be taken into account in the effect as the chemical affinity between the surface of the dots and the specific metal ions in solution.

To further investigate the mechanism, time resolved measurements on CDs in the presence of two different ions (Cu^{2+}, Zn^{2+}) were performed at three different concentrations. In presence of copper ions the emission is quenched (Figure 7.2) and it is possible to distinguish two quenching regimes: static and dynamic. The former involves the formation of stable CD-Cu^{2+} complexes and

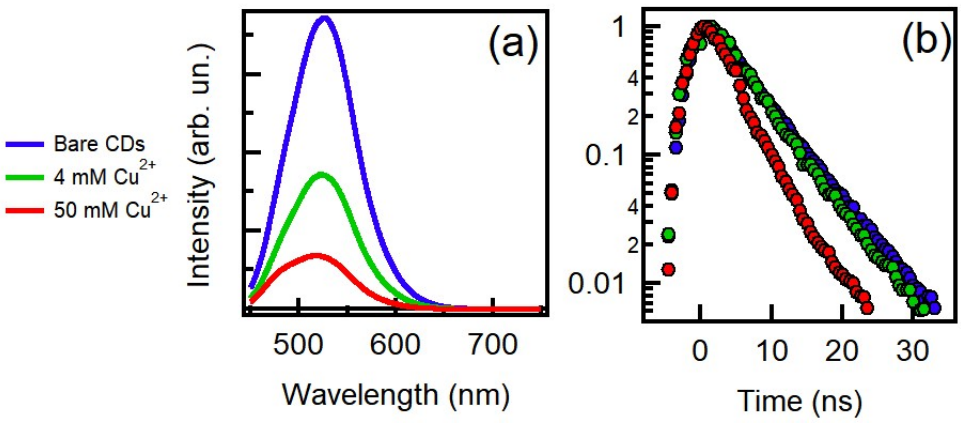

Figure 7.2: (a) Steady-state emission spectra and (b) normalized decay fluorescence excited at 440 nm of CDs dissolved in water (blue curve) together with Cu^{2+} ions at 4 mM (green curve) and 50 mM (red curve) concentration [Adapted from [232]].

it is suggested by the quenching of emission (green curve in Figure 7.2a) at low ion concentration without relevant changes in the lifetime (green curve in Figure 7.2b). This view is supported by absorption measurements (Figure 7.3), which show a variation on the absorption profile already at low concentration highlighting the formation of CD-Cu^{2+} complexes.

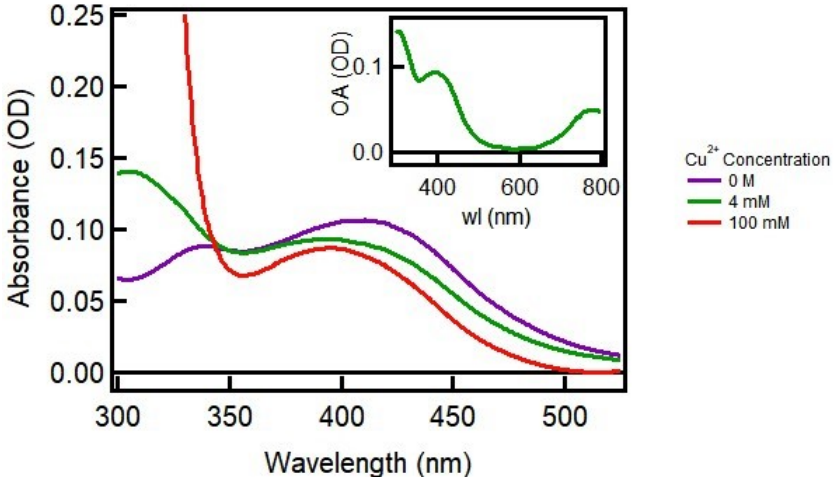

Figure 7.3: Absorption spectra of CDs as measured in the presence of different Cu^{2+} concentrations. Inset: OA spectrum of CDs with 4 mM of Cu^{2+} in the entire investigated spectral range. The edge below 350 nm is due to the electronic transitions of the counterion (NO_3^-), and the transition at 800 nm is due to d-d transition of copper ions. [232].

Besides, complex formation is also supported by IR measurements as shown in Figure 7.4. They display small, but appreciable variations in the region between 1550–1800 cm^{-1}, associated

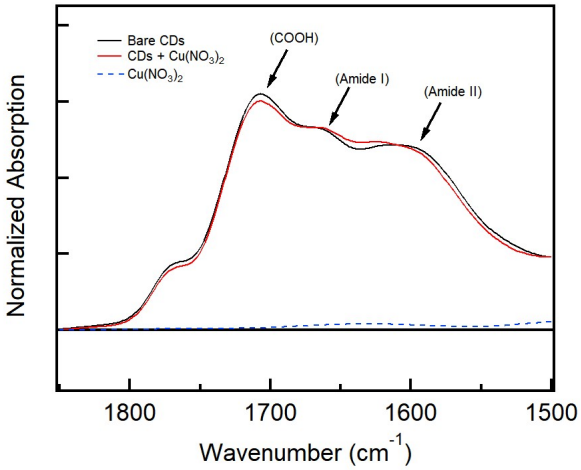

Figure 7.4: Infrared absorption spectra of bare CDs (black line) and of CDs with 400 μM $Cu(NO_3)_2$ (red line) and of pure $Cu(NO_3)_2$ (blue line). The arrows point at the signals and their attributions [232].

with the vibrations of amide and carboxylic surface groups. Although the observed changes are too complex to infer a simple binding pattern, IR data seem to confirm that the surface groups of the dots are involved in the formation of the complexes between Cu^{2+} and CDs confirming the formation of complexes CD-Cu^{+2}. This static quenching is related to the formation of CD-Cu^{2+}

complexes and to the following electron transfer from the excited CD to the ion.

Beside the above discussion based on the comparison between different metal ions, on the grounds of their redox properties, other theoretical arguments can be put forward to support our interpretation of the quenching effect as an electron transfer from excited CDs to Cu^{2+} ions. In fact, the only optical transition of copper in the UV/VIS range is located at 800 nm and is due to a d-d transition (inset of Figure 7.3). Thereby, other common mechanisms of fluorescence quenching appear very unlikely: in particular, both resonance and Dexter-type energy transfer to the d–d absorption transition of aqueous Cu^{2+} ions around 800 nm should be extremely inefficient because the latter is forbidden and has no spectral overlap with CD emission.

The dynamical quenching is due to the collision between CDs and ions, occurring within the lifetime of the excited-state, and it is suggested by the simultaneous and correlated decrease of the intensity and of the lifetime (from 6.0 ns to 4.6 ns) as it is evident from the red curves in Figure 7.2. Collisional quenching has been detected in other works [233,234] by the use of nanoseconds techniques but with different electron acceptors than copper ions.

The results are very different when CDs are interacting with zinc ions. Considering the redox properties of Zn^{2+} ions, an emission quenching is not expected. In fact, the emission of CDs increases and blueshifts at any concentration of zinc ions and the lifetime becomes longer (Figure 7.5). All of these effects can be explained as an effect of electrostatic screening provided by

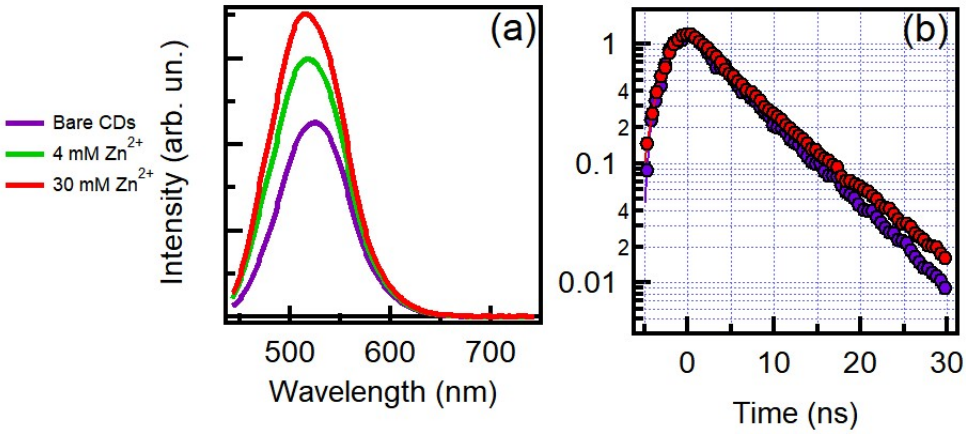

Figure 7.5: (a) Emission spectra and (b) normalized decay fluorescence excited at 440 nm of CDs dissolved in water (purple curve) together with 4 mM (green curve) and 30 mM of Zn^{2+} (red curve) [232].

Zn^{2+} ions on the negatively-charged surface of CDs. This is expected to reduce the strong solvation effects on the CD surfaces, due to dielectric and H-bonding interactions with water that red shift CD emission and reduce their QYs (chapter 5). Through this mechanism, Zn-induced screening increases the HOMO/LUMO gap and provokes a blue shift of the band, accompanied by an increase of the lifetime and quantum yield of the transition. Additionally, the attached Zn^{2+} may increase QY by limiting the geometrical rearrangement of the surface groups that provide non-radiative dissipation channels.

Electron Transfer Investigation

To further investigate the electron transfer mechanism and the static and dynamic quenching regime pointed out in Figure 7.2 and 7.3, the interaction between CDs and copper ions has been deeply analysed by combining several experimental techniques in a comprehensive experiment.

We dispersed CDs in water (8 mg/L), together with different amounts of Cu^{2+} ions, and studied how their optical properties change with the increase of ion concentration. Figure 7.6 displays

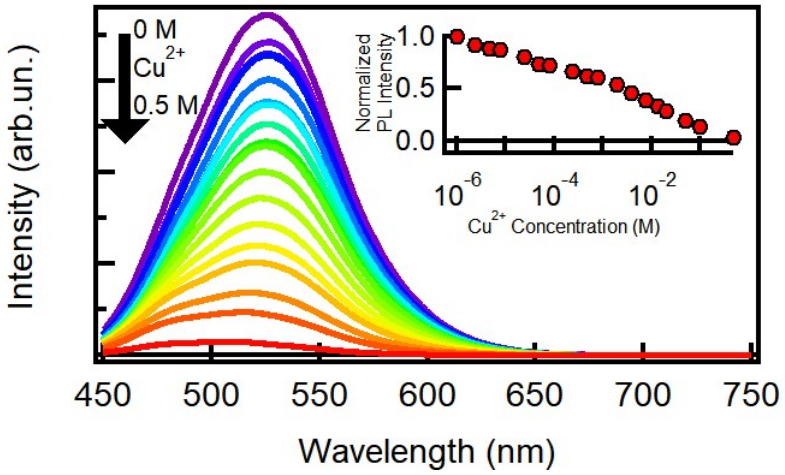

Figure 7.6: Steady-state emission spectra excited at 440 nm of CDs dissolved in water together with Cu2+ ions in concentrations ranging from zero to 500 mM (increasing along the arrow). Inset: Photoluminescence intensity, normalized to bare CDs, versus Cu2+ concentration [232].

the steady state emission spectra excited at 440 nm of CDs aqueous solution and variable concentrations of $Cu(NO_3)_2$. In the inset of Figure 7.6, how the luminescence intensity decreases with increasing copper concentration is reported: appreciable variations of the emission intensity are observed at concentrations as low as 2 μM, where we detect a $\Delta I/I_0 \approx 10\%$ reduction, and a very marked quenching is observed when the copper concentration reaches the millimolar range, with a $\Delta I/I_0 \approx 50\%$ loss of the luminescence efficiency recorded at $[Cu^{2+}]$ = 2 mM. A blue shift of the band from 525 nm down to 512 nm is measured at $[Cu^{2+}]$ = 500 mM together with an intensity reduction of $\Delta I/I_0 \approx 96\%$.

Time resolved measurements have been performed at different copper concentrations. The decay kinetics of bare CDs are single-exponential (6 ns), as reported in section 4.1 and Figure 4.13, and displays no spectral evolution. As already highlighted, the diffusion-controlled (i.e. dynamic) quenching comes into play only above a certain copper concentration, as revealed by a decrease of the lifetime (as already anticipated in Figure 7.2 for selective concentrations and demonstrated in Figure 7.7): the first deviations of the fluorescence kinetics is at 20 mM (5.0 ns, green curve in Figure 7.7), and the lifetimes continue to decrease at higher quencher concentrations down to <2.0 ns. At lower concentration the lifetime does not change but the intensity is quenched. The decrease of the amplitude without shortening of the lifetime, typical of a static quenching, can only be explained by the presence of non-radiative channels affecting the excited state population on time scales much shorter than the time resolution. On these time scales, the mechanism cannot be diffusional and it points to a mechanism where copper ions interact with the dots before and during photoexcitation. Hence, the quenching is purely static, i.e. occurring without collisions, up to millimolar concentrations: ground-state interactions between CDs and copper ions lead to the formation of weakly or non-luminescent CD–Cu^{2+} complexes.

Therefore, we used fs TA to study the photocycle of these CD-Cu^{2+} complexes, in order to directly detect the electron transfer events on a ultrafast time scale. Broadband TA measurements on an aqueous solution of bare CDs, and on a solution of CDs with $[Cu^{2+}]$ = 100 mM have been performed and the data are shown as time-wavelength 2D-plots in Figure 7.8a-b. The signal of bare CDs is described in chapter 6. The shape of the signal in the presence of copper is almost the

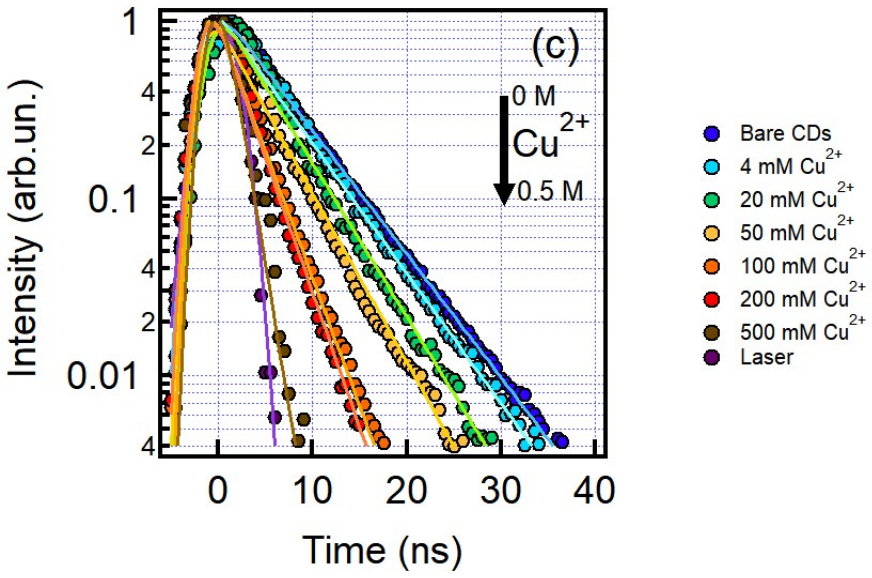

Figure 7.7: Normalized decay fluorescence of CDs excited at 440 nm in water with zero (blue markers), 4 mM (light blue markers), 20 mM (green markers), 50 mM (yellow markers), 100 mM (orange markers), 200 mM (red markers), and 500 mM (brown markers) concentration of copper ions, together with the laser pulse (purple markers), with the respective least-squares fitting curves. [232].

same as bare CDs. However, in the presence of ions, all the components of the signal undergo a decay over a time scale of a few picoseconds, which is not observed for bare CDs. The main effect of ions is to alter the overall evolution with minimal effects on the spectral features (Figure 7.8c-d). Thus, the SE signal of CDs with different amount of copper ions at single-wavelength has been detected in order to achieve a higher signal-to-noise ratio. The kinetic traces were collected at 550 nm (Figure 7.9a) close to the peak position of the SE after 10 ps, to monitor specifically contributions to the SE and thus excited-state relaxation of CDs. As shown in Figure 7.8a and explained in chapter 6, the single-wavelength TA signal at 550 nm of bare dots undergoes a rise within few ps after photo-excitation which corresponds to dynamical Stokes shift of the entire SE band. In presence of Cu^{2+} a strong reduction of the signal can be detected. In particular, there is a decay component over a time scale of a few ps, which becomes more and more evident with increasing ion concentration (Figure 7.9b). The kinetics have been analyzed by fitting them with multi-exponential functions. Every trace can be reproduced by three different time components. Although the amplitudes associated with these three time scales depend on copper concentration, the time scales obtained by the fitting procedure show indeed slight variations across the different traces, and can be simultaneously fitted by common time constants: their values, as obtained by the fit, are $\tau_1 = 0.21 \pm 0.05$ ps, $\tau_2 = 1.9 \pm 0.1$ ps, $\tau_3 \geq 1000$ ps, and their amplitudes A_i are reported in Table 7.3.

The τ_3 component can be identified with the nanosecond lived fluorescence surviving after all the ultrafast dynamics are completed: in fact, increasing copper content reduces its weight A_3 (see Table 7.3) similarly to the intensity decrease observed in the steady state measurements (Figure 7.6). Focusing on the fast dynamics, the SE signal undergoes a bi-exponential rise over two time scales of 0.21 ps and 1.9 ps (A1 and A2 positive in bare CDs) describing its dynamical Stokes shift caused by the solvation (see chapter 6). The addition of copper decreases the weight of the first component and converts the $\tau_2 = 1.9$ ps rise into a decay, as seen from the change of sign of its amplitude (Table 7.3). Therefore, the ultrafast decay τ_2 directly represents a real-

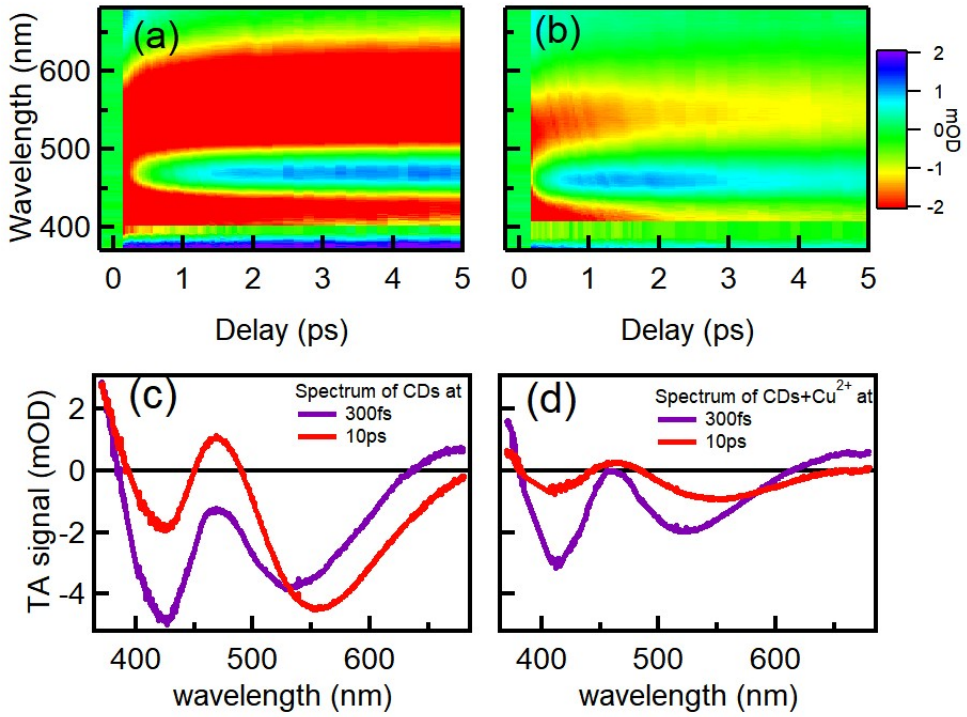

Figure 7.8: Transient absorption 2D-plot of an aqueous solution of bare CDs (a) and with [Cu^{2+}] = 100 mM (b) excited at 400 nm. Transient absorption spectra of bare CDs (c) and with 100 mM of Cu^{2+} (d) recorded at 300 fs and 10 ps after photoexcitation, as obtained by vertical cuts of the 2D-plots in panels (a) and (b). Data between 388 nm and 405 nm were removed because of distortions by pump scattering around 400 nm [232].

time observation of static quenching events. Although the CD–Cu^{2+} complexes involved in these decays are seen as "non-emissive" by steady state and nanosecond methods, they actually yield a transient fluorescence: in fact, the SE observed in the presence of Cu^{2+} is very close to bare CDs, except for the ultrafast decay (Figure 7.8).

The ultrafast decay channels related to the complexes match those of CD surface solvation. This coincidence is indeed unexpected and leads to presume a key role of solvation in the quenching process. It is reasonable to expect a very close proximity of the photo-excited surface electron to the acceptor Cu^{2+} ion, and a very strong coupling between the Franck–Condon (FC) state and the electron transfer (ET) state. Speculating on this, it is possible to say that the mixing between the FC and the ET states must be initially rather small, since the initial excited state is very close to the FC state of the bare CDs, as revealed by: (i) the fact that the shape of the SE at time zero is essentially unchanged in the presence of Cu^{2+} (Figure 7.8); (ii) by the independence of the extrapolated SE signal amplitude at time zero from copper concentration (Figure 7.10), indicating that the nature of the initially excited state is independent of the presence of copper. The preservation of the FC state requires the existence of a defined barrier separating it from the ET state. On the other hand, ET occurs bi-exponentially on the same time scales (0.21 and 1.9 ps) that characterize aqueous solvation on bare CDs, ruling out a direct, through-barrier, transition from the FC to the ET states, since it would imply new decay components in the fitting procedure. Conversely, it speaks for an adiabatic ET process driven by a solvent rearrangement. Thus, probably solvation progressively decreases the barrier between the FC state and the ET state (see Figure 7.11) until the charge transfer is allowed and decouples the surface electron from the core hole, depopulating the

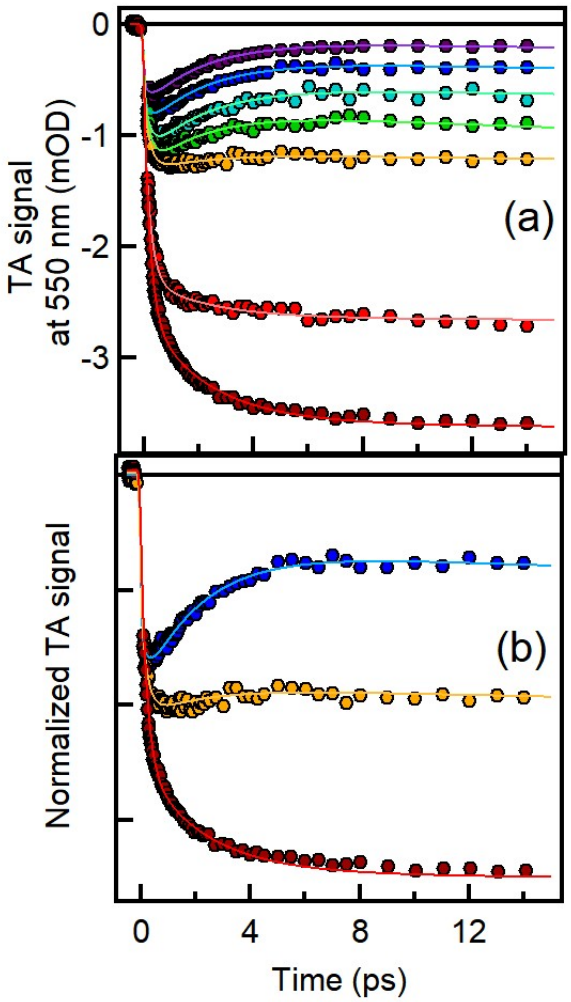

Figure 7.9: (a) Transient absorption time traces at 550 nm (excitation at 400 nm) of CDs with no copper ions in solution (dark red), 4 mM (red), 20 mM (orange), 50 mM (green), 100 mM (light blue), 200 mM (blue), and 500 mM (purple) copper concentrations, with the respective least-squares fitting curves (continuous lines). (b) Three time traces normalized at the first point after time zero, with the same color scale. [232].

emissive state. A deep involvement of solvent relaxation in this reaction is actually expected: in fact, the photo-induced change of the surface charge distribution, directly exposed to the solvent, is expected to trigger a dramatic solvent rearrangement, as observed in similar cases [235]. As a consequence of such a solvent-controlled mechanism, the time required for water rearrangement limits the efficiency of ET notwithstanding a strong coupling. The last step of the photocycle involves the transition of the CD–Cu^{2+} system back to the ground state. In this respect, Figure 7.8 shows that the ultrafast SE decay is accompanied by the disappearance of all the other components of the TA signal. The decay of the GSB on the same time scale, in particular, implies an extremely fast repopulation of the ground state immediately after ET. To be consistent with the data, the ground-state recovery must be much faster than 1 ps (or otherwise the GSB would disappear later than the SE), and cannot be directly observed here because the time scale τ_2 is a bottleneck of the overall dynamics. The nature of this final step is ultimately a back electron transfer inducing a non-radiative electron–hole recombination. This process completes the photo-cycle and hinders

Concentration	TA decay Amplitudes (mOD)		
	$\tau_1 = 0.21 \pm 0.05$ ps	$\tau_2 = 1.9 \pm 0.1$ ps	$\tau_3 =>$ 1000 ps
$[Cu^{2+}]$ (mM)	A_1	A_2	A_3
0	2.00	1.07	-3.57
4	1.60	0.40	-2.64
20	0.69	-0.12	-1.19
50	0.77	-0.42	-0.87
100	0.66	-0.66	-0.61
200	0.30	-0.59	-0.37
500	0.21	-0.56	-0.19

Table 7.3: Summary of the characteristic time scales and amplitudes of the kinetics from Figure 7.9 [232].

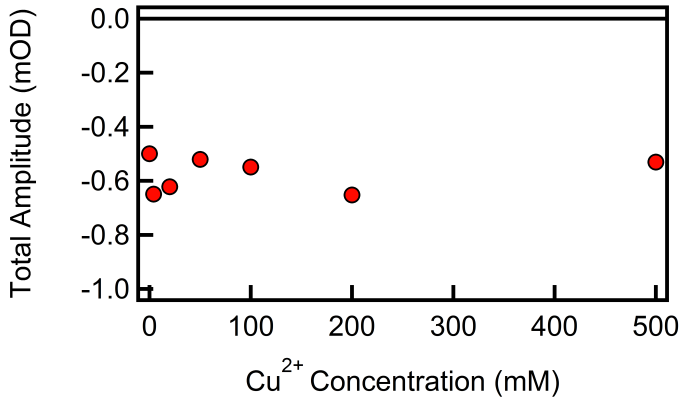

Figure 7.10: Total amplitudes obtained by the sum of all the amplitudes in Table 7.3, extrapolated from the fitting procedures. The independence of the value from increasing copper concentration indicates that the nature of the excited state at time zero is independent from the presence of copper [232].

steady state emission from CD–Cu^{2+} complexes. The fast reverse process suggests that the ET reaction is only partial, or otherwise the complete loss of the electron– hole overlap would render non-radiative recombination relatively inefficient. Indeed, within the model in Figure 7.11, the final state produced by the ET reaction can be more realistically pictured as one where the electron has become completely delocalized between the surface group and the metal ion, rather than a state where the electron has been fully transferred from the surface carboxylic/amide group to the nearby Cu^{2+}.

7.2 Conclusions

By comparing the response of CDs to a variety of metal cations, we demonstrate that the ability of a given ion to quench CD fluorescence through an electron transfer mechanism can be simply explained by their redox potential.

Choosing copper ions as model of electron acceptor and focusing on electron transfer mechanism, the combined use of several optical techniques provided a detailed picture of the dynamics responsible for CD fluorescence quenching from the femtosecond to the nanosecond time

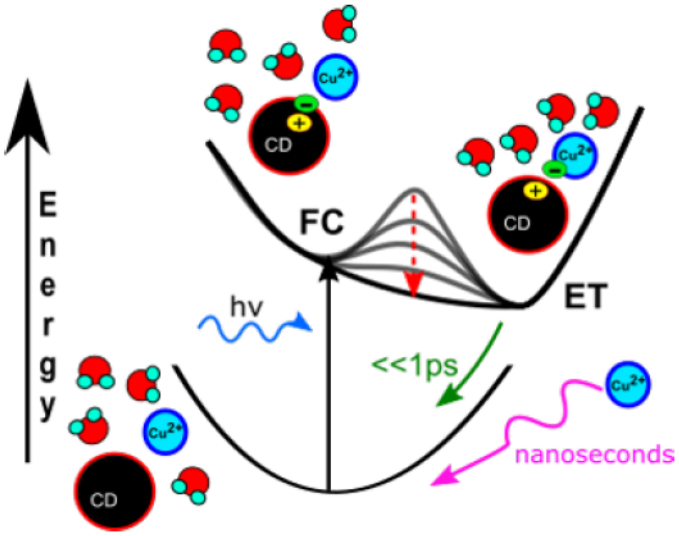

Figure 7.11: Model which represents the photo-cycle of CD–Cu^{2+} complexes (static quenching) and the collision between CDs and ions (dynamical quenching). After photoexcitation, a charge separation occurs and the system is in an electronic state (FC) which relaxes due to solvent motions in 0.21 + 1.9 ps (red arrow) and causing a partial electron transfer from the CD to Cu^{2+}. The cycle is closed by an ultrafast non-radiative electron–hole recombination ($\ll$ ps, green arrow). During the lifetime of CD emission, the collision with ions in solution produces a non-radiative recombination, thus, a quenching (pink arrow) [Adapted from [232]].

range. The majority of CDs are efficiently quenched by Cu^{2+} ions through the formation of stable CD–Cu^{2+} complexes, and a minority of CDs are quenched by a collisional mechanism, reflecting variations of their nanosecond decay kinetics. In both cases, quenching involves an electron transfer mechanism. The ultrafast study of CD–Cu^{2+} complexes reveals the ET process is only partial and the characteristic time scales and mechanism of its dynamics are 0.21 ps and 1.9 ps suggesting that the ET process is mostly controlled by a strong, and very fast, solvent rearrangement around the dot, initiated by photo-excitation, and driving a progressive reduction of the barrier for the ET reaction. The photocycle of CDs is completed by a fast, non-radiative recombination of the electron–hole pair.

Chapter 8

Fluorescence Tunability

In this chapter the tunability of CD fluorescence is investigated and using the $\beta - C_3N_4$ sample as a model studied by a combination of different methods. Single molecule experiments, fractionation and ultrafast hole burning data on $\beta - C_3N_4$ demonstrate that the tunability is a feature which is associated to the optical properties of CDs at the ensemble-level and that it is strongly related to dot-to-dot variations, thus, to the inhomogeneity of the sample, as it was suggested in section 5.2 and section 6.2 regarding a different family of dots. Furthermore, these experiments allow to isolate the homogeneous absorption and emission lineshapes, unveiling spectroscopic properties otherwise hidden by disorder. Thus, it is possible to isolate the individual contribution of a single chromophore out from a complex absorption/emission spectrum arising from the superposition of many unresolved components.

8.1 Tunability of Carbon Nitride

Introduction

As mentioned in section 1.3, emission tunability is one of the most important and unclear characteristics of CDs. Although several authors attributed it to a distribution of different surface chromophores or sizes [27,48], direct experimental evidences of such distributions remain scarce [147], and recent reports have fundamentally questioned this view [146].

To address the origin of tunability, we investigate the visible emission of $\beta - C_3N_4$ and used single molecule experiments combined with the results from size exclusion chromatography low temperature measurements, hole burning experiments. This set of data allows to demonstrate that the tunability comes from dot-to-dot variations and, thus, it is strictly related to the disorder and inhomogeneity of the system.

Fractionation and Single-dot Experiments

The absorption spectrum of $\beta - C_3N_4$ displays a low-energy wing at $\lambda > 450nm$, which is the spectral range where the dots display their characteristic fluorescence tunability, as shown in Figure 8.1 where CDs are dispersed in Dimethylformamide - DMF. Considering that in this spectral region the OA spectrum hardly shows any obvious peaks, by simple analysis of this spectrum it is very difficult to make any statement on the underlying structure of the electronic transitions that contribute to the spectrum. On the contrary, the emission band excited at any energy displays a well-defined peak and width ranging from $\approx$ 0.2-0.3 eV. Besides, each of these emission bands is related to a single electronic transition, considering that the band is a single signal in which the

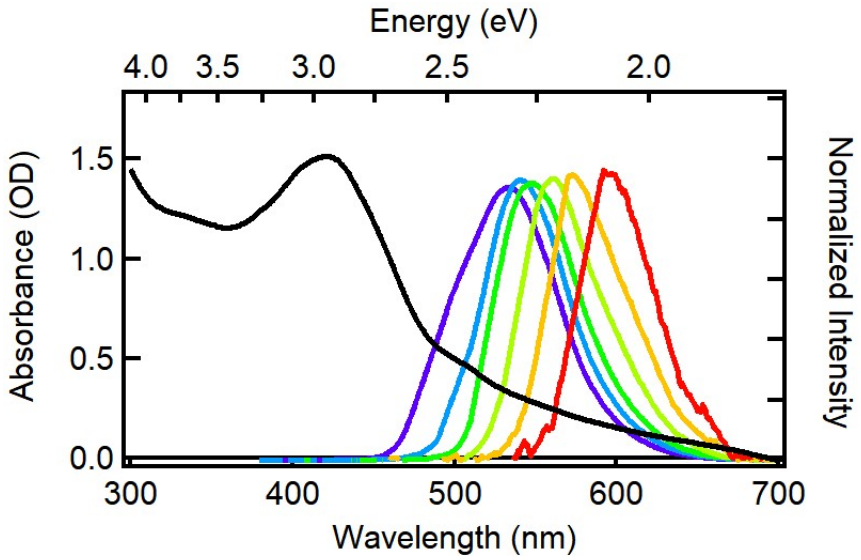

Figure 8.1: Absorption spectrum of CDs in DMF (1.25 g/L, recorded in 1 mm cell) and their normalized steady-state fluorescence (0.02 g/L) excited from 480 nm (purple curve peaking at 533 nm) to 580 nm (red curve peaking at 597 nm), in steps of 20 nm [236].

decay does not depend on the emission wavelength as shown in Figure 4.13. The largely unstructured low-energy absorption tail, combined with the strong tunability of the fluorescence, points to strong inhomogeneous effects affecting the optical properties of CDs.

One of the result of fractionation in chapter 4 is to produce a very homogeneous sample composed by particles with diameter of 6 nm (Figure 4.6) which display a very simple absorption (Figure 4.14) with a specified structure, and an almost not tunable emission (Figure 8.2). This strongly suggests that the absence of disorder produces the decrease of tunability.

Another evidence of the disorder as the cause of tunability comes from single molecule measurements. In fact, after that sample has been drop-casted on a substrate and dried, a rather uniform distribution of brightly emitting CD displaying no blinking effects (Figure 8.3) is recorded, as already achieved before [1]. Spectra from single and isolated CD have been recorded and are shown in Figure 8.3. Every spectrum is narrower than the bulk emission and differs from the others in terms of emission wavelength and shape, revealing that a statistical distribution of fluorescence spectra affects both the peak and the shape of the ensemble fluorescence. Moreover, spectra in Figure 8.3 show the homogeneous width of the emission which is definitely smaller (0.05 eV) than the fluorescence width of CDs ensemble (0.2-0.3 eV). These dot-to-dot variations are comparable to the literature [147] and are responsible for the large inhomogeneous width of CD broad and structureless fluorescence bands. These single-dot data allow to explain the characteristic fluorescence tunability of CDs considering that a particular excitation energy will single out a specific emissive fraction of the overall CD ensemble, and varying the excitation energy will cause a continuous shift of the entire emission spectrum. This interpretation contrasts with recent papers that interpreted the tunability as a violation of Kasha's rule due to an unusually slow relaxation of polar solvents around photoexcited CDs [146]. On the contrary, the solvatochromic study in chapter 5 and in chapter 6 demonstrates that the width of the band is solvent-independent (Figure 5.4), suggesting that solvent fluctuations have a negligible role in broadening the emission and, thus, the inhomogeneity of the band is related only to dot-to-dot fluctuations. On the other hand, our interpretation is in agreement with very recent paper [207] where, where the emission tunability is associated with the inhomogeneity of the sample, although the emission is attributed to a quantum confinement effect, which is absent in our case.

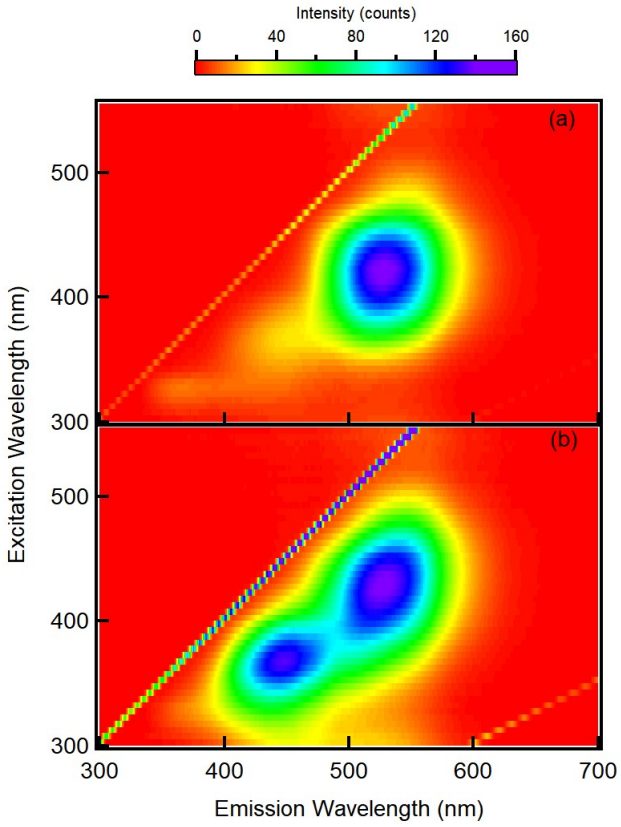

Figure 8.2: Photoluminescence two dimensional plot of (a) 6 nm CDs in water and (b) unfractionated sample. The oblique line across the entire plot derives from crossing of excitation and emission monochromators [Adapted form [206]].

8.2 Disentangling Homogeneous and Inhomogeneous Width by Ultrafast Hole Burning

Introduction

A further approach to address both the issue of tunability and the question on the true homogeneous lineshapes of electronic low-energy transitions is dynamical hole burning, a type of ultrafast transient absorption (TA) experiment in which tunable femtosecond light pulses selectively excite a narrow subset of chromophores in a disordered system, burning a "hole" into the overall absorption spectrum [237, 238].

Here, for the first time, hole burning methods have been applied to the study of CDs. As described in the following, these experiments allow to explain the fluorescence tunability as a photo-selection effect across a family of transitions with continuously variable energies, associated to the diverse surface structures of CDs, confirming the results obtained in section 8.1.

Ultrafast Hole burning

The ultrafast hole burning measurements have been performed on a solution of CDs dispersed in DMF at different excitation wavelengths from 495 to 570 nm. TA data at different excitation wavelengths are shown in Figure 8.4.

Extracting spectra at 50 ps from all the measurements (Figure 8.5), it is evident that the signal

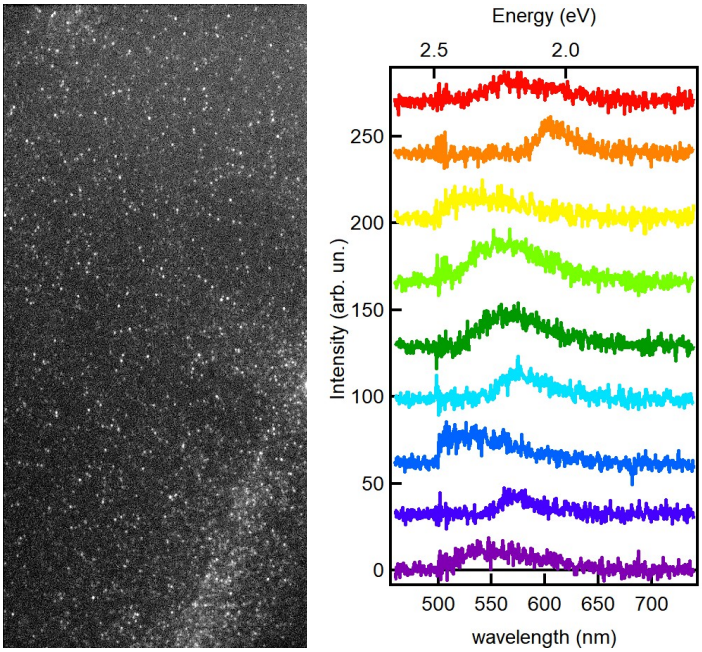

Figure 8.3: Left: Micro-photograph of a sample of CDs deposited on a quartz substrate and excited at 488 nm. Right: Single-molecule fluorescence spectra of CDs deposited on a quartz substrate and excited at 488 nm [219].

has similar structure at every excitation wavelength. The signal is the same at every excitation wavelength except for a rigid redshift which is a clear manifestation of the tunability. The entire signal can be described as a positive signal, an ESA, blueshifted from λ_{exc}, and a negative signal which corresponds to the sum of a GSB around the excitation wavelength plus a SE corresponding to the steady state fluorescence. All the signal undergoes a decay without changes on shape which involves all the features (GSB, SE, ESA), indicating that only a depopulation occurs (Figure 8.6).

These data contain two important results. On one hand, despite the shape of the low-energy OA tail (Figure 8.1) appears unstructured, very broad and covering ≈1 eV (450-650 nm), the GSB shown in Figure 8.5 corresponds only to a limited portion of the OA spectrum, and appears as a relatively narrow, Gaussian-shaped hole. This result is a direct evidence of inhomogeneity, because it indicates photo-selection of a subset of transitions resonant at excitation wavelength, out of a distribution of CDs having different transition energies. On the other hand, the rigid redshift of all the signal varying the excitation wavelength (Figure 8.5) is a proof that tunability affects all the three spectral features probed, and not only the emission.

From TA spectra at long delay (after the solvation is completed) one can subtract the normalized steady-state fluorescence spectra, considering that at this time the fluorescence necessarily matches the SE contributions to the TA, as displayed in Figure 8.7a.

In fact,the signal can be decomposed as in Figure 8.8 with three functions which represent the ESA (black curve in Figure 8.8), blueshifted from λ_{exc}, the GSB (purple curve in Figure 8.8), peaking around λ_{exc}, and a Stokes-shifted SE which resembles the steady state fluorescence (green curve in Figure 8.8). After the subtraction of the emission, the SE contribution is eliminated, and the residual consists only in a combination of the GSB and ESA contributions. Finally, these curves can be reproduced by the sum of two Gaussian shapes through a fitting procedure (Figure 8.7b). The results of the Gaussian fits are reported in Table 8.1, yielding the position and width of GSB and ESA as a function of λ_{exc}. The separation between GSB and ESA (Δ_{12}) is very similar whatever the excitation is (≈0.3-0.4 eV), and both signals have constant FWHM (≈0.4 and ≈ 0.8 eV,

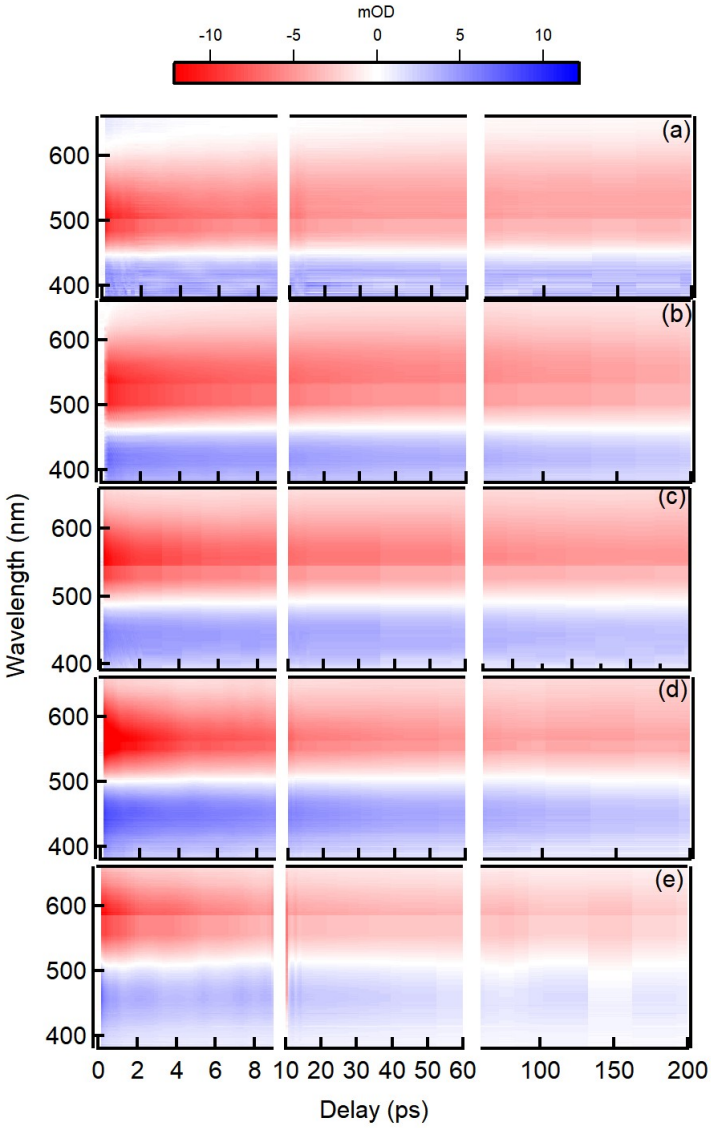

Figure 8.4: Two-dimensional time-wavelength plots of transient absorption measurements recorded with a pump wavelength of 495 nm (a), 520 nm (b), 537 nm (c), 554 nm (c) and 570 nm (d). These measurements were all performed at the same pump intensity and at magic angle polarization condition between pump and probe [236].

respectively).

These results confirm that each TA experiment shows the same signal except for a rigid shift. The unstructured absorption spectrum in the long-wavelength region, as it appears in steady-state OA (Figure 8.1), suggests that the latter consist in a superposition of an indefinite number of unresolved transitions with unknown spectral shapes. The hole-burning data provide a remarkably clear picture of these unresolved contributions: the tunable GSB, in fact, reflects the transient hole burned out by photo-excitation from the inhomogeneous distribution of OA transitions. These GSB "holes", if represented with a positive sign, can be seen as an individual homogeneous contribution to the overall OA band, as illustrated in Figure 8.9. Thus, we infer that the OA spectrum simply consists of a family of identical transitions with simple Gaussian shapes and continuously variable energies. For very large inhomogeneous width, the GSB width should be $\sqrt{2}$ times larger

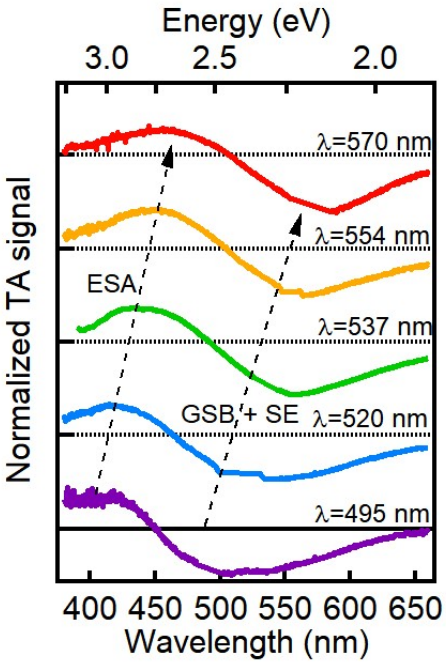

Figure 8.5: Spectra at 50 ps extracted from Figure 8.4 at different pump wavelengths are shown [236].

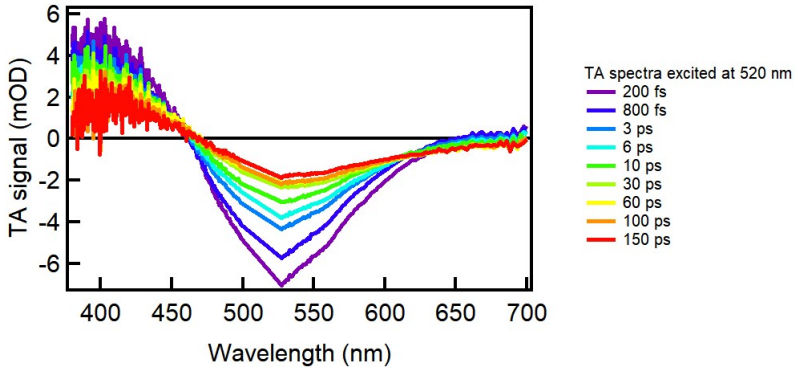

Figure 8.6: Transient absorption spectra recorded at 520 nm excitation of CDs in DMF as recorded at different delays between pump and probe. Data were recorded at magic angle condition between pump and probe. The region around 520 nm is removed because contaminated by the pump scattering [236].

than the underlying homogeneous width σ_h of the excited electronic transition [239], due to the convolution of two identical Gaussians (the photo-selection efficiency and the homogeneous line). Thereby, the OA homogeneous width of these transitions is $\sigma_h \approx 0.28$ eV. In contrast, the substantial broadness of the OA spectrum (>1 eV) comes from the superposition of many of these narrower OA bands, associated to different dots, with unequal chemical structures. In this picture, when tuning the excitation, the emission comes only from CDs photo-selected within σ_h. Considering this and that single-CD emission is very narrow (Figure 8.3), the ensemble steady-state emission is the superposition of single-dot bands, which defines the width of the band and should roughly match σ_h, which is verified in Figure 8.1. The values of σ_h are rather large if compared with typical semiconductor NP of comparable size [240], and larger than other CDs [207]. This

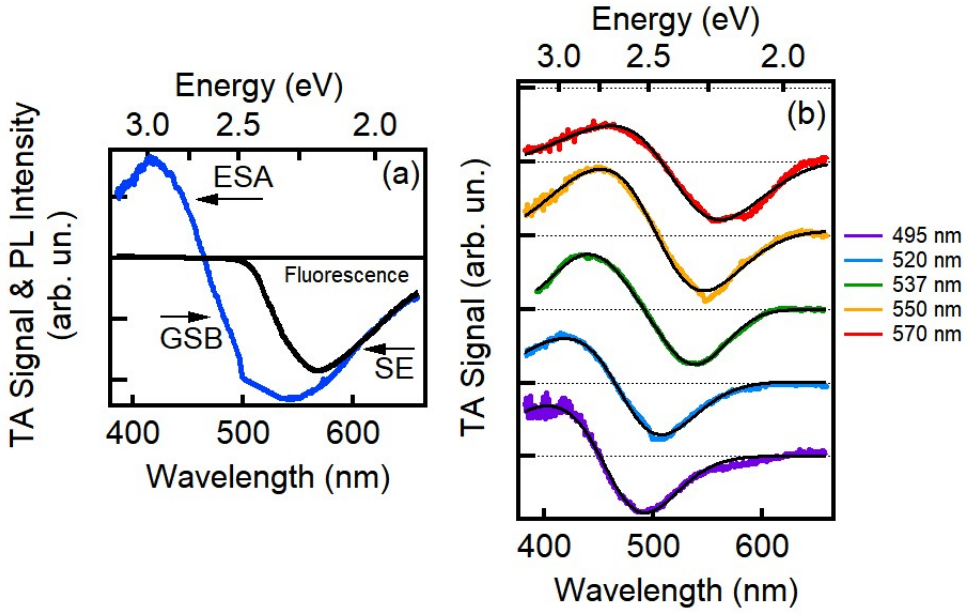

Figure 8.7: (a) Example of the subtraction procedure of the steady-state fluorescence band (black curve) from the TA spectrum excited at 520 nm (blue curve) used to eliminate the SE from the TA spectra and isolate only the GSB and the ESA contributions (b) The results of the subtraction procedure for the experiments at every pump wavelength (from 495 nm to 570 nm) are shown and fitted by the sum of two Gaussian curves representing the ESA (positive Gaussian profile) and the GSB (negative Gaussian profile) [236].

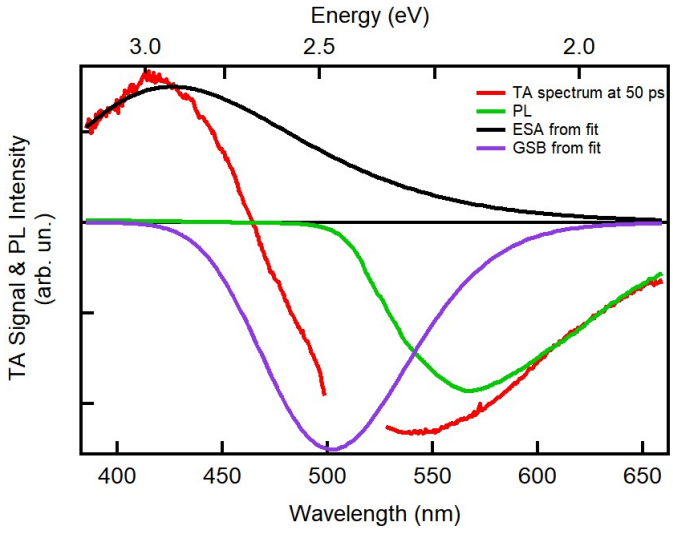

Figure 8.8: TA spectrum after 50 ps of the pulse excitation of CDs in DMF excited at 520 nm (red curve) decomposed with three curves which represent the ESA (black curve), the GSB (purple curve), and the SE/PL (green curve) [236].

width may arise from strong geometrical distortions of surface moieties caused by the photo induced electron transfer in these CDs, or from the involvement of different electronic substates in OA, the lowest of which yields the emission.

Considering the nature of the electronic transition as a core-to-surface electron transfer transi-

	GSB		ESA		
λ_{exc} (nm)	Peak (eV)	FWHM (eV)	Peak (eV)	FWHM (eV)	Δ_{12} (eV)
495	2.56 (484 nm)	0.42	3.00 (413 nm)	0.76	0.44
520	2.47 (502 nm)	0.40	2.91 (428 nm)	0.83	0.44
537	2.35 (528 nm)	0.38	2.70 (459 nm)	0.80	0.35
554	2.30 (539 nm)	0.38	2.67 (464 nm)	0.90	0.37
570	2.22 (558 nm)	0.37	2.65 (468 nm)	0.86	0.43

Table 8.1: Fit parameters of the curves in Figure 8.7 reproducing the GSB and ESA signal vs λ_{exc}. The accuracy on the peak position and on the FWHM is 0.05 eV. Δ_{12} is the separation between the two peaks [236].

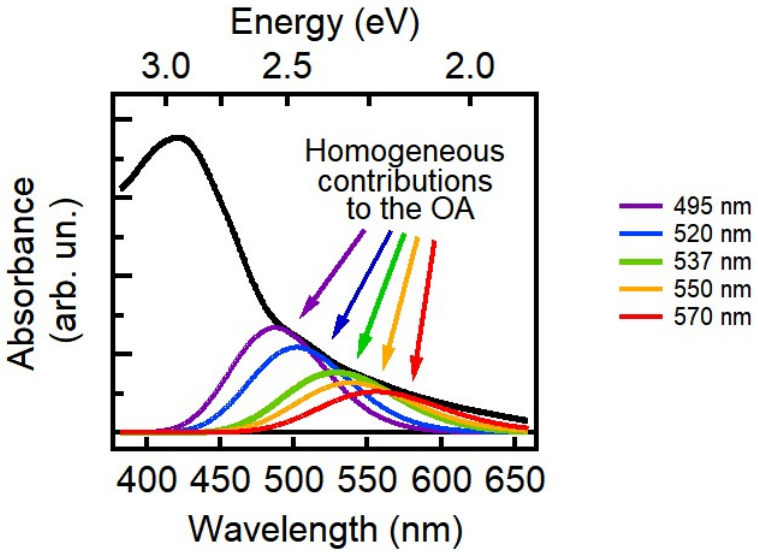

Figure 8.9: Comparison between steady-state OA and the individual homogeneous contributions (the GSB) obtained from the fitting procedure in Figure 8.7 represented with a positive sign [236].

tion (described in chapter 5) we suggest a tentative model to explain the tunability of these CDs.

It is worth remembering the results of section 4.1 and, in particular, the finding on the different-sized fractions of CDs. After the fractionation of an as-synthesized $\beta - C_3N_4$ sample, we obtained different sub-sets with different properties. To explain our tunability model, we focused the attention on the contrast between the homogeneity and the inhomogeneity of the fractions. Considering the size and the complex surface of the dots, as it was demonstrated in section 4.1, the bigger fraction (6 nm diameter) is the most homogeneous, and, on the contrary, the small fraction is the most inhomogeneous. Moreover, the absorption profile of bigger dots is well-defined and narrower than the one of the smallest fraction as shown in Figure 8.10.

The scheme of the tunability model is displayed in Figure 8.11. The acceptor state on the surface is built from mixing of local surface states such as surface states at the crystal boundary, or those of surface functional groups. Because the number of available surface states decreases with dot size, we expect smaller dots to feature a sparse density of surface states, while the smaller radius of curvature will work against their mutual mixing. In this regime, excited state energies will be very sensitive to minimal structural changes, like the change of a functional group, or the small deviation from a spherical shape, resulting in their broad inhomogeneous absorption (as the one of the smaller dots reported in Figure 8.10) which is depicted in the top part of Figure 8.11. Be-

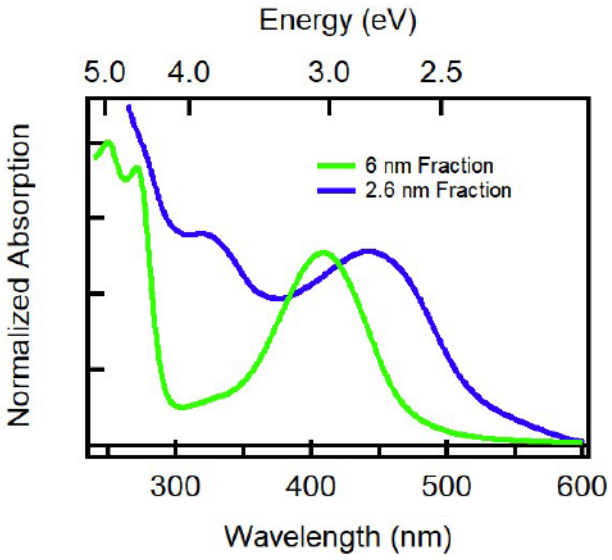

Figure 8.10: Absorption spectra of the biggest (green curve) and of the smallest fraction (blue curve) of $\beta - C_3N_4$ [?]

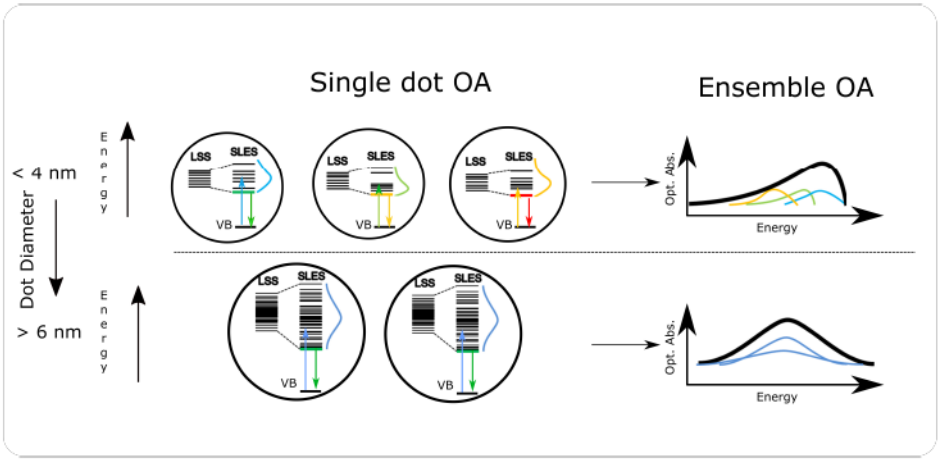

Figure 8.11: Graphical representation of the model proposed to explain the electronic properties of CDs in their low energy manifold. The distribution of local surface states (LSS) on each CD and their mutual coupling determines the distribution of the surface localized exciton (SLEs) states. The latter ultimately controls the emission energy. In small dots (Top panel), the small number of LSS per dot, and their large surface-to-volume ratio both cause strong dot-to-dot variations of the energy structure. As a consequence, the absorption and emission energies of each dot are unique and widely fluctuating, explaining their large fluorescence tunability. The sum of all single dot absorption spectra yields the overall absorption spectrum at the ensemble level (right part), very broad and highly asymmetrical. Large dots (Bottom panel) enter a statistical regime characterized by a large number of highly coupled LSS. In this case, dot-to-dot statistical fluctuations of the excited state energy become much smaller, and the ensemble OA absorption (lower right) becomes much narrower and Gaussian-like, with an increase of the homogeneous behaviour with respect to smaller dots. [236].

sides, structural variations of these CDs essentially occur at the surface, and therefore the effect of dot-to-dot variations will be crucial in small dots, where surface atoms are a significant fraction of

the entire structure. Conversely, an increase of the dot size will progressively increase the number of surface states per dot and enhance their coupling, entering into a statistical regime where the transition energies of excited states will be much less sensitive to small structural variations. In this case, the inhomogeneous broadening should become much smaller and the OA will assume a comparatively narrow, Gaussian-like shape, as depicted in bottom part of Figure 8.11 and suggested by the absorption profile of the biggest fraction (Figure 8.10). Our model is just a tentative one and more detailed studies are necessary to address the variation on the electronic properties to specific structural and chemical variations.

8.3 Conclusions

Single molecule measurements, fractionation, and ultrafast hole burning technique are different experimental approaches which have been useful to address the problem of emission tunability and to disentangle, for the first time, the homogeneous width of the absorption and emission from the inhomogeneous one. All of the results demonstrate that the tunability derives from dot-to-dot variations and, thus, it is directly linked with the inhomogeneity of the sample. These variations are probably related to the small size and the variable surface structure of each dot and this coupling determines the specific emission colour of the single dot, explaining the fluorescence tunability.

Chapter 9

Conclusions

The main goal of this work has been the systematic investigation of the fundamental optical response and electronic properties of carbon nanodots, as a function of possible different structures and under the influence of various interactions.

We succeeded in studying various families of CDs which, at a first glance, appear quite different being synthesized in a various ways (bottom up or top down methods) and displaying complex optical properties. But, by a deep investigation which includes the combined use of various characterization techniques, we were able to demonstrate the similarities and the differences among the samples. We found out a few fundamental features of CDs which appear to be general and independent of the specific type of nanodots, and others characteristics which drastically depend on the structure.

Bottom up synthesis allows to produce CDs with a fine control of the level of N-doping, which can be used to tailor their optical properties. Therefore, in a first set of studies, we carried out a systematic investigation on the structure and optical properties of these CDs as a function of their N content. By HRTEM and IR spectroscopy, we discovered that, in specific conditions, it is possible to synthesize an entirely new family of CDs, consisting in $\beta - C_3N_4$ core structure covered by a shell hosting a variety of different functional groups. These CDs, beside the particular core structure, display two bright emission bands with very different origin, here named *blue* and *visible* band.

The *blue* is quite common in CDs synthesized by bottom-up methods, as repeatedly reported in the literature. It is almost not tunable and seems to stem from an electronic transition which involves some molecular fluorophores produced during this type of synthesis, rather than from the carbonaceous dots in themselves.

In contrast, *visble* is directly associated to the dots, and shows the typical spectroscopic features of CDs, such as the fluorescence tunability. Therefore we focused most of our studies on this optical activity. In particular, we unravelled the entire photocycle of the visible band by the use of various optical techniques with time resolution which ranges from 10s of fs (transient absorption and fluorescence upconversion techniques) to the steady-state.

As a result, we demonstrated that the optical transition responsible of the visible band involves a coupling between the core and the surface of the nanoparticle, a novel interpretation with respect to the existing models of CD fluorescence transitions. In particular, photoexcitation of the dots produces a charge separation whereby the hole remains in the core and the electron is transferred on the surface. If the excitation is direct (that is, if these CDs are photoexcited at 400 nm), this charge separation and the population of the excited state (the transfer of the electron)

are instantaneous. Considering that the negative charge is on the surface, this transition is very sensitive to the environment, in particular, to H-bonds with solvent molecules. This sensitivity results in a solvation relaxation of the excited state which we directly revealed in the femto- and picosecond regime as a redshift of the band driven by the relaxation time of the specific solvent. Going to a longer time range (nanosecond), the effect of the solvent is evident not only in the shift of the band but also in a different emission lifetime and in a different non-radiative rate decay. All of the variations are regular with respect to the polarity of the solvent and to the capability to form H-bonds. The experiments demonstrated also that the depopulation of the system occurs in the nanosecond range indicating that the losses of emission quantum yield are only in this temporal range.

The sensitivity to the environment is also highlighted by the investigation on the interactions of CDs and ions in solution. Our studies show that the specific interaction between CDs and a given ion is determined by the interplay between the capability of CDs of donating an electron with the capability of the specific ion to accept it. This entails the possible decrease or increase of the emission intensity, observed in different cases. In fact, if the photoexcited CD can donate an electron to the ion, as observed when CDs interact with copper, iron or silver ions, the emission intensity decreases. On the contrary, if the ion cannot accept it, as in the case of zinc ions, the emission intensity undergoes an increase simply due to a screening effect which avoids the strong effects produced by the H-bonds with water molecules. In this context, we studied in detail the emission quenching mechanism within CD-ion complexes. Thereby we discovered that after the photoexcitation of the CD, an electron transfer occurs from the surface of the dot to the ion, hindering the radiative recombination. Our experiments revealed for the first time the ultrafast time scales of the electron transfer (0.2 ps and 2.1 ps) and highlighted that the reaction is driven by solvent molecules.

Beside the photocycle of the visible band and its interaction with the external environment, we studied its tunability, one of the most recurrent and characteristic features of CD fluorescence. By single molecule measurements and ultrafast hole burning, we were able to conclusively explain the tunability as due to the existence of a manifold of electronic states with continuously tunable energies which are an effect of inhomogeneity and disorder of the system related to the small size and to the variability of the surface groups. Moreover, for the first time, we disentangled the homogeneous width of the absorption and of the emission from the inhomogeneous one.

Beside our studies on $\beta - C_3N_4$ dots, especially interesting because of their novel structure, we also investigated CDs fabricated by other methods, trying to fully address the relation between structure and photocycle. In a series of studies, we compared two types of graphitic CDs synthesized either by bottom up or top down techniques. The former consists in graphitic CDs with low amount of nitrogen. Nitrogen impurities are partly hosted in the core and on the surface, in the form of amide groups. We found that this family of CDs displays only the blue emission already found for the $\beta - C_3N_4$, suggesting its common origin stemming from an electronic transition of a molecular fluorophore synthesized during the carbonization of citric acid and urea.

The top down graphitic sample, instead, does not include nitrogen in the core. It shows the typical tunable emission in the visible range which, as for $\beta - C_3N_4$ dots, is associated to the great inhomogeneity of the surface of the system. However, we demonstrate that the emission mechanism of these dots is completely different from the one we found for bottom up CDs. On one hand, we experimentally show that passivation is compulsory to have an emission, suggesting a key role of surface states. Yet, we find that the emission of these dots neither involves a coupling between core and surface states, nor can be associated to a single specific group. Instead, we find that the emitting chromophores are associated to the presence of several and different

groups which determine, by the mixing of wavefunctions, the existence of an emissive electronic transitions delocalized on the surface of the nanoparticle.

Also for these dots, we used a variety of femtosecond methods to fully elucidate the photocycle down to the fundamental level. Photoexciting the sample, the population of the excited state is instantaneous (faster than 70 fs), as for carbon nitride dots. At variance with $\beta - C_3N_4$, after the photoexcitation, the system undergoes ultrafast multi-exponential depopulations which are the main factor determining the low emission quantum yield.

Overall, our studies clarified many open issues in the understanding of the fundamental behaviour of CDs under photo-excitation.

Besides, they highlighted some fundamental features of CDs which appear to be "universal" and independent of the specific structure, and others which are dramatically structure-dependent. An example of the former is fluorescence tunability, that for all CDs we studied seems to arise from the dot-to-dot variations of surface structure, which give rise to a manifold of electronic levels with continuously tunable energies. An example of the latter is the fluorescence mechanisms, which appears to be completely different depending on the type of dot: core-to-surface coupling for $\beta - C_3N_4$ dots, surface-adsorbed or free molecular fluorophores for graphitic dots produced by bottom-up methods, delocalized surface states for top down graphitic dots.

Anyway, several interesting questions remain open and could be investigated by further experiments. It would certainly be very interesting to conduct more systematic studies to exploit the information gained here to fully optimize CDs in many different applications, such as lasing. On the other hand, further studies should address the sub-nanosecond non-radiative depopulation phenomena we observe in some CDs, in order to formulate strategies to improve their QY, or, more experiments with different techniques, as for example 2-dimensional ultrafast spectroscopy, could be very useful to understand the photocycle of the blue band and its precise nature.

Lastly, to conclude it is worth remembering that CDs are the focal point of several fundamental physical and chemical investigations and of studies in several different fields of application ranging from optoelectronics to bio-oriented nanotechnologies. The studies reported in this Thesis confirm the importance of Carbon Nanodots which definitely are very promising in several applications and are definitely revolutionising the world of light-emitting nanomaterials.

Bibliography

[1] Y. Sun, B. Zhou, Y. Lin, W. Wang, K. A. S. Fernando, P. Pathak, M. J. Meziani, B. A. Harruff, X. Wang, H. Wang, P. G. Luo, H. Yang, M. E. Kose, B. Chen, L. M. Veca, and S. Xie. Quantum-sized carbon dots for bright and colorful photoluminescence. *Journal of the American Chemical Society*, 128(24):7756–7757, 2006.

[2] X. Xu, R. Ray, Y. Gu, H. J. Ploehn, L. Gearheart, K. Raker, and W. A. Scrivens. Electrophoretic analysis and purification of fluorescent single-walled carbon nanotube fragments. *Journal of the American Chemical Society*, 126(40):12736–12737, 2004.

[3] V. Nguyen, J. Si, L. Yan, and X. Hou. Direct demonstration of photoluminescence originated from surface functional groups in carbon nanodots. *Carbon*, 108:268 – 273, 2016.

[4] L. Pan, S. Sun, A. Zhang, K. Jiang, L. Zhang, C. Dong, Q. Huang, A. Wu, and H. Lin. Truly fluorescent excitation-dependent carbon dots and their applications in multicolor cellular imaging and multidimensional sensing. *Advanced Materials*, 27:7782–7787, 2015.

[5] A. Cayuela, M. L. Soriano, and M. Valcàrcel. Photoluminescent carbon dot sensor for carboxylated multiwalled carbon nanotube detection in river water. *Sens. Actuators*, 207:596–601, 2015.

[6] D. B. Shinde and V. K. Pillai. Electrochemical preparation of luminescent graphene quantum dots from multiwalled carbon nanotubes. *Chem. Eur. J.*, pages 5801–5806, 2012.

[7] J. Zhou, Y. Yang, and C.-Y. Zhang. A low-temperature solid-phase method to synthesize highly fluorescent carbon nitride dots with tunable emission. *Chem. Commun.*, 49:8605–8607, 2013.

[8] M. Rong, X. Song, T. Zhao, Q. Yao, Y. Wang, and X. Chen. Synthesis of highly fluorescent p,o-g-c_3n_4 nanodots for the label-free detection of cu^{2+} and acetylcholinesterase activity. *J. Mater. Chem. C*, 3:10916–10924, 2015.

[9] A. B. Bourlinos, A. Stassinopoulos, D. Anglos, R. Zboril, M. Karakassides, and E. P. Giannelis. Surface functionalized carbogenic quantum dots. *Small*, pages 455–458, 2008.

[10] J. Zhou, C. Booker, R. Li, X. Zhou, T.-K. Sham, X. Sun, and Z. Ding. An electrochemical avenue to blue luminescent nanocrystals from multiwalled carbon nanotubes (mwcnts). *J. Am. Chem. Soc.*, pages 744–745, 2007.

[11] X. Miao, X. Yan, D. Qu, D. Li, F. F. Tao, and Z. Sun. Red emissive sulfur, nitrogen codoped carbon dots and their application in ion detection and theraonostics. *ACS Applied Materials & Interfaces*, 9(22):18549–18556, 2017.

[12] J. Lin Y. Fan Y. Li Y. Lv X. Liu Y. Zhang, Y. Hu. Excitation wavelength independence: toward low-threshold amplified spontaneous emission from carbon nanodot. *ACS Appl. MAter. Interfaces*, 8:25454–25460, 2016.

[13] S. Liu, J. Tian, L. Wang, Y. Zhang, X. Qin, Y. Luo, A. M. Asiri, A. O. Al-Youbi, and X. Sun. Hydrothermal treatment of grass: A low-cost, green route to nitrogen-doped, carbon-rich, photoluminescent polymer nanodots as an effective fluorescent sensing platform for label-free detection of cu(ii) ions. *Advanced Materials*, 24:2037–2041, 2012.

[14] H. Huang, J.-J. Lv, D.-L. Zhou, N. Bao, Y. Xu, A.-J. Wang, and J.-J. Feng. One-pot green synthesis of nitrogen-doped carbon nanoparticles as fluorescent probes for mercury ions. *RSC Adv.*, 3:21691–21696, 2013.

[15] Q. Xu, P. Pu, J. Zhao, C. Dong, C. Gao, Y. Chen, J. Chen, Y. Liu, and H. Zhou. Preparation of highly photoluminescent sulfur-doped carbon dots for fe(iii) detection. *J. Mater. Chem. A*, 3:542–546, 2015.

[16] H. Zhu, X. Wang, Y. Li, Z. Wang, F. Yang, and X. Yang. Microwave synthesis of fluorescent carbon nanoparticles with electrochemiluminescence properties. *Chem. Commun.*, pages 5118–5120, 2009.

[17] B. De and N. Karak. Recent progress in carbon dot-metal based nanohybrids for photochemical and electrochemical applications. *J. Mater Chem A*, 5:1826–1859, 2017.

[18] M. Liu, Y. Xu, F. Niu, J. J. Gooding, and J. Liu. Carbon quantum dots directly generated from electrochemical oxidation of graphite electrodes in alkaline alcohols and the applications for specific ferric ion detection and cell imaging. *Analyst*, page 2657, 2016.

[19] Z.-A. Qiao, Y. Wang, Y. Gao, H. Li, T. Dai, Y. Liu, and Q. Huo. Commercially activated carbon as the source for producing multicolor photoluminescent carbon dots by chemical oxidation. *Chem. Comm.*, pages 8812–8814, 2010.

[20] S. Qu, X. Wang, Q. Lu, X. Liu, and L. Wang. A biocompatible fluorescent ink based on water-soluble luminescent carbon nanodots. *Angew. Chem. Int. Ed.*, pages 12215–12218, 2012.

[21] L. Sui, W. Jin, S. Li, D. Liu, Y. Jiang, A. Chen, H. Liu, Y. Shi, D. Ding, and M. Jin. Ultrafast carrier dynamics of carbon nanodots in different ph environments. *Phys. Chem. Chem. Phys.*, pages 3838–3845, 2016.

[22] L. Wang, Y. Bi, J. Gao, Y. Li, H. Ding, and L. Ding. Carbon dots based turn-on fluorescent probes for the sensitive determination of glyphosate in environmental water samples. *RSC Adv.*, pages 85820–85828, 2016.

[23] V. Amendola and M. Meneghetti. What controls the composition and the structure of nanomaterials generated by laser ablation in liquid solution? *Phys. Chem. Chem. Phys.*, 15:3027–3046, 2013.

[24] D. Reyes, M. Camacho, M. Camacho, M. Mayorga, D. Weathers, G. Salamo, Z. Wang, and A. Neogi. Laser ablated carbon nanodots for light emission. *Nanoscale Research Letters*, 11(1):424, 2016.

[25] S. Hu, J. Liu, J. Yang, Y. Wang, and S. Cao. Laser synthesis and size tailor of carbon quantum dots. *J. Nanopart Res*, pages 7247–7252, 2011.

[26] G. H. A. Therese and P. V. Kamath. Electrochemical synthesis of metal oxides and hydroxides. *Chemistry of Materials*, 12(5):1195–1204, 2000.

[27] H. Li, X. He, Z. Kang, H. Huang, Y. Liu, J. Liu, S. Lian, C. H. A. Tsang, X. Yang, and S.-T. Lee. Water-soluble fluorescent carbon quantum dots and photocatalyst design. *Angew. Chem. Int. Ed.*, pages 4430–4434, 2010.

[28] L. Bao, Z.-L. Zhang, Z.-Q. Tian, L. Zhang, C. Liu, Y. Lin, B. Qi, and D.-W. Pang. Electrochemical tuning of luminescent carbon nanodots: from preparation to luminescence mechanism. *Adv. Mater.*, pages 5801–5806, 2011.

[29] S. Sahu, B. Behera, T. K. Maiti, and S. Mohapatra. Simple one-step synthesis of highly luminescent carbon dots from orange juice: application as excellent bio-imaging agents. *Chem. Commun.*, 48:8835–8837, 2012.

[30] L. Wang, Y. Wang, T. Xu, H. Liao, C. Yao, Y. Liu, Z. Li, Z. Chen, D. Pan, L. Sun, and M. Wu. Gram-scale synthesis of single-crystalline graphene quantum dots with superior optical properties. *Nature Comm*, 5:5357, 2014.

[31] Q. Liu, B. Guo, Z. Rao, B. Zhang, and J. R. Gong. Strong two-photon-induced fluorescence from photostable, biocompatible nitrogen-doped graphene quantum dots for cellular and deep-tissue imaging. *Nano Letters*, 13(6):2436–2441, 2013.

[32] W. Guan, W. Gu, L. Ye, C. Guo, S. Su, P. Xu, and M. Xue. Microwave-assisted polyol synthesis of carbon nitride dots from folic acid for cell imaging. *Int. J. Nanomed.*, 9:5071–5078, 2014.

[33] D. Wang, X. Wang, Y. Guo, W. Liu, and W. Qin. Luminescent properties of milk carbon dots and their sulphur and nitrogen doped analogues. *RSC Adv.*, 4:51658–51665, 2014.

[34] N. A. Travlou, J. Secor, and T. J. Bandosz. Highly luminescent s-doped carbon dots for the selective detection of ammonia. *Carbon*, 114:544 – 556, 2017.

[35] A. B. Bourlinos, G. Trivizas, M. A. Karakassides, M. Baikousi, A. Kouloumpis, D. Gournis, A. Bakandritsos, K. Hola, O. Kozak, R. Zboril, I. Papagiannouli, P. Aloukos, and S. Couris. Green and simple route toward boron doped carbon dots with significantly enhanced nonlinear optical properties. *Carbon*, 83:173 – 179, 2015.

[36] X. Shan, L. Chai, J. Ma, Z. Qian, J. Chen, and H. Feng. B-doped carbon quantum dots as a sensitive fluorescence probe for hydrogen peroxide and glucose detection. *Analyst*, 139:2322–2325, 2014.

[37] X. Hai, Q.-X. Mao, W.-J. Wang, X.-F. Wang, X.-W. Chen, and J.-H. Wang. An acid-free microwave approach to prepare highly luminescent boron-doped graphene quantum dots for cell imaging. *J. Mater. Chem. B*, 3:9109–9114, 2015.

[38] L. Zhang, Z.-Y. Zhang, R.-P. Liang, Y.-H. Li, and J.-D. Qiu. Boron-doped graphene quantum dots for selective glucose sensing based on the "abnormal" aggregation-induced photoluminescence enhancement. *Analytical Chemistry*, 86(9):4423–4430, 2014.

[39] S. Sarkar, K. Das, M. Ghosh, and P. K. Das. Amino acid functionalized blue and phosphorous-doped green fluorescent carbon dots as bioimaging probe. *RSC Adv.*, 5:65913–65921, 2015.

[40] J. Zhou, X. Shan, J. Ma, Y. Gu, Z. Qian, J. Chen, and H. Feng. Facile synthesis of p-doped carbon quantum dots with highly efficient photoluminescence. *RSC Adv.*, 4:5465–5468, 2014.

[41] L. Guo, J. Ge, W. Liu, G. Niu, Q. Jia, H. Wang, and P. Wang. Tunable multicolor carbon dots prepared from well-defined polythiophene derivatives and their emission mechanism. *Nanoscale*, 8:729–734, 2016.

[42] Y. H. Yuan, Z. X. Liu, R. S. Li, H. Y. Zou, M. Lin, H. Liu, and C. Z. Huang. Synthesis of nitrogen-doping carbon dots with different photoluminescence properties by controlling the surface states. *Nanoscale*, 8:6770–6776, 2016.

[43] K. Holá, M. Sudolská, S. Kalytchuk, D. Nachtigallová, A. L. Rogach, M. Otyepka, and R. Zbořil. Graphitic nitrogen triggers red fluorescence in carbon dots. *ACS Nano*, 11(12):12402–12410, 2017.

[44] Y. Liu, P. Wang, K. A. F. Shiral, G. E. LeCroy, H. Maimaiti, B. A. Harruff-Miller, W. K. Lewis, C. E. Bunker, Z.-L. Hou, and Y.-P. Sun. Enhanced fluorescence properties of carbon dots in polymer films. *J. Mater. Chem. C*, 4:6967–6974, 2016.

[45] H. Zheng, Q. Wang, Y. Long, H. Zhang, X. Huang, and R. Zhu. Enhancing the luminescence of carbon dots with a reduction pathway. *Chem. Commun.*, 47:10650–10652, 2011.

[46] Z.-C. Yang, M. Wang, A. M. Yong, S. Y. Wong, X.-H. Zhang, H. Tan, A. Y. Chang, X. Li, and J. Wang. Intrinsically fluorescent carbon dots with tunable emission derived from hydrothermal treatment of glucose in the presence of monopotassium phosphate. *Chem. Commun.*, 47:11615–11617, 2011.

[47] J. Schneider, C. J. Reckmeier, Y. Xiong, M. von Seckendorff, A. S. Susha, P. Kasák, A. L. Rogach, and Andrey L. Molecular fluorescence in citric acid-based carbon dots. *The Journal of Physical Chemistry C*, 121(3):2014–2022, 2017.

[48] Z.-H. Wen and X.-B. Yin. Excitation-independent carbon dots, from photoluminescence mechanism to single-color application. *RSC Adv.*, 6:27829, 2016.

[49] F. Arcudi, L. Dordovic, and M. Prato. Synthesis, separation, and characterization of small and highly fluorescent nitrogen-doped carbon nanodots. *Angew. Chem. Int. Ed.*, 55:2107–2112, 2016.

[50] A. Das, V. Gude, D. Roy, T. Chatterjee, C. K. De, and P. K. Mandal. On the molecular origin of photoluminescence of nonblinking carbon dot. *The Journal of Physical Chemistry C*, 121(17):9634–9641, 2017.

[51] N. Fuyuno, D. Kozawa, Y. Miyauchi, S. Mouri, R. Kitaura, H. Shinohara, T. Yasuda, N. Komatsu, and K. Matsuda. Drastic change in photoluminescence properties of graphene quantum dots by chromatographic separation. *Adv. Optical Mater.*, 2:983–989, 2014.

[52] J. C. Vinci, I. M. Ferrer, S. J. Seedhouse, A. K. Bourdon, J. M. Reynard, B. A. Foster, F. V. Bright, and L. A. Colòn. Hidden properties of carbon dots revealsed after HPCL fractionation. *J. Phys Chem Lett*, 4:239–243, 2013.

[53] A. Cayuela, M. L. Soriano, C. Carrillo-Carrion, and M. Valcarcel. Semiconductor and carbon-based fluorescent nanodots: the need for consistency. *Chem. Commun.*, 52:1311–1326, 2016.

[54] A. Cayuela, M. L. Soriano, and M. Valcàrcel. Strong luminescence of carbon dots induced by acetone passivation: efficient sensor for a rapid analysis of two different pollutants. *Anal. Chim. Acta*, 804:246–251, 2013.

[55] A. Cayuela, M. L. Soriano, and M. Valcàrcel. Reusable sensor based on functionalized carbon dots for the detection of silver nanoparticles in cosmetics via inner filter effect. *Anal. Chim. Acta*, 872:70–76, 2015.

[56] A. Cayuela, M. L. Soriano, M. C. Carriòn, and M. Valcàrcel. Functionalized carbon dots as sensors for gold nanoparticles in spiked samples: formation of nanohybrids. *Anal. Chim. Acta*, 820:133–138, 2014.

[57] H. Ding, P. Zhang, T.-Y. Wang, J.-L. Kong, and H.-M. Xiong. Nitrogen-doped carbon dots derived from polyvinyl pyrrolidone and their multicolor cell imaging. *Nanotechnology*, 25:205804, 2014.

[58] D. Pan, J. Zhang, Z. Li, and M. Wu. Hydrothermal route for cutting graphene sheets into blue-luminescent graphene quantum dots. *Adv. Mater.*, 22:734–738, 2010.

[59] S. Zhang, J. Li, M. Zeng, J. Xu, X. Wang, and W. Hu. Polymer nanodots of graphitic carbon nitride as effective fluorescent probes for the detection of fe3+ and cu2+ ions. *Nanoscale*, 6:4157–4162, 2014.

[60] G. Tong, J. Wang, R. Wang, X. Guo, L. He, F. Qiu, G. Wang, B. Zhu, X. Zhu, and T. Liu. Amorphous carbon dots with high two-photon fluorescence for cellular imaging passivated by hyperbranched poly(amino amine). *J. Mater. Chem. B*, 3:700–706, 2015.

[61] J-T. Margraf, V. Strauss, D. M. Guldi, and T. Clark. The electronic structure of amorphous carbon nanodots. *The Journal of Physical Chemistry B*, 119(24):7258–7265, 2015.

[62] H. Peng and J. Travas-Sejdic. Simple aqueous solution route to luminescent carbogenic dots from carbohydrates. *Chemistry of Materials*, 21(23):5563–5565, 2009.

[63] A. Sharma, T. Gadly, S. Neogy, S. K. Ghosh, and M. Kumbhakar. Molecular origin and self-assembly of fluorescent carbon nanodots in polar solvents. *The Journal of Physical Chemistry Letters*, 8(5):1044–1052, 2017.

[64] W. Zhang, L. Shi, Y. Liu, X. Meng, H. Xu, Y. Xu, B. Liu, X. Fang, H.-B. Li, and T. Ding. Supramolecular interactions via hydrogen bonding contributing to citric-acid derived carbon dots with high quantum yield and sensitive photoluminescence. *RSC Adv.*, 7:20345–20353, 2017.

[65] M. Varisco, D. Zufferey, A. Ruggi, Y. Zhang, R. Erni, and O. Mamula. Synthesis of hydrophilic and hydrophobic carbon quantum dots from waste of wine fermentation. *R Soc Open Sci*, 4:170900, 2017.

[66] C. Liu, P. Zhang, F. Tian, W. Li, F. Li, and W. Liu. One-step synthesis of surface passivated carbon nanodots by microwave assisted pyrolysis for enhanced multicolor photoluminescence and bioimaging. *J. Mater. Chem.*, 21:13163–13167, 2011.

[67] Y. Ding, F. Zhang, J. Xu, Y. Miao, Y. Yang, X. Liu, and B. Xu. Synthesis of short-chain passivated carbon quantum dots as the light emitting layer towards electroluminescence. *RSC Adv*, 7:28754, 2017.

[68] C. Wang, Z. Xu, and C. Zhang. Polyethyleneimine-functionalized fluorescent carbon dots: Water stability, ph sensing, and cellular imaging. *ChemNanoMat*, 1:122–127, 2015.

[69] H. Liu, T. Ye, and C. Mao. Fluorescent carbon nanoparticles derived from candle soot. *Angewandte Chemie International Edition*, 46(34):6473–6475, 2007.

[70] S. Lu, L. Sui, J. Liu, S. Zhu, A. Chen, M. Jin, and B. Yang. Near-infrared photoluminescent polymer–carbon nanodots with two-photon fluorescence. *Advanced Materials*, 29(15):1603443–n/a, 2017.

[71] S. Lu, G. Xiao, L. Sui, T. Feng, X. Yong, S. Zhu, B. Li, Z. Liu, B. Zou, M. Jin, J. S. Tse, H. Yan, and B. Yang. Piezochromic carbon dots with two-photon fluorescence. *Angewandte Chemie International Edition*, 56(22):6187–6191, 2017.

[72] X. Wang, S.-T. Wang, F. Lu, M. J. Meziani, L. Tian, K. W. Sun, M. A. Bloodgood, and Y.-P. Sun. Bandgap-like strong fluorescence in functionalized carbon nanoparticles. *Angew. Chem. Int. Ed*, 122:5438–5442, 2010.

[73] S. Zhu, Q. Meng, L. Wang, J. Zhang, Y. Song, H. Jin, K. Zhang, H. Sun, H. Wang, and B. Yang. Highly photoluminescent carbon dots for multicolor patterning, sensors and bioimaging. *Angew. Chem. Int. Ed.*, 52:3953–3957, 2013.

[74] J. Hou, W. Wang, T. Zhou, B. Wang, H. Li, and L. Ding. Synthesis and formation mechanistic investigation of nitrogen- doped carbon-dots with high quantum yield and yellowish-green fluorescence. *Nanoscale*, 8:11185–11193, 2016.

[75] D. Pan, J. Zhang, Z. Li, C. Wu, X. Yan, and M. Wu. Observation of pH, solvent-, spin-, and excitation-dependent blue photoluminescence from carbon nanoparticles. *Chem. Commun.*, 46:3681–3683, 2010.

[76] O. Kozák, K. K.R. Datta, M. Greplová, V. Ranc, J. Kašlík, and R. Zbořil. Surfactant-derived amphiphilic carbon dots with tunable photoluminescence. *The Journal of Physical Chemistry C*, 117(47):24991–24996, 2013.

[77] D. Zhou, D. Li, P. Jing, Y. Zhai, D. Shen, S. Qu, and A. L. Rogach. Conquering aggregation-induced solid-state luminescence quenching of carbon dots through a carbon dots-triggered silica gelation process. *Chemistry of Materials*, 29(4):1779–1787, 2017.

[78] Y. Chen, M. Zheng, H. Xiao, Y. Dong, H. Zhang, J. Zhuang, H. Hu, B. Lei, and Y. Liu. A self-quenching-resistan carbon-dot powder with tunable solid-state fluorescence and construction of dual-fluorescence morphologies for white light-emission. *Adv. MAter*, 28, 2015.

[79] G E. LeCroy, F. Messina, A. Sciortino, C. E. Bunker, P. Wang, K. A. F. Shiral, and Y.-P. S. Characteristic excitation wavelength dependence of fluorescence emissions in carbon "quantum" dots. *The Journal of Physical Chemistry C*, 121(50):28180–28186, 2017.

[80] Y. Shi, C. Li, Z. Liu, J. Zhu, J. Yang, and X. Hu. Facile synthesis of lfuorescent carbon dots for determination of curcumin based on fluorescence resonance enrgy transfer. *RSC Adv*, 5:64790–64796, 2015.

[81] M. Muhammad, F. Baig, and Y.-C. Chen. Bright carbon dots as fluorescence sensing agents for bacteria and curcumin. *Journal of Colloid and Interface Science*, 501:341 – 349, 2017.

[82] X. Wu, Y. Song, X. Yan, C. Zhu, Y. Ma, D. Du, and Y. Lin. Carbon quantum dots as fluorescence resonance energy transfer sensors for organophosphate pesticides determination. *Biosensors and Bioelectronics*, 94:292 – 297, 2017.

[83] Z. Zhu, J. Ma, Z. Wang, C. Mu, Z. Fan, L. Du, Y. Bai, L. Fan, H. Yan, D. L. Phillips, and S. Yang. Efficiency enhancement of perovskite solar cells through fast electron extraction: The role of graphene quantum dots. *Journal of the American Chemical Society*, 136(10):3760–3763, 2014.

[84] I. Mihalache, A. Radoi, M. Mihaila, C. Munteanu, A. Marin, M. Danila, M. Kusko, and C. Kusko. Charge and energy transfer interplay in hybrid sensitized solar cells mediated by graphene quantum dots. *Electrochimica Acta*, 153:306 – 315, 2015.

[85] Q.-L. Chen, C.-F. Wang, and S. Chen. One-step synthesis of yellow-emitting carbogenic dots toward white light-emitting diodes. *J Material Science*, 48:2352–2357, 2012.

[86] J. B. Essner and G. A. Baker. The emerging roles of carbon dots in solar photovoltaics: a critical review. *Environ. Sci.: Nano*, 4:1216–1263, 2017.

[87] S. Zhu, Q. Meng, L. Wang, J. Zhang, Y. Song, H. Jin, K. Zhang, H. Sun, H. Wang, and B. Yang. Highly photoluminescent carbon dots for multicolor patterning, sensors, and bioimaging. *Angewandte Chemie*, 125:4045–4049, 2013.

[88] X. Yang, Y. Zhuo, S. Zhu, Y. Luo, Y. Feng, and Y. Dou. Novel and green synthesis of high-fluorescent carbon dots originated from honey for sensing and imaging. *Biosensors and Bioelectronics*, 60:292 – 298, 2014.

[89] H. Zhang, Y. Chen, M. Liang, L. Xu, S. Qi, H. Chen, and X. Chen. Solid-phase synthesis of highly fluorescent nitrogen-doped carbon dots for sensitive and selective probing ferric ions in living cells. *Analytical Chemistry*, 86(19):9846–9852, 2014.

[90] Y.-L. Zhang, L. Wang, H.-C. Zhang, Y. Liu, H.-Y. Wang, Z.-H. Kang, and S.-T. Lee. Graphitic carbon quantum dots as a fluorescent sensing platform for highly efficient detection of fe^{3+} ions. *RSC Adv.*, 3:3733–3738, 2013.

[91] W. Lu, X. Qin, S. Liu, G. Chang, Y. Zhang, Y. Luo, A. M. Asiri, A. O. Al-Youbi, and X. Sun. Economical, green synthesis of fluorescent carbon nanoparticles and their use as probes for sensitive and selective detection of mercury(ii) ions. *Analytical Chemistry*, 84(12):5351–5357, 2012.

[92] H. X. Zhao, L. Q. Liu, Z. D. Liu, Y. Wang, X. J. Zhao, and C. Z. Huang. Highly selective detection of phosphate in very complicated matrixes with an off-on fluorescent probe of europium-adjusted carbon dots. *Chem. Commun.*, 47:2604–2606, 2011.

[93] X. Hou, F. Zeng, F. Du, and S. Wu. Carbon-dot-based fluorescent turn-on sensor for selectively detecting sulfide anions in totally aqueous media and imaging inside live cells. *Nanotechnology*, 24:335502, 2013.

[94] S. Li, I. Skromne, Z. Peng, J. Dallman, A. O. Al-Youbi, A. S. Bashammakh, M. S. El-Shahawi, and R. M. Leblanc. "dark" carbon dots specifically "light-up" calcified zebrafish bones. *J. Mater. Chem. B*, 4:7398–7405, 2016.

[95] H. Tao, K. Yang, Z. Ma, J. Wan, Y. Zhang, Z. Kang, and Z. Liu. In vivo nir fluorescence imaging, biodistribution, and toxicology of photoluminescent carbon dots produced from carbon nanotubes and graphite. *Small*, 8(2):281–290, 2012.

[96] M. Zheng, S. Ruan, S. Liu, T. Sun, D. Qu, H. Zhao, Z. Xie, H. Gao, X. Jing, and Z. Sun. Self-targeting fluorescent carbon dots for diagnosis of brain cancer cells. *ACS Nano*, 9(11):11455–11461, 2015.

[97] Y.-F. Kang, Y.-H. Li, Y.-W. Fang, Y. Xu, X.-M. Wei, and X.-B. Yin. Carbon quantum dots for zebrafish fluorescence imaging. *Scientific reports*, 5:11835, 2015.

[98] Z.-B. Qu, X. Zhou, L. Gu, R. Lan, D. Sun, D. Yu, and G. Shi. Boronic acid functionalized graphene quantum dots as a fluorescent probe for selective and sensitive glucose determination in microdialysate. *Chem. Commun.*, 49:9830–9832, 2013.

[99] R. M. Shereema, T. V. Sruthi, V. B. S. Kumar, T. P. Rao, and S. S. Shankar. Angiogenic profiling of synthesized carbon quantum dots. *Biochemistry*, 54(41):6352–6356, 2015.

[100] C. Liu, P. Zhang, X. Zhai, F. Tian, W. Li, J. Yang, Y. Liu, H. Wang, W. Wang, and W. Liu. Nano-carrier for gene delivery and bioimaging based on carbon dots with pei-passivation enhanced fluorescence. *Biomaterials*, 33(13):3604 – 3613, 2012.

[101] J. Xu, F. Zeng, H. Wu, C. Hu, C. Yu, and S. Wu. Preparation of a mitochondria-targeted and no-releasing nanoplatform and its enhanced pro-apoptotic effect on cancer cells. *Small*, 10:3750–3760, 2014.

[102] J. Pardo, Z. Peng, and R. M. Leblanc. Cancer targeting and drug delivery using carbon-based quantum dots and nanotubes. *Molecules*, 23(2), 2018.

[103] X. Dong, M. M. Moyer, F. Yang, Y.-P. Sun, and L. Yang. Carbon dots' antiviral functions against noroviruses. *Scientific reports*, 7:519, 2017.

[104] A. Barras, Q. Pagneux, F. Sane, Q. Wang, R. Boukherroub, D. Hober, and S. Szunerits. High efficiency of functional carbon nanodots as entry inhibitors of herpes simplex virus type 1. *ACS Applied Materials & Interfaces*, 8(14):9004–9013, 2016.

[105] A. K. Roy, S.-M. Kim, P. Paoprasert, S.-Y. Park, and I. In. Preparation of biocompatible and antibacterial carbon quantum dots derived from resorcinol and formaldehyde spheres. *RSC Adv.*, 5:31677–31682, 2015.

[106] N. Sultana, P. K. Raul, D. Goswami, B. Das, H. K. Gogoi, and P. S. Raju. Nanoweapon: control of mosquito breeding using carbon-dot-silver nanohybrid as a biolarvicide. *Environmental Chemistry Letters*, 2018.

[107] J. Zong, X. Yang, A. Trinchi, S. Hardin, I. Cole, Y. Zhu, C. Li, T. Muster, and G. Wei. Carbon dots as fluorescent probes for "off–on" detection of cu^{2+} and l-cysteine in aqueous solution. *Biosensors and Bioelectronics*, 51:330 – 335, 2014.

[108] L. Zhang, Y. Han, J. Zhu, Y. Zhai, and S. Dong. Simple and sensitive fluorescent and electrochemical trinitrotoluene sensors based on aqueous carbon dots. *Analytical Chemistry*, 87(4):2033–2036, 2015.

[109] D. Shi, F. Yan, T. Zheng, Y. Wang, X. Zhou, and L. Chen. P-doped carbon dots act as a nanosensor for trace 2,4,6-trinitrophenol detection and a fluorescent reagent for biological imaging. *RSC Adv.*, 5:98492–98499, 2015.

[110] R. Liu, H. Li, W. Kong, J. Liu, Y. Liu, C. Tong, X. Zhang, and Z. Kang. Ultra-sensitive and selective hg^{2+} detection based on fluorescent carbon dots. *Materials Research Bulletin*, 48(7):2529 – 2534, 2013.

[111] C. Liu, B. Tang, S. Zhang, M. Zhou, M. Yang, Y. Liu, Z.-L. Zhang, B. Zhang, and D.-W. Pang. Photoinduced electron transfer mediated by coordination between carboxyl on carbon nanodots and cu^{2+} quenching photoluminescence. *The Journal of Physical Chemistry C*, 122(6):3662–3668, 2018.

[112] S. Hu, Q. Zhao, Q. Chang, J. Yang, and J. Liu. Enhanced performance of fe^{3+} detection via fluorescence resonance energy transfer between carbon quantum dots and rhodamine b. *RSC Adv.*, 4:41069–41075, 2014.

[113] Y. Wang, K. Jiang, J. Zhu, L. Zhang, and H. Lin. A fret-based carbon dot-mno_2 nanosheet architecture for glutathione sensing in human whole blood samples. *Chem. Commun.*, 51:12748–12751, 2015.

[114] Y. Hu, J. Yang, L. Jia, and J.-S. Yu. Ethanol in aqueous hydrogen peroxide solution: Hydrothermal synthesis of highly photoluminescent carbon dots as multifunctional nanosensors. *Carbon*, 93:999 – 1007, 2015.

[115] X. Sun and Y. Lei. Fluorescent carbon dots and their sensing applications. *Trends in Analytical Chemistry*, 89:163–180, 2017.

[116] S. Chandra, P. Patra, S. H. Pathan, S. Roy, S. Mitra, A. Layek, R. Bhar, P. Pramanik, and A. Goswami. Luminescent s-doped carbon dots: an emergent architecture for multimodal applications. *J. Mater. Chem. B*, 1:2375–2382, 2013.

[117] D. Zhao, C. Chen, L. Lu, F. Yang, and X. Yang. A dual-mode colorimetric and fluorometric "light on" sensor for thiocyanate based on fluorescent carbon dots and unmodified gold nanoparticles. *Analyst*, 140:8157–8164, 2015.

[118] Q. Qu, A. Zhu, X. Shao, G. Shi, and Y. Tian. Development of a carbon quantum dots-based fluorescent cu^{2+} probe suitable for living cell imaging. *Chem. Commun.*, 48:5473–5475, 2012.

[119] X. Lin, G. Gao, L. Zheng, Y. Chi, and G. Chen. Encapsulation of strongly fluorescent carbon quantum dots in metal–organic frameworks for enhancing chemical sensing. *Analytical Chemistry*, 86(2):1223–1228, 2014.

[120] Sa. Mohapatra, S. Sahu, S. Nayak, and S. K. Ghosh. Design of fe_3o_4@sio_2@carbon quantum dot based nanostructure for fluorescence sensing, magnetic separation, and live cell imaging of fluoride ion. *Langmuir*, 31(29):8111–8120, 2015.

[121] X. Wang, J. Zhang, W. Zou, and R. Wang. Facile synthesis of polyaniline/carbon dot nanocomposites and their application as a fluorescent probe to detect mercury. *RSC Adv.*, 5:41914–41919, 2015.

[122] A. Zhu, Q. Qu, X. Shao, B. Kong, and Y. Tian. Carbon-dot-based dual-emission nanohybrid produces a ratiometric fluorescent sensor for in vivo imaging of cellular copper ions. *Angewandte Chemie International Edition*, 51(29):7185–7189, 2012.

[123] S. Qu, H. Chen, X. Zheng, J. Cao, and X. Liu. Ratiometric fluorescent nanosensor based on water soluble carbon nanodots with multiple sensing capacities. *Nanoscale*, 5:5514–5518, 2013.

[124] S. Xie, H. Su, W. Wei, M. Li, Y. Tong, and Z. Mao. Remarkable photoelectrochemical performance of carbon dots sensitized tio_2 under visible light irradiation. *J. Mater. Chem. A*, 2:16365–16368, 2014.

[125] H. Zhang, H. Ming, S. Lian, H. Huang, H. Li, L. Zhang, Y. Liu, Z. Kang, and S.-T. Lee. Fe_2o_3/carbon quantum dots complex photocatalysts and their enhanced photocatalytic activity under visible light. *Dalton Trans.*, 40:10822–10825, 2011.

[126] L. Cao, S. Sahu, P. Anilkumar, C. E. Bunker, J. Xu, K. A. S. Fernando, P. Wang, E. A. Guliants, K. N. Tackett, and Y.-P. Sun. Carbon nanoparticles as visible-light photocatalysts for efficient co_2 conversion and beyond. *Journal of the American Chemical Society*, 133(13):4754–4757, 2011.

[127] A. Mehta, P. D., A. Thakur, and S. Basu. Enhanced photocatalytic water splitting by gold carbon dot core shell nanocatalyst under visible/sunlight. *New J. Chem.*, 41:4573–4581, 2017.

[128] Y. Song, S. Zhu, S. Zhang, Y. Fu, L. Wang, X. Zhao, and B. Yang. Investigation from chemical structure to photoluminescent mechanism: a type of carbon dots from the pyrolysis of citric acid and an amine. *J. Mater. Chem. C*, 3:5976–5984, 2015.

[129] L.-S. Li and X. Yan. Colloidal graphene quantum dots. *The Journal of Physical Chemistry Letters*, 1(17):2572–2576, 2010.

[130] M. L. Mueller, X. Yan, B. Dragnea, and L.-S. Li. Slow hot-carrier relaxation in colloidal graphene quantum dots. *Nano Letters*, 11(1):56–60, 2011.

[131] L. Cao, M. J. Meziani, S. Sahu, and Y.-P. Sun. Photoluminescence properties of graphene versus other carbon nanomaterials. *Accounts of Chemical Research*, 46(1):171–180, 2013.

[132] P. Reineck, D. W. M. Lau, E. R. Wilson, K. Fox, M. R. Field, C. Deeleepojananan, V. N. Mochalin, and B. C. Gibson. Effect of surface chemistry on the fluorescence of detonation nanodiamonds. *ACS Nano*, 11(11):10924–10934, 2017.

[133] S. Zhu, L. Wang, L. Bo, Y. Song, X. Zhao, G. Zhang, S. Zhang, S. Lu, J. Zhang, H. Wang, H. Sun, and B. Yang. Investigation of photoluminescence mechanism of graphene quantum dots and evaluation of their assembly into polymer dots. *Carbon*, 77:462 – 472, 2014.

[134] M. A. Sk, A. Ananthanarayanan, L. Huang, K. H. Lim, and P. Chen. Revealing the tunable photoluminescence properties of graphene quantum dots. *J. Mater. Chem. C*, 2:6954–6960, 2014.

[135] G. Eda, Y.-Y. Lin, C. Mattevi, H. Yamaguchi, H.-A. Chen, I-S. Chen, C.-W. Chen, and M. Chhowalla. Blue photoluminescence from chemically derived graphene oxide. *Advanced Materials*, 22(4):505–509.

[136] J. Peng, W. Gao, B. K. Gupta, Z. Liu, R. Romero-Aburto, L. Ge, L. Song, L. B. Alemany, X. Zhan, G. Gao, S. A. Vithayathil, B. A. Kaipparettu, A. A. Marti, T. Hayashi, J.-J. Zhu, and P. M. Ajayan. Graphene quantum dots derived from carbon fibers. *Nano Letters*, 12(2):844–849, 2012.

[137] S. Zhu, J. Zhang, X. Liu, B. Li, X. Wang, S. Tang, Q. Meng, Y. Li, C. Shi, R. Hu, and B. Yang. Graphene quantum dots with controllable surface oxidation, tunable fluorescence and up-conversion emission. *RSC Adv.*, 2:2717–2720, 2012.

[138] L. Wang, S.-J. Zhu, H.-Y. Wang, S.-N. Qu, Y.-L. Zhang, J.-H. Zhang, Q.-D. Chen, H.-L. Xu, W. Han, B. Yang, and H.-B. Sun. Common origin of green luminescence in carbon nanodots and graphene quantum dots. *ACS Nano*, 8(3):2541–2547, 2014.

[139] L. Shi, J. H. Yang, H. B. Zeng, Y. M. Chen, S. C. Yang, C. Wu, H. Zeng, O. Yoshihito, and Q. Zhang. Carbon dots with high fluorescence quantum yield: the fluorescence originates from organic fluorophores. *Nanoscale*, 8:14374–14378, 2016.

[140] W. Wang, B. Wang, H. Embrechts, C. Damm, A. Cadranel, V. Strauss, M. Distaso, V. Hinterberger, D. M. Guldi, and Wolfgang Peukert. Shedding light on the effective fluorophore structure of high fluorescence quantum yield carbon nanodots. *RSC Adv.*, 7:24771–24780, 2017.

[141] C. J. Reckmeier, J. Schneider, Y. Xiong, J. Häusler, P. Kasák, W. Schnick, and A. L. Rogach. Aggregated molecular fluorophores in the ammonothermal synthesis of carbon dots. *Chemistry of Materials*, 29(24):10352–10361, 2017.

[142] X. Liu, H.-B. Li, L. Shi, X. Meng, Y. Wang, X. Chen, H. Xu, W. Zhang, X. Fang, and T. Ding. Structure and photoluminescence evolution of nanodots during pyrolysis of citric acid: from molecular nanoclusters to carbogenic nanoparticles. *J. Mater. Chem. C*, 5:10302–10312, 2017.

[143] W. Kasprzyk, S. Bednarz, P. Zmudzki, M. Galica, and D. Bogdal. Novel efficient fluorophores synthesized from citric acid. *RSC Adv.*, 5:34795–34799, 2015.

[144] A. P. Demchenko and M. O. Dekaliuk. The origin of emissive states of carbon nanoparticles derived from ensemble-averaged and single-molecular studies. *Nanoscale*, 8:14057–14069, 2016.

[145] S. Khan, N. C. Verma, R. Chethana, and C. K. Nandi. Carbon dots for single-molecule imaging of the nucleolus. *ACS Applied Nano Materials*, 1(2):483–487, 2018.

[146] S. Khan, A. Gupta, N. C. Verma, and C. K. Nandi. Time-resolved emission reveals ensemble of emissive states as the origin of multicolor fluorescence in carbon dots. *Nano Letters*, 15(12):8300–8305, 2015.

[147] S. Ghosh, A. M. Chizhik, N. Karedla, M. O. Dekaliuk, I. Gregor, H. Schuhmann, M. Seibt, K. Bodensiek, I. A. T. Schaap, O. Schulz, A. P. Demchenko, J. Enderlein, and A. I. Chizhik. Photoluminescence of carbon nanodots: Dipole emission centers and electron–phonon coupling. *Nano Letters*, 14(10):5656–5661, 2014.

[148] S. K. Das, Y. Liu, S. Yeom, D. Y. Kim, and C. I. Richards. Single-particle fluorescence intensity fluctuations of carbon nanodots. *Nano Letters*, 14(2):620–625, 2014.

[149] B. van Dam, H. Nie, B. Ju, E. Marino, J. M. J. Paulusse, P. Schall, M. Li, and K. Dohnalová. Excitation-dependent photoluminescence from single-carbon dots. *Small*, 13(48):1702098, 2017.

[150] H. Lin, R. P. Hania, R. Bloem, O. Mirzov, D. Thomsson, and I. G. Scheblykin. Single chain versus single aggregate spectroscopy of conjugated polymers. where is the border? *Phys. Chem. Chem. Phys.*, 12:11770–11777, 2010.

[151] F. Ehrat, S. Bhattacharyya, J. Schneider, A. Löf, R. Wyrwich, A. L. Rogach, J. K. Stolarczyk, A. S. Urban, and J. Feldmann. Tracking the source of carbon dot photoluminescence: Aromatic domains versus molecular fluorophores. *Nano Letters*, 17(12):7710–7716, 2017.

[152] X. Wang, L. Cao, F. Lu, M. J. Meziani, H. Li, G. Qi, B. Zhou, B. A. Harruff, F. Kermarrec, and Y.-P. Sun. Photoinduced electron transfers with carbon dots. *Chem. Commun.*, pages 3774–3776, 2009.

[153] S. Chandra, S. H. Pathan, S. Mitra, B. H. Modha, A. Goswami, and P. Pramanik. Tuning of photoluminescence on different surface functionalized carbon quantum dots. *RSC Adv.*, 2:3602–3606, 2012.

[154] Z. Qian, J. Ma, X. Shan, H. Feng, L. Shao, and J. Chen. Highly luminescent n-doped carbon quantum dots as an effective multifunctional fluorescence sensing platform. *Chemistry – A European Journal*, 20(8):2254–2263, 2014.

[155] J. C. Wang, K. Violette, O. O. Ogunsolu, and K. Hanson. Metal ion mediated electron transfer at dye-semiconductor interfaces. *Phys. Chem. Chem. Phys.*, 19:2679–2682, 2017.

[156] W. Wei, C. Xu, J. Ren, B. Xu, and X. Qu. Sensing metal ions with ion selectivity of a crown ether and fluorescence resonance energy transfer between carbon dots and graphene. *Chem. Commun.*, 48:1284–1286, 2012.

[157] C. Yuan, B. Liu, F. Liu, M.-Y. Han, and Z. Zhang. Fluorescent "turn on" detection of mercuric ion based on bis(sithiocarbamato)copper(ii) complex fnctionalized carbon nanodots. *Anal. Chem.*, 86:1123–1130, 2014.

[158] S. Mondal, S. K. Seth, P. Gupta, and P. Purkayastha. Ultrafast photoinduced electron transfer between carbon nanoparticles and cyclometalated rhodium and iridium complexes. *The Journal of Physical Chemistry C*, 119(44):25122–25128, 2015.

[159] M. K. Barman, B. Jana, S. Bhattacharyya, and A. Patra. Photophysical properties of doped carbon dots (n, p, and b) and their influence on electron/hole transfer in carbon dots–nickel (ii) phthalocyanine conjugates. *The Journal of Physical Chemistry C*, 118(34):20034–20041, 2014.

[160] F. Rigodanza, L. Dordevic, F. Arcudi, and M. Prato. Customizing the electrochemical properties of carbon nanodots by using quinones in bottom up synthesis. *Angewandte Chemie International Edition*, 0(0), 2018.

[161] P. Jing, D. Han, D. Li, D. Zhou, L. Zhang, H. Zhang, D. Shen, and S. Qu. Origin of anisotropic photoluminescence in heteroatom-doped carbon nanodots. *Advanced Optical Materials*, 5(8):1601049–n/a, 2017.

[162] Y. Song, S. Zhu, S. Xiang, X. Zhao, J. Zhang, H. Zhang, Y. Fu, and B. Yang. Investigation into the fluorescence quenching behaviors and applications of carbon dots. *Nanoscale*, 6:4676–4682, 2014.

[163] I. H. M. van Stokkum, D. S. Larsen, and R. van Grondelle. Global and target analysis of time-resolved spectra. *Biochimica et Biophysica Acta*, 1657:82–104, 2004.

[164] H. Tetsuka, A. Nagoya, T. Fukusumi, and T. Matsui. Molecularly designed, nitrogen-functionalized graphene quantum dots for optoelectronic devices. *Advanced Materials*, 28(23):4632–4638, 2016.

[165] L. Wang, S.-J. Zhu, H.-Y. Wang, Y.-F. Wang, Y.-W. Hao, J.-H. Zhang, Q.-D. Chen, Y.-L. Zhang, W. Han, B. Yang, and H.-B. Sun. Unraveling bright molecule-like state and dark intrinsic state in green-fluorescence graphene quantum dots via ultrafast spectroscopy. *Advanced Optical Materials*, 1(3):264–271, 2013.

[166] X. Wen, P. Yu, Y.-R. Toh, X. Hao, and J. Tang. Intrinsic and extrinsic fluorescence in carbon nanodots: Ultrafast time-resolved fluorescence and carrier dynamics. *Advanced Optical Materials*, 1(2):173–178, 2013.

[167] P. Yu, X. Wen, Y.-R. Toh, Y.-C. Lee, K.-Y. Huang, S. Huang, S. Shrestha, G. Conibeer, and J. Tang. Efficient electron transfer in carbon nanodot-graphene oxide nanocomposites. *J. Mater. Chem. C*, 2:2894–2901, 2014.

[168] Victor I. Klimov. Spectral and dynamical properties of multiexcitons in semiconductor nanocrystals. *Annual Review of Physical Chemistry*, 58:635–673, 2008.

[169] Z. Zhu, J. Ma, Z. Wang, C. Mu, Z. Fan, L. Du, Y. Bai, L. Fan, H. Yan, D. L. Phillips, and S. Yang. Efficiency enhancement of perovskite solar cells through fast electron extraction: The role of graphene quantum dots. *Journal of the American Chemical Society*, 136(10):3760–3763, 2014.

[170] J. T. Margraf, F. Lodermeyer, V. Strauss, P. Haines, J. Walter, W. Peukert, R. D. Costa, T. Clark, and D. M. Guldi. Using carbon nanodots as inexpensive and environmentally friendly sensitizers in mesoscopic solar cells. *Nanoscale Horiz.*, 1:220–226, 2016.

[171] K. J. Williams, C. A. Nelson, X. Yan, L.-S. Li, and X. Zhu. Hot electron injection from graphene quantum dots to tio_2. *ACS Nano*, 7(2):1388–1394, 2013.

[172] V. Strauss, J. T. Margraf, K. Dirian, Z. Syrgiannis, M. Prato, C. Wessendorf, A. Hirsch, T. Clark, and D. M. Guldi. Carbon nanodots: Supramolecular electron donor–acceptor hybrids featuring perylenediimides. *Angewandte Chemie International Edition*, 54(28):8292–8297, 2015.

[173] D. H. Hasenohrl, A. Saha, V. Strauss, L. Wibmer, S. Klein, D. M. Guldi, and A. Hirsch. Bulbous gold-carbon nanodot hybrid nanoclusters for cancer therapy. *J. Mater. Chem. B*, 5:8591–8599, 2017.

[174] G. B. Rybicki and A. P. Lightman. *Radiative processes in Astrophysics*. Wiley-vch, 2004.

[175] M. Weissbluth. *Photon-Atom Interactions*. Academic Press, inc, 1989.

[176] P. Atkins and R. Friedman. *Molecular quantum mechanics*. Oxford University Press, 2005.

[177] M. Weissbluth. *Atoms and Molecules*. Academic Press, inc, 1978.

[178] Joseph R. Lakowicz. *Principles of fluorescence spectroscopy*. Springer, third edition, 2006.

[179] B. Valeur. *Molecular Fluorescence Principles and Applications*. Wiley-vch, 2001.

[180] W. W. Parson. *Modern Optical Spectroscopy*. Springer, 2015.

[181] S. J. Strickler and R. A. Berg. Relationship between absorption intensity and fluorescence lifetime of molecules. *The Journal of Chemical Physics*, 37(4):814–822, 1962.

[182] G. Brancato, G. Signore, P. Neyroz, D. Polli, G. Cerullo, G. Abbandonato, L. Nucara, V. Barone, F. Beltram, and R. Bizzarri. Dual fluorescence through kasha's rule breaking: An unconventional photomechanism for intracellular probe design. *The Journal of Physical Chemistry B*, 119(20):6144–6154, 2015.

[183] R. Jimenex, G. R. Fleming, P. V. Kumar, and M. Maroncelli. Femtosecond solvation dynamics of water. *Nature*, 369:471–473, 1994.

[184] M. L. Horng, J. A. Gardecki, A. Papazyan, and M. Maroncelli. Subpicosecond measurements of polar solvation dynamics: Coumarin 153 revisited. *J. Phys. Chem.*, 99:17311–17337, 1995.

[185] P. A. Demchenko. The red-edge effects: 30 years of exploration. *Luminescence*, 17:19–42, 2002.

[186] P. A. Demchenko. Chapter 4: Site-selective red-edge effects. In *Fluorescence Spectroscopy*, volume 450 of *Methods in Enzymology*, pages 59 – 78. Academic Press, 2008.

[187] P. Ferrut, N. Mauro, A. Manfredi, and E. Ranucci. Hetero-difunctional dimers as building blocks for the synthesis of poly amidoamine s with hetero-difunctional chain terminals and their derivatives. *J of Polym Sci A: Polym Chem*, 50:4947–4957, 2012.

[188] C. Ruckebusch, M. Sliwa, P. Pernot, A. de Juan, and R. Tauler. Comprehensive data analysis of femtosecond transient absorption spectra: A review. *Journal of Photochemistry and Photobiology C: Photochemistry Reviews*, 13:1–27, 2012.

[189] Claude Rullière. *Femtosecond Laser Pulses Principles and Experiments*. Springer, 2003.

[190] Jean-Claude Diels and Wolfgang Rudolph. *Ultrashort Laser Pulse Phenomena*. Elsevier, 2006.

[191] G. Cerullo and S. De Silvestri. Ultrafast optical parametric amplifiers. *Review of scientific instruments*, 74, 2002.

[192] Robert R. Alfano. *The Supercontinuum Laser Source*. Springer, 2006.

[193] C. Gadarmaier, V. V. Kabanov, A. S. Alexandrov, L. Stojchevska, T. Mertelj, C. Manzoni, G. Cerullo, N. D. Zhigadlo, J. Karpinski, Y. Q. Cai, X. Yao, Y. Toda, M. Oda, S. Sugai, and D. Mihailovic. High superconducting critical temperatures depend systematically on the electron-phonon interaction strength. *Phys. Rev.*, 4, 2014.

[194] M. Nazari Haghighi Pashaki. *Long-Range Energy Transfer in DNA-Hosted Multichromophoric Systems by Ultrafast 1D and 2D fs UV-Vis Transient Absorption Spectroscopy*. Ph.d. thesis, University of Bern, 2018.

[195] M. Akbarimoosavi. *THz Stark Spectroscopy of Molecules and Solids*. Ph.d. thesis, University of Bern, 2017.

[196] A. Maciejewski, R. Naskrecki, M. Lorenc, M. Ziolek, J. Karolczak, J. Kubicki, and M. Matysiak, M. Szymanski. Transient absorption experimental set-up with femtosecond time resolution. femto- and picosecond study of dcm molecule in cyclohexane and methanol solution. *Journal of Molecular Structure*, 555:1–13, 2000.

[197] R. Garcia. *Amplitude Modulation Atomic Force Microscopy*. Wiley-VCH, 2010.

[198] R. F. Egerton. *Physical Principles of Electron Microscopy*. Springer, 2005.

[199] M. Zelisko, Y. Hanlumyuang, S. Yang, Y. Liu, C. Lei, J. Li, P. M. Ajayan, and P. Sharma. Anomalous piezoelectricity in two-dimensional graphene nitride nanosheets. *Nature Communications*, 5:4284, 2014.

[200] F. Messina, L. Sciortino, R. Popescu, A. M. Venezia, A. Sciortino, G. Buscarino, S. Agnello, R. Schneider, D. Gerthsen, M. Cannas, and F. M. Gelardi. Fluorescent nitrogen-rich carbon nanodots with an unexpected $\beta - c_3n_4$ nanocrystalline structure. *J. Mater. Chem. C*, 4:2598–2605, 2016.

[201] D. W. He, F. X. Zhang, X. Y. Zhang, Z. C. Qin, M. Zhang, R. P. Liu, Y. F. Xu, and W. K. Wang. Synthesis of carbon nitride crystals at high pressures and temperatures. *Journal of Materials Research*, 13(12):3458–3462, 1998.

[202] Y.-A. Li, S. Xu, H.-S. Li, and W.-Y. Luo. Polycrystalline carbon nitride $\beta - c_3n_4$ films synthesized by radio frequency magnetron sputtering. *Journal of Materials Science Letter*, 17(1):31–35, 1998.

[203] M. Marqués, J. Osorio, R. Ahuja, M. Flórez, and J. M. Recio. Pressure effects on the structure and vibrations of β- and $\gamma-c_3n_4$. *Phys. Rev. B*, 70:104114, 2004.

[204] L.-W. Yin, M.-S. Li, G. Luo, J.-L. Sui, and J.-M. Wang. Nanosized beta carbon nitride crystal through mechanochemical reaction. *Chemical Physics Letters*, 369(3):483 – 489, 2003.

[205] L. Fang, H. Ohfuji, T. Shinmei, and T. Irifune. Experimental study on the stability of graphitic c_3n_4 under high pressure and high temperature. *Diamond and Related Materials*, 20(5):819 – 825, 2011.

[206] A. Sciortino, N. Mauro, G. Buscarino, L. Sciortino, R. Popescu, R. Schneider, G. Giammona, D. Gerthsen, M. Cannas, and F. Messina. $\beta - c_3n_4$ nanocrystals: Carbon dots with extraordinary morphological, structural, and optical homogeneity. *Chemistry of Materials*, 30(5):1695–1700, 2018.

[207] F. Yuan, T. Yuan, L. Sui, Z. Wang, Z. Xi, Y. Li, X. Li, L. Fan, Z. Tan, A. Chen, M. Jin, and S. Yang. Engineering triangular carbon quantum dots with unprecedented narrow bandwidth emission for multicolored leds. *Nature Communications*, 9:2249, 2018.

[208] J. Hu, P. Jang, and C. M. Lieber. Nitrogen-drive sp^3 to sp^2 transformation in carbon nitride materials. *Physical Review B*, 57:R3185, 1998.

[209] X. Yan, X. Cui, B. Li, and L.-S. Li. Large, solution-processable graphene quantum dots as light absorbers for photovoltaics. *Nano Letters*, 10(5):1869–1873, 2010.

[210] U. Resch-Genger, M. Grabolle, S. Cavaliere-Jaricot, R. Nitschke, and T. Nann. Quantum dots versus organic dyes as fluorescent labels. *Nature Methods*, 5:763–775, 2008.

[211] W. W. Yu, L. Qu, W. Guo, and X. Peng. Experimental determination of the extinction coefficient of cdte, cdse, and cds nanocrystals. *Chemistry of Materials*, 15(14):2854–2860, 2003.

[212] C. A. Leatherdale, W.-K. Woo, F. V. Mikulec, and M. G. Bawendi. On the absorption cross section of cdse nanocrystal quantum dots. *The Journal of Physical Chemistry B*, 106(31):7619–7622, 2002.

[213] H. Zhu, W. Zhang, and S. F. Yu. Realization of lasing emission from graphene quantum dots using titanium dioxide nanoparticles as light scatterers. *Nanoscale*, 5, 2013.

[214] W. F. Zhang, H. Zhu, S. F. Yu, and H. Y. Yang. Observation of lasing emission from carbon nanodots in organic solvents. *Advanced Materials*, 24, 2012.

[215] W. Zhang, Y. Ni, X. Xu, W. Lu, P. Ren, P. Yan, C. K. Siu, S. Ruan, and S. F. Yu. Realization of multiphoton lasing from carbon nanodot microcavities. *Nanoscale*, 9:5957–5963, 2017.

[216] Luisa Sciortino, Alice Sciortino, Radian Popescu, Reinhard Schneider, Dagmar Gerthsen, Simonpietro Agnello, Marco Cannas, and Fabrizio Messina. Tailoring the emission color of carbon dots through nitrogen-induced changes of their crystalline structure. *The Journal of Physical Chemistry C*, 122(34):19897–19903, 2018.

[217] M. J. Kamlet, J. L. M. Abboud, M. H. Abraham, and R. W. Taft. Linear solvation energy relationships. 23. a comprehensive collection of the solvatochromic parameters, π^*, α, and β, and some methods for simplifying the generalized solvatochromic equation. *The Journal of Organic Chemistry*, 48(17):2877–2887, 1983.

[218] C. Reichardt. Solvatochromic dyes as solvent polarity indicators. *Chemical Reviews*, 94(8):2319–2358, 1994.

[219] A. Sciortino, E. Marino, B. van Dam, P. Schall, M. Cannas, and F. Messina. Solvatochromism unravels the emission mechanism of carbon nanodots. *The Journal of Physical Chemistry Letters*, 7(17):3419–3423, 2016.

[220] P. Kumar and H.B. Bohidar. Observation of fluorescence from non-functionalized carbon nanoparticles and its solvent dependent spectroscopy. *Journal of Luminescence*, 141:155 – 161, 2013.

[221] S. Mukherjee, E. Prasad, and A. Chadha. H-bonding controls the emission properties of functionalized carbon nano-dots. *Phys. Chem. Chem. Phys.*, 19:7288–7296, 2017.

[222] S. S. Jones, P. Sahatiya, and S. Badhulika. One step, high yield synthesis of amphiphilic carbon quantum dots derived from chia seeds: a solvatochromic study. *New J. Chem.*, 41:13130–13139, 2017.

[223] A. Pramanik, S. Biswas, and P. Kumbhakar. Solvatochromism in highly luminescent environmental friendly carbon quantum dots for sensing applications: Conversion of bio-waste into bio-asset. *Spectrochimica Acta Part A: Molecular and Biomolecular Spectroscopy*, 191:498 – 512, 2018.

[224] J. Luo, B. Wen, and R. Melnik. Relative stability of nanosized $\beta - c_3n_4$ and graphitic-c_3n_4 from first principles calculations. *Physica E: Low-dimensional Systems and Nanostructures*, 45:190 – 193, 2012.

[225] Messina F., Prèmont-Schwarz M., Braem O., Xiao D., Batista V. S., Nibbering E. T. J., and Chergui M. Ultrafast solvent-assisted electronic level crossing in 1-naphthol. *Angewandte Chemie International Edition*, 52(27):6871–6875, 2013.

[226] Mohammed O. F., Kwon O.-H., Othon C. M., and Zewail A. H. Charge transfer assisted by collective hydrogen-bonding dynamics. *Angewandte Chemie International Edition*, 48(34):6251–6256, 2009.

[227] A. Sciortino, A. Cayuela, M. L. Soriano, F. M. Gelardi, M. Cannas, M. Valcarcel, and F. Messina. Different natures of surface electronic transitions of carbon nanoparticles. *Phys. Chem. Chem. Phys.*, 19:22670–22677, 2017.

[228] A. Cayuela, M.L. Soriano, S.R. Kennedy, J.W. Steed, and M. Valcárcel. Fluorescent carbon quantum dot hydrogels for direct determination of silver ions. *Talanta*, 151:100 – 105, 2016.

[229] Strauss V., Kahnt A., Zolnhofer E. M., Meyer K., Maid H., Placht C., Bauer W., Nacken T. J., Peukert W., Etschel S. H., Halik M., and Guldi D. M. Assigning electronic states in carbon nanodots. *Advanced Functional Materials*, 26(44):7975–7985, 2016.

[230] Xiaohua Shen and Jay R. Knutson. Femtosecond internal conversion and reorientation of 5-methoxyindole in hexadecane. *Chemical Physics Letters*, 339(3):191 – 196, 2001.

[231] S. Zhu, J. Shao, Y. Song, X. Zhao, J. Du, L. Wang, H. Wang, K. Zhang, J. Zhang, and B. Yang. Investigating the surface state of graphene quantum dots. *Nanoscale*, 7:7927–7933, 2015.

[232] A. Sciortino, A. Madonia, M. Gazzetto, L. Sciortino, E. J. Rohwer, T. Feurer, F. M. Gelardi, M. Cannas, A. Cannizzo, and F. Messina. The interaction of photoexcited carbon nanodots with metal ions disclosed down to the femtosecond scale. *Nanoscale*, 9:11902–11911, 2017.

[233] S. Mondal, T. Das, P. Ghosh, A. Maity, A. Mallick, and P. Purkayastha. Surfactant chain length controls photoinduced electron transfer in surfactant bilayer protected carbon nanoparticles. *Materials Letters*, 141:252 – 254, 2015.

[234] Martindale B. C. M., Hutton G. A. M., Caputo C. A., Prantl S., Godin R., Durrant J. R., and Reisner E. Enhancing light absorption and charge transfer efficiency in carbon dots through graphitization and core nitrogen doping. *Angewandte Chemie International Edition*, 56(23):6459–6463, 2017.

[235] F. Messina, O. Bram, A. Cannizzo, and M. Chergui. Real-time observation of the charge transfer to solvent dynamics. *Nature Comm.*, 4:2119, 2013.

[236] Alice Sciortino, Michela Gazzetto, Gianpiero Buscarino, Radian Popescu, Reinhard Schneider, Gaetano Giammona, Dagmar Gerthsen, Egmont J. Rohwer, Nicolò Mauro, Thomas Feurer, Andrea Cannizzo, and Fabrizio Messina. Disentangling size effects and spectral inhomogeneity in carbon nanodots by ultrafast dynamical hole-burning. *Nanoscale*, 10:15317–15323, 2018.

[237] S. C. Doan and B. J. Schwartz. Nature of excess electrons in polar fluids: Anion-solvated electron equilibrium and polarized hole-burning in liquid acetonitrile. *The Journal of Physical Chemistry Letters*, 4(9):1471–1476, 2013.

[238] K. Nishiyama, T. Honda, H. Reis, U. Muller, K. Mullen, W. Baumann, and T. Okada. Electronic structures of 9,10-anthrylene dimers and trimers in solution: formation of charge separation states depending on alkyl substituent groups. *The Journal of Physical Chemistry A*, 102(17):2934–2943, 1998.

[239] T. R. Middendorf, L. T. Mazzola, D. F. Gaul, C. C. Schenck, and S. G. Boxer. Photochemical hole-burning spectroscopy of a photosynthetic reaction center mutant with altered charge separation kinetics: properties and decay of the initially excited state. *The Journal of Physical Chemistry*, 95(24):10142–10151, 1991.

[240] T. A. Gellen, J. Lem, and D. B. Turner. Probing homogeneous line broadening in cdse nanocrystals using multidimensional electronic spectroscopy. *Nano Letters*, 17(5):2809–2815.

Acknowledgements

Doing a PhD research has been one of the best experiences I have ever done. Despite some insanities (everybody becomes crazy during a PhD... and this happens also to me!), the PhD period was very funny, and I am really sad about its end. These three years have been full of news and events, and facing them allowed me to learn a lot from a professional point of view but mostly allows me to learn a lot about myself and about my capabilities. This period would not be such important for me without a lot of people which contributed to make these years so rich and pleasant, so for this reason, I wish to thank all of them.

First and foremost, I wish to express my infinite gratitude to Fabrizio. I thank you as my supervisor but mostly I thank you as a friend who taught me a lot, who learnt with me a lot, who supported and encouraged me constantly during these years, and who listened me when I freaked out. I thank you for having played (...danced and sung...) with me in the lab and for having made funny all the work. I thank you for all the interesting discussions and for your great passion for this work. You have been able to transmit this passion to me, and I will be for ever grateful for this.

I would like to thank my colleagues and friends who shared with me my PhD period and my (our!)...PhD room: Michela, Luisa, Luisella, Angelo, Piero, Angela, Mattia. Our days together, our discussions, our shared lunches have been very important during these years... so, thank you guys! :)

Of course, I would like to thank the "senior" part of the group: Franco, Marco, Simone and Gianpiero. I thank you for having welcomed me in the group, for the scientific discussions and for the continuously support.

I wish to thank the swiss part of my PhD research. I would like to thank my supervisor, Andrea. I thank you for having welcomed me in your group, and for the possibility to learn and do science outside of my country. I am grateful for the deep and long discussions which have been fundamental for my scientific formation.

I would like to thank Michela and Maryam who welcomed me in Bern, with you the days in the lab .... were not so long.

In these years, the support of my family and my friends has been fundamental. I thank the "Giampaoli worldwide" group for being always with me despite the distance. I am very lucky to have you as friends.

I want to express my gratitude to my family. You have been always to my side, supporting me and pushing me to face the difficulties, and I will be for ever grateful for this.

Last but not least, I thank the person who was always with me: Salvo. You always encouraged me and always believed in me when I needed it more. I am very lucky to have you by my side and I will never stop to thank you for this.

Scientific Publications

- **Carbon Nanodots: a Review. From the Current Understanding of the Fundamental Photophysics to the Full Control of the Optical Response.**. A. Sciortino, A. Cannizzo, F. Messina. Submitted to C. Invited article.

- **Carbon Dots Dispersed on Graphene/SiO_2/Si: a Morphological Study** G. Faggio, A. Gnisci, G. Messina, N. Lisi, A. Capasso, G. H. Lee, A. Armano, A. Sciortino, F. Messina, M. Cannas, F. M. Gelardi , E. Schilirò, F. Giannazzo, S. Agnello. Submitted to Physica Status Solidi A.

- **Photoinduced charge transfer from Carbon Dots to Graphene in solid composite** A. Armano, G. Buscarino, F. MEssina, A. Sciortino, M. Cannas, F. M. Gelardi, F. Giannazzo, E. Schilirò, S. Agnello. Submitted to Thin Solid Films.

- **Tailoring the Emission Color of Carbon dots through Nitrogen-induced Changes of their Crystalline Structure**. L. Sciortino, A. Sciortino, R. Popescu, R. Schneider, D. Gerthsen, S. Agnello, M. Cannas, F. Messina. The Journal of Physical Chemistry C, 2018, 122, 19897-19903

- **One-pot synthesis of graphene quantum dot and simultaneous nanostructured self-assembly via a novel microwave-assisted method: Impact on triazines removal and efficiency monitoring**. B. Fresco-Cala, M. L. Soriano, A. Sciortino, M. Cannas, F. Messina, M. Cardenas. RSC Advances, 2018, 8, 29939-29946

- **Disentangling Size Effects and Spectral Inhomogeneity in Carbon Nitride Nanodots by Ultrafast Dynamical Hole-Burning**. A. Sciortino, M. Gazzetto, G. Buscarino R. Popescu, R. Schneider, G. Giammona, D. Gerthsen, Egmont J. Rohwer, N. Mauro, T. Feurer, A. Cannizzo, F. Messina. Nanoscale, 2018, 10, 15317-15323

- $\beta - C_3N_4$ **nanocrystals: Carbon dots with extraordinary Morphological, Structural and Optical Homogeneity**. A. Sciortino, N. Mauro, G. Buscarino, L. Sciortino, R. Popescu, R. Schneider, G. Giammona, D. Gerthsen, M. Cannas, F. Messina. Chemistry of Materials, 2018, 30, 1695-1700.

- **Characteristic Excitation Wavelength Dependence of Fluorescence Emissions in Carbon "Quantum" Dots**. G. LeCroy, F. Messina, A. Sciortino, C. Bunker, P. Wang, S. K. A. Fernando, Y-.P. Sun. The Journal of Physical Chemistry C, 2017, 50, 28180-28186.

- **Different Natures of Surface Electronic Transitions of Carbon Nanoparticles**. A. Sciortino, A. Cayuela, M. L. Soriano, F. M. Gelardi, M. Cannas, M. Varcàrcel and F. Messina. Physical Chemistry Chemical Physics, 2017, 19, 22670.

  Selected for **2017 PCCP HOT Articles**

- **The interaction of photoexcited Carbon nanodots with metal ions disclosed down to the femtosecond scale**. A. Sciortino, A. Madonia, M. Gazzetto, L. Sciortino, E.J. Rohwer, T. Feurer, F. M. Gelardi, M. Cannas, A. Cannizzo, F. Messina. Nanoscale, 2017, 9, 11902.

  Selected for back cover of the journal.

- **Solvatochromism Unravels the Emission Mechanism of Carbon Nanodots**. A. Sciortino, E. Marino, B. van Dam, P. Schall, M. Cannas, F. Messina. The Journal of Physical Chemistry Letters, 2016, 7, 3419-3423.

- **Fluorescent nitrogen-rich carbon nanodots with a β-C_3N_4 nanocrystalline structure**. F. Messina, L. Sciortino, R. Popescu, A.M. Venezia, A. Sciortino, G. Buscarino, S. Agnello, R. Schneider, D. Gerthsen, M. Cannas, F. M. Gelardi. Journal of Materials Chemistry C, 2016, 4, 2598-2605.